

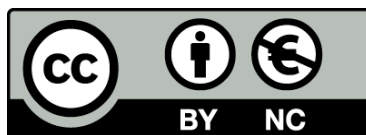


UNIVERSITAT<sub>DE</sub>  
BARCELONA

## Image processing techniques for plant phenotyping using RGB and thermal imagery

Técnicas de procesamiento de imágenes RGB y térmicas  
como herramienta para fenotipado de cultivos

José Armando Fernández Gallego



Aquesta tesi doctoral està subjecta a la llicència **Reconeixement- NoComercial 4.0. Espanya de Creative Commons.**

Esta tesis doctoral está sujeta a la licencia **Reconocimiento - NoComercial 4.0. España de Creative Commons.**

This doctoral thesis is licensed under the **Creative Commons Attribution-NonCommercial 4.0. Spain License.**



**IMAGE PROCESSING TECHNIQUES  
FOR PLANT PHENOTYPING USING  
RGB AND THERMAL IMAGERY**

Jose A. Fernandez-Gallego

UNIVERSITAT DE BARCELONA

IMAGE PROCESSING TECHNIQUES FOR PLANT PHENOTYPING USING RGB AND THERMAL IMAGERY

Jose A. Fernandez-Gallego

Doctoral Thesis  
BARCELONA, 2019



**IMAGE PROCESSING TECHNIQUES FOR PLANT PHENOTYPING USING  
RGB AND THERMAL IMAGERY**

**TÉCNICAS DE PROCESAMIENTO DE IMÁGENES RGB Y TÉRMICAS  
COMO HERRAMIENTA PARA FENOTIPADO DE CULTIVOS**

Memoria presentada por Jose Armando Fernández Gallego para optar el título de Doctor de la Universitat de Barcelona. Este trabajo se enmarca dentro del programa de doctorado de Biología Vegetal de la Facultad de Biología de la Universidad de Barcelona. Este trabajo se realizó en el Departamento de Biología Evolutiva, Ecología y Ciencias Ambientales, Unidad de Fisiología Vegetal de la Facultad de Biología de la Universidad de Barcelona bajo la dirección del Dr. José Luis Araus y el Dr. Shawn Carlisle Kefauver.

Doctorando

**Jose Armando Fernández Gallego**

Director y tutor

Director

**Dr. Jose Luis Araus Ortega**

**Dr. Shawn Carlisle Kefauver**



UNIVERSITAT DE  
BARCELONA



BARCELONA, SEPTIEMBRE 2019



*a Vivi por hacer parte cada día de este proceso,  
a ella todo mi agradecimiento y admiración.*

*a mi Familia por ser verdaderamente ellos los que  
motivaron en mi el gusto por el aprendizaje  
serán siempre mi mayor ejemplo.*



# Content

<u>ACKNOWLEDGMENTS</u>	<u>7</u>
<u>INTRODUCTION</u>	<u>9</u>
1. CEREALS, CLIMATE CHANGE AND PHENOTYPING FOR GLOBAL FOOD SECURITY	11
2. IMAGING, APPLICATIONS AND PLATFORMS FOR PLANT PHENOTYPING	14
3. DIGITAL IMAGE PROCESSING AND MACHINE LEARNING FOR PLANT PHENOTYPING	22
<u>OBJECTIVES</u>	<u>25</u>
<u>REPORT OF THE THESIS DIRECTORS</u>	<u>29</u>
<u>RESULTS</u>	<u>39</u>
CHAPTER 1	41
CHAPTER 2	61
CHAPTER 3	75
CHAPTER 4	117
CHAPTER 5	135
<u>DISCUSSION</u>	<u>153</u>
1. EAR COUNTING USING IMAGE PROCESSING SYSTEMS	156
2. PHOTOSYNTHETIC AREA OF THE CANOPY USING IMAGE PROCESSING SYSTEMS	160
3. EQUIPMENT CONSIDERATIONS AND FUTURE WORKS	164
<u>CONCLUSIONS</u>	<u>169</u>
<u>RESUMEN DE LA TESIS</u>	<u>175</u>
<u>REFERENCES</u>	<u>189</u>





## **Acknowledgments**

La primera persona que conocí al llegar a la Universidad fue la Dr. Isabel Muñoz, mi más sincero agradecimiento por ayudarme en esta primera etapa, se hizo fácil el ingreso al programa gracias a su apoyo. Nunca olvidaré el grato recibimiento al grupo por parte de Rut y Shawn, fue muy importante para mi empezar a ser parte del grupo de esta forma. Muchas gracias Jose Luis y Dolors por darnos a Vivi y a mi la bienvenida a la ciudad, sus recomendaciones nos ayudaron a iniciar nuestra estancia mucho mejor.

A mis directores de tesis, Jose Luis y Shawn, mil gracias por su paciencia y ayuda, por todas las correcciones y retos; pero sobre todo por enseñarme, sin que fueran conscientes, lo valioso de ser una persona sencilla desde el trabajo de campo hasta la presentación de los resultados. Muchas gracias a Nieves y Mariate por ayudarme durante todo este tiempo con el difícil trabajo de campo y todas las dudas que iban surgiendo sobre el ensayo. Muchas gracias a los integrantes del grupo; Jordi Bort, Dolors, Rut, Rubén, Cristina, Susan, Omar, Fadia, Adrián, Luisa, Fatima, Thomas, Melissa y Joel por ayudarme a entender conceptos e ideas que estaban fuera de mi alcance, todos ellos hacen parte activa de este trabajo.

A la Gobernación del Tolima (Colombia) por apostar por la educación a través del proyecto “Formación del Talento Humano de Alto Nivel” liderado por la Universidad del Tolima. Muchas gracias al director del proyecto Jonh Jairo Méndez, la coordinadora Angélica Torres, a Ángela Collazos, Julián Murillo, Gustavo Gallardo y Katherine Leiva por su disposición y ayuda ante todas las

dudas y trámites a lo largo de este proceso, ellos hicieron posible la realización de este trabajo.

Muchas gracias a nuestras Familias, bien saben todo el aprecio y cariño que les tenemos, no fue fácil para Vivi y para mi alejarnos, pero todo fue más fácil con su apoyo. Muchas gracias a los amigos que fui conociendo poco a poco en el transcurso de este trabajo y a los amigos de siempre.





## **GENERAL INTRODUCTION**

### **1. Cereals, climate change and phenotyping for global food security**

World cereal stocks need to increase in order to meet growing demands (FSIN, 2017). Currently, maize, rice, wheat, are the main crops worldwide, while other cereals such as barley, sorghum, oat or different millets are also well placed in the top list; in 2019 FAO's forecast an increase in the cereal production of 1.2% from 2018, to 2.685 million tons. As a reduction in maize production is expected and rice production is likely to remain similar to previous years, the increase in the cereal production globally is attributed to wheat and barley (FAO, 2019). Europe contributes with around 20% of the global cereal production, consisting mostly of wheat and barley covering more than the 70% of the cultivated area (Schils et al., 2018).

Crop productivity is affected directly by climate change factors such as heat, drought, floods or storms. In fact, in countries experiencing high exposure and risk related to climate variability and extremes, at least the 80% of the interannual production variability can be explained by climate related factors (FAO et al., 2018). Researchers agree that global climate change is having a major impact on crop productivity (Wang et al., 2018). Moreover, the temperatures are anticipated to rise by at least 0.2 °C per decade over the next 30 years and additionally, by the end of this century, the temperature will increase by up to 4.5°C (Bernstein et al., 2008). Directly, this global warming will increase plant respiration (not only dark respiration but also photorespiration) rates, while shortening crop duration, and therefore will reduce crop productivity and yield (Wang et al., 2018).

In that way, several studies have been focused on climate change scenarios and more specifically abiotic stresses in cereals. For instance, in the case of heat stress, high temperatures between anthesis to grain filling can decrease grain yield (Asseng et al., 2011), most likely due to the reduced time to capture resources related to accelerated senescence (Farooq et al., 2011). Water stress either associated to a decrease in precipitation, due to an increase in the heat-driven transpirative demand, or both together, can result in stomatal closure as a means to reduce the loss of water, subsequently causing leaf temperatures to increase (Vicente et al., 2018). Salinity stress, often due to rising sea levels (a direct by product of temperature increases causing ice melting and subsequent expansion of sea water volumes globally) can also affect plant cereal growth and grain yield (Abhinandan et al., 2018; Coccozza et al., 2013).

In order to deal with the climate change and future environmental scenarios, plant breeding is one of the main alternatives (Araus et al., 2018; Araus and Kefauver, 2018); breeding is even considered to contribute to the larger component of yield growth compared to management (Fischer and Edmeades, 2010). Plant breeding programs are focused on identifying genotypes with high yields and quality to act as a parentals and further the best individuals among the segregating population thus develop new varieties of plants. Breeders use the phenotypic data, plant and crop performance, and genetic information to improve the yield by selection (GxE, with G and E indicating genetic and environmental factors) (Fischer and Edmeades, 2010). More factors must be taken into account to increase the yield, such as, for instance, the education of farmers, economic incentives and the use of new technologies (GxExM, with M indicating management). This process started in the twentieth century when evolution

principles became firmly established. In order to develop new varieties, the experimental design in plant breeding has been established through different spatial approaches and multisite scheme. Thus for example randomized blocks; where each block or plot contain one variety, called randomized complete plot design (Bos and Caligari, 1995); or using split-plot replicates per each variety, called randomized split plot design (Sharma, 2006). Currently, this design is still used as a strategy to develop new varieties more resilient to environmental changes while the grain yield remains constant or increase. After the Green Revolution where semi-dwarf and dwarf cultivars were induced and thus a higher harvest index (HI) and yield were achieved (Sharma, 2006), a multidisciplinary approach, combining the different components of the breeding pipeline, is crucial to have a new Green Revolution (Martin-Guay et al., 2018). Among these components plant phenotyping is nowadays realized a major bottleneck limiting the genetic advance (Araus et al., 2018; Araus and Cairns, 2014).

Plant phenotyping have been carried out by farmers for a very long time as they, year after year, followed a natural tendency to select the best seed from the top performing varieties for replanting (Yol et al., 2015). Plant phenotyping is related with the observable (or measurable) characteristics of the plant while the crop growing as well as the association between the plant genetic background and its response to the environment (GxE). In traditional phenotyping the measurements are collated manually, which is tedious, time consuming and prone to subjective errors. Nonetheless, nowadays the technology is involved in many applications. From the point of view of plan phenotyping, technology has been incorporated as a tool. The use of image processing techniques integrating



sensors and algorithm processes, is therefore, an alternative to assess automatically (or semi-automatically) these traits.

## **2. Imaging, applications and platforms for plant phenotyping**

Images have become a useful tool for plant phenotyping because most frequently data from the sensors are processed and analyzed as an image in two (2D) or three (3D) dimensions (Pound and French, 2014). An image is the arrangement of pixels in a regular Cartesian coordinates as a matrix, each pixel has a numerical value into the matrix which represents the number of photons captured by the sensor within the exposition time (Peres, 2017). Therefore, an image is the optical representation of the object illuminated by a radiating source (Pitas, 2000). The main characteristics of images can be defined by the sensor spectral and spatial properties, with the spatial properties of the resulting image also heavily dependent on the sensor platform (which determines the distance from the target object).

### **2.1. Imaging spectrometers, wavelength spectrum**

Imaging spectrometers, or hyperspectral imagers, are designed to measure the energy or photons collected from an object. These sensors can be classified on two different categories based in: (i) the method by they achieve the spatial discrimination, and (ii) the method by they achieve spectral discrimination (Sellar and Boreman, 2005). Regarding spatial acquisition for images, there are two main technologies: (i) push-broom sensors, that scan the object in along-track and cross-track directions (pixels by pixel or by row of pixels), and (ii) frame sensors, that acquire a scene (all pixels at the same time) (Prieto-Blanco et al.,

2008). Regarding acquire discriminations for images, there are three main techniques: (i) filtering, that uses a band-pass optical filter, (ii) dispersive, that uses a prism, a grading, or its combination to spread out the wavelengths, and (iii) interferometric, that uses the calculation of the Fourier transform by two-beam interference to spectrally filter the image (Prieto-Blanco et al., 2008). As example, a conventional digital camera acquires the spectral information of three broad bands of the spectrum (red, green and blue); but also, hundreds of narrow different spectral bands can be acquired using hyperspectral sensors. It is close related with the sensor sensibility.

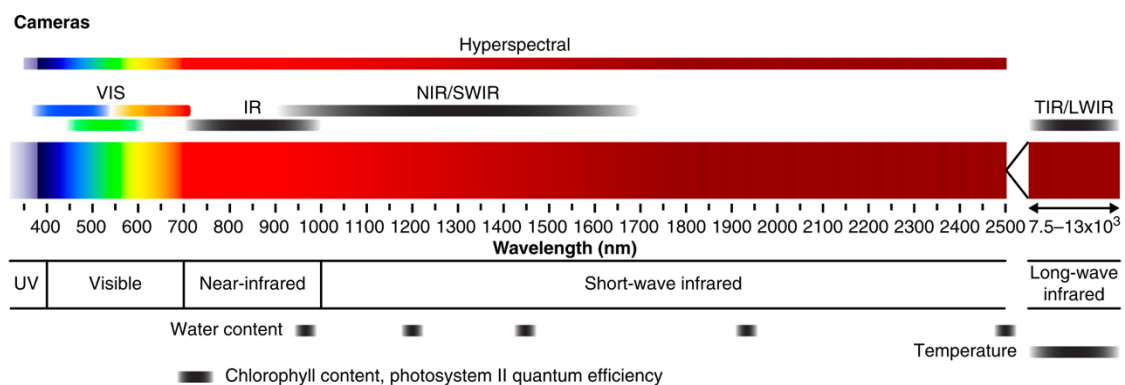


Figure 1. Wavelength spectrum and variety of camera sensors available to capture different wavelengths (Fahlgren et al., 2015). Ultraviolet (UV) cameras (Brugger et al., 2019). Visible (VIS) cameras. Infrared (IR) cameras detect near infrared (NIR) and short-wave infrared (SWIR). Thermal infrared (TIR) cameras detect long-wave infrared (LWIR). Hyperspectral cameras detect hundreds of spectral bands with nm-level resolution providing continuous coverage, often covering between 350 and 1000 nm or even reaching 2500 nm (Fahlgren et al., 2015). Multispectral cameras detect few spectral bands (usually from three to twelve bands) also from 350 to even 2500 nm (Lleó et al., 2009).

The sensor sensitivity defines the spectral and spatial characteristics that can be measured; and moreover, the wavelength is related to the technology of the sensor being used and the plant characteristics to be measured (L. Li et al., 2014) (Fig. 1). Camera or frame sensor devices are widely used, for instance, Red/Green/Blue (RGB) broad band multispectral cameras are used for visible wavelengths (VIS, 400-700 nm), and laser devices such as Light Detection and Ranging (LiDAR) sensor (visible red light, 650 nm). This wavelength range is associated with chlorophyll absorption primary in the blue and the red wavelengths and data acquisition for visual characteristics and structure of the plant and the canopy (Rasmussen et al., 2016). Near-infrared (NIR, 700-1000 nm) and shortwave infrared (SWIR, 1200-2500 nm) are associated with water absorption features and cellulose absorption in the region between 2200-2500 nm, for this absorption features, IR cameras are used (Manley et al., 2011; Perez-Sanz et al., 2017; Sankaran et al., 2015). Long wavelengths or thermal (LWIR, 7500-14000 nm) are most often used to study the dynamic plant responses related to water status and transpiration rates, where lower temperatures reflect higher rates of leaf transpiration due to the loss of energy from the latent heat of vaporization (Cozzolino, 2017; Fernandez-Gallego et al., 2019a; Hou et al., 2019). Recently, ultraviolet range (UV, 200-380 nm) have also been used for monitoring stress processes in barley through a UV camera under controlled conditions (Brugger et al., 2019).

## **2.2. Spatial resolution**

Spatial resolution is related to many factors like sensor field of view (FOV), distance between the sensor and the object of study, and the number of detectors

in the sensor. In aerial photogrammetry this resolution is referred as Ground Sampling Distance (GSD) and it refers to the area covered on the ground by a single pixel (Navulur, 2006). In the case of frame sensors like a RGB-camera sensor, the spatial resolution is related to the sensor size, image ratio, camera focal length and the distance between the camera and the object of study (Jensen, 2007). In general, the spatial resolution or GSD is mainly defined by the platform used such as satellite, aerial or ground platform (Fig. 2).

The spatial resolution cannot be easily changed in some cases, as for example in a satellite platform. While in aerial and ground platforms the spatial resolution can be defined in most cases using a higher/lower resolution sensor at a higher/lower distance, allowing more or less details of the object. Therefore, the spatial resolution specifications and the low- or high-resolution assumptions, depends exclusively on the application itself. In the same way, the concept of high resolution is relative to the image; if the image has more pixels than the number of pixels required to achieve the goals of the study, it can be considered high resolution.

### **2.3. Platform scale**

The platform scale and the spatial resolution are in fact closely related by the sensor resolution and technology (Fig. 2). The most common devices used for crop and plant phenotyping include multispectral, hyperspectral, thermal and fluorescence sensors mounted on a platform (Araus et al., 2018). The phenotyping platforms can be classified on three main categories:

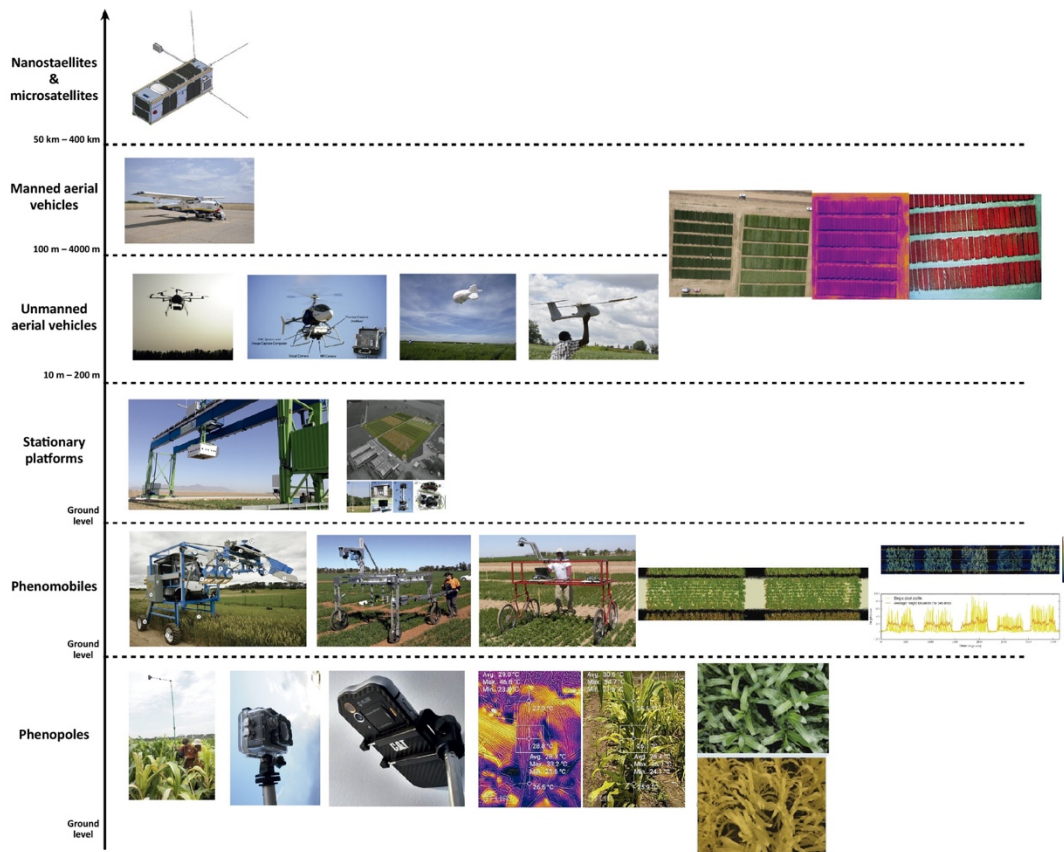


Figure 2. Phenotyping platforms scales from satellite to ground. Satellite, manned and unmanned aerial vehicles, phenotyping platforms, phenomobiles and phenopoles (Araus et al., 2018).

## Satellites

The biggest platform scale is the satellite (Fig. 2), where multispectral data and high spatial resolution are combined. At this scale, general details from the surface can be observed with a spatial resolution of meters [m] at height distances up to 400 km. For instance, the Sentinel-2 MSI sensor launched in 2015, it is located at approximately 800 km distance with 10 m and 20 m spatial resolution and sensor wavelengths from 443 nm to 2190 nm (Drusch et al., 2012). The WorldView-2 sensor allows spatial resolution up to 0.46 m (Tattaris et al., 2016). Satellite image data is mainly used for wide cover areas; it is a fast and

labor-saving tool, and furthermore, in most of cases, freely available and open access to users. Satellites have been used in related studies such as yellow rust discrimination for winter wheat (Zheng et al., 2018), leaf rust and infection levels discrimination in coffee (Chemura et al., 2017), identification of intra-field variations in winter wheat (Jeppesen et al., 2017), crop and tree species classification (Drusch et al., 2012), and for instance, fire burn severity discrimination (Drusch et al., 2012).

### **Aerial vehicles**

The next scale is related with aerial vehicles (Fig. 2), for this approach the multispectral sensors and spatial resolution can be fixed according to the requirements of each application, thus providing more control over image acquisition and image characteristics. In this case, sky conditions can be avoided before acquisition (sunny or cloudy conditions), optimal daytime can be selected (minimizing variation in solar view angle) and more information data can be also acquired. At this scale, more canopy detail can be observed with a spatial resolution of centimeters [cm] at height distances up to 4 km and 200 m for manned and unmanned aerial vehicle, respectively. For example, using distances up to 25 m, in the case of cereals, soil, leaves and ears can be differentiated. Several types of aerial vehicles have been used for phenotyping such as multi-rotors, helicopters, fixed-wing, blimps and flying wings (Yang et al., 2017). For instance, manned helicopters have been used to assess the canopy temperature in wheat (Deery et al., 2016) and crop status and land topographical features (Sugiura et al., 2003); as well as unmanned vehicles multi-rotor have been used for assessing grain yield and nitrogen use efficiency in barley

(Kefauver et al., 2017), phosphorous in maize (Gracia-Romero et al., 2017), automatic wheat ear counting (Fernandez-Gallego et al., paper under review), plant density estimation (Jin et al., 2017), growth status assessment in wheat (Du and Noguchi, 2017) and weed control (Gonzalez-de-Soto et al., 2016).

## **Ground platforms**

At ground scale and field conditions (Fig. 2); phenotyping platforms, ground vehicles and handheld alternatives have been widely used. Those alternatives allow to acquire more canopy detail from the multispectral sensors with a spatial resolution of millimeters [mm] at height distances up to 10 m. In the case of cereals, soil, leaves and ears, images can be acquired with considerably higher detail, compared to the previous larger scales, and sky conditions before acquisition and optimal daytime can be established. In addition, the close distance to the crops allows the use of low-cost sensors with high spatial resolution. As phenotyping platforms (Fig. 2), the ETH field phenotyping platform have been designed using a cable-suspended system above the crop (Spidercam system) in wheat, maize and soybean (Kirchgessner et al., 2017); this platform is used to assess canopy cover, canopy height and acquire thermal and multi-spectral imaging. The Scanalyzer platform is another example based on an industrial portal crane system (Virlet et al., 2017); this system can also assess canopy cover, canopy height, canopy temperature, heading and flowering time, and automatic wheat ear counting. A simple platform has been also used for assessing heading time in wheat using a conventional camera at 5 m above the crop (Zhu et al., 2016). As for terrestrial vehicles, wheeled vehicles are mainly used on difficult terrain conditions (Bonadies et al., 2016) for weed management

(Bawden et al., 2017) and estimate plant height, plant moisture content, tiller density and dry biomass in wheat (Busemeyer et al., 2013), three dimensional (3D) canopy structure in wheat (Liu et al., 2017), vegetation indexes and canopy temperature in cotton (Andrade-Sanchez et al., 2014). The wheeled vehicles, which use basic or standard wheels, (e.g. phenomobiles) (Fig. 2) are mainly used on flat terrain conditions and usually driven if motorized or pushed by the user; for instance, this alternative has been used for quantifying the plant height, ground cover and above-ground biomass in wheat (Jimenez-Berni et al., 2018) and wheat ear counting (Zhou et al., 2018a).

Finally, in the case of handheld alternatives; the data is acquired supporting the sensor by hand (or using a phenopole, Fig. 2) walking along the extent of the crop. Moreover, data can be acquired without previous training and may provide for more consistent results than afforded by the human eye, where subjectivity may influence quantification. For this approach, several studies have been also developed for instance, for counting individual red grapes in vineyards (Font et al., 2014), apple fruits (Stajanko et al., 2004), mango fruit (Payne et al., 2013), wheat ear counting (Cointault et al., 2008; Madec et al., 2019; Zhou et al., 2018b), wheat and barley ear counting (Fernandez-Gallego et al., 2019b, 2019a, 2018a, 2018b), blueberry identification (H. Li et al., 2014), segmentation of vegetation (Arroyo et al., 2016; Guo et al., 2017, 2013), canopy cover and photosynthetic area (Casadesús et al., 2007; Fernandez-Gallego et al., 2019c; Meyer and Neto, 2008; Power and Alessi, 1978; Wang et al., 2013; Woebbecke et al., 1995; Yu et al., 2017), crop sensibility to yellow rust in wheat (Vergara-Diaz et al., 2015), assessing maize lethal necrosis (Kefauver et al., 2016), estimating canopy



temperature in vineyards (Leinonen and Jones, 2004) and wheat (Thapa et al., 2018).

### 3. Digital image processing and machine learning for plant phenotyping

From the digital image processing point of view, an automatic image processing and quantification system is a pipeline system with four main steps (i) acquisition (ii) pre-processing (iii) segmentation and (iv) classification (Fig. 3).

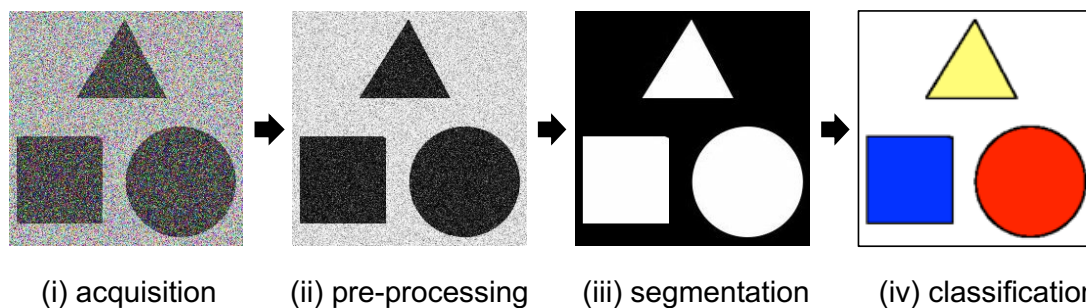


Figure 3. Pipeline image processing system example (i) acquisition: input image (ii) pre-processing: useless information is avoided (iii) segmentation: areas of interests are isolated (iv) classification: areas are labeled.

In each step, different algorithm techniques are used in order to interpret images much as human do but with the use of more quantitative than qualitative metrics that can provide greater precision and consistency (Jähne, 2005). Although in fact, image interpretation can be conducted by human eye inspection from the acquisition step onwards and avoiding further steps; the image processing systems have been introduced in order to deal with repetitive and tedious processes, subjective measurements, automatic object identification and, in general, to interpret visual appearance or geometric properties and transform

it into another type of dataset (Aber et al., 2010). Therefore, each step in the pipeline system (Fig. 3) has a specific task: (i) in the acquisition step, the image data is recorded. Properties such as spatial resolution, light conditions, camera technology, file and data format and calibration are defined (Sonka et al., 1993); (ii) the pre-processing step is mainly related with the improvement of the image, avoiding distortions or enhancing features that contribute to the next image processing step (Sonka et al., 1993); (iii) then, the image analysis pipeline may continue to the segmentation phase, which is one of the most important and difficult tasks in image processing (Tyagi, 2018); this step recognizes the areas, pixel or pixels, where the object of study is in the image and, in that way, the image is divided into parts to provide the spatial location of each object; (iv) the classification step identifies by labels each segmented object (Vasuki and Govindaraju, 2017). Thus, at this point in the end of the pipeline system, the individual pixels belong to a single area into the image as well as each area is labeled. The image processing system has reached its goal when the object of study has been recognized (measured, described or counted) into the input image.

From the plant phenotyping point of view, researchers in general, and agronomists and breeders in particular, routinely detect, measure and classify a wide variety of phenotypes, mainly using visual inspection in field conditions (Kelly et al., 2015). Because of these circumstances, image processing systems have a great challenge; far from laboratory or photography studies under controlled conditions, field conditions increase algorithm complexity. For instance, the development of robust techniques to operate under changing sunlight conditions or shadows (for acquisition and preprocessing steps) and

overlapping for adjacent plant's organs (for segmentation and classification steps) (L. Li et al., 2014). Additionally, "field plants do not pose nicely for the camera" (Kelly et al., 2015). Besides, although many image processing techniques were originally developed for medicine diagnostic and industrial automation, several image processing techniques have been applied for plant phenotyping using platforms equipped with multiples sensors (Fahlgren et al., 2015). Moreover, these platforms can acquire samples several times per day and over the entire season; therefore, large volume of data is involved. In order to understand all this data, different types of image processing and machine learning techniques have been adapted, especially for the segmentation and classification steps (Fig. 3) where its implementation and meaning is mostly rooted in mathematics instead of human eye interpretation (Gori, 2018).

As a summary, sensors and image processing systems can be used as useful tools for plant phenotyping. Sensors allow the detection of visible and eye-invisible characteristics of the plant, and automatic image processing systems can be used to avoid manual or subjective tasks, that may be considered as time consuming or difficult to quantify by the human eye. This data can be used for phenotype selection in plant breeding programs or for crop management in agronomy.





## OBJECTIVES

The main objective of this thesis is to develop image processing techniques for plant phenotyping using RGB and thermal imagery.

Specific objectives:

- Develop algorithms for wheat ear detection and counting using RGB and thermal zenithal images above the crop and validate using manual image-based counting. In the case of RGB images an additional objective is to develop specific settings for ground and UAV platforms. Use this variable as agronomical component to study its relationship with grain yield.
- Develop a protocol using RGB vegetation indexes to phenotype and predict wheat grain yield under different growing conditions.



A horizontal banner with a background of green leaves and a small yellow flower. The text is overlaid on this banner.

# Report of the thesis directors







UNIVERSITAT DE  
BARCELONA

**B:KC** Barcelona  
Knowledge  
Campus  
Campus of Internacional Excellence

### Integrative Crop Ecophysiology Group

<https://integrativecropecophysiology.com>

Plant Physiology Section, Department of Evolutionary Biology, Ecology and  
Environmental Sciences, Faculty of Biology, University of Barcelona, Diagonal 643,  
08028, Barcelona, Spain. Tel. 934 021 465, Fax 934 112 842

Dr. José Luis Araus and Dr. Shawn Carlisle Kefauver, as directors of the thesis  
titled “Image processing techniques for plant phenotyping using RGB and thermal  
imagery” which was developed by the doctoral student Jose Armando Fernández  
Gallego,

Report about the impact factor and the participation of the doctoral student in the  
articles included as chapters in the doctoral thesis.

**Chapter 1:** The article “Wheat ear counting in-field conditions: high throughput  
and low-cost approach using RGB images,” was published in the open access  
journal *Plant Methods* with an impact factor of 4.16 in 2018, is a journal placed  
within the first decile of the science area: agricultural and biological sciences -

plant science. In this study, we have developed an automatic ear counting system to estimate the ear density under field conditions using RGB images without using any particular physical arrangement in the field (such as artificial lights, platform or light blackout). The results demonstrate high success rate between the algorithm and manual image-based counting. The relationship between the algorithm ear counts and grain yield was greater than the correlation with manual (field-based) ear counts. The doctoral student has developed the algorithms, manual image-based counting, statistical analysis, validation and results; moreover, the doctoral student has drafted the manuscript.

**Chapter 2:** The article “Cereal Crop Ear Counting in Field Conditions Using Zenithal RGB Images” was published in the *Journal of Visualized Experiments (JoVE)*, with an impact factor of 1.13 in 2019. In this study, we have developed open source plugin (the CerealScanner plugin) for ImageJ (in Java). This plugin can be downloaded from the Integrative Crop Ecophysiology Research Group’s website (a previous permission is required). The algorithm for wheat ear counting was extended for barley ear counting using RGB images under field conditions as well. The image acquisition protocol, light conditions and image processing using the plugin were documented in video. The results demonstrate high success rate between the algorithm and manual image-based counting for wheat and barley images. The doctoral student has developed the algorithms, adaptation for barley images, manual image-based counting, statistical analysis, validation and results; moreover, the doctoral student has collected the field data and drafted the manuscript in both written and audiovisual formats.

**Chapter 3:** The article “Automatic wheat ear counting using machine learning based on RGB UAV imagery,” was submitted to the *journal Remote Sensing of Environment* with an impact factor of 8.89 in 2019, is a journal placed in the first place of the science areas: agricultural and biological Sciences - soil science, earth and planetary sciences – geology, and earth and planetary sciences - computers in earth sciences science. In this study, we have developed an automatic ear counting system to estimate the ear density under field conditions using RGB images from an aerial platform including machine learning techniques. The ear counting system was able to identify wheat ears with high accuracy and efficiency. The relationship between the algorithm ear counting and grain yield was better than the correlation with manual (field-based) ear counting. The doctoral student has collected the field validation data as part of a scientific stay at ILVO in Belgium and developed the algorithms, machine learning techniques, statistical analysis, validation and results; moreover, the doctoral student has drafted the manuscript.

**Chapter 4:** The article “Automatic wheat ear counting using thermal imagery,” was published in the open access journal *Remote Sensing* with an impact factor of 4.12 in 2019, is a journal placed in the first seven journals of the science area: earth and planetary sciences - general earth and planetary sciences. In this study, we have developed an automatic ear counting system to estimate the ear density under field conditions using thermal images. The relationship between the thermal counting values and the in-situ visual counting was fairly weak, which highlights the difficulties in estimating ear density from one single image-

perspective. However, the results show that the automatic thermal ear counting system performed quite well in counting the ears that do appear in the thermal images, exhibiting high correlations with the manual image-based counts. The doctoral student has collected the field data and developed the algorithms, statistical analysis, validation and results; moreover, the doctoral student has drafted the manuscript.

**Chapter 5:** The article “Low-cost assessment of grain yield in durum wheat using RGB images” was published in the *Journal European Journal of Agronomy* with an impact factor of 4.13 in 2019, is a journal placed in the first decile of the science areas: agricultural and biological sciences - agronomy and crop science, agricultural and biological sciences - plant science, and agricultural and biological sciences - soil science. In this study, we have developed new the  $u^*v^*A$  index to estimate the photosynthetic area of the canopy using high-resolution images. The results demonstrate the best phenotypic predictions of grain yield during the last part of the crop cycle for irrigated and late planting trial and during the middle part of the crop cycle for rainfed conditions. The heritability and genetic correlation demonstrated the capacity of the RGB indexes to serve as an indirect selection tool for assessing grain yield. Overall the study highlights the capability of an affordable approach based in the acquisition of RGB images at the plot level for crop phenotyping. The doctoral student has managed the field data collection and developed the algorithms, light concept studies, statistical analysis, validation and results; moreover, the doctoral student has drafted the manuscript.

**Proceedings papers in conference that include oral presentation:**

- Conference SPIE Remote Sensing 2018.

**(Best student paper of the conference)**

Fernandez-Gallego, J.A., Kefauver, S.C., Gutiérrez, N.A., Nieto-Taladriz, M.T., Araus, J.L., 2018. Automatic wheat ear counting in-field conditions: simulation and implication of lower resolution images, in: Neale, C.M., Maltese, A. (Eds.), *Proc. SPIE 10783, Remote Sensing for Agriculture, Ecosystems, and Hydrology XX*, 107830M. SPIE, p. 23. doi:10.1117/12.2500083

- Conference SPIE Remote Sensing 2018.

Fernandez-Gallego, J.A., Kefauver, S.C., Kerfal, S., Araus, J.L., 2018. Comparative canopy cover estimation using RGB images from UAV and ground, in: *Proc. SPIE 10783, Remote Sensing for Agriculture, Ecosystems, and Hydrology XX*, 107830M. p. 20. doi:10.1117/12.2501531

- Conference SPIE Remote Sensing 2019.

Fernandez-Gallego, J.A., Buchailot M., Gutiérrez, N.A., Nieto-Taladriz, M.T., Araus, J.L., Kefauver, S.C., 2019. Wheat ear temperature estimation using a thermal radiometric camera, in: *Proc. SPIE 11149, Remote Sensing for Agriculture, Ecosystems, and Hydrology XXI*, 11149.

**Other articles where the doctoral student participated as a co-author:**

- Frontiers in Plant Science. Impact factor 4.14 in 2017.  
Kefauver, S.C., Vicente, R., Vergara-Díaz, O., Fernandez-Gallego, J.A., Kerfal, S., Lopez, A., Melichar, J.P.E., Serret Molins, M.D., Araus, J.L., 2017. Comparative UAV and Field Phenotyping to Assess Yield and Nitrogen Use Efficiency in Hybrid and Conventional Barley. *Front. Plant Sci.* 8, 1–15.  
doi:10.3389/fpls.2017.01733
  
- Journal of Experimental Botany. Impact factor 5.47 in 2018.  
Vergara-Díaz, O., Chairi, F., Vicente, R., Fernandez-Gallego, J.A., Nieto-Taladriz, M.T., Aparicio, N., Kefauver, S.C., Araus, J.L., 2018. Leaf dorsoventrality as a paramount factor determining spectral performance in field-grown wheat under contrasting water regimes. *J. Exp. Bot.* 69, 3081-3094. doi:10.1093/jxb/ery109.
  
- Remote Sensing. Impact factor 4.12 in 2019.  
Sancho-Adamson, M., Trillas, M.I., Bort, J., Fernandez-Gallego, J.A., Romanyà, J., 2019. Use of RGB Vegetation Indexes in Assessing Early Effects of Verticillium Wilt of Olive in Asymptomatic Plants in High and Low Fertility Scenarios. *Remote Sensing* 11, 607 doi:10.3390/rs11060607
  
- Remote Sensing. Impact factor 4.12 in 2019.  
Gracia-Romero, A., Kefauver, S.C., Fernandez-Gallego, J.A., Vergara-Díaz, O., Nieto-Taladriz, M.T., Araus, J.L., 2019. UAV and Ground Image-Based

Phenotyping: A Proof of Concept with Durum Wheat. *Remote Sens.* 11, 1244.  
doi:10.3390/rs11101244.

### **Internships:**

- Wheat ear counting using dron images. Research Institute for Agriculture, Fisheries and Food (ILVO). Melle, Belgium, 2018.
- Tree crown segmentation (*Pinus pinea* L.) using RGB and multispectral imagery. Centre de Ciència i Tecnologia Forestal de Catalunya (CTFC). Solsona, Spain, 2019.

### **Training courses, courses and workshops:**

- Workshop. Computer vision problems in plant phenotyping (CVPPP). Venice, Italia, 2017.
- Course. Breeding small grain cereal crops in a climate change scenario. IAMZ-CIHEAM. Zaragoza, Spain, 2018.
- Workshop. Field Phenomics. EMPHASIS. Melle, Belgium, 2018.
- Training course. High-Throughput Wheat Phenotyping. Wheat Initiative. Bologna, Italia, 2018.



- Training course. Wheat Phenotyping using UAVs. Wheat Initiative. Saskatoon, Canada, 2019.

**Symposiums that include oral presentation:**

- I Spanish symposium on physiology and cereal breeding. Zaragoza, Spain, 2018.
- II Spanish Symposium on Physiology and Cereal Breeding. Cordoba, Spain, 2019.

To certify this for corresponding purposes,

Dr. Jose Luis Araus Ortega

Dr. Shawn Carlisle Kefauver

Barcelona, 6<sup>th</sup> September 2019







Wheat ear counting in-field conditions: high throughput and low-cost approach using RGB images

Jose A. Fernandez-Gallego<sup>1</sup>, Shawn C. Kefauver<sup>1</sup>, Nieves Aparicio Gutiérrez<sup>2</sup>,  
María Teresa Nieto-Taladriz<sup>3</sup> and José Luis Araus<sup>1</sup>

<sup>1</sup> Plant Physiology Section, Department of Evolutionary Biology, Ecology and Environmental Sciences, Faculty of Biology, University of Barcelona, Diagonal 643, 08028 Barcelona, Spain.

Published in:

Plant Methods (2018), Vol. 14, No. 22

## ABSTRACT

The number of ears per unit ground area (ear density) is one of the main agronomic yield components in determining grain yield in wheat. A fast evaluation of this attribute may contribute to monitoring the efficiency of crop management practices, to an early prediction of grain yield or as a phenotyping trait in breeding programs. Currently the number of ears is counted manually, which is time consuming. Moreover, there is no single standardized protocol for counting the ears. An automatic ear-counting algorithm is proposed to estimate ear density under field conditions based on zenithal color digital images taken from above the crop in natural light conditions. Field trials were carried out at two sites in Spain during the 2014/2015 crop season on a set of 24 varieties of durum wheat with two growing conditions per site. The algorithm for counting uses three steps: (i) a Laplacian frequency filter chosen to remove low and high frequency elements appearing in an image, (ii) a Median filter to reduce high noise still present around the ears and (iii) segmentation using Find Maxima to segment local peaks and determine the ear count within the image. The results demonstrate high success rate (higher than 90%) between the algorithm counts and the manual (image-based) ear counts, and precision, with a low standard deviation (around 5%). The relationships between algorithm ear counts and grain yield was also significant and greater than the correlation with manual (field-based) ear counts. In this approach, results demonstrate that automatic ear counting performed on data captured around anthesis correlated better with grain yield than with images captured at later stages when the low performance of ear counting at late grain filling stages was associated with the loss of contrast between canopy and ears.

Developing robust, low-cost and efficient field methods to assess wheat ear density, as a major agronomic component of yield, is highly relevant for phenotyping efforts towards increases in grain yield. Although the phenological stage of measurements is important, the robust image analysis algorithm presented here appears to be amenable from aerial or other automated platforms.



METHODOLOGY

Open Access



# Wheat ear counting in-field conditions: high throughput and low-cost approach using RGB images

Jose A. Fernandez-Gallego<sup>1</sup>, Shawn C. Kefauver<sup>1\*</sup> , Nieves Aparicio Gutiérrez<sup>2</sup>, María Teresa Nieto-Taladriz<sup>3</sup> and José Luis Araus<sup>1</sup>

## Abstract

**Background:** The number of ears per unit ground area (ear density) is one of the main agronomic yield components in determining grain yield in wheat. A fast evaluation of this attribute may contribute to monitoring the efficiency of crop management practices, to an early prediction of grain yield or as a phenotyping trait in breeding programs. Currently the number of ears is counted manually, which is time consuming. Moreover, there is no single standardized protocol for counting the ears. An automatic ear-counting algorithm is proposed to estimate ear density under field conditions based on zenithal color digital images taken from above the crop in natural light conditions. Field trials were carried out at two sites in Spain during the 2014/2015 crop season on a set of 24 varieties of durum wheat with two growing conditions per site. The algorithm for counting uses three steps: (1) a Laplacian frequency filter chosen to remove low and high frequency elements appearing in an image, (2) a Median filter to reduce high noise still present around the ears and (3) segmentation using *Find Maxima* to segment local peaks and determine the ear count within the image.

**Results:** The results demonstrate high success rate (higher than 90%) between the algorithm counts and the manual (image-based) ear counts, and precision, with a low standard deviation (around 5%). The relationships between algorithm ear counts and grain yield was also significant and greater than the correlation with manual (field-based) ear counts. In this approach, results demonstrate that automatic ear counting performed on data captured around anthesis correlated better with grain yield than with images captured at later stages when the low performance of ear counting at late grain filling stages was associated with the loss of contrast between canopy and ears.

**Conclusions:** Developing robust, low-cost and efficient field methods to assess wheat ear density, as a major agronomic component of yield, is highly relevant for phenotyping efforts towards increases in grain yield. Although the phenological stage of measurements is important, the robust image analysis algorithm presented here appears to be amenable from aerial or other automated platforms.

**Keywords:** Digital image processing, Ear counting, Field phenotyping, Laplacian frequency filter, Median filter, Find maxima, Wheat

## Background

The number of ears per unit ground area (ear density) is one of the main agronomical components that determines

grain yield in wheat and other cereals, together with the number of grains per ear and the thousand kernel weight [1]. Nevertheless, different studies have shown that while the number of grains per unit ground area is usually the best correlated parameter with grain yield, the correlations of other major agronomical components such as ear density or number of grain per ear are weaker, and grain size is usually the least correlated trait when compared to

\*Correspondence: [sckefauver@ub.edu](mailto:sckefauver@ub.edu); [sckefauver@gmail.com](mailto:sckefauver@gmail.com)

<sup>1</sup> Plant Physiology Section, Department of Evolutionary Biology, Ecology and Environmental Sciences, Faculty of Biology, University of Barcelona, Diagonal 643, 08028 Barcelona, Spain

Full list of author information is available at the end of the article



© The Author(s) 2018. This article is distributed under the terms of the Creative Commons Attribution 4.0 International License (<http://creativecommons.org/licenses/by/4.0/>), which permits unrestricted use, distribution, and reproduction in any medium, provided you give appropriate credit to the original author(s) and the source, provide a link to the Creative Commons license, and indicate if changes were made. The Creative Commons Public Domain Dedication waiver (<http://creativecommons.org/publicdomain/zero/1.0/>) applies to the data made available in this article, unless otherwise stated.



grain yield [2–4]. Dynamic compensation mechanisms among agronomical yield components appear to be the cause for such contrasts in performance. In current studies of wheat crops, ear counting is performed manually (in situ), which takes time and severely limits its use in breeding as a phenotyping trait, in crop management to monitor plant performance, or to predict grain yield. On the other hand, there is no a single protocol for counting wheat ears, which may further increase experimental variability, particularly when results produced with different methodologies are compared. Moreover, some of the methodological approaches for ear counting are based in the use of grain yield and other traits collected at maturity and therefore, they are not amenable for early yield prediction. Automatic image processing techniques may represent an alternative for high throughput evaluation of ear density. For example, the use of thermal images may be considered an alternative for ear counting since the temperature of the ear may often be several degrees hotter than the surrounding canopy [5]. However, two major limitations of this approach include the low resolution and high cost of thermal cameras, which makes this approach unfeasible for aerial platforms and prohibitively expensive. Alternatively, techniques based on red/green/blue (RGB) digital images of wheat crops captured under field conditions have been reported previously. These approaches have mainly used techniques of image data extraction that were related to characteristics of texture, segmentation of color, morphological operators and skeletonization [6–8]. In the case of a recent paper [6] aiming to automatically determine the heading time, authors made use of a fixed observation device on a platform located above ground level and provided with two cameras facing the crop from opposite directions that recorded daily photographs of the crop. In the same sense, an earlier study focused specifically on ear counting in wheat has shown fairly good results [7], but required a large camera platform and a matte black background structure supported by a tripod for the acquisition of controlled digital images. This structure allowed for avoiding excessive light conditions and unwanted image effects produced by sunlight and shadows, but would greatly hinder its practical application under field conditions. Moreover, these previous approaches have been tested on only one single awnless variety of wheat. In similar work done by Liu et al. [8], they developed an algorithm to calculate the wheat ear count using a database of images in RGB color space and different conditions of planting (drilling and broadcasting); however, the performance was not deemed satisfactory [6], most likely because the counting accuracy was calculated using different sections of a single image rather than testing accuracy in the whole image.

Another example is the automatic ear counting algorithm developed at Rothamsted Research (UK) and tested for example on the FieldScanalyzer of Lemnatec Ltd. This automatic ear counting algorithm, based on RGB images, includes edge detection methods, dilating the lines detected and filling the holes and empty regions. It has been used with good accuracy for counting ear density in a panel composed by five awnless wheat varieties growing under different nitrogen conditions [9]. The camera was installed in an automatic system which moves above the crop in a three dimensional space. Besides its huge cost, this platform can only be used at this particular site, the image processing system uses greyscale images, and thus omits potentially useful RGB information, and to date it has been tested mostly on awnless wheat varieties and across a wide range of ear densities generated largely through different nitrogen fertilization levels, which is not representative of typical growing conditions [2, 3].

Other similar automatic counting approaches using high resolution zenithal RGB images have been developed to estimate tree density. For that purpose, different image processing techniques have been used, which are closely related with the algorithm proposed in this work. Tree crown detection through aerial and high resolution satellite images has often employed smoothing filters to simplify crown form and reduce image noise [10–13]. Also, local maxima filters have been applied on high spatial resolution to detect possible tree crown centers [10–14]. In the case of applications aiming at fruit measure and recognition (e.g. apple, blueberry, grape, mango) like systems have used high resolution images in RGB color space, in order to optimize the visual characteristics of the target objects, followed by segmentation process tasks [15–17]. Alternatively, different color space transformations have been used [18–23]. In most cases, the use of regular digital cameras have been proposed [24–28] due to their high resolution, cost-effectiveness, speed and reliability.

This work proposes a simple system for the automatic quantification of ear density under field conditions based on images acquired by conventional digital cameras. The system uses natural light conditions and therefore is simple to use and may be adaptable to work from aerial platforms. In our study, zenithal images were taken by holding an RGB camera by hand above the crop. Ears per square meter units are calculated using the camera specifications, lens focal length and the distance between the canopy and the camera [29]. First, we applied a Laplacian frequency enhancement to remove part of the soil, leaves and unwanted brightness from the image. Then, similar to other previous automatic image enhancement, segmentation and counting approaches, we employed a median filter as a smoothing technique to further reduce

high frequency noise and finally local maximums to determine local peaks within the image for the purpose of wheat ear counting. We also tested this ear counting system on simulated greyscale and reduced resolution images using the same data.

## Methods

### Plant material and growth conditions

Field trials were carried out, during the 2014/2015 crop season at the experimental stations of Colmenar de Oreja (40°04'N, 3°31'W) near Aranjuez and Zamadueñas (41°42'N, 4°42'W) near Valladolid belonging to the Instituto Nacional de Investigación y Tecnología Agraria y Alimentaria (INIA) of Spain and to the Instituto de Tecnología Agraria de Castilla y León (ITACyL), respectively. The average annual precipitation corresponding to Aranjuez area is about 425 mm and the average annual temperature is 13.7 °C, whereas in the case of Valladolid annual averages are 386.2 mm and 11.6 °C. In the case of the Aranjuez trials, the field was fertilized before planting with 400 kg ha<sup>-1</sup> of a 15:15:15 N:P:K (15% N, 15% P<sub>2</sub>O<sub>5</sub>, 15% K<sub>2</sub>O) fertilizer. A second application of 150 kg ha<sup>-1</sup> of urea 46% dilution was applied before stem elongation. For the Valladolid trials the field was fertilized before planting with 300 kg ha<sup>-1</sup> of a 8:15:15 N:P:K (8% N, 15% P<sub>2</sub>O<sub>5</sub>, 15% K<sub>2</sub>O) fertilizer and a second application of 300 NAC-fertilizer kg ha<sup>-1</sup> was applied before stem elongation.

Twenty-four durum wheat cultivars (*Triticum turgidum* L. subsp. *durum* (Desf) Husn.) post Green Revolution and cultivated in Spain during the past four decades were grown (cvs Amilcar, Avispa, Bólido, Bolo, Burgos, Claudio, Don Ricardo, Don Pedro, Dorondón, Don Sebastian, Gallareta, Iríde, Kiko Nick, Mexa, Pelayo, Ramírez, Pelayo, Simeto, Sula Olivador, Tussur, Martinur, Scupur and Vitrón), all of which had awns. For each site, two growing conditions were assayed: rainfed and supplemental irrigation. For each growing condition, the experimental design was established in randomized blocks with three replicates and a total of 72 plots. Planting took place on November 21, 2014 and November 24, 2014, for Aranjuez and Valladolid, respectively, with a planting density of 250 seeds per square meter. The plots had an area of 7 × 1.5 m<sup>2</sup> with a spacing distance of 0.2 m between rows. Rainfall during the 2014/2015 crop season was 206 mm and 257 mm and the average temperature was 11.3 and 10.3 °C for Aranjuez and Valladolid, respectively. For the trial under supplemental irrigation, six irrigations were provided at both sites from stem elongation to around 2 weeks after anthesis, totaling 125 mm of water. Harvest was carried out on July 20, 2015 and July 22, 2015, for Aranjuez and Valladolid, respectively and then grain yield was evaluated. In addition, the number

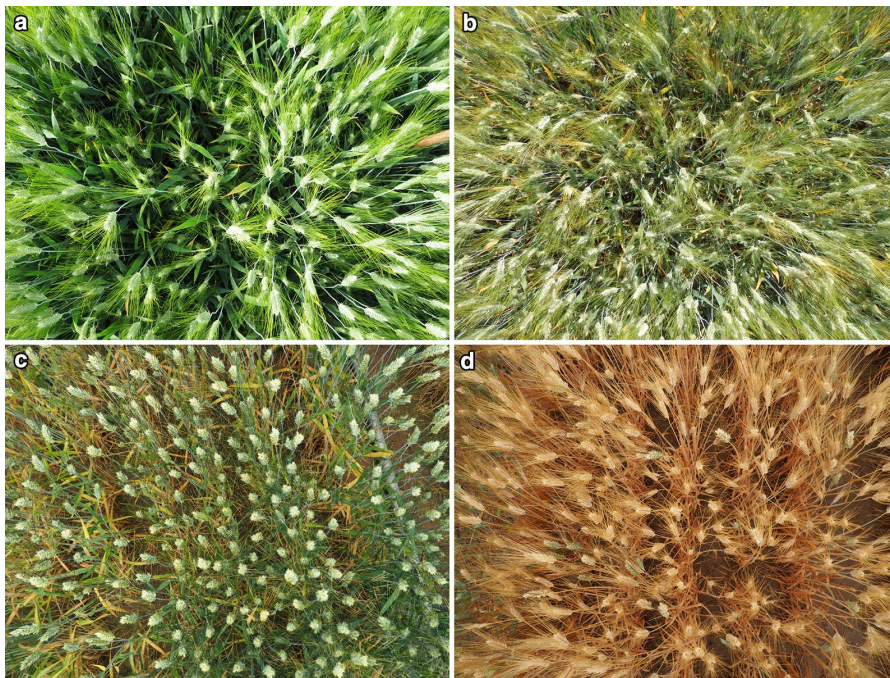
of ears per unit of grown area (ear density) was measured manually using different approaches. In Aranjuez it was calculated from the total grain yield divided by the weight of kernels per ear. To that end 10 ears per plot were sampled at maturity, threshed and the total kernel weight per spike ear measured. In the case of Valladolid, the total number of ears was counted in two half-a-meter row sections per plot and then the number of ears per unit area calculated.

### RGB images

For each plot, one digital RGB picture was taken under natural light conditions by holding the camera at approximately 1.0 m above the plant canopy, in a zenithal plane and focusing near the center of each plot. The images from the first and third visits were acquired with an Olympus E-M10, 16-megapixel resolution camera with a 4/3" sensor using a 14 mm lens, triggered at a speed of 1/125 s with the aperture programmed in automatic mode. For the second date of measurement, the images were acquired with an Olympus DZ-105, 16-megapixel resolution camera with a 1/2.3" sensor using a 35 mm lens, triggered at a speed of 1/250 s with the aperture programmed in automatic mode. All images had a native resolution of 4608 × 3456 pixels and were stored in JPG format using the sRGB color standard [30].

Measurements were performed at three dates: May 12, May 25 and June 8, for both rainfed and support irrigation trials at Aranjuez, and May 14, May 28 and June 9, 2015 for both trials at Valladolid, coincident with the development stages of anthesis (first measurement), middle grain filling (second measurement) and late grain filling (third measurement), respectively, thereby, the colors within the scene changed and depended on not only on the wheat variety but also on its growth stage (Fig. 1). The calculated ear densities (ears/m<sup>2</sup>) remained constant for each date of measurement as the same camera and specification were used for each field visit. The normalized difference vegetation index (NDVI) was measured using a portable spectroradiometer (GreenSeeker handheld crop sensor; Trimble, USA) for the same plots and on the same dates as the RGB image captures.

Preliminary evaluations discarded all images taken late in the afternoon due to the shadows created inside the canopy by the low angle of the incident sunlight, such that all pictures used for further analysis were acquired within 2 h of solar noon or diffuse light conditions. The Additional file 1: Fig. S1 shows images of plots taken under different incident sunlight conditions and growth stages for crops grown under different water regimes. The image (A) was acquired under direct sunlight within 2 h of solar noon, and (B) and (C) were acquired under diffuse light conditions. The ears in (A) and (B) remain



**Fig. 1** Images of plots at different stages of growth and treatments (Image Database). **a** Aranjuez Irrigated (first measurement) cv Martinur, **b** Aranjuez Rainfed (second measurement) cv Martinur, **c** Valladolid Irrigated (third measurement) cv Amilcar, **d** Valladolid Rainfed (third measurement) cv Amilcar

contrasted between ears, leaves, and soil due to the irrigated treatment. The ears in (C) are not contrasted due to the change (yellowing) in canopy color by the later stage of growth (earlier senescence) of the rainfed treatment. Although (C) was taken under optimal sunlight conditions, the stage of growth is not appropriate because of the lack of contrast; this was considered as not an optimal phenological condition. As such, both (A) and (B) are considered as taken under optimal light and/or phenological conditions. On the other hand, the ears in (D) are poorly contrasted even though the growth stage was considered appropriate, as the image was taken late in the afternoon; we had to discard these images due to shadows and brightness created inside the canopy by the low angle of the incident sunlight.

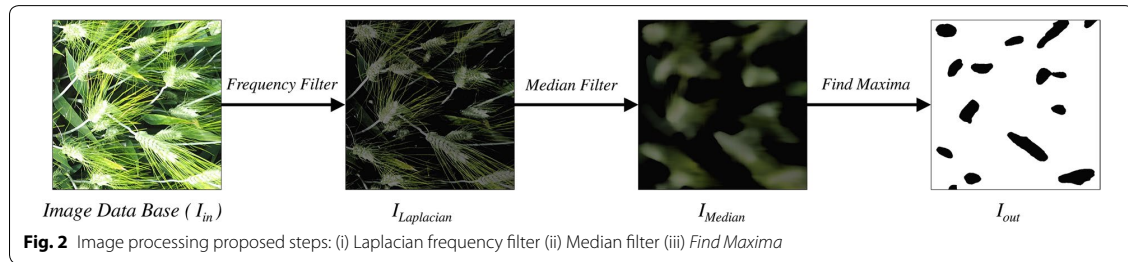
#### Automatic ear-counting system

The pipeline algorithm for counting consists of three steps: (1) Laplacian frequency filter, (2) Median filter, and (3) segmentation using *Find Maxima*. Greyscale and reduced resolution image simulations were conducted by applying the image conversion prior to the first step. As first step of the image processing system we have chosen

a Laplacian filter, due to the wide frequency range of the elements (such as awns, leaves, soil and others unwanted objects) appearing in an image. The second step uses a median spatial filter to reduce the high frequency noise still present around the ears. Finally, we apply the *Find Maxima* segmentation technique, where ears detection was determined by local peaks found within the image. The output of the system is the binary image  $I_{out}$  (Fig. 2). The algorithm was developed in ImageJ software [31].

The Laplacian filter has been used with the aim of detecting changes in the different directions of the image by using a second-order derivative filter [32]. Implementation of the filter was done using *ImageJ* and an extension with a Laplacian filter [33]. This isotropic filter performs as a high frequency enhancement [34] and responds independently of the discontinuities within the image [35]. Equation (1) shows the mathematical frequency model of the Laplacian filter.

$$H(u, v) = -4\pi^2 \left[ \left( u - \frac{M}{2} \right)^2 + \left( v + \frac{N}{2} \right)^2 \right], \quad (1)$$



where  $H(u,v)$  represents the transfer function of the Laplacian filter in the frequency domain. The variables  $u$  and  $v$  define the frequency axis and the variables  $M$  and  $N$  are the shifter constants ( $M/2$ ,  $N/2$ ) from the origin  $(0,0)$ , as the result of working with a centered spectrum. The constant  $-4\pi^2$  is obtained in the Laplacian filter mathematical calculations. The Laplacian enhancement in the frequency domain was used applying Eq. (2).

$$I_{Laplacian}(x,y) = \mathcal{F}^{-1}\{[1 - H(u,v)] * \mathcal{F}(I_{in}(x,y))\}, \quad (2)$$

where  $I_{in}(x,y)$  is the input image,  $\mathcal{F}$  represents the Fourier transform and  $[1 - H(u,v)]$  denotes the Laplacian frequency enhancement. The resulting image is saved in  $I_{Laplacian}(x,y)$ . In reference to this stage, Fig. 2 shows the initial image  $I_{in}$  and the output image  $I_{Laplacian}$  where Eq. (2) was used. Using this type of filter, the high frequency information is controlled and appends the image filtered with the original image as a background. This enables the removal of part of the soil, leaves and unwanted brightness in the image of the crop as part of the background elements of the image (Fig. 1).

Further, to reduce the high frequency noise in the image and decrease the influence of the awns and leaves, we employed a median filter. The Median filter uses the values in the neighboring cells and sets up a moving window array to calculate the statistical median function of that array; the result is the new pixel in the output image ( $I_{median}$ ), as seen in Fig. 2. The Median filter results in the visual effect of smoothing the image [36]. This effect depends of the size of window used, with larger sizes producing a greater smoothing effect. This step used a window size of  $64 \times 64$  pixels to prevent removing the small ears. Equation (3) shows a representation of the spatial filter applied to  $I_{Laplacian}$  who represents the image filtering in the frequency domain. The output of this step is  $I_{median}$

$$I_{median} = median(I_{Laplacian}) \quad (3)$$

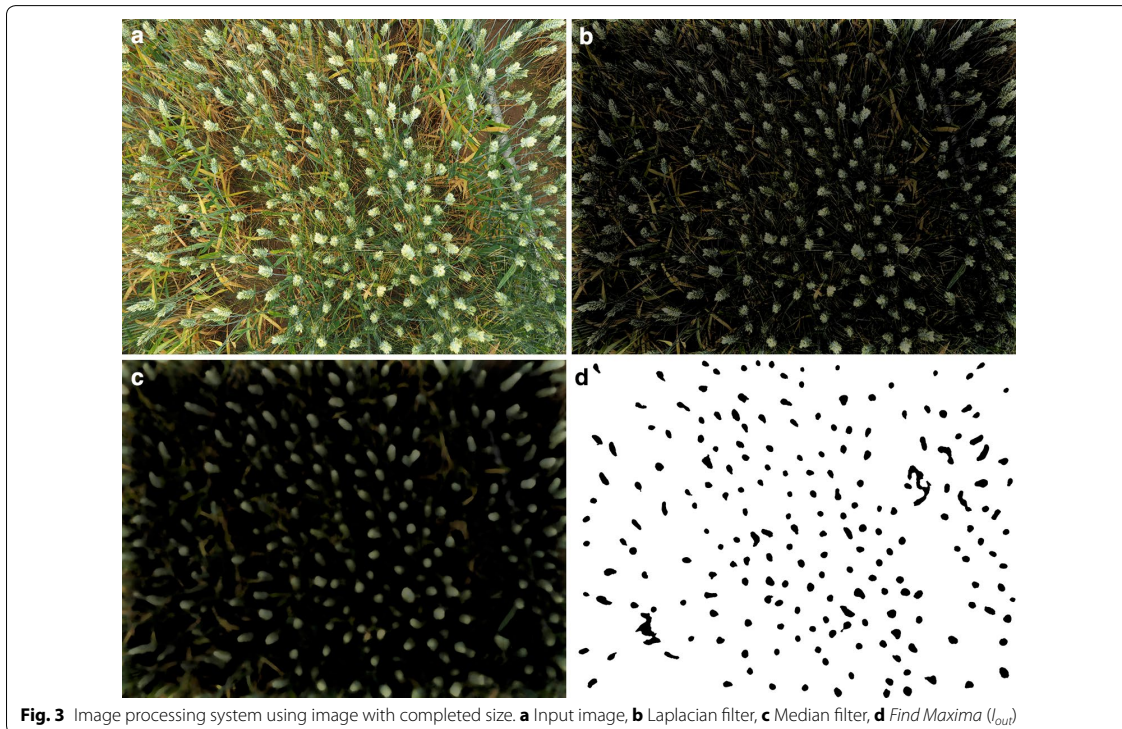
This filter guarantees as output an image with same pixel values as from the input image and contributes to the reduction of high frequency noise [37]. In the final

stage of image processing, the local maximums were detected using the *Find Maxima* algorithm implemented in *ImageJ* [38]. The technique determines local peaks within the image; in that way, it finds the ears because, after filtering, each peak in the image represents a wheat ear. The algorithm creates a binary image segmentation using the pixel value from each local maxima and the nearest neighbor pixel variance to identify the wheat ear shapes in the filtered image, with the white pixels indicating soil, leaves or awns; and the black pixels indicating wheat ears detected in the image.

Figure 3 shows the stages of image processing systems using a full-size image. The output image ( $I_{out}$ ) is used for counting the number of ears in each scene. Each isolated region in black color is considered an ear. The number of regions in  $I_{out}$  image is counted using *Analyzed Particles* implemented in *ImageJ* [38].

#### Algorithm validation

The performance of the image processing system for to automatically counting the ears appearing in an image was tested in the images taken from anthesis to maturity (Fig. 1). In order to validate the algorithm, the output of  $I_{out}$  was compared with the manual image-based ear counting on the same image.  $I_{out}$  in Fig. 2, depicts the binary image where the connected pixels in black color are considered like a wheat ear automatically detected by the image processing system; each of these regions are added and the final result is referred to as the *algorithm counting*. Besides, the number of ears in a subset of images has been counted manually (ground truth) and is referred to as the *manual counting*. For Aranjuez, the validation-data manual counting included 72 images, corresponding to the irrigated trial and 24 images belonging to the first block of the rainfed trial from the *first measurement*. For Valladolid, the validation database included 24 ground truth images, taken at the third data measurement, corresponding to the first block of the irrigation and rainfed trials, respectively. For the manual counting we manually marked each ear in the original image and then the number of marks in the image were



**Fig. 3** Image processing system using image with completed size. **a** Input image, **b** Laplacian filter, **c** Median filter, **d** Find Maxima ( $low$ )

counted using a simple algorithm developed for counting the number of marks manually selected within the image. In order to determine the success of the automatic ear-counting algorithm, we employed the percentage of error. The success rate in percentage was obtained as the difference between 100% and the relative difference between the manual counting and the algorithm counting (expressed as the difference in the absolute values of the manual and automatic counting, divided by manual counting and multiplied by 100%). We have converted the corresponding image ear-counting numbers in terms of ears per square meter in order to correlate these values with grain yield using the standard agronomical units.

#### Statistical analysis

Data was analyzed using InfoStat version 2014 ([39], [www.infostat.com.ar](http://www.infostat.com.ar)) from the National University of Córdoba, Argentina. Pearson correlation coefficients and linear regression were used to analyze the relationship between automatic and manual counting and compare the automatic counting against grain yield. The data was plotted using SigmaPlot version 12 (Systat Software, Inc., San Jose California USA).

## Results

### Success rate and linear regression between the algorithm and manual counts

The success rate in the number of detected ears using the ground truth (manual counting) compared with the automatic counting derived from the image processing was calculated (Table 1).

Furthermore, the linear regression between the manual counting and the algorithm counting was calculated for the 72 irrigated and 24 rainfed plots from Aranjuez at anthesis (first sampling date) as well as across 24 plots from the irrigated and another 24 plots from the rainfed trials of Valladolid at leaf grain filling (Fig. 4).

The success rate demonstrated the high accuracy of the algorithm counting with regard the manual ear counting and the standard deviation values imply a small data dispersion (Table 1). Thus, mean and standard deviation values for Aranjuez derived from the images taken at anthesis (mid-May) in the irrigated trial exhibited robust accuracy when applied to only one replicate ( $\mu=91.06\%$ ,  $\sigma=6.37$ ) or to the three replicates of each genotype ( $\mu=92.39$ ,  $\sigma=6.23$ ). Performance for the rainfed trial at Aranjuez during the first measurement data was similar ( $\mu=91.71\%$ ,  $\sigma=6.96$ ). Performance was almost as strong ( $\mu=89.79\%$ ,  $\sigma=10.14$ ) at the irrigated

**Table 1 Percentage of success of the automatic counting at the original RGB resolution, greyscale and the resized imagery validation results**

Trial, date of sampling		Original RGB	Greyscale	x 1/2	x 1/4	x 1/8	x 1/16	x 1/32
Aranjuez, May 12	$\mu$	92.39%	88.52%	92.14%	91.6%	88.98%	81.10%	62.94%
Irrigated	$\sigma$	6.23	9.90	5.89	6.04	7.06	8.75	7.51
72 images	$r$	0.79	0.73	0.78	0.78	0.76	0.71	0.64
Aranjuez, May 12	$\mu$	91.06%	90.78%	90.30%	89.25%	85.50%	77.41%	60.12%
Irrigated	$\sigma$	6.37	8.99	6.29	6.79	7.48	8.66	6.89
24 images	$r$	0.78	0.76	0.77	0.79	0.77	0.76	0.74
Aranjuez, May 12	$\mu$	91.70%	93.01%	91.15%	89.41%	84.92%	76.59%	59.59%
Rainfed	$\sigma$	6.96	4.57	7.79	8.7	9.37	8.82	7.60
24 images	$r$	0.72	0.80	0.69	0.67	0.65	0.62	0.47
Valladolid, June 9	$\mu$	89.79%	80.56%	89.22%	87.67%	82.47%	72.47%	50.97%
Irrigated	$\sigma$	10.14	12.19	10.52	11.07	12.47	15.32	14.09
24 images	$r$	0.87	0.87	0.87	0.86	0.824	0.80	0.73
Valladolid, June 9	$\mu$	31.86%	65.36%	31.12%	29.64%	27.01%	22.65%	14.02%
Rainfed	$\sigma$	7.54	11.53	7.38	7.02	6.51	5.8	4.32
24 images	$r$	0.42	0.35	0.39	0.38	0.39	0.34	0.34

Different sites and phenological stages across the set of 24 durum wheat varieties were assayed. Values presented are the means of percentage of success ( $\mu$ ), standard deviation ( $\sigma$ ) and Pearson correlation coefficient ( $r$ )

Valladolid trial measured at late grain filling (third valuation, early June). However the performance in the rainfed trial of Valladolid measured on early June was much lower ( $\mu = 31.86\%$ ,  $\sigma = 7.54$ ), suggesting the growth stage affect the correct identification of ears. In the same sense the relationships between the manual and algorithm ear counting for Aranjuez at mid-May (*irrigated*  $R^2 = 0.62$ ; *rainfed*  $R^2 = 0.51$ ) and irrigated Valladolid at late grain filling ( $R^2 = 0.75$ ) were positive and strong (Fig. 4), with the irrigated Valladolid late grain filling additionally demonstrating a close 1:1 relationship. In the case of rainfed Valladolid at late grain filling the correlation, even if significant, was weaker ( $R^2 = 0.17$ ) and much further from a 1:1 slope than the rest.

#### Simulating greyscale and lower resolution imagery

The performance of the algorithm was further tested through the simulation of images in greyscale and at lower resolutions using the original high resolution image data. The greyscale images were converted by averaging the RGB color bands. The lower resolution images were resized to five different resolutions by dividing the original image size by two (obtaining an image of  $2304 \times 1729$  pixels) as far as obtain the smallest image size dividing by 32 ( $114 \times 108$  pixels). The images were resized using average pixel values, with no interpolation techniques applied. We have used the same algorithm pipeline proposed for greyscale and lower resolution, although in the Median filter step (Eq. 3), we reduced the moving window size in proportion to the image resizing to match the

subsequent size of the wheat ears in the reduced image. Manual image-based counting was used as the validation data as before. Table 1 gives the statistical summary results obtained for Aranjuez and Valladolid plots. Additional file 2: Fig. S2 shows the resized imagery simulation; the images were resized using average pixel values, with no interpolation of values.

The greyscale results show, with respect to the original RGB images, a decrease in up to 9.23% in success rate while maintaining a similar correlation as the RGB results in the irrigated trials. While the greyscale resulted in an increase in success rate for the Valladolid rainfed trial, little changes were observed in correlation and success rate for the Aranjuez rainfed trial.

The lower resolution results show a decrease of < 1% in success rate when the images were reduced to a half of its original size. Success rates decreased by a maximum of 2.29, 7.32 and 17.32% for image size divided by four, eight and 16 values, respectively. For the smallest image size, success rate decreases as much as 38.82%. Standard deviation values exhibited robust accuracy at moderately lower resolutions and Pearson correlation coefficients remained close to original values, for all but the smallest simulated image size where the correlation values shifted markedly from the original values.

#### Understanding algorithm errors

Figure 5 shows the input and output images, with each blue pixels representing an ear automatically detected by the proposed algorithm. There are three regions in the

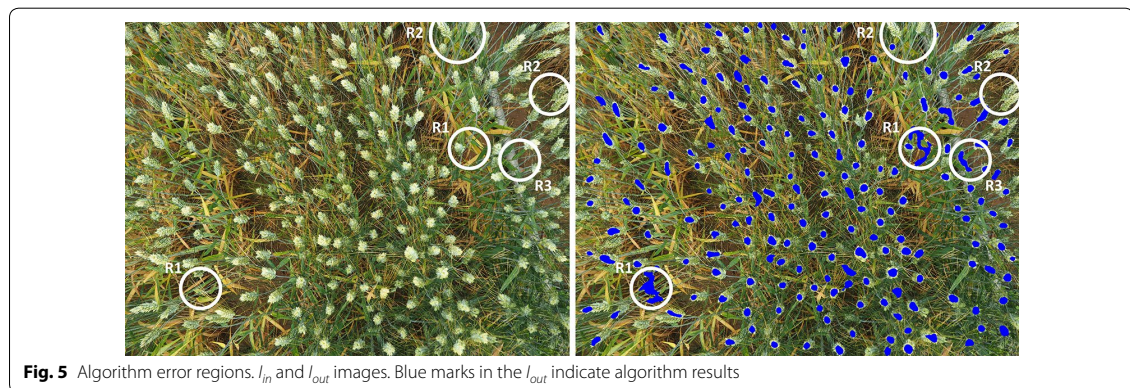
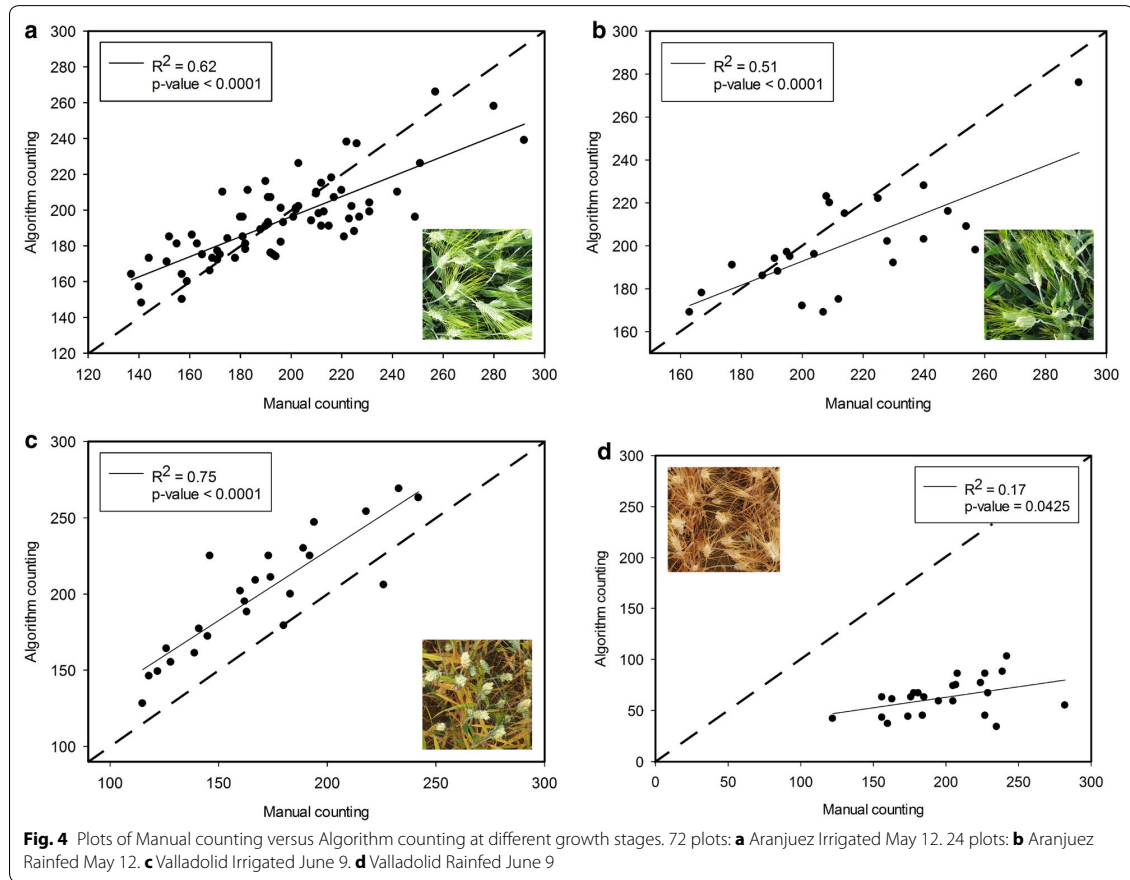


image indicating examples where the algorithm has not worked properly. For example, region *R1* shows false positives where pixels labeled as ear actually corresponded to leaves and resulted in irregularities in the ear counting.

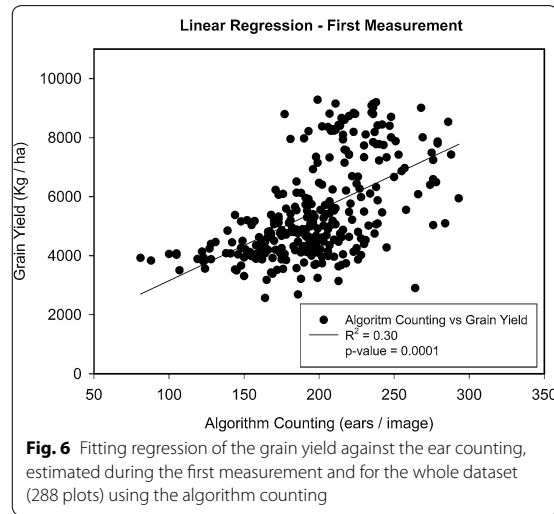
As a result, pixels from leaves were united with ear pixels in the *Find Maxima* step and included together as one combined area. In region *R2*, false negatives resulted in ears that were not detected by the algorithm because the

contrast between the ear and soil was not great enough and the segmentation algorithm discarded that region. In case of region R3, whereas the algorithm labeled the area as an ear, those pixels are soil and noise being a result of background brightness caused by a foreign object.

**Relationship between algorithm counting and grain yield**

The relationship of grain yield against the ear counting calculated with the algorithm in terms of ears per square meter (ears/m<sup>2</sup>) at the three measurement dates as well as the manual in situ counting values were assessed. In Table 2 we provide a statistical summary of the results obtained with the complete dataset of plots from the rainfed and support-irrigation trials of the two experimental sites (288 plots), as well as within each trial and experimental site (72 plots). Moreover, NDVI is included as a standard indicator of crop greenness and vigor.

The results show that the ear-counting algorithm correlated better with grain yield at the *first measurement date* (R<sup>2</sup>=0.30) than at the *second measurement date* (R<sup>2</sup>=0.08) or the *third measurement date* (R<sup>2</sup>=0.05). The relationship of the manual in situ counting against grain yield was R<sup>2</sup>=0.24. The pattern of the relationship between the automatic ear counting and grain yield was in all cases lineal (Fig. 6).



**Fig. 6** Fitting regression of the grain yield against the ear counting, estimated during the first measurement and for the whole dataset (288 plots) using the algorithm counting

**Discussion**

Working in field conditions implies many considerations, especially when plant phenotyping tasks are developed. Ear density is frequently identified as the main agronomical component of yield and it appears to be the most relevant towards future increases in grain yield ([4] and

**Table 2** Statistical results of the relationships across the whole set of plots (288), as well as across the set of plots of each trial (72) between grain yield and the ear counting using the algorithm (ears/m<sup>2</sup>) in the first, second and third date of measurement as well as the manual in situ counting

Determination coefficient (R <sup>2</sup> ), Pearson correlation (r) and mean (μ) ± standard deviation for NDVI	First measurement	Second measurement	Third measurement	Manual in situ counting
Whole dataset (288)	R <sup>2</sup> = 0.30*** r = 0.55***	R <sup>2</sup> = 0.08*** r = 0.28***	R <sup>2</sup> = 0.05*** r = 0.21***	R <sup>2</sup> = 0.24*** r = 0.49***
Aranjuez Irrigated Dataset (72)	R <sup>2</sup> = 0.05 <sup>ns</sup> r = 0.22 <sup>ns</sup> μ = 0.78 ± 0.03	R <sup>2</sup> = 0.05 <sup>ns</sup> r = -0.04 <sup>ns</sup> μ = 0.71 ± 0.07	R <sup>2</sup> = 0.02 <sup>ns</sup> r = 0.14 <sup>ns</sup> μ = 0.29 ± 0.14	R <sup>2</sup> = 0.18** r = 0.43**
Aranjuez Rainfed Dataset (72)	R <sup>2</sup> = 0.05 <sup>ns</sup> r = 0.22 <sup>ns</sup> μ = 0.76 ± 0.02	R <sup>2</sup> = 0.02 <sup>ns</sup> r = 0.16 <sup>ns</sup> μ = 0.67 ± 0.04	R <sup>2</sup> = 0.02 <sup>ns</sup> r = 0.14 <sup>ns</sup> μ = 0.17 ± 0.11	R <sup>2</sup> = 0.53*** r = 0.73***
Valladolid Irrigated Dataset (72)	R <sup>2</sup> = 0.06* r = -0.24* μ = 0.73 ± 0.03	R <sup>2</sup> = 0.0049 <sup>ns</sup> r = -0.07 <sup>ns</sup> μ = 0.67 ± 0.05	R <sup>2</sup> = 0.06* r = 0.25* μ = 0.45 ± 0.10	R <sup>2</sup> = 0.01 <sup>ns</sup> r = 0.07 <sup>ns</sup>
Valladolid Rainfed Dataset (72)	R <sup>2</sup> = 0.07* r = 0.26* μ = 0.66 ± 0.04	R <sup>2</sup> = 0.05 <sup>ns</sup> r = 0.22 <sup>ns</sup> μ = 0.41 ± 0.05	R <sup>2</sup> = 0.18*** r = 0.43*** μ = 0.18 ± 0.14	R <sup>2</sup> = 0.05* r = 0.23*

The mean (μ) ± standard deviation of the normalized difference vegetation index (NDVI) values, across the whole set of plots within each trial is also included for reference

<sup>ns</sup> no significant

\*p value < 0.05; \*\*p value < 0.01; \*\*\*p value < 0.001



references therein). Developing low-cost, fast and easy-to-implement field methods to assess wheat ear density is therefore critical to developing wheat varieties with greater yield. We propose the use of a simple RGB image acquisition method holding the camera above the crop canopy, whereas the automatic image processing includes robust algorithms designed for different wheat varieties and growth stages. Previous studies in ear recognition have used acquisition methods/structures which include the use of enclosing structure or a fixed camera support [7, 8] or even artificial light [40] that would greatly limit their practical application under field conditions. Moreover, even if good results were achieved, in most cases only a single awnless wheat variety was used. By contrast, our study included 24 wheat varieties with awns of different colors and culms with ears ranging from erect to floppy, which eventually may affect negatively the performance of the algorithm compared to its application on a single awnless variety.

Unlike the use of artificial light and enclosures, together with a camera support (e.g. tripod), our flexible and fast image acquisition technique presents some major challenges related to image processing. Some ears in the image may appear blurred due to plant movements as a result of wind or absolute camera stability. Sharp shadows and bright surfaces may appear in the images as a product of the light conditions (e.g. in a sunny day). The more erect or floppy attitude of the ears may also affect the counting, whereas the presence of awns represents an additional problem since the awns visually overlap with the body of the ear. This is the case of our study performed in durum wheat, a species which always exhibits awns. Finally, changes in the color of the leaves and ears due to crop growth stage, together with differences in crop density and the soil background may also interfere.

As such, in order to provide robust results, the image processing algorithm pipeline must consider different disturbing effects related with shadows, brightness, leaf color, the presence of awns or even overlapping ears. The Laplacian frequency filter contributes to removing or minimizing visual effects from unwanted brightness and background elements, and the Median spatial filter provides an important contribution to smoothing regions and removing noise from regions that still contained high frequency noise because of the presence of awns [33, 36]. Even so, the lower performance of the counting algorithm in the rainfed trial of Valladolid at late grain filling, compared with the results of the irrigated trial at the same date or compared with the trials at anthesis, was most likely due to the differences in color between the first compared with the other three cases. In the case of the rainfed trial of Valladolid at late grain filling, plants were much more senescent compared with the other

three cases (Fig. 4). The lack of contrast in the images of the rainfed plots on late grain filling between ears, leaves and soil did not permit consistent ear identification. We consider the stage of growth of this treatment too late for the proposed algorithm. In comparison, the irrigated trial at Valladolid still exhibited sufficient contrast in the upper part of the canopy at the third date of measurements, which contributed to the better performance of the counting algorithm compared to manual counts in terms of precision,  $r$  correlation value, and 1:1 relationship between modeled and predicted counts. During grain filling, particularly under Mediterranean conditions, the ears often remain greener longer compared to the leaves and the culm [41], which is essential to provide the necessary contrast between ears, leaves and soil.

In our study, phenotypic correlations across mean values for the 24 genotypes between ear density and grain yield were very poor (in fact absent in most cases) and regardless of whether ear density was directly measured directly in the field or inferred from the automatic counting algorithm. Only in one of the 4 individual trials was manual counting correlated with grain yield, whereas automatic counting was only found to be correlated with grain yield in another trial; in both cases the correlations were found in the rainfed trials (data not shown), explaining in each case about 35% on genotypic variability in grain yield. In fact, compensatory mechanisms between ear density and number of kernels per ear have been reported widely [4, 42], which may account for the lack of correlation between ear density and grain yield in our study. For example, in Valladolid ear density was negatively correlated with the number of grains per ear in both rainfed ( $r = -0.31$ ;  $p < 0.01$ ) and irrigated ( $r = -0.36$ ;  $p < 0.01$ ) conditions. Additional file 3: Table S1 gives the statistical summary results of mean, standard error, minimum and maximum value for the whole set of four trials as well as within each trial, for grain yield, thousand kernel weight (TKW), number of grains per unit ground area and ear density (number of ears per unit ground area).

Automatic ear counting performed around anthesis correlated better with grain yield than at later stages, when canopy color shifts to yellow. The low performance of ear counting at the late grain filling stages associated with a change (yellowing) in canopy color, including the ears, with the subsequent loss of contrast, may be a reason. An additional factor may be due to the fact ears in the two trials of Aranjuez suffered lodging during middle grain filling and strongly increased at late grain filling. In any case, the solid performance of the algorithm at earlier growth stages is viewed as one of its strong points as it may contribute to earlier yield prediction for crop management purposes. In fact, this method may be fully

amenable for management purposes since frequently the range of variability in ear density due to environmental causes and agronomical factors (e.g. availability of water, nutrients, other abiotic and biotic factors, planting date and density, etc.) is larger than that due exclusively to genotypic variability. Therefore, the level of precision provided by the method is less critical for crop management than for phenotype selection in breeding programs.

The greyscale image simulations resulted in a decrease in success rate for the irrigated trials, while on the other hand contributing to an improvement in success rate for rainfed trial images, especially for the Valladolid rainfed trial, but the correlation against manual counting for that trial still remained the lowest. This may be a result of the increased senescence of the rainfed trials at the time of data capture, in which the benefits of color contrast between the leaves and the ears had passed, indicating that it was not an optimal moment for data capture. These results therefore suggest that at a specific growth stage the full RGB color information may provide significant improvements over greyscale images.

Further still, in our study, two different models of cameras were used in image acquisition (Olympus E-M10 and DZ-105) and the algorithm was tested for accuracy with greyscale images without color information and at lower resolutions, in order to provide an idea about the possibility of optimizing processing requirements (less computing time with single band images) and using other types of cameras with lower resolution, such as mobile phones, action cameras (GoPro), or even similar or higher quality cameras at a greater distance (with or without zoom lens, etc.) such that the same robust algorithm for ear counting may be adaptable to mobile, field or aerial (UAV) phenotyping and precision agriculture platforms.

## Conclusions

This study proposes a low-cost and easy-to implement approach for ear counting. The system uses a handheld camera that easily can be moved across the plots. Moreover, the image analysis algorithm is amenable to other applications, such as early assessment of yield through the acquisition of RGB images from aerial or other automated platforms. Nevertheless, the performance of this image processing system depends on the phenological stage when measurements took place. Mature canopies, with the ears already yellow, are not adequate for ear counting. In our study, different hybrid color spaces were considered as an image pre-processing stage, but there was no difference in input image enhancement or algorithm results. We chose to use the original RGB color space for its benefits in contrast at specific growth stages, although greyscale images can be useful in low color

contrast conditions; nevertheless, in future studies it may be interesting to investigate hybrid color spaces or high resolution RGB imagery combined with multispectral or thermal imagery to enhance the performance of the ear counting algorithm.

## Additional files

**Additional file 1. Figure S1.** Images of plots taken under different incident sunlight conditions, and growth stages on crops grown under different water regimes. **A** Image taken at anthesis with direct sunlight within two hours of solar noon in an irrigated plot. **B** Image taken at late grain filling under diffuse light conditions in the morning in an irrigated plot. **C** Image taken during late grain filling under diffuse light conditions near solar noon in a rainfed plot. **D** Image taken late at middle grain filling with direct sunlight in the afternoon.

**Additional file 2. Figure S2.** Resized imagery simulation—input and output images. The images were resized using average pixel values, with no interpolation techniques applied.

**Additional file 3. Table S1.** Values for the whole set of four trials as well as within each trial, for grain yield, thousand kernel weight (TKW), number of grains per unit ground area (grains/m<sup>2</sup>) and ear density (number of ears per unit ground area). For each trait, mean, standard error (SE) and minimum and maximum value across the individual plot.

## Authors' contributions

JAF wrote the majority manuscript, collected the field imagery, and developed the code for applying the functions of the final algorithm. SCK contributed to the manuscript writing, edition and translation, field data acquisition, and preliminary conceptual developments of the image analyses employed in the final algorithm and is also co-director of JAF's Ph.D. NAG and MTN are the coordinators of the research stations at Zamadueñas and Colmenar de Oreja, respectively, and provided significant contributions to the data through field crop management and final agronomical data for comparison with the image analysis algorithm results. JLA is the head of the Integrative Crop Ecophysiology research group and Principal Investigator of the MINECO project which funds this research, contributed significantly to field data acquisition, conceptual framework of the research, and manuscript edition, and is also co-director to JAF's Ph.D. All authors read and approved the final manuscript.

## Author details

<sup>1</sup> Plant Physiology Section, Department of Evolutionary Biology, Ecology and Environmental Sciences, Faculty of Biology, University of Barcelona, Diagonal 643, 08028 Barcelona, Spain. <sup>2</sup> Instituto Tecnológico Agrario de Castilla y León (ITACyL), Ctra. Burgos Km. 119, 47071 Valladolid, Spain. <sup>3</sup> Instituto Nacional de Investigación y Tecnología Agraria y Alimentaria (INIA), Ctra. de la Coruña Km. 7.5, 28040 Madrid, Spain.

## Acknowledgements

The authors of this research would like to thank the field management staff at the experimental stations of Colmenar de Oreja (Aranjuez) of the Instituto Nacional de Investigación y Tecnología Agraria y Alimentaria (INIA) and Zamadueñas (Valladolid) of the Instituto de Tecnología Agraria de Castilla y León (ITACyL) for their continued support of our research. The authors would also like to recognize the contributions from the University of Ibagué, Colombia in facilitating the international PhD support for JAF.

## Competing interests

The authors declare that they have no competing interests.

## Availability of data and materials

The datasets used and/or analyzed during the current study available from the corresponding author on reasonable request.

## Consent for publication

Not applicable.

**Ethics approval and consent to participate**

Not applicable.

**Funding**

This study was supported by the research project, AGL2016-76527-R from MINECO, Spain as the primary funding support for the research project, the BPIN 2013000100103 fellowship from the "Formación de Talento Humano de Alto Nivel, Gobernación del Tolima - Universidad del Tolima, Colombia" as the sole funding source of the first author Jose Armando Fernandez-Gallego, and the Juan de la Cierva postdoctoral research fellowship IJCI-2014-20595 "Incorporación" from the MCOC, Spain as the primary funding source of the corresponding author, Shawn C. Kefauver.

**Publisher's Note**

Springer Nature remains neutral with regard to jurisdictional claims in published maps and institutional affiliations.

Received: 10 January 2017 Accepted: 9 March 2018

Published online: 17 March 2018

**References**

- Pask A, Pietragalla J, Mullan D, Reynolds M, editors. Physiological breeding II: a field guide to wheat phenotyping. Mexico, DF: CIMMYT; 2012.
- Ferrante A, Cartelle J, Savin R, Slafer GA. Yield determination, interplay between major components and yield stability in a traditional and a contemporary wheat across a wide range of environments. *Food Crop Res.* 2017;203:114–27.
- Slafer GA, Calderini DF, Miralles DJ. Yield components and compensation in wheat: opportunities for further increasing yield potential. In: Reynolds MP, Rajaram S, McNab A, editors. Increasing yield potential wheat: breaking the barriers. Mexico: CIMMYT International Symposium; 1996. p. 101–33.
- Slafer GA, Savin R, Sadras VO. Coarse and fine regulation of wheat yield components in response to genotype and environment. *Food Crop Res.* 2014;157:71–83.
- Tambussi EA, Bort J, Guimet JJ, Nogués S, Araus JL. The photosynthetic role of ears in C3 cereals: metabolism, water use efficiency and contribution to grain yield. *Crit Rev Plant Sci.* 2007;26:1–16.
- Zhu Y, Cao Z, Lu H, Li Y, Xiao Y. In-field automatic observation of wheat heading stage using computer vision. *Biosyst Eng.* 2016;143:28–41.
- Cointault F, Guerin D, Guillemin J, Chopinet B. In-field *Triticum aestivum* ear counting using colour-texture image analysis. *N Z J Crop Hortic Sci.* 2008;36:117–30.
- Liu T, Sun C, Wang L, Zhong X, Zhu X, Guo W. In-field wheatear counting based on image processing technology. *Nongye Jixie Xuebao/Trans Chin Soc Agric Mach.* 2014;45:282–90.
- Dornbusch T, Hawkesford M, Jansen M, Nagel K, Niehaus B, Paulus S, et al. Digital field phenotyping by LemnaTec. Aachen: LemnaTec; 2015.
- Erikson M. Species classification of individually segmented tree crowns in high-resolution aerial images using radiometric and morphologic image measures. *Remote Sens Environ.* 2004;91:469–77.
- Leckie DG, Gougeon FA, Tinis S, Nelson T, Burnett CN, Paradine D. Automated tree recognition in old growth conifer stands with high resolution digital imagery. *Remote Sens Environ.* 2005;94:311–26.
- Leckie DG, Gougeon FA, Walsworth N, Paradine D. Stand delineation and composition estimation using semi-automated individual tree crown analysis. *Remote Sens Environ.* 2003;85:355–69.
- Pouliot DA, King DJ, Bell FW, Pitt DG. Automated tree crown detection and delineation in high-resolution digital camera imagery of coniferous forest regeneration. *Remote Sens Environ.* 2002;82:322–34.
- Wulder M, Niemann KO, Goodenough DG. Local maximum filtering for the extraction of tree locations and basal area from high spatial resolution imagery. *Remote Sens Environ.* 2000;73:103–14.
- Font D, Pallejà T, Tresanchez M, Teixidó M, Martínez D, Moreno J, et al. Counting red grapes in vineyards by detecting specular spherical reflection peaks in RGB images obtained at night with artificial illumination. *Comput Electron Agric.* 2014;108:105–11.
- Stajko D, Lakota M, Hočevar M. Estimation of number and diameter of apple fruits in an orchard during the growing season by thermal imaging. *Comput Electron Agric.* 2004;42:31–42.
- Tian LF, Slaughter DC. Environmentally adaptive segmentation algorithm for outdoor image segmentation. *Comput Electron Agric.* 1998;21:153–68.
- Arroyo J, Guijarro M, Pajares G. An instance-based learning approach for thresholding in crop images under different outdoor conditions. *Comput Electron Agric.* 2016;127:669–79.
- Guijarro M, Pajares G, Riomoros I, Herrera PJ, Burgos-Artizzu XP, Ribeiro A. Automatic segmentation of relevant textures in agricultural images. *Comput Electron Agric.* 2011;75:75–83.
- Li H, Lee WS, Wang K. Identifying blueberry fruit of different growth stages using natural outdoor color images. *Comput Electron Agric.* 2014;106:91–101.
- Payne AB, Walsh KB, Subedi PP, Jarvis D. Estimation of mango crop yield using image analysis – segmentation method. *Comput Electron Agric.* 2013;91:57–64.
- Payne A, Walsh K, Subedi P, Jarvis D. Estimating mango crop yield using image analysis using fruit at "stone hardening" stage and night time imaging. *Comput Electron Agric.* 2014;100:160–7.
- Ruiz-Ruiz G, Gómez-Gil J, Navas-Gracia LM. Testing different color spaces based on hue for the environmentally adaptive segmentation algorithm (EASA). *Comput Electron Agric.* 2009;68:88–96.
- Aquino A, Millan B, Gutiérrez S, Tardáguila J. Grapevine flower estimation by applying artificial vision techniques on images with uncontrolled scene and multi-model analysis. *Comput Electron Agric.* 2015;119:92–104.
- Chang YK, Zaman Q, Farooque AA, Schumann AW, Percival DC. An automated yield monitoring system II for commercial wild blueberry double-head harvester. *Comput Electron Agric.* 2012;81:97–103.
- Ji W, Zhao D, Cheng F, Xu B, Zhang Y, Wang J. Automatic recognition vision system guided for apple harvesting robot. *Comput Electr Eng.* 2012;38:1186–95.
- Maldonado W, Barbosa JC. Automatic green fruit counting in orange trees using digital images. *Comput Electron Agric.* 2016;127:572–81.
- Zhou R, Damerow L, Sun Y, Blanke MM. Using colour features of cv. "Gala" apple fruits in an orchard in image processing to predict yield. *Precis Agric.* 2012;13:568–80.
- Jensen JR. Remote sensing of the environment: an earth resource perspective. Upper Saddle River: Pearson Prentice Hall; 2007.
- Susstrunk S, Buckley R, Swen S. Standard RGB color spaces. In: 7th color imaging conference on final progress proceedings on society for imaging science and technology; 1999. p. 127–34.
- Schneider CA, Rasband WS, Eliceiri KW. NIH Image to ImageJ: 25 years of image analysis. *Nat Methods.* 2012;9:671–5.
- Bourne R. Image filters., Fundamentals of digital imaging in medicine. London: Springer; 2010. p. 137–72.
- Cappello A. Estensione del software ImageJ con tecniche di enhancement nel dominio della frequenza. Dipartimento di Matematica e Informatica. Corso di Laurea Specialistica in Informatica. Università degli Studi di Catania. 2005. p. 1–23.
- Smolka B. Nonlinear techniques of noise reduction in digital color images. Gliwice: Wydawnictwo Politechniki Śląskiej; 2004.
- Das A. Image enhancement in spatial domain., Guide to signals and patterns in image processing. Cham: Springer; 2015. p. 43–92.
- Ko S-J, Lee YH. Center weighted median filters and their applications to image enhancement. *IEEE Trans Circuits Syst.* 1991;38:984–93.
- Jähne B. Digital image processing. Berlin: Springer; 2005.
- Tiago F, Rasband W. ImageJ user guide. Bethesda: National Institute of Mental Health; 2012.
- Di Rienzo JA, Casanovas F, Balzarini MG, Gonzalez L, Tablada M, Robledo CW. InfoStat. Applied Statistics and Biometry of the Agricultural College. National University of Córdoba. Grupo InfoStat, FCA. Universidad Nacional de Córdoba, Argentina; 2008.
- Cointault F, Journaux L, Rabatel G, Germain C, Ooms D, Destain M-F, et al. Texture, color and frequential proxy-detection image processing for crop characterization in a context of precision agriculture. In: Godwin A, editor. Agricultural science. InTech: Rijeka; 2012. p. 49–70.
- Abbad H, El Jaafari S, Bort J, Araus JL. Comparative relationship of the flag leaf and the ear photosynthesis with the biomass and grain yield of durum wheat under a range of water conditions and different genotypes. *Agronomie.* 2004;24:19–28.
- Slafer GA, Savin R. Physiology of crop yield. In: Goodman RE (ed) Encyclopedia of plant and crop science. New York: Taylor & Francis; 2007. p. 1–4.

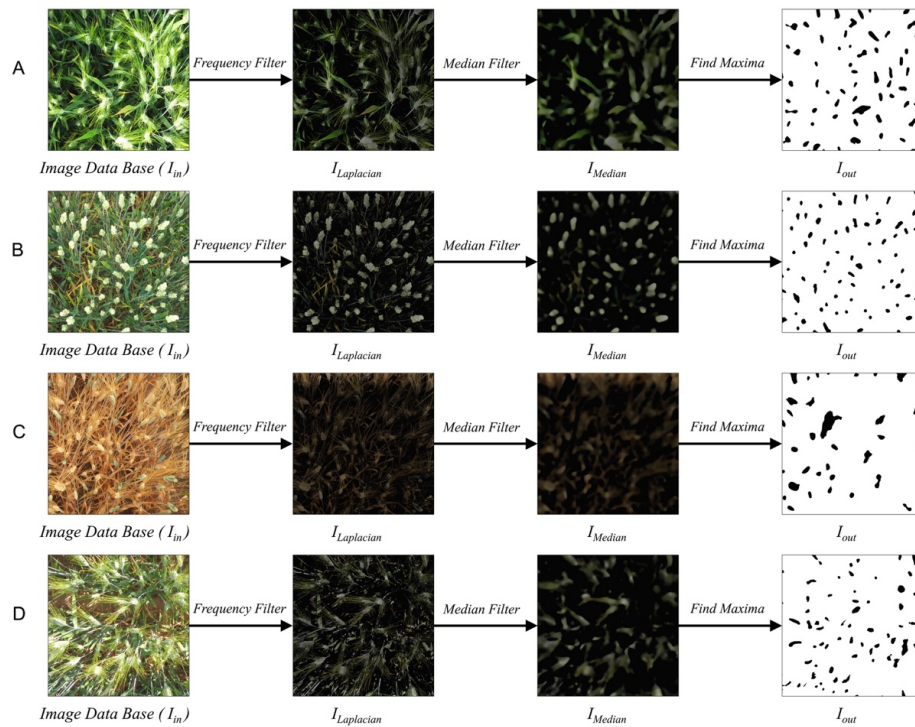
Wheat ear counting in-field conditions: high throughput and low-cost approach  
using RGB images

Jose A. Fernandez-Gallego<sup>1</sup>, Shawn C. Kefauver<sup>1</sup>, Nieves Aparicio Gutiérrez<sup>2</sup>,  
María Teresa Nieto-Taladriz<sup>3</sup> and José Luis Araus<sup>1</sup>

Supplemental material:

## Wheat ear counting in-field conditions: high throughput and low-cost approach using RGB images

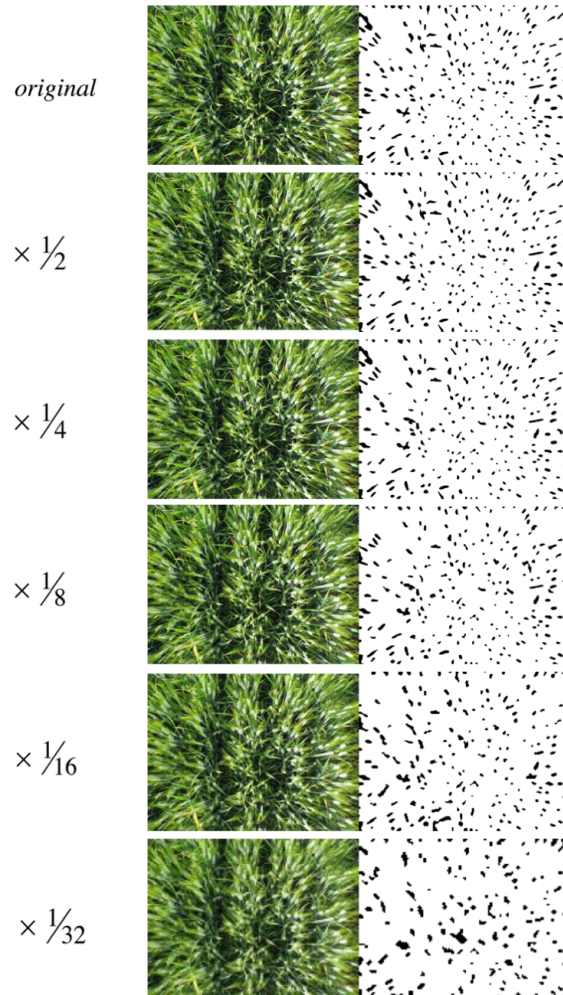
Jose A. Fernandez-Gallego<sup>a</sup>, Shawn C. Kefauver<sup>a\*</sup>, Nieves Aparicio Gutiérrez<sup>b</sup>, Maria Teresa Nieto-Taladriz<sup>c</sup>, José Luis Araus<sup>a</sup>



**Supplementary Figure 1.** Images of plots taken under different incident sunlight conditions, and growth stages on crops grown under different water regimes. A) Image taken at anthesis with direct sunlight within two hours of solar noon in an irrigated plot. B) Image taken at late grain filling under diffuse light conditions in the morning in an irrigated plot. C) Image taken during late grain filling under diffuse light conditions near solar noon in a rainfed plot. D) Image taken late at middle grain filling with direct sunlight in the afternoon

**Wheat ear counting in-field conditions: high throughput and low-cost approach using RGB images**

Jose A. Fernandez-Gallego<sup>a</sup>, Shawn C. Kefauver<sup>a\*</sup>, Nieves Aparicio Gutiérrez<sup>b</sup>, Maria Teresa Nieto-Taladriz<sup>c</sup>, José Luis Araus<sup>a</sup>



**Supplementary Figure 2.** Resized imagery simulation – input and output images. The images were resized using average pixel values, with no interpolation techniques applied

## Wheat ear counting in-field conditions: high throughput and low-cost approach using RGB

### images

Jose A. Fernandez-Gallego<sup>a</sup>, Shawn C. Kefauver<sup>a\*</sup>, Nieves Aparicio Gutiérrez<sup>b</sup>, Maria Teresa

Nieto-Taladriz<sup>c</sup>, José Luis Araus<sup>a</sup>

**Supplementary Table 1.** Values for the whole set of four trials as well as within each trial, for grain yield, thousand kernel weight (TKW), number of grains per unit ground area (grains/m<sup>2</sup>) and ear density (number of ears per unit ground area). For each trait, mean, standard error (SE) and minimum and maximum value across the individual plot

<i>Trial, database</i>	<i>Variable</i>	<i>Mean</i>	<i>SE</i>	<i>Min.</i>	<i>Max.</i>
<i>Whole set (288 plots)</i>	<i>grain yield [kg/ha]</i>	5499	97	2220	9281
	<i>TKW [g]</i>	42.3	0.5	27.9	63.8
	<i>grains/m<sup>2</sup></i>	13266	168	6154	20361
	<i>ears/m<sup>2</sup></i>	410.0	5.2	205.6	709.0
<i>Aranjuez Irrigated (72 plots)</i>	<i>grain yield [kg/ha]</i>	5126	88	3245	6924
	<i>TKW [g]</i>	40.3	0.5	32.3	48.6
	<i>grains/m<sup>2</sup></i>	14014	306	8100	19663
	<i>ears/m<sup>2</sup></i>	487.0	11.1	313.8	709.0
<i>Aranjuez Rainfed (72 plots)</i>	<i>grain yield [kg/ha]</i>	4648	104	2220	6397
	<i>TKW [g]</i>	40.8	0.5	32.0	50.1
	<i>grains/m<sup>2</sup></i>	12549	303	6154	17846
	<i>ears/m<sup>2</sup></i>	405.8	10.8	205.6	642.5
<i>Valladolid Irrigated (72 plots)</i>	<i>grain yield [kg/ha]</i>	7971	91	6101	9281
	<i>TKW [g]</i>	52.0	0.8	33.9	63.8
	<i>grains/m<sup>2</sup></i>	14882	347	9074	20361
	<i>ears/m<sup>2</sup></i>	388.7	6.3	244.0	524.0
<i>Valladolid Rainfed (72 plots)</i>	<i>grain yield [kg/ha]</i>	4231	67	2566	6510
	<i>TKW [g]</i>	36.0	0.6	27.9	47.1
	<i>grains/m<sup>2</sup></i>	11618	242	7718	16517
	<i>ears/m<sup>2</sup></i>	358.3	5.4	260.0	488.0



Cereal crop ear counting in field conditions using zenithal RGB Images

José A. Fernandez-Gallego<sup>1,2,3</sup>, María Luisa Buchailot<sup>1,2</sup>, Adrian Gracia-Romero<sup>1,2</sup>, Thomas Vatter<sup>1,2</sup>, Omar Vergara Diaz<sup>1,2</sup>, Nieves Aparicio Gutiérrez<sup>4</sup>, María Teresa Nieto-Taladriz<sup>5</sup>, Samir Kerfal<sup>6</sup>, Maria Dolors Serret<sup>1,2</sup>, José Luis Araus<sup>1,2</sup>, Shawn C. Kefauver<sup>1,2</sup>

<sup>1</sup> Plant Physiology Section, Faculty of Biology, University of Barcelona.

<sup>2</sup> Agrotecnio.

<sup>3</sup> Programa de Ingeniería Electrónica, Facultad de Ingeniería, Universidad de Ibagué.

<sup>4</sup> Instituto Tecnológico Agrario de Castilla y León (ITACyL).

<sup>5</sup> Instituto Nacional de Investigación y Tecnología Agraria y Alimentaria (INIA).

<sup>6</sup> Syngenta Spain.

Published in:

Journal of Visualized Experiments (2019), Vol. e58695



## **ABSTRACT**

Ear density, or the number of ears per square meter (ears/m<sup>2</sup>), is a central focus in many cereal crop breeding programs, such as wheat and barley, representing an important agronomic yield component for estimating grain yield. Therefore, a quick, efficient, and standardized technique for assessing ear density would aid in improving agricultural management, providing improvements in preharvest yield predictions, or could even be used as a tool for crop breeding when it has been defined as a trait of importance. Not only are the current techniques for manual ear density assessments laborious and time-consuming, but they are also without any official standardized protocol, whether by linear meter, area quadrant, or an extrapolation based on plant ear density and plant counts postharvest. An automatic ear counting algorithm is presented in detail for estimating ear density with only sunlight illumination in field conditions based on zenithal (nadir) natural color (red, green, and blue [RGB]) digital images, allowing for high-throughput standardized measurements. Different field trials of durum wheat and barley distributed geographically across Spain during the 2014/2015 and 2015/2016 crop seasons in irrigated and rainfed trials were used to provide representative results. The three-phase protocol includes crop growth stage and field condition planning, image capture guidelines, and a computer algorithm of three steps: (i) a Laplacian frequency filter to remove low- and high-frequency artifacts, (ii) a median filter to reduce high noise, and (iii) segmentation and counting using local maxima peaks for the final count. Minor adjustments to the algorithm code must be made corresponding to the camera resolution, focal length, and distance between the camera and the crop canopy. The results

demonstrate a high success rate (higher than 90%) and  $R^2$  values (of 0.62-0.75) between the algorithm counts and the manual image-based ear counts for both durum wheat and barley.



## Video Article

## Cereal Crop Ear Counting in Field Conditions Using Zenithal RGB Images

José A. Fernandez-Gallego<sup>1,2,3</sup>, María Luisa Buchailot<sup>1,2</sup>, Adrian Gracia-Romero<sup>1,2</sup>, Thomas Vatter<sup>1,2</sup>, Omar Vergara Diaz<sup>1,2</sup>, Nieves Aparicio Gutiérrez<sup>4</sup>, María Teresa Nieto-Taladriz<sup>5</sup>, Samir Kerfal<sup>6</sup>, Maria Dolores Serret<sup>1,2</sup>, José Luis Araus<sup>1,2</sup>, Shawn C. Kefauver<sup>1,2</sup>

<sup>1</sup>Plant Physiology Section, Faculty of Biology, University of Barcelona

<sup>2</sup>Agrotecnio

<sup>3</sup>Programa de Ingeniería Electrónica, Facultad de Ingeniería, Universidad de Ibagué

<sup>4</sup>Instituto Tecnológico Agrario de Castilla y León (ITACyL)

<sup>5</sup>Instituto Nacional de Investigación y Tecnología Agraria y Alimentaria (INIA)

<sup>6</sup>Syngenta Spain

Correspondence to: Shawn C. Kefauver at [sckefauver@ub.edu](mailto:sckefauver@ub.edu)

URL: <https://www.jove.com/video/58695>

DOI: [doi:10.3791/58695](https://doi.org/10.3791/58695)

Keywords: Wheat, barley, ear counting, segmentation, breeding, phenotyping, precision agriculture, Laplacian

Date Published: 1/16/2019

Citation: Fernandez-Gallego, J.A., Buchailot, M.L., Gracia-Romero, A., Vatter, T., Diaz, O.V., Aparicio Gutiérrez, N., Nieto-Taladriz, M.T., Kerfal, S., Serret, M.D., Araus, J.L., Kefauver, S.C. Cereal Crop Ear Counting in Field Conditions Using Zenithal RGB Images. *J. Vis. Exp.* (), e58695, doi:10.3791/58695 (2019).

### Abstract

Ear density, or the number of ears per square meter (ears/m<sup>2</sup>), is a central focus in many cereal crop breeding programs, such as wheat and barley, representing an important agronomic yield component for estimating grain yield. Therefore, a quick, efficient, and standardized technique for assessing ear density would aid in improving agricultural management, providing improvements in preharvest yield predictions, or could even be used as a tool for crop breeding when it has been defined as a trait of importance. Not only are the current techniques for manual ear density assessments laborious and time-consuming, but they are also without any official standardized protocol, whether by linear meter, area quadrant, or an extrapolation based on plant ear density and plant counts postharvest. An automatic ear counting algorithm is presented in detail for estimating ear density with only sunlight illumination in field conditions based on zenithal (nadir) natural color (red, green, and blue [RGB]) digital images, allowing for high-throughput standardized measurements. Different field trials of durum wheat and barley distributed geographically across Spain during the 2014/2015 and 2015/2016 crop seasons in irrigated and rainfed trials were used to provide representative results. The three-phase protocol includes crop growth stage and field condition planning, image capture guidelines, and a computer algorithm of three steps: (i) a Laplacian frequency filter to remove low- and high-frequency artifacts, (ii) a median filter to reduce high noise, and (iii) segmentation and counting using local maxima peaks for the final count. Minor adjustments to the algorithm code must be made corresponding to the camera resolution, focal length, and distance between the camera and the crop canopy. The results demonstrate a high success rate (higher than 90%) and  $R^2$  values (of 0.62-0.75) between the algorithm counts and the manual image-based ear counts for both durum wheat and barley.

### Video Link

The video component of this article can be found at <https://www.jove.com/video/58695/>

### Introduction

The world cereal utilization in 2017/2018 is reported expand by 1% from the previous year<sup>1</sup>. Based on the latest predictions for cereal production and population utilization, world cereal stocks need to increase yields at a faster rate in order to meet growing demands, while also adapting to increasing effects of climate change<sup>2</sup>. Therefore, there is an important focus on yield improvement in cereal crops through improved crop breeding techniques. Two the most important and harvested cereals in the Mediterranean region are selected as examples for this study, namely, durum wheat (*Triticum aestivum* L. ssp. *durum* [Desf.]) and barley (*Hordeum vulgare* L.). Durum wheat is, by extension, the most cultivated cereal in the south and east margins of the Mediterranean Basin and is the 10th most important crop worldwide, owing to its annual production of 37 million tons annually<sup>3</sup>, while barley is the fourth global grain in terms of production, with a global production at 144.6 million tons annually<sup>4</sup>.

Remote sensing and proximal image analysis techniques are increasingly key tools in the advancement of field high-throughput plant phenotyping (HTPP) as they not only provide more agile but also, often, more precise and consistent retrievals of target crop biophysiological traits, such as assessments of photosynthetic activity and biomass, preharvest yield estimates, and even improvements in trait heritability, such as efficiency in resource use and uptake<sup>5,6,7,8,9</sup>. Remote sensing has traditionally focused on multispectral, hyperspectral, and thermal imaging sensors from aerial platforms for precision agriculture at the field scale or for plant phenotyping studies at the microplot scale<sup>10</sup>. Common, commercially available digital cameras that measure only visible reflected light were often overlooked, despite their very high spatial resolution, but have recently become popular as new innovative image-processing algorithms are increasingly able to take advantage of the detailed color and spatial information that they provide. Many of the newest innovations in advanced agricultural image analyses increasingly rely on the interpretation of data provided by very high-resolution (VHR) RGB images (for their measurement of red, green, and blue visible light

reflectance), including crop monitoring (vigor, phenology, disease assessments, and identification), segmentation and quantification (emergence, ear density, flower and fruit counts), and even full 3D reconstructions based on a new structure from motion workflows<sup>11</sup>.

One of the most essential points for improvement in cereal productivity is a more efficient assessment of yield, which is determined by three major components: ear density or the number of ears per square meter (ears/m<sup>2</sup>), the number of the grains per ear, and the thousand-kernel weight. Ear density can be obtained manually in the field, but this method is laborious, time-consuming, and lacking in a single standardized protocol, which together may result in a significant source of error. Incorporating the automatic counting of ears is a challenging task because of the complex crop structure, close plant spacing, high extent of overlap, background elements, and the presence of awns. Recent work has advanced in this direction by using a black background structure supported by a tripod in order to acquire suitable crop images, demonstrating fairly good results in ear counting<sup>12</sup>. In this way, excessive sunlight and shadow effects were avoided, but such a structure would be cumbersome and a major limitation in an application to field conditions. Another example is an automatic ear counting algorithm developed using a fully automated phenotyping system with a rigid motorized gantry, which was used with good accuracy for counting ear density in a panel composed of five awnless bread wheat (*Triticum aestivum* L.) varieties growing under different nitrogen conditions<sup>13</sup>. Recent work by Fernandez-Gallego<sup>14</sup> has optimized this process for quicker and easier data capture, using VHR RGB color images followed by more advanced, yet still fully automated, image analyses. The efficient and high-quality data collection in field conditions emphasizes a simplified standardized protocol for consistency and high data capture throughput, while the image-processing algorithm employs the novel use of Laplacian and frequency domain filters to remove undesired image components before applying a segmentation for counting based on finding local maxima (as opposed to full delineation as in other previous studies, which may result in more errors with overlapping ears).

This work proposes a simple system for the automatic quantification of ear density in field conditions, using images acquired from commercially available digital cameras. This system takes advantage of natural light in field conditions and, therefore, requires consideration of some related environmental factors, such as time of day and cloud cover, but remains, in effect, simple to implement. The system has been demonstrated on examples for durum wheat and barley but should be extendable in application to bread wheat, which, besides exhibiting ears with similar morphology, are frequently awnless, but further experiments would be required in order to confirm this. In the data capture protocol presented here, zenithal images are taken by simply holding the camera by hand or using a monopod for positioning the digital camera above the crop. Validation data can be acquired by counting the ears manually for subplots in the field or during postprocessing, by counting ears in the image itself. The image-processing algorithm is composed of three processes that, first, effectively remove unwanted components of the image in a manner that, then, allows for the subsequent segmentation and counting of the individual wheat ears in the acquired images. First, a Laplacian frequency filter is used in order to detect changes in the different spatial directions of the image using the default ImageJ filter settings without window kernel size adjustments (Find Maxima segmentation technique determines the local peaks after the median spatial filter step, at which stage the pixels related with ears have higher pixel values than soil or leaves. Therefore, Find Maxima is used to segment the high values in the image, and those regions are labeled as ears, which identifies ears while also reducing overlapping ear errors. Analyze Particles is then used on the binary images to count and/or measure parameters from the regions created by the contrast between the white and black surface created by the Find Maxima step. The result is then processed to create a binary image segmentation by analyzing the nearest neighbor pixel variance around each local maximum to identify the wheat ear shapes in the filtered image. Finally, the ear density is counted using Analyze Particles, as implemented in Fiji<sup>15</sup>. Both Find Maxima and Analyze Particles are standalone functions and available as plugins in Fiji (<https://imagej.nih.gov/ij/plugins/index.html>). Though not presented specifically in the protocol here, preliminary results presented as supplementary material suggest that this technique may be adaptable to conducting ear count surveys from unmanned aerial vehicles (UAVs), providing that the resolution remains sufficiently high<sup>14</sup>.

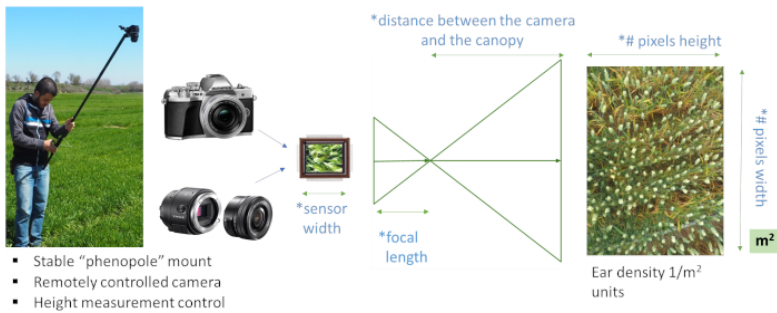
## Protocol

### 1. Prefield crop growth stage and environmental conditions

1. Make sure that the crop growth stage is approximately between grain filling and near crop maturity, with ears that are still green even if the leaves are senescent (which corresponds in the case of wheat to the range 60-87 of Zadoks' scale<sup>16</sup>). Some yellowing of the leaves is acceptable but not necessary.
2. Prepare a sampling plan for image capture with various replicates (pictures per plot) in order to capture plot/area variability; the image-processing algorithm will count the number of ears in the image and convert that to ears per square meter (ears/m<sup>2</sup>) based on the camera specifications.
3. Plan the field excursions to capture the images within two hours of solar noon or, alternatively, on an overcast day in diffuse lighting conditions in order to avoid the negative effects of ear shadowing on the ear counting algorithm.
4. Once in the field, check the top of the crop canopy to make sure that it is dry in order to avoid specular light reflection from moisture. NOTE: In considering the objectives of this protocol, it is important to first consider whether the growth stage of the crop is suitable for applying ear counts. Capturing images outside of the recommended growth stage will either result in suboptimal or in meaningless results (if ears are not present or fully emerged). Image quality also has a considerable impact on processing the results, including resolution and sensor size, and some environmental conditions, such as time of day and cloud cover, need to be carefully considered before proceeding with image capture.

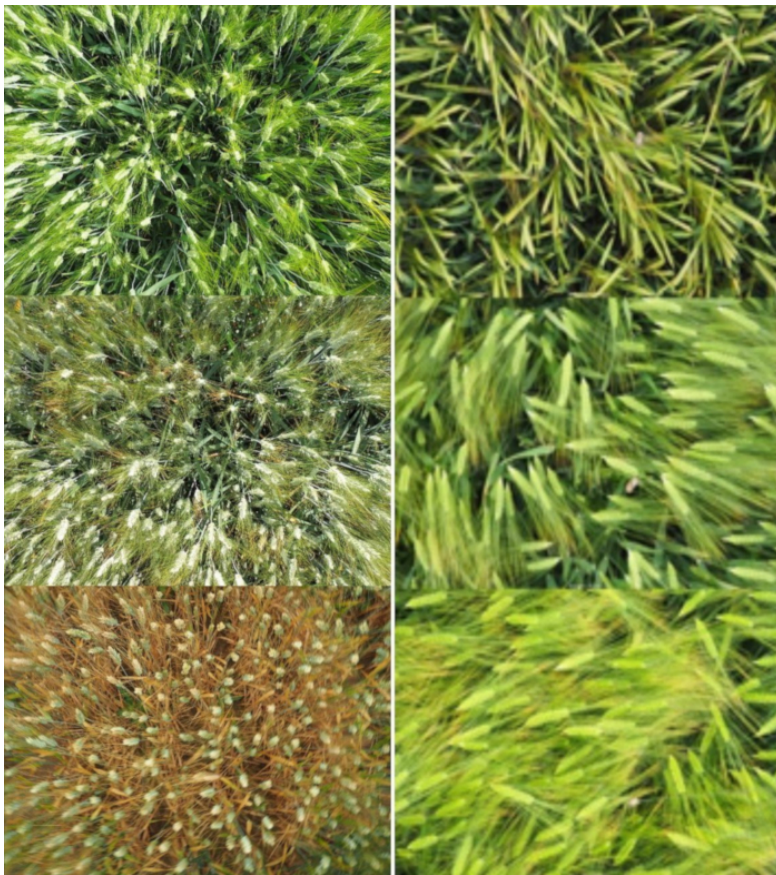
### 2. Image capture in field conditions with natural light

1. Prepare a "phenopole" as shown in **Figure 1** or a similar acquisition system (even handheld) to capture images quickly and yet in a standardized and consistent manner at each plot or target location.



**Figure 1: Ear counting system.** Ear counting system using the "phenopole" shown in the field on the left, with a remotely controlled natural color (RGB) large sensor and high-resolution digital camera system with camera tilt and height, indicating the necessary parameters for adjusting the image-processing algorithm. The sensor and image resolution are detected automatically by the image properties, while the user should input the specifics for the lens focal length and the distance from the canopy. These are necessary to adjust the algorithm for the estimated number of pixels per ear and also the conversion of the image-based total ear count to ear density (ears/ $m^2$ ). For that reason, it is recommended to use the same camera and lens focal length for all field images. [Please click here to view a larger version of this figure.](#)

2. Position the camera on a suitable monopod or "selfie" pole so that it may be maintained level, either using level bubbles or an in-camera stabilization system, to obtain zenithal images.
3. Use a mobile phone, tablet, or another device to connect the camera for both remote control image capture and image visualization for the best results with correctly focused images. Program the camera for autofocus in order to reduce any errors in case the user is not familiar enough with their camera or photography techniques to set a correct manual focus, as demonstrated by the examples of zenithal images with correct focus and exposure in **Figure 2**.



**Figure 2: Zenithal crop images.** Durum wheat and barley ear zenithal images for ear counting data set examples with an acceptable stage of growth and senescence from approximately 61 to 87 according to Zadoks' scale. (Left) Durum wheat zenithal image data set example. (Right) Barley zenithal image data set example. [Please click here to view a larger version of this figure.](#)

4. Take note of the image number prior to image capture in order to match the images correctly with the field plots. Record one image of the general field area at the start and one image of the ground/field between blocks for postprocessing controls.
5. Position the camera at approximately 80 cm above the top of the crop canopy, using a ruler or measurement string to periodically check the camera height above the canopy. Ensure that the camera is level and capture the image. This technique may require 1-2 researcher(s).
6. If additional field ear count validation is desired apart from a manual image count validation, install an extension arm to the frame (e.g., a small circle) and position it in the middle of the image in order to conduct manual field counts of a precise image subset; this technique may require 2-3 people to implement.

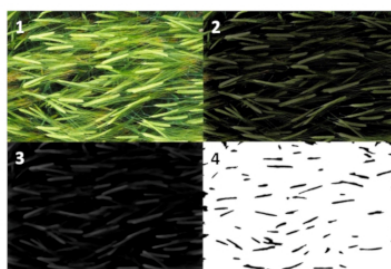
NOTE: Three major considerations in selecting a camera, therefore, include: (1) camera specifications; in this case, the sensor's physical size; (2) focal length of the image lens; (3) distance between the canopy and the camera: smaller distances or greater zoom lenses will capture a smaller area while images captured from a greater distance will capture a bigger crop area. See **Figure 1** for the details on the relevant camera specifications.

### 3. Algorithm implementation and adjustments

NOTE: Here we present algorithm implementation and adjustments for different camera specifications (sensor size, megapixels, focal length, distance to crop) and crop (durum wheat or barley) for automatic ear counting. An overview of the algorithm is presented graphically in **Figure 3**.

**CerealScanner**

1. Image acquisition
2. Laplacian Filter
3. Median Filter
4. Ear counting and m<sup>2</sup>

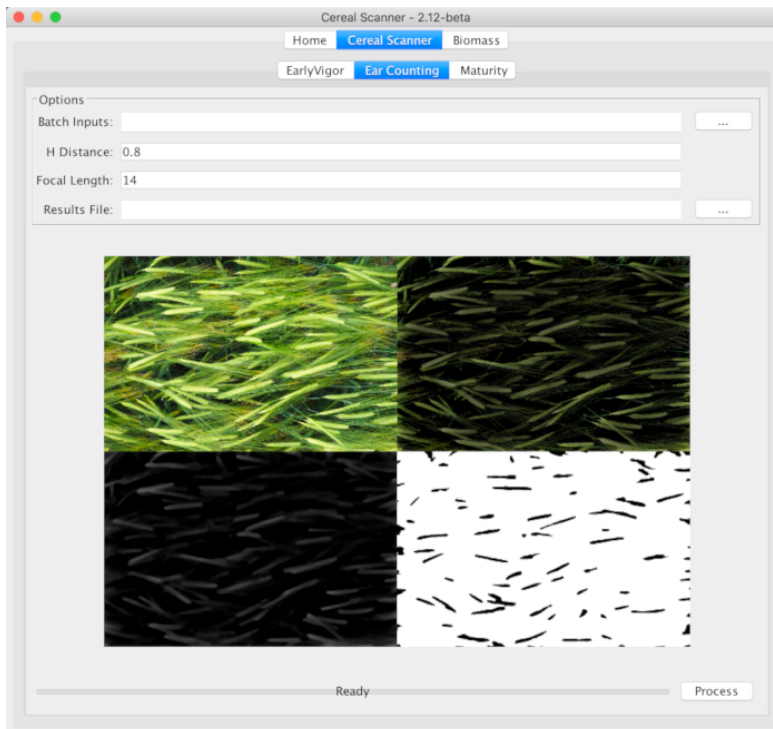


Dataset: Arazuri and Zamadueñas (R+ R-)  
Date: May 2016

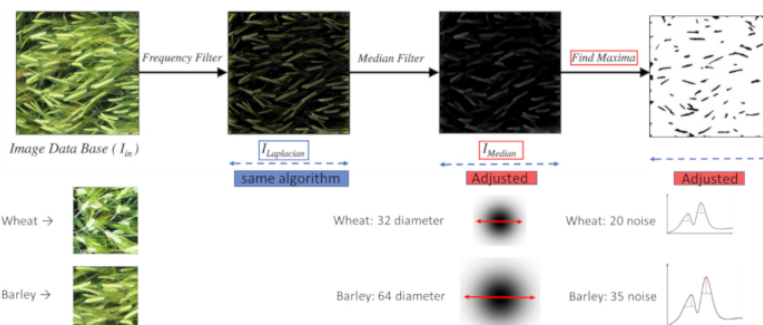
**Figure 3: Image-processing pipeline for two-row barley ear counting.** Image-processing pipeline for two-row barley ear counting as implemented using specific computer code or using the **CerealScanner** software, both of which operate within Fiji (ImageJ). Panel 1 shows the original image. Panel 2 shows the results of the applications of the Laplacian filter. Panel 3 shows the application of the median filter, and Panel 4 shows the results of the final Find Maxima and segmentation for producing the final ear count. Then, the calculations are made to convert the image count to ear density, as shown in **Figure 1**. These images are an example taken from the Arazuri field site (Northeastern Spain, 42°48'33.9"N 1°43'37.9"W) in diffuse light conditions. [Please click here to view a larger version of this figure.](#)

1. Download and install Fiji, Java 8, and the processing code or the University of Barcelona's proprietary **CerealScanner** plugin (<https://fiji.sc/>, <https://www.java.com/en/download/>, and <https://integrativecropecophysiology.com/software-development/cerealscanner/> [information] or <https://gitlab/sckefauver/CerealScanner> [code repository]); contact the corresponding authors for access permissions. The plugin is installed within Fiji by simply copying it into the plugins folder.
2. Open the plugin from the top menu through **Plugins > CerealScanner > Open Cereal Scanner**.  
NOTE: Apart from the work presented here, the CerealScanner plugin includes several different RGB-based vegetation indices related to crop vigor, stress, or chlorophyll<sup>17,18</sup>. The specific CerealScanner portion includes specific algorithms for **Early Vigor** (Fernandez-Gallego, In review), **Ear Counting**<sup>14</sup>, and **Crop Senescence**<sup>19</sup>, as shown in **Figure 4**.
3. Enter the adjustments of the camera specifications and image capture details if they are different from the default values (see **Figure 1** and **Figure 4** for details).
  1. Adjust the algorithm parameter for the camera focal length.
  2. Adjust the algorithm parameter for the distance from the crop canopy.





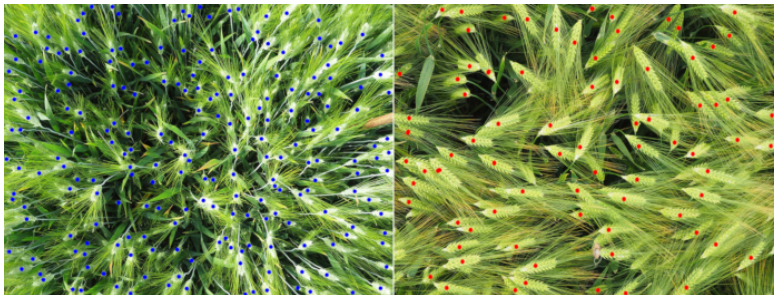
**Figure 4: The CerealScanner 2.12 Beta central tab on both levels, marking the Ear Counting function within the CerealScanner algorithm collection.** The user must select the ... button to the right of **Batch Inputs** to select the folder where the image files are stored, change the default values of the H Distance (distance from the camera to the top of the crop canopy) and Focal Length, if different from the default values, and then select the ... button to the right of **Results File** to choose the name and location of the final results file. The other tabs of the CerealScanner provide algorithms for trait-based phenotyping for **Early Vigor** and onset of **Maturity** as part of the CerealScanner code suite. Under the **Biomass** tab, there are several algorithms for estimations of more general crop vigor and biomass calculations, also for RGB digital images. The example refers to two-row barley, as it was demonstrated in detail in **Figure 3**. [Please click here to view a larger version of this figure.](#)



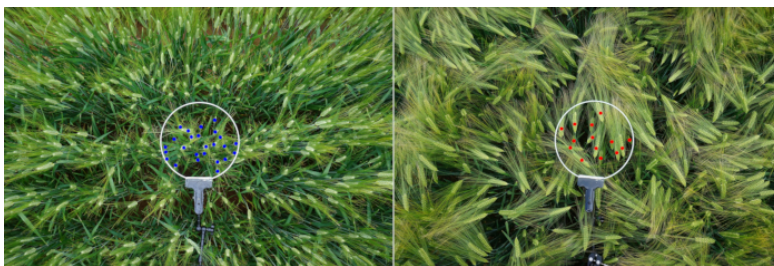
**Figure 5: Algorithm adjustments.** Adjustments required in the image-processing pipeline in order to successfully count both wheat and barley ears using the same algorithm are managed automatically as part of the camera-specific adjustments of H Distance (distance between the camera and the crop canopy) and Focal Length and serve to ensure that the number of pixels per ear remains more or less constant between different applications. [Please click here to view a larger version of this figure.](#)

4. Select the center tab **CerealScanner** and the subsequent central tab **Ear Counting** in order to calculate the number of ears in each image of a field data set.
  1. Under **Options**, enter, in **Batch Inputs**, the location of the photos to analyze.
  2. In the **Results Files**, select where to save the results file. The results file will include two columns with the image file name and the ear counting results.

3. Finally, click on **Process**, and the results file with the ear density in square meters (ears/m<sup>2</sup>), using a simple ratio using the camera settings and the distance between canopy and camera to convert the image area to an actual canopy area in square meters following **Figure 1**, will be automatically produced in a few minutes, depending on the computer speed.
5. Conduct a post-processing validation after the data collection by manually counting the number of wheat or barley ears in the image and then converting this to the number of ears per square meters (ears/m<sup>2</sup>), as is shown in **Figure 1**, to compare the results with those based on the algorithm values.
  1. Use the simple point placement tool built within Fiji, which provides easy support for this process, and the Fiji **Analyze Particles** function for producing the counts automatically; this is shown graphically in **Figure 6**.
  2. Optionally, conduct a validation using a small area circle during field data acquisition as described in step 2.6; manual counts in the field and manual image counts in the laboratory can, then, be used for algorithm validation as shown in **Figure 7**.



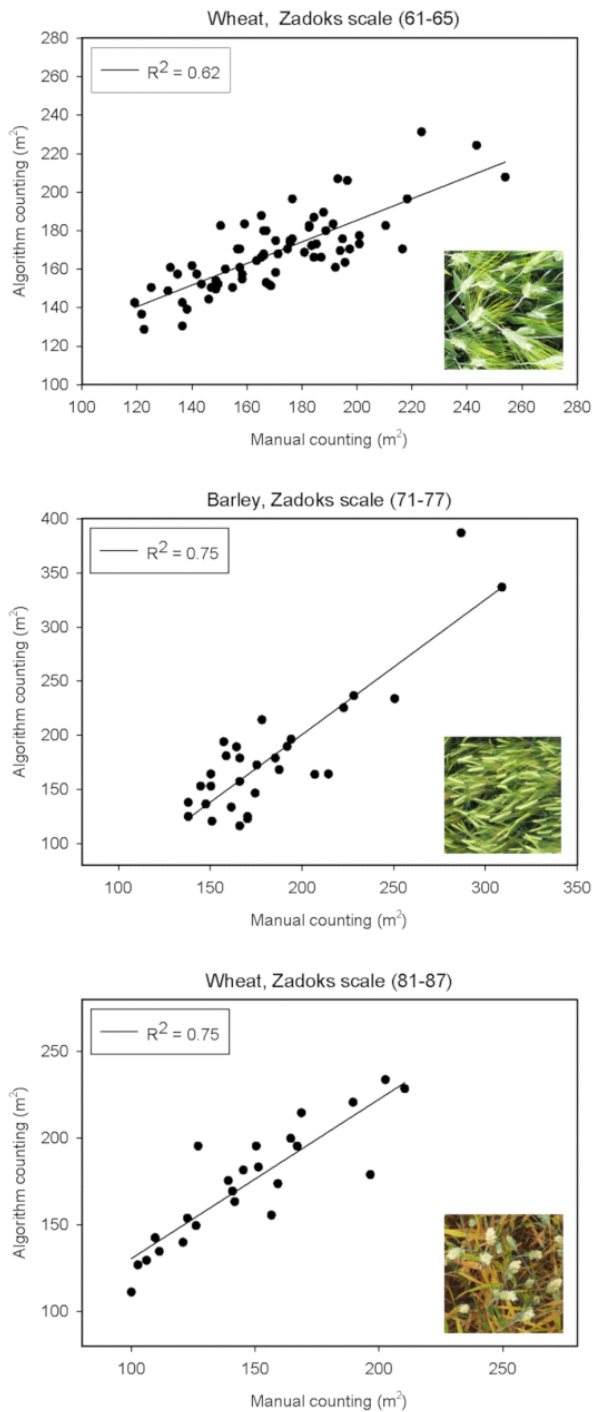
**Figure 6: Algorithm validation using manual in-image ear counts. Manual in-image ear counts for (left) durum wheat and (right) barley.** The small dots were created using the Fiji **Point Tool** and then counted using the **Analyze Particles Function** with a 0.90-1.00 **Circularity constraint** after applying a **Color Threshold** from the **Hue Saturation Intensity** color space for the color specified by the **Point Tool**. This method ensures more accurate image-based manual ear counts. [Please click here to view a larger version of this figure.](#)



**Figure 7: Algorithm validation using manual counts in the field and manual in-image ear counts of wheat and barley, using a circle.** (Left) Wheat image count validation example using a circle. (Right) Barley image count validation example using a circle. The subset counts of the ears within the white circle were counted using the same technique as described in **Figure 6** with the **Point Tool**, **Color Threshold**, and then, **Analyze Particles Function** with **Circularity constraints** and color selection using Hue. [Please click here to view a larger version of this figure.](#)

## Representative Results

In **Figure 8**, the results show the determination coefficient between the ear density (number of ears per square meters) using manual counting and the ear counting algorithm for wheat and barley at three different crop growth stages. The first one is durum wheat with a Zadoks' scale between 61 and 65 ( $R^2 = 0.62$ ). The second one is two-row barley with a Zadoks' scale between 71 and 77 ( $R^2 = 0.75$ ), and the last one is durum wheat with a Zadoks' scale between 81 and 87 ( $R^2 = 0.75$ ).



**Figure 8: The coefficient of determination between ear density (number of ears/ $m^2$ ) using manual image-based counting and the image algorithm for ear counting of durum wheat and two-row barley at different acceptable crop growth stages (at Zadoks' scale 61-87). Both axes show calculations, including conversions to ear density, rather than image-based results only. The representative results are presented here for two different crops over three different growth stages, as well as under different light conditions, namely direct sunlight images of durum wheat at Zadoks' scale 61-65 on the top ( $R^2 = 0.62$ ,  $n = 72$ ), diffuse light images of barley at Zadoks' scale 71-77 in the middle ( $R^2 = 0.75$ ,  $n =$**

30), and diffuse light conditions for durum wheat at Zadoks' scale 81-87 at the bottom ( $R^2 = 0.75$ ,  $n = 24$ ). An example image of each is also shown as an inset in the bottom right corner of each graph. [Please click here to view a larger version of this figure.](#)

## Discussion

Increased agility, consistency, and precision are key to developing useful new phenotyping tools to assist the crop-breeding community in their efforts to increase grain yield despite negative pressures related to global climate change. Efficient and accurate assessments of cereal ear density, as a major agronomic component of yield of important staple crops, will help provide the tools needed for feeding future generations. Focusing on the improvement and support of crop-breeding efforts in field conditions helps keep this research and the techniques presented here more closely tied to real-world climate change scenarios and the needs of the breeding community but also presents technical difficulties. As such, it is important to pay close adherence not only to the data capture and image processing in this protocol but also to the recommendations for optimal environmental conditions and crop growth stages for its successful implementation<sup>11</sup>. As a major agronomic component of yield, ear density is considered one of the most important target traits in the push for increasing cereal crop yields (see the article by Slafer et al.<sup>20</sup> and references therein). The focus in this protocol toward an optimally cost-efficient, agile, and straightforward field phenotyping technique considers that these aspects of the protocol are key to its adoption and implementation by the breeding community at large. In contrast, previous related studies with similar aims at assessing ear density or other yield component quantification have used more involved data capture and environmental control structures, such as enclosing structures and fixed camera supports or even artificial light inputs, that effectively impede practical application under field conditions and implementation in actual breeding programs<sup>12,20,22</sup>.

Thus, we have presented here a detailed protocol that is the result of testing various different techniques in an iterative optimization process, resulting in a simple but effective image data capture method requiring only a commercially available, moderately high-resolution RGB digital camera and a rudimentary "phenopole" for holding the camera above the crop canopy. Other image-filtering attempts based on RGB color or alternative color spaces, such as hue-saturation-intensity or CIELAB, were not as effective or consistent as the use of the Laplacian and median frequency domain filters in removing unwanted image elements, especially the awns. We have designed the image capture pipeline system with different elements, some of which can be easily adjusted with minor changes in the image-processing algorithm implementation. In the case studies presented here, we have used two different compact cameras with relatively large sensors and 20.1 megapixels (MP) and 16.0 MP resolutions for capturing images with wide-angle lenses of 16-20 mm from a distance of 80 cm from the crop canopy. This has proven more than sufficient to produce detailed canopy barley and wheat information, with simulations demonstrating that the technique maintains high levels of precision down to approximately 8 MP<sup>14</sup> (with similar lenses and distances from the canopy).

Although the consistency and precision of the presented image-processing techniques depend on the environmental conditions and phenological stage at the time of image capture, the algorithms show promise in providing a robust performance in their application to different small-grain cereals, including durum and bread wheat and two-row and six-row barley varieties. While this algorithm has yet to be fully tested, the image capture would be the same, with perhaps some minor adjustments with regard to the relative size and position of the ear in the images in order to provide for optimal ear counting results. In the presented protocol, the image-based ear density estimates achieved maximal accuracy and correlated best with manual image counts and grain yield compared to images captured at later growth stages, when crop senescence resulted in a loss of color and illumination contrast between the rest of the crop canopy and the ears. This may be a result of higher temperatures or lower water availability at the later parts of grain filling, which are especially common in typical Mediterranean conditions, that can cause the leaves and culm to senesce before the ears do<sup>23</sup>; this contrast is essential for the effectiveness of the separation between the ears, leaves, and soil. In overly mature or senescent canopies with the ears already yellow, the contrast between the different image elements is not adequate for ear counting. As such, in other climates, the optimal timing may be slightly different if there is no water stress during senescence onset.

Even though the data collection in field conditions requires close attention to such environmental conditions as sunlight intensity and sunlight illumination angles, the robust image analysis algorithm presented here provides some leeway in the image capture window by using spatial techniques that ignore image albedo effects, given that the correct image exposure was used for the particular light conditions at the moment of image capture; automatic settings have worked well in that respect. In previous work, a fuller range of lighting effects was tested, indicating that the only major source of error with regard to light effects is the production of strong shadows in the image when capturing images in direct sunlight either early or late in the day, due to the angle of the sun<sup>14</sup>. The first two image filter applications help to minimize any apparent effects from excess illumination (although not via camera overexposure) while also reducing any background components of the image; at the same time, these filters also contribute to smoothing and noise reduction, both of which aid in the subsequent Find Maxima process<sup>23,24</sup>. Therefore, while the natural illumination factors must be accounted for, such as the angle of the sun when the images are taken in direct rather than in diffuse light conditions, this is mainly in order to reduce errors related to shadow artifacts.

Furthermore, correlations between algorithm ear counts from the presented protocol and grain yield were greater and more significant than manual (field-based) ear counts of the same experiment<sup>11</sup>, which supports the claim that this protocol is not only more precise but also more consistent as a standardized protocol for the assessment of ear density. While not presented here specifically, similar data capture and processing techniques appears to be feasible using mobile phone, aerial or other automated platforms as they perform quite well under simulated reduced image resolutions. Additional tests for greyscale reduction (for faster image processing) and reduced resolution image simulations (from the application of other cameras or UAVs) were conducted by applying the image conversions before the first filter<sup>14</sup> and suggested that, in optimal conditions, processing times may be reduced in these ways without any loss of accuracy. As for possible future directions, the image-processing algorithms presented here only take advantage of the VHR RGB color data as it is captured by the camera (similar to the human eye), but other potential improvements may result from the conversion to hybrid color spaces, such as hue-saturation-intensity, or through data fusion in combination with other more advanced scientific sensors, such as multispectral or thermal, which both have become more affordable recently and offer the potential for improvement in ear density estimations, although perhaps at different growth stages or in different field conditions.

In summary, the critical steps for the implementation of this protocol include first and foremost proper planning for the time of year and environmental conditions of the crop, which are optimal when the crop is in growth stages 60-87 of Zadoks' scale and either at solar noon or in diffuse light conditions. Furthermore, the acquisition of digital images should be conducted in a controlled manner accounting for camera angle, distance from the canopy, and camera focus for each image. Finally, optimized computer-processing options are presented in detail for

reproducing the processing code pipeline, or contact the authors for either the original code or the code integrated as a graphical user interface (GUI) in a plug-in for Fiji, namely, the CerealScanner.

## Disclosures

The authors have nothing to disclose.

## Acknowledgements

The authors of this research would like to thank the field management staff at the experimental stations of Colmenar de Oreja (Aranjuez) of the Instituto Nacional de Investigación y Tecnología Agraria y Alimentaria (INIA) and Zamadueñas (Valladolid) of the Instituto de Tecnología Agraria de Castilla y León (ITACyL) for their field support of the research study crops used. This study was supported by the research project AGL2016-76527-R from MINECO, Spain and part of a collaboration project with Syngenta, Spain. The BPIN 2013000100103 fellowship from the "Formación de Talento Humano de Alto Nivel, Gobernación del Tolima - Universidad del Tolima, Colombia" was the sole funding support for the first author Jose Armando Fernandez-Gallego. The primary funding source of the corresponding author, Shawn C. Kefauver, came from the ICREA Academia program through a grant awarded to Prof. Jose Luis Araus.

## References

1. Food and Agriculture Organization (FAO). *Food outlook: Biannual report on global food markets (November)*. Food and Agriculture Organization of the United Nations (2017).
2. Araus, J.L., Kefauver, S.C. Breeding to adapt agriculture to climate change: affordable phenotyping solutions. *Current Opinion in Plant Biology*. (2018).
3. Ranieri, R. Geography of the Durum Wheat Crop. *Pastaria International*. **6** (2015).
4. Food and Agriculture Organization (FAO). *The State of Food Insecurity in the World*. Food and Agriculture Organization of the United Nations (2014).
5. Araus, J.L., Cairns, J.E. Field high-throughput phenotyping: the new crop breeding frontier. *Trends in Plant Science*. **19** (1), 52–61 (2014).
6. Fiorani, F., Schurr, U. Future Scenarios for Plant Phenotyping. *Annual Review of Plant Biology*. **64** (1), 267–291 (2013).
7. Cabrera-Bosquet, L., Crossa, J., von Zitzewitz, J., Serret, M.D., Luis Araus, J. High-throughput Phenotyping and Genomic Selection: The Frontiers of Crop Breeding Converge. *Journal of Integrative Plant Biology*. **54** (5), 312–320 (2012).
8. Araus, J.L., Ferrio, J.P., Voltas, J., Aguilera, M., Buxó, R. Agronomic conditions and crop evolution in ancient Near East agriculture. *Nature Communications*. **5** (1), 3953 (2014).
9. Furbank, R.T., Tester, M. Phenomics – technologies to relieve the phenotyping bottleneck. *Trends in Plant Science*. **16** (12), 635–644 (2011).
10. Araus, J.L., Kefauver, S.C., Zaman-Allah, M., Olsen, M.S., Cairns, J.E. Translating High-Throughput Phenotyping into Genetic Gain. *Trends in Plant Science*. **23** (5), P451–466 (2018).
11. Duan, T. et al. Dynamic quantification of canopy structure to characterize early plant vigour in wheat genotypes. *Journal of Experimental Botany*. **67** (15), 4523–4534 (2016).
12. Cointault, F., Guerin, D., Guillemin, J., Chopinet, B. In-field *Triticum aestivum* ear counting using colour-texture image analysis. *New Zealand Journal of Crop and Horticultural Science*. **36** (2), 117–130 (2008).
13. Dornbusch, T. et al. *Digital Field Phenotyping by LemnaTec*. (2015).
14. Fernandez-Gallego, J.A., Kefauver, S.C., Gutiérrez, N.A., Nieto-Taladriz, M.T., Araus, J.L. Wheat ear counting in-field conditions: high throughput and low-cost approach using RGB images. *Plant Methods*. **14** (1), 22 (2018).
15. Schneider, C.A., Rasband, W.S., Eliceiri, K.W. NIH Image to ImageJ: 25 years of image analysis. *Nature Methods*. **9** (7), 671–675 (2012).
16. Zadoks, J., Chang, T., Konzak, C. A decimal growth code for the growth stages of cereals. *Weed Research*. **14** (14), 415–421 (1974).
17. Casadesús, J. et al. Using vegetation indices derived from conventional digital cameras as selection criteria for wheat breeding in water-limited environments. *Annals of Applied Biology*. **150** (2), 227–236 (2007).
18. Hunt, E.R. et al. A visible band index for remote sensing leaf chlorophyll content at the canopy scale. *International Journal of Applied Earth Observation and Geoinformation*. **21** (1), 103–112 (2013).
19. Zaman-Allah, M. et al. Unmanned aerial platform-based multi-spectral imaging for field phenotyping of maize. *Plant Methods*. **11** (1), 35 (2015).
20. Slafer, G.A., Savin, R., Sadras, V.O. Coarse and fine regulation of wheat yield components in response to genotype and environment. *Field Crops Research*. **157**, 71–83 (2014).
21. Liu, T. et al. In-field wheatear counting based on image processing technology. *Nongye Jixie Xuebao/Transactions of the Chinese Society for Agricultural Machinery*. **45** (2), 282–290 (2014).
22. Cointault, F. et al. Texture, Color and Frequential Proxy-Detection Image Processing for Crop Characterization in a Context of Precision Agriculture. *Agricultural Science*. 49–70 (2012).
23. Abbad, H., El Jaafari, S., Bort, J., Araus, J.L. Comparative relationship of the flag leaf and the ear photosynthesis with the biomass and grain yield of durum wheat under a range of water conditions and different genotypes. *Agronomie*. **24**, 19–28 (2004).
24. Ko, S.-J., Lee, Y.H. Center weighted median filters and their applications to image enhancement. *IEEE Transactions on Circuits and Systems*. **38** (9), 984–993 (1991).
25. Smolka, B. *Nonlinear techniques of noise reduction in digital color images*. Wydawnictwo Politechniki Śląskiej (2004).



# Chapter 3

Automatic wheat ear counting using machine learning based on RGB UAV imagery

Jose A. Fernandez-Gallego<sup>1,2,3</sup>, Peter Lootens<sup>4</sup>, Irene Borra-Serrano<sup>4,5</sup>, Veerle Derycke<sup>6</sup>, Geert Haesaert<sup>6</sup>, Isabel Roldán-Ruiz<sup>4,7</sup>, Jose L. Araus<sup>1,2,\*</sup>, Shawn C. Kefauver<sup>1,2,\*</sup>

<sup>1</sup> Plant Physiology Section, Department of Evolutionary Biology, Ecology and Environmental Sciences, Faculty of Biology, University of Barcelona, Diagonal 643, 08028, Barcelona, Spain.

<sup>2</sup> AGROTECNIO (Center for Research in Agrotechnology), Av. Rovira Roure 191, 25198, Lleida, Spain.

<sup>3</sup> Programa de Ingeniería Electrónica, Facultad de Ingeniería, Universidad de Ibagué, Carrera 22 Calle 67, 730001, Ibagué, Colombia

<sup>4</sup> Plant Sciences Unit, Institute of Agricultural, Fisheries and Food Research (ILVO), Caritasstraat 39, 9090 Melle, Belgium.

<sup>5</sup> Department of Biosystems, MeBios, KU Leuven, Leuven, Belgium

<sup>6</sup> Ghent University, Department Plants and Crops, Faculty of Bioscience Engineering, Valentin Vaerwyckweg1, 9000 Ghent, Belgium.

<sup>7</sup> Ghent University, Department of Plant Biotechnology and Bioinformatics, Technologiepark 71, 9052 Ghent, Belgium.

Submitted to:

Remote Sensing of Environment

## **ABSTRACT**

In wheat and other cereals, the number of ears per unit area is one of the main yield determining components. An automatic evaluation of this parameter may contribute to the advance of wheat phenotyping and monitoring. There is no standard protocol for wheat ear counting in the field, and moreover it is time-consuming. An automatic ear counting system is proposed using machine learning techniques based on RGB images acquired from an aerial platform. Evaluation was performed on a set of 12 winter wheat cultivars with 3 nitrogen treatments during the 2017-2018 crop season. The automatic system developed uses frequency filter, segmentation, feature extraction and classification techniques to discriminate ears into the image. The relationship between the image-based manual counting and the algorithm counting for training and classifying, and validation exhibited high accuracy and efficiency. In addition, manual ear counting was conducted in the field. The correlations between the automatic and the manual in-situ ear counting with grain yield were compared. Correlations between both ear counting systems were strong, particularly for the lower N treatment. Methodological requirements and limitations are discussed.





# **Automatic wheat ear counting using machine learning based on RGB UAV imagery**

Jose A. Fernandez-Gallego<sup>1,2,3</sup>, Peter Lootens<sup>4</sup>, Irene Borra-Serrano<sup>4,5</sup>, Veerle Derycke<sup>6</sup>, Geert Haesaert<sup>6</sup>, Isabel Roldán-Ruiz<sup>4,7</sup>, Jose L. Araus<sup>1,2,\*</sup>, Shawn C. Kefauver<sup>1,2,\*</sup>

<sup>1</sup> Plant Physiology Section, Department of Evolutionary Biology, Ecology and Environmental Sciences, Faculty of Biology, University of Barcelona, Diagonal 643, 08028, Barcelona, Spain; jfernaga46@alumnes.ub.edu, jaraus@ub.edu, sckefauver@ub.edu

<sup>2</sup> AGROTECNIO (Center for Research in Agrotechnology), Av. Rovira Roure 191, 25198, Lleida, Spain

<sup>3</sup> Programa de Ingeniería Electrónica, Facultad de Ingeniería, Universidad de Ibagué, Carrera 22 Calle 67, 730001, Ibagué, Colombia

<sup>4</sup> Plant Sciences Unit, Institute of Agricultural, Fisheries and Food Research (ILVO), Caritasstraat 39, 9090 Melle, Belgium; peter.lootens@ilvo.vlaanderen.be, irene.borra-serrano@ilvo.vlaanderen.be, isabel.roldan-ruiz@ilvo.vlaanderen.be

<sup>5</sup> Department of Biosystems, MeBios, KU Leuven, Leuven, Belgium

<sup>6</sup> Ghent University, Department Plants and Crops, Faculty of Bioscience Engineering, Valentin Vaerwyckweg1, 9000 Ghent, Belgium; veerle.derycke@ugent.be; geert.haesaert@ugent.be

<sup>7</sup> Ghent University, Department of Plant Biotechnology and Bioinformatics, Technologiepark 71, 9052 Ghent, Belgium

\*Corresponding authors:

José L. Araus, Tel. + 34 934021469; E-mail address: jaraus@ub.edu

Shawn C. Kefauver, Tel. +34 934021465; M. +Fax +34 934112842

E-mail address: sckefauver@ub.edu

**Abstract:**

In wheat and other cereals, the number of ears per unit area is one of the main yield determining components. An automatic evaluation of this parameter may contribute to the advance of wheat phenotyping and monitoring. There is no standard protocol for wheat ear counting in the field, and moreover it is time-consuming. An automatic ear counting system is proposed using machine learning techniques based on RGB images acquired from an aerial platform. Evaluation was performed on a set of 12 winter wheat cultivars with 3 nitrogen treatments during the 2017-2018 crop season. The automatic system developed uses frequency filter, segmentation, feature extraction and classification techniques to discriminate ears into the image. The relationship between the image-based manual counting and the algorithm counting for training and classifying, and validation exhibited high accuracy and efficiency. In addition, manual ear counting was conducted in the field. The correlations between the automatic and the manual in-situ ear counting with grain yield were compared. Correlations between both ear counting systems were strong, particularly for the lower N treatment. Methodological requirements and limitations are discussed.

**Keywords:** Digital image processing, ECOFE, Field phenotyping, Machine learning, Wheat

## 1. Introduction

High throughput plant phenotyping (HTPP) relies on the availability of advanced sensors, suitable image analysis and data mining tools (Araus and Cairns, 2014; Deery et al., 2014). In recent years, research in this area is growing exponentially, but field phenotyping is still perceived as a bottleneck for crop breeding due to the need for massive data collection and processing (Araus and Kefauver, 2018), image analysis tasks (Kefauver et al., 2018; Kelly et al., 2015; Minervini et al., 2015), science community adaptation to new technologies (Singh et al., 2016), and the need to adapt sensors, algorithms and data management to the wide array of traits needed for phenotyping (Qiu et al., 2018).

Grain weight, number of grains per ear and ear density (understood as the number of ears or spikes per unit ground area) are the most important yield components in wheat (del Moral et al., 2010; Simane et al., 1993; Slafer et al., 2014). An appropriate quantification of these components is therefore essential for wheat breeders to assess yield potential of breeding material in early generation. Traditionally, ear density is determined manually in-situ, by counting the number of ears present in a given area, which is time-consuming. In addition, as only a small subsection of the plot is usually considered, intra-plot heterogeneity might result in inaccurate estimations.

As an alternative to this approach, on-ground automatic ear counting systems have been developed, based on RGB (Red/Green/Blue), thermal, multispectral and laser images. In the case of thermal, multispectral and laser sensors, few image processing techniques have been developed. For instance, color thermal maps and contrast limited adaptive histogram equalization (CLAHE) (Fernandez-Gallego et al., 2019a); threshold segmentation and denoising based on

morphological filters (Zhou et al., 2018a) for multispectral images; and in case of a laser sensor, voxel-based tree detection and mean shift approach (Velumani et al., 2017). Nevertheless, RGB sensors have been widely used as a major remote sensing tool in many phenotyping tasks (Araus et al., 2018) due to their relatively low cost (Araus et al., 2018; Qiu et al., 2018), high resolution (Deery et al., 2014; Minervini et al., 2015), and a fast adaptation to natural light conditions (Cointault et al., 2008; Fernandez-Gallego et al., 2019b) that allows RGB sensors to acquire a faithful representation of an original scene even mounted on aerial platforms with continuous and unforeseen movements.

Different image processing techniques have been developed for ear counting using RGB sensors. These image processing techniques include (i) hybrid spaces with texture parameters (Cointault et al., 2008); (ii) decorrelation stretching, scale-invariant feature transform (SIFT) descriptors and support vector machine (SVM) (Sadeghi-Tehran et al., 2017; Zhu et al., 2016); (iii) multi-feature extraction using color, texture and histogram, kernel principal component analysis (KPCA) and the twin-support-vector-machine (TWSVM) model (Zhou et al., 2018b); (iv) Laplacian frequency filter, median spatial filter and local peak segmentation (Fernandez-Gallego et al., 2018a), including a simulation and implications of lower resolution (Fernandez-Gallego et al., 2018b); and (v) convolutional neural networks (CNNs) using fast region-based CNN (Madec et al., 2019). However, to date automatic ear counting systems have been implemented only on the ground for resolution reasons, using zenithal RGB images acquired at less than one meter (Cointault et al., 2008), around one meter (Fernandez-Gallego et al., 2018a) or at few meters above the crop: 2.5 m (Madec et al., 2019), 2.9 m (Sadeghi-Tehran et al., 2017), 3.5 m (Zhou et al., 2018a), and

even 5 m (Zhu et al., 2016).

To the best of our knowledge, there is no information in the literature regarding the use of RGB images acquired at further distances above the crop, for example from an Unmanned Aerial Vehicle (UAV), for ear counting. Resolution is a key factor for image processing: higher resolution allows to extract more features from the input image in comparison to lower resolution (Syrris et al., 2015), which is critical for the detection of ears from any aerial platform. While this limited application in the past, the increasing availability of high resolution RGB imaging devices that provide high pixel density and thus improved ground sampling distance (GSD) from a greater distance, may make it feasible to use UAV platforms for ear counting.

In this study, we propose an automatic wheat ear counting system using RGB images acquired from an UAV. A field trial comprising 12 modern wheat varieties tested under three fertilization conditions in four replicates was used for method development and validation. Orthophotos with a GSD of 0.24 cm/pixel were used. An image processing pipeline was developed using filtering, segmentation, feature extraction and machine learning techniques. Manual in-situ and image-based counting were conducted for validation purposes.

## **2. Material and methods**

### **2.1. Plant material and growing conditions**

A field trial with twelve winter wheat (*Triticum aestivum* L.) varieties (Benchmark, Bologna, Nara, Chambo, Henrik, Hondia, Diego, Julius, Lilli, Siskin, RGT Reform and Sobervio) and 3 nitrogen levels was established on a sandy loam soil at the experimental farm of Ghent University in Bottelare, Belgium (lat. 50.96 N, long.

3.78 E). Nitrogen fertilization levels included the standard recommended in the area (N.std), standard+30% (N+30) and standard-50% (N-50) (Fig. 1). The trial was part of a multi-location field trial run by the European Consortium for Open Field Experimentation (ECOFE, <https://www.ecofe.eu>) (Stützel et al., 2016). The field trial was set-up as a split-plot design with varieties grown in plots of 1,5 m by 12 m at a sowing density of 350 seeds m<sup>-2</sup>, and with four replicates. Nitrogen fractions were given on March 22, 2018, on April 27, 2018 and on May 25, 2018 respectively. Nitrogen fertilizer used was Ammonium nitrate 27%. The accumulated rainfall during the growing season was 513.7 mm and the average temperature was 10.2 °C (Fig. 1). Plots were mechanically harvested on July 14, 2018.

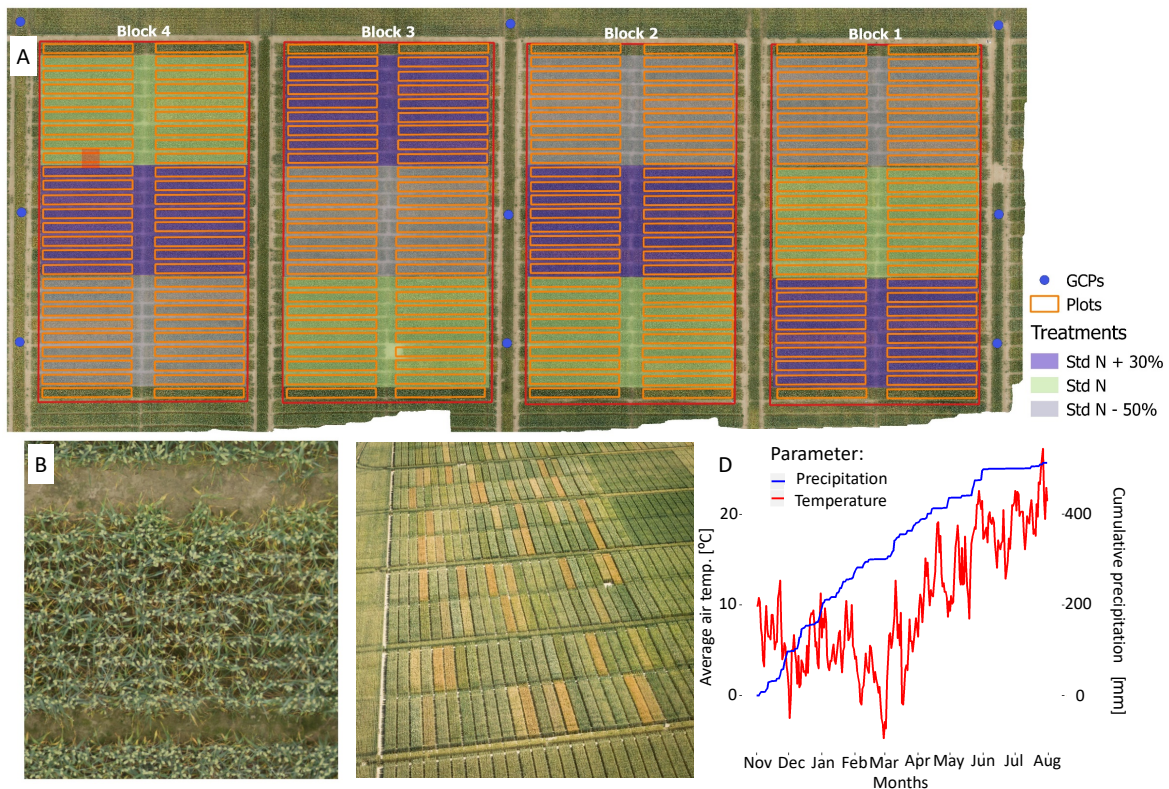


Figure 1. A) Schematic overview of the field trial with the nine ground control points (GCPs), the four blocks division, plots delimited and the treatments

applied; B) Zoom of one plot (central part indicated in red in A); C) overview of the field trial and D) average air temperature (°C) and cumulative precipitation (mm) for the entire growing period (November 1, 2017 – July 15, 2018) of the winter wheat trial.

## **2.2. Orthophotos, plot and subplot images**

RGB images were acquired using a 12-rotor UAV (Model Onyxstar Hydra-12, Altigator, Belgium) at 25 m flight altitude under natural sunlight conditions with an overlap of 70% in both directions (forward-lap and side-lap). The images were acquired with a Sony α6000 DLSR (Sony Corporation, Japan), 24.5-megapixel resolution camera with a 23.5 x 15.6 mm sensor size, native resolution of 6000 x 4000 pixels and equipped with a 35 mm focal length lens. All images were taken in manual mode to avoid different settings in successive images. Trigger speed, aperture and sensitivity to light (ISO) were adjusted in the field before the start of the flight, and the focus was set to automatic mode. Files were stored in RAW and JPG format. Images were acquired under diffuse light conditions (cloudy) at two dates: June 4 and June 19, 2018 corresponding to 61 and 75 growth stages (GS) of the Zadoks scale (Zadoks et al., 1974), respectively. Agisoft Photoscan software (version 1.2.3, Agisoft LLC, St. Peterburg, Russia) was used to build geo-referenced orthophotos using nine ground control points (Fig. 1). The coordinates of those points were determined with an RTK GPS (Stonex S10 GNSS, Stonex SRL, Italy). The spatial resolution was defined automatically by the software based on the camera parameters and flight altitude. In practice it ranged from 0.23 cm/pixel to 0.24 cm/pixel. For comparison reasons the orthomosaics of both dates were exported at the lowest spatial resolution, which



was 0.24 cm/pixel. Halcon Image Analysis software (version 11, MVTec Software GmbH, Munich, Germany) was used to delineate each plot avoiding borders and to divide it into nine subplots (Fig. 2). The resulting plots had a footprint size of 0.96 m x 8.64 m; therefore, each subplot had a footprint size of 0.96 m x 0.96 m. Images from the centre of each plot (subplot #5, Fig. 2) were selected for training and validation purposes in order to avoid possible errors due to the distortion or perspective (Jaud et al., 2018). The complete plots (from subplot #1 to #9) were used for the automatic wheat ear counting system. In total 2592 subplot images were processed.

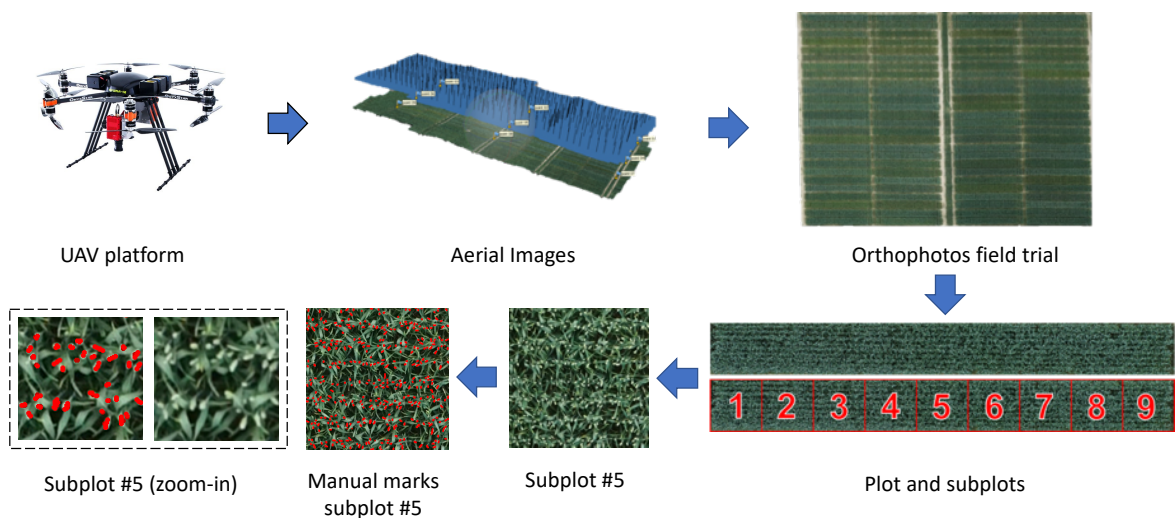


Figure 2. Schematic representation of the image acquisition system and image-based validation. Each plot was divided in nine subplots. The central subplot (subplot #5) was selected for training and validation, to avoid possible errors due to the distortion or perspective. Red marks were placed manually on each ear. The dotted line rectangle shows a zoom-in of subplot #5 including the manual marks corresponding to the complete area covered by each single ear. These marks were used for training and classification purposes. For algorithm validation,

a single dot per ear was used, as the final purpose of this work was to develop a methodology for wheat ear counting and not to determine their shape or size.

### **2.3. Automatic wheat ear counting system using UAV imagery**

The algorithm for ear counting is based on the pipeline developed by Fernandez-Gallego et al. (2018) which includes three main steps: Laplacian frequency filter, median filter and Find Maxima. For the case presented in this study based on UAV imagery, we have used the Laplacian frequency filter and Find Maxima steps (Fernandez-Gallego et al., 2018a), and have included two additional steps: (a) feature extraction and (b) training and classifying (Fig. 3). In this adaptation of the original algorithm, the median filter step was excluded in order to maintain the high frequency information of the canopy after the Laplacian frequency filter step, considering the greater distance between the sensor and canopy. The algorithms were developed in ImageJ (version 2.0.0-rc-69, NIH, Bethesda, MD, USA) and MATLAB (version R2014b, Mathworks, Inc., MA, USA). Therefore, the final pipeline algorithm consists of four steps: (1) Laplacian frequency filter, (2) Find Maxima, (3) features extraction and (4) training and classifying. The Laplacian filter was applied as a wide frequency filter to avoid unwanted objects such as awns, leaves and soil. Find Maxima was then used for local peak detection in order to define image areas where ears could be located (segmentation). We developed a feature extraction step in order to obtain numerical characteristics related to shape, color and statistical measurements (such as mean and standard deviation) for each local peak detected in the previous step. Finally, a training and classifying step was developed to decide between two classes; *Class1*: Ear, *Class2*: Non-Ear. The image processing

system proposed uses as input subplot images (Fig. 3). This means that the estimation of the number of ears per plot is the sum of each subplot (from the subplot #1 to #9) not including the buffer area, which was excluded in the preliminary plot delineation). The sequence of steps implemented is described in Fig. 4. Laplacian frequency filter and Find Maxima steps are widely discussed in (Fernandez-Gallego et al., 2018a).

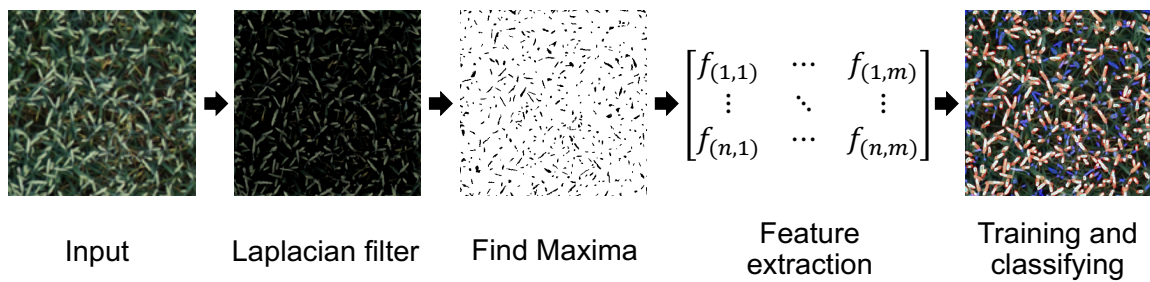


Figure 3. Image processing system proposed. The input is a subplot image. Laplacian filter and Find Maxima are used for filtering and segmentation tasks respectively. Numerical characteristics such as shape, color and statistical measurement for each segmented area are calculated in the feature extraction step. Areas in color were used for training and classifying purposes: (i) red: manual image-based ears; (ii) white (*Class1: Ear*): overlap between the areas automatically selected and the areas manually marked as ear; (iii) blue (*Class2: Non-Ear*): no overlap between the areas automatically selected and the areas manually marked as ear; these blue areas corresponding to soil, leaves and unwanted objects that were wrongly identified by ear by the automatic counting algorithm. The  $m$  features (columns) per  $n$  segmented areas (rows) were calculated to obtain the feature matrix.

### **2.3.1. Features extraction**

The features extraction was developed using *Analyze Particles* after Find Maxima (Schneider et al., 2012). The binary areas from the Find Maxima step were used as masks to calculate features (Fig. 3). We have extracted shape descriptors and statistical information from the original RGB image and its color channels, such as area, height, width, Feret, circularity, mean, standard deviation, mode and more measurements, totaling 30 features ( $m = 30$  in Fig. 4). An overview of the complete set of features extracted and their definition can be found in Supplementary File 1. A feature selection was developed in order to reduce the dimensionality of the data in preference to feature reduction by transformation. This allowed us to keep the units and meaning of all variables (Tripathy and Sahoo, 2015), thereby losing less of the information contained in the original features space (Khalid et al., 2014). For this purpose the Sequential Feature Selection (SFS) (Kohavi and John, 1997) was used with forward direction and stop criterium of 20 features ( $s = 20$  in Fig. 4). Supplementary File 1 also shows the selected features.

### **2.3.2. Training and classifying**

The training and classifying steps were developed using diverse machine learning techniques in order to compare the capability of each technique to discriminate between the *Class1* and the *Class2* labeled objects using the manual marks as a reference.

For labeling purposes (*Class1* or *Class2*), red marks were used to delineate all the ears manually. We marked the complete area covered by each single ear in order to maximize information gained in this step. Figure 2 shows in the dotted

line rectangle a sample of the manual marks. For each date of measurement (June 4 and June 19), 16 subplots images were manually marked for training and classifying; totalling 32 subplots. Different subplots we used for each data of measurement. The overlapping areas between automatic and manual selection were represented in white color and correspond to the *Class1*; the non-overlapping areas were represented in blue color and correspond to the *Class2* (Fig. 3 and Fig. 4). The same data was used for training and validation purposes for each classification technique.

The supervised machine learning techniques implemented for classification were: (i) discriminant analysis (DA) (Box, 1949) using linear discriminant, (ii) generalized linear models (GLM) (Dobson and Barnett, 2008) using binomial distribution, (iii) k-nearest neighbors (kNN) (Mitchell, 1997) using Euclidian distance, (iv) native Bayes (nB) (Mitchell, 1997), (v) neural feedforward neural networks (NN) (Beale et al., 2015) with ten hidden layers, (vi) support vector machine (SVM) (Cristianini and Shawe-Taylor, 2000) with a Gaussian radial basis kernel (Cristianini and Scholkopf, 2002; Liu et al., 2012), decision trees (DT) (Sheppard, 2017) and random forest (RF) (Breiman, 2001). Figure 4 shows the pipeline system used for training and classifying, the same data from the feature extraction step were used to train each classifier. The classification accuracy was calculated using cross-validation in terms of true positives (TP) and false positives (FP) and true negatives (TN) and false negatives (FN) based on the confusion matrix (Tso and Mather, 2009). The TP and TN correspond to the *Class1* and *Class2* correctly classified by the automatic system, respectively.

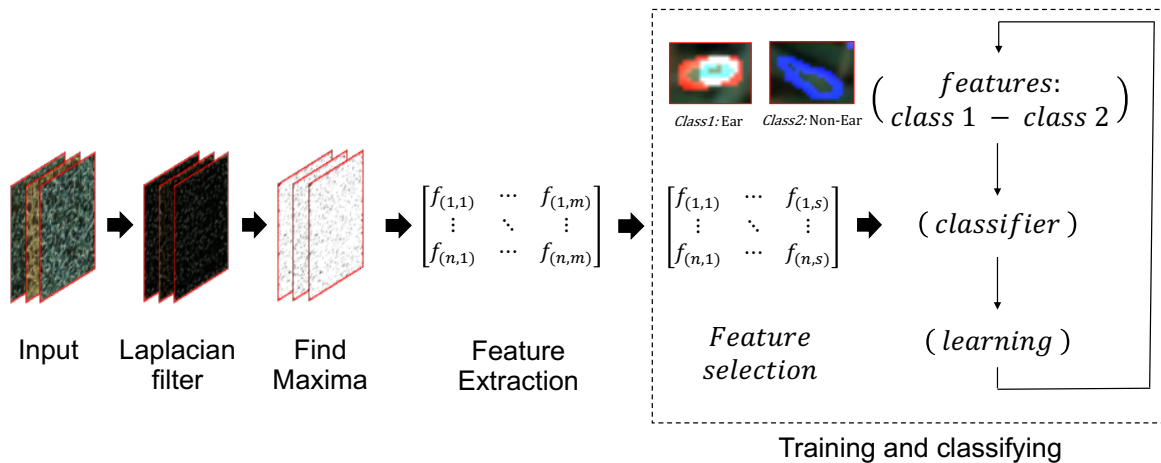


Figure 4. Image processing system proposed including training and classifying processes. The subplot images were batch processed, such that each row of the feature extraction matrix contained the features of each particular area detected per subplot image. Inside the dotted line rectangle, each matrix row was labelled automatically *Class1* or *Class2*. Feature selection reduced the dimensionality of the data and then the classifier was trained. The  $m$  features per each  $n$  area were used for training and classifying, and  $s$  features were selected. The same data from the feature extraction step was used to train each classifier. Classification accuracy was calculated using cross-validation.

### 2.3.3. Algorithm validation

In addition to the training and classification section, the performance of the image processing system using an UAV platform was also tested at anthesis (June 4, GS = 65) and early grain filling (June 19, GS = 75) growth stages using additional subplots from the total dataset of subplot images. These additional subplots were not used at the training and classifying procedure (previous section). In order to further validate the automatic ear counting system, the algorithm results were compared with the manual image-based marks on the

same images. The number of ears automatically detected by the image processing system is referred to as the *algorithm counting* and the number of ears manually marked is referred to as *manual image-based counting*. For each N treatment and date of measurement we have used 24 subplots, totalling 144 subplots. For this *manual image-based counting*, only one red dot was marked per ear in the original image with the same color value, circular shape and size; then, we used a simple algorithm to search the same color and shape marks and count them. The corresponding *manual image-based counting* and *algorithm counting* numbers were expressed in terms of ears per square meter in order to use standard units. To determine the prediction power of the automatic ear counting, we calculated cross-validation  $R^2$  values between *manual image-based counting* and *algorithm counting* for each discrimination technique and date of measurement.

A *manual in-situ counting* at crop maturity was carried out. For each plot, two half linear meter counts were used as a reference for the number of ears. Two different rows near the centre of the plot were selected. The *manual in-situ counting* was calculated as the sum of the number of ears counted in each half linear meter divided by the ratio between the plot width and the number of rows per plot.

#### **2.3.4. Statistical analysis**

Data analyses were performed using R Studio (version 1.2.135, R Foundation for Statistic Computing, Vienna 2018) and MATLAB (version R2014b, Mathworks, Inc., MA, USA). Determination coefficients of linear regressions (LR) and multiple linear regression (MLR), as well as the root mean square error

(RMSE), were calculated. The effects of genotype (G) and nitrogen (N) fertilization factors on grain yield (GY) were also calculated using LR and MLR. The G by N interactions (G\*N) were analysed using analysis of variance (ANOVA). To validate the robustness of the classification and validation a five-fold cross-validation (CV) was performed. In total, 100 CV runs (20 times five-fold CV) were performed. The data was plotted using SigmaPlot (version 12, Systat Software, Inc., San Jose California USA).

### **3. Results**

#### **3.1. Algorithm development and validation**

The classification accuracy of each classifier was calculated (Table 1). The determination coefficient ( $R^2$ ) of the *manual image-based counting* and the *algorithm counting* for each classifier was calculated (Table 2). Furthermore, the linear regression between *manual image-based counting* and the *algorithm counting* for the best classifier was calculated (Fig. 5).

First, the classification accuracy demonstrated a high percentage of correct prediction with a low standard error for k-nearest neighbors (kNN), support vector machine (SVM), decision trees (DT) and and random forest (RF) (Table 1). The RF classifier reached the highest percent of accuracy of true positives (TP) and true negatives (TN) for both dates (June 4: TP = 98.0%, TN = 96.9%; June 19: TP = 98.8%, TN = 95.8%), while the generalized linear models (GLM) (TP = 65.2%) and native Bayes (nB) (TN = 78.5%) showed the lowest accuracy in terms of TP and TN, respectively, for June 4; and (nB) (TP = 87.9%) and discriminant analysis (DA) (TN = 75.3%) showed the lowest accuracy of TP and TN, respectively, in the case of June 19.



Table 1. Classification accuracy of the automatic wheat ear counting system using UAV imagery for each classification technique and date. Training and classifying step used cross-validation to calculate the confusion matrix. Standard error (se) was calculated for each result for each true positives (TP) and true negatives (TN). For details about the classification techniques assayed see Material and Methods. Discriminant analysis (DA), generalized linear models (GLM), k-nearest neighbors (kNN), native Bayes (nB), neural feedforward neural networks (NN), support vector machine (SVM), decision trees (DT) and random forest (RF).

Classification technique	June 4				June 19			
	TP (%) <i>Class1</i>	se	TN (%) <i>Class2</i>	se	TP (%) <i>Class1</i>	se	TN (%) <i>Class2</i>	se
DA	90.7	0.09	80.2	0.16	93.2	0.07	75.3	0.17
GLM	65.2	0.13	93.7	0.08	92.2	0.08	77.5	0.17
kNN	96.4	0.17	94.1	0.28	97.0	0.15	93.9	0.27
nB	86.1	0.11	78.5	0.15	87.9	0.11	75.6	0.16
NN	90.5	0.09	79.7	0.16	93.1	0.08	79.8	0.15
SVM	94.0	0.14	93.5	0.10	95.3	0.14	91.7	0.13
DT	94.3	0.13	93.0	0.16	94.3	0.13	91.6	0.20
RF	98.0	0.10	96.8	0.16	98.8	0.06	95.8	0.20

The *manual image-based counting* and the *algorithm counting* demonstrated high determination coefficient ( $R^2$ ) cross-validation results with low standard error for SVM, DT and RF under further subplot inputs (Table 2). The RF classifier reached the highest  $R^2$  cross-validation values for both dates (June 4:  $R^2 = 0.82$ ; June 19:  $R^2 = 0.87$ ), while GLM showed the lowest  $R^2$  cross-validation values for both dates (June 4:  $R^2 = 0.33$ ; June 19:  $R^2 = 0.36$ ).

Table 2. Determination coefficient ( $R^2$ ) of the cross-validation results between *manual image-based counting* and *algorithm counting* for each classification technique and date. Standard error (se) was calculated for each result. Discriminant analysis (DA), generalized linear models (GLM), k-nearest neighbors (kNN), native Bayes (nB), neural feedforward neural networks (NN), support vector machine (SVM), decision trees (DT) and random forest (RF).

Classification technique	cross-validation $R^2$ value			
	June 4	se	June 19	se
DA	0.59	0.02	0.63	0.02
GLM	0.33	0.03	0.36	0.03
kNN	0.58	0.02	0.71	0.02
nB	0.44	0.02	0.38	0.02
NN	0.60	0.02	0.64	0.02
SVM	0.80	0.01	0.71	0.01
DT	0.77	0.01	0.76	0.01
RF	0.82	0.01	0.87	0.01

Furthermore, the relationship between the *manual image-based counting* and the *algorithm counting* for the best classifier (RF), also shows high determination coefficient on both dates (June 4:  $R^2 = 0.83$ , June 19:  $R^2 = 0.89$ ) using a linear regression without cross-validation (Figure 5).

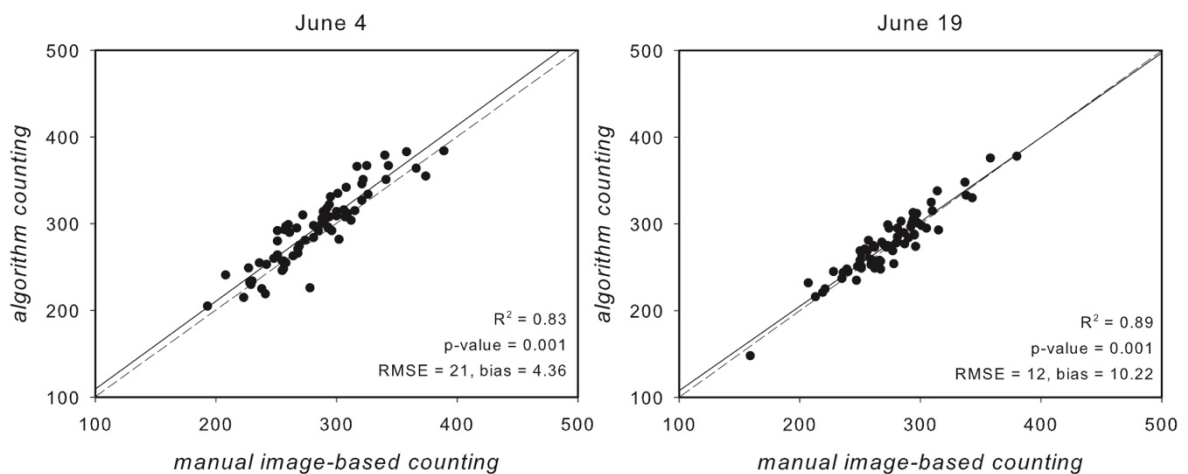


Figure 5. Linear regression for *algorithm counting* vs. *manual image-based counting* on the same image using the RF classifier. Two dates of measurement with the whole data were used. The dotted line indicates the 1:1 slope. The root mean square error (RMSE) was calculated for each date.

### 3.2. Relationship between manual in-situ and algorithm counting

The relationship between *manual in-situ counting* and *algorithm counting* were calculated using the determination coefficient of the cross-validation and the complete data set for each date of measurement (June 4, June 19) and also combining both dates (June 4 + June 19).

Moreover, the genotype (G), nitrogen fertilization (N) and G+N effects were tested. G\*N interactions were not observed. Additionally, we also grouped the data by N treatments in order to analyze the correlation between the manual in situ counting and the algorithm counting. Although, very low determinations coefficients were observed ( $R^2 \approx 0.0$ ) for all cases (results not shown).

Table 3. Determination coefficient ( $R^2$ ) of the cross-validation results between *manual in-situ counting* and *algorithm counting* (June 4, June 19 and June 4 + June 19) with grain yield (GY) using the linear regression (LR) for all data (n = 144) and also for data grouping by N fertilization (N.std, N+30 and N+50) are shown (n = 48). The results are also shown for the same data and dates with GY including the effects of G (all data + G) and N (all data + N) and also both combined (all data + G + N) factors (n = 144) using multiple linear regression (MLR). G by N interactions were not observed. The root mean square error (RMSE) was calculated for each model.

Input data	n = 144								n = 48					
	all data		all data + G		all data + N		all data + G + N		N.std		N+30		N-50	
	R <sup>2</sup>	RMSE	R <sup>2</sup>	RMSE	R <sup>2</sup>	RMSE	R <sup>2</sup>	RMSE	R <sup>2</sup>	RMSE	R <sup>2</sup>	RMSE	R <sup>2</sup>	RMSE
Manual in-situ counting	<b>0.02</b>	806.0	<b>0.06</b>	807.5	<b>0.34</b>	664.8	<b>0.41</b>	631.0	<b>0.11</b>	733.6	<b>0.14</b>	735.1	<b>0.08</b>	442.4
Algorithm counting (June 4)	<b>0.04</b>	798.5	<b>0.11</b>	781.8	<b>0.34</b>	662.9	<b>0.45</b>	609.4	<b>0.14</b>	740.0	<b>0.20</b>	737.4	<b>0.17</b>	447.2
Algorithm counting (June 19)	<b>0.14</b>	766.2	<b>0.16</b>	766.2	<b>0.36</b>	764.8	<b>0.41</b>	630.1	<b>0.11</b>	752.3	<b>0.17</b>	732.2	<b>0.42</b>	376.2
Algorithm counting (June 4 + June 19)	<b>0.28</b>	737.7	<b>0.20</b>	745.5	<b>0.35</b>	656.6	<b>0.46</b>	606.8	<b>0.10</b>	766.0	<b>0.16</b>	727.9	<b>0.46</b>	368.5

### 3.3. Relationship between manual in-situ and algorithm counting with grain yield

The relationship between *manual in-situ counting* and *algorithm counting* with grain yield were assessed using the R<sup>2</sup> of the cross-validation. In the case of *algorithm counting*, the mean of nine subplots from the RF classifier were used (Table 3).

Using all data, determination coefficients showed no correlation between *manual in-situ counting* and *algorithm counting* for June 4 with grain yield (R<sup>2</sup> = 0.02 and R<sup>2</sup> = 0.04). In the case of *algorithm counting* for June 19 and June 4 + June 19 together, low correlations (R<sup>2</sup> = 0.14, R<sup>2</sup> = 0.28; respectively) were observed. Including G effects, the results showed low correlation for all four input data (R<sup>2</sup> = 0.06, R<sup>2</sup> = 0.11, R<sup>2</sup> = 0.16 and R<sup>2</sup> = 0.20). By contrast including N effects the correlation increased (R<sup>2</sup> = 0.34–0.36). In the case of G+N effects, the determination coefficient also increased (R<sup>2</sup> = 0.41–0.46). Grouping by N treatments, the best correlations were achieved for N.std and N+30 (R<sup>2</sup> = 0.14 and R<sup>2</sup> = 0.20; respectively) on June 4; while for N-50 (R<sup>2</sup> = 0.42) it was on June 19. Additionally, using two input data together (June 4 + June 19), the correlation increased for N-50 (R<sup>2</sup> = 0.46). Moreover, *manual in-situ counting* did not improve the strength of the correlations of the *algorithm counting* against grain yield when this variable was added in a multiple linear regression model (results not shown).

#### 4. Discussion

Agronomical yield components are key to dissect how wheat responds to growing conditions as well the basis of the genetic advance of grain yield (Slafer et al., 2014). In our study, the classification showed high accuracy for TP and TN in the training and classifying step; four classification techniques showed results above 90% for TP and TN, which means relevant information contributed by the feature extraction step to classification (Kumar and Bhatia, 2014) (Table 1). Across all machine learning techniques, RF achieved the highest classification accuracy at both date of measurement for *Class1* and *Class2* (June 4: TP = 98.0%, TN = 96.9%; June 19: TP = 98.8%, TN = 95.8%) (Table 1). In the case of validation using *manual image-based counting*, RF also achieved the highest cross-validation results (June 4:  $R^2 = 0.82$ , June 19:  $R^2 = 0.87$ ), but the other classifiers achieved much lower results (Table 2). Particularly, the best three classifications techniques using *manual image-based counting* and *algorithm counting* cross-validation were SVM, DT and RF (Table 2). In the linear regression, RF also achieved the highest determination coefficient on both dates (June 4:  $R^2 = 0.83$ , June 19:  $R^2 = 0.89$  in Fig 5), in this case cross-validation was not performed. In our case, RF have performed better than the other classifiers for our shape and statistic features; this may be due to RF have shown higher performance in classification tasks when multi-dimensional data is used (Belgiu and Drăgu, 2016), as it is usually in remote sensing applications. RF robustness to outliers and noise (Breiman, 2001) and bootstrapping aggregations together with the many tree learners used in the RF classifier proved less sensitive to the quality of the training samples than other machine learning classifiers (Belgiu and Drăgu, 2016). These characteristics allowed for an effective prediction capacity

and also resulted in less overfitting (Berk, 2013). Moreover, for remote sensing approaches, parametric classifiers such as DA, GLM, nB have shown limitations dealing with multimodal distributions (Liu et al., 2011), while by contrast, nonparametric classifiers such as kNN, NN, SVM, DT and RF have shown better results under multimodal distributions (Marsum et al., 2018; Maulik and Chakraborty, 2017).

To date, automatic ear counting systems, regardless of the acquisition equipment, have been evaluated from ground, using only a portion of the area of the plot (Cointault et al., 2008; Fernandez-Gallego et al., 2019a, 2018a, 2018b; Madec et al., 2019; Sadeghi-Tehran et al., 2017; Velumani et al., 2017; Zhou et al., 2018a, 2018b; Zhu et al., 2016). Although the use of an UAV platform allows the acquisition of the complete area plot, multispectral and thermal sensors have low spatial resolution from aerial platforms and laser sensors are still costly. RGB sensors are not without their limitations; images taken on June 6, June 25 and July 3 under direct sunlight conditions (sunny days) were discarded. Due to the sunlight reflections on bending leaves it was hard to differentiate between ears and reflections on the leaves making it impossible to do a correct visual (i.e. manual) ear detection on the orthomosaic images. Therefore, the relatively low spatial resolution from the UAV combined with sunny day restrictions (blurring and degraded orthophotos due to sunlight reflections) do not permit precise reconstruction of the orthophoto at the canopy scale (Ortega-Terol et al., 2017). As a result, these resolution and light conditions affect the number of matching features found for the Structure from Motion (SfM) process used to build the orthophoto (Aasen et al., 2018). Nonetheless, under cloudy sky conditions, RGB orthophotos can precisely reconstruct the ears, leaves and soil for recognition

purposes.

On the other hand, although the ear density is part of the yield components, previous studies in ear recognition have not further used this information in order to understand the relationship between (automatic) ear counting systems with grain yield. In this study using the complete plot size area, the automatic ear counting system and cross-validation technique overall results showed no correlation with grain yield at June 4 ( $R^2 = 0.04$ ) and low correlation at June 19 ( $R^2 = 0.14$ ). In the same way, for *manual in-situ counting* any correlation with grain yield ( $R^2 = 0.02$ ) was observed. Nevertheless, when including G and N effects the determination coefficient increased. Furthermore, the correlation for N effects is higher ( $R^2 = 0.34$ – $0.36$ ) compared with G effects ( $R^2 = 0.06$ – $0.20$ ) for manual and algorithm counting as input data, which suggests that the relationship between the *manual in-situ counting* and *algorithm counting* with grain yield is more supported by the nitrogen treatment factors than genotype differences. In fact, Slafer et al. (2014) also concluded that the effect of nitrogen fertilization may affect ear density far more than the genotypic differences across cultivars. In addition, the determination coefficient including G+N effects also increased ( $R^2 = 0.41$ – $0.46$ ) in all cases. In general, for grain yield assessment, *algorithm counting* performed better in terms of correlation with grain yield than *manual in-situ counting*. Regarding this relationship, no correlations were observed between manual and algorithm counting. This may be due to the limited reference measurement of two half linear meters used for *manual in-situ counting* compared to the complete plot area footprint acquired from the UAV platform. On the other hand, automatic counting from zenithal images only considers the upper (i.e. exposed) ears, which usually correspond to the main and primary tillers, while

manual counting considers all the ears, including those from secondary and tertiary tillers, which frequently are placed to lower levels within the canopy. Since the contribution of secondary and tertiary tillers to grain yield is usually minor if not negative (Ishag and Taha, 1974), this might explain the fact that in-situ ear counting correlated even weaker with grain yield than the values of the automatic counting.

Grouping by nitrogen treatments, the best correlations of ear density against grain yield were achieved for June 4 and June 19 in N+30 and N-50 ( $R^2 = 0.20$  and  $R^2 = 0.42$ , respectively). June 4 + June 19 achieved the best correlation in N-50 ( $R^2 = 0.46$ ). In this way, the number of ears can be affected by genotype characteristics and N treatments, therefore these considerations should be added as variables into the model for grain yield assessment. The higher correlation between ear density and grain yield was observed at the lower N treatment (N-50). This could be explained by less hidden ears as less nitrogen fertilization diminishes tillering capacity (Power and Alessi, 1978) which decreases hidden ears out of the reach of the automatic counting system. Considering the massive amount of data acquired from an aerial platform and the lower spatial resolution due to increased distance between object and camera, the image processing systems combined with machine learning techniques demonstrated an effective data management and image interpretation capacity.

## **5. Conclusions**

In this study, we proposed an automatic system for ear counting using RGB aerial images from a UAV platform, together with machine learning techniques. Previously, similar techniques had been implemented from ground imagery, but,



with adaptation to UAVs, improved throughput is provided for more complete microplot coverage and feasibility in application to larger phenotyping studies. The ear counting system is able to identify wheat ears with high accuracy and efficiency. In that way, the system can be used for targeted trait breeding in cereal phenotyping, critical to developing wheat varieties that could be translated into yield gain (Araus et al., 2018).

The algorithm counting demonstrated better correlation with the grain yield compared with the manual counting using all data and grouping by N treatments. Although the correlation between the algorithm counting and grain yield was relatively low using all data, when including the effects of G+N factors the determinations coefficient ( $R^2$ ) increased. Furthermore, the  $R^2$  with grain yield were higher including N than G factors, which suggests that ear counting relationship with grain yield is more supported by the N treatment factors than G differences. Moreover, the highest correlation between automatic counting and grain yield were achieved at the lower N treatment, where less hidden ears and lower tillering capacity occurs. In turn, it could indicate more applicability to real growing conditions in production fields, commonly under rainfed or low N conditions.

Sunlight conditions were an important factor for this application, while direct sunlight (sunny days) did not allow for the correct visual identification of ears on the orthomosaic images; under diffuse light conditions (e.g. due to cloudy days or eventually measuring just before sunrise or just after sunset), the ears could be differentiated from leaves, soil or unwanted objects. In future studies with more spatial resolution from an aerial platform, the algorithm could be trained for direct sunlight conditions. Perhaps 3-dimensional imaging, along with ear size/volume

estimation, could be the next step to achieve higher correlation with grain yield.

## **6. Acknowledgments**

The authors want to thank the technical staff of UGent for the setup and maintenance of the trial and the technical staff of ILVO, especially to Thomas Vanderstocken, for the UAV flights and the pre-processing of the data and the technical assistance of Viviana Espejo for the in-situ measurements in the field and the image-based validation. The multilocation trial was executed in the framework of the ECOFE network ([www.ecofe.eu](http://www.ecofe.eu)). This work was established during an internship of Jose A. Fernandez-Gallego at ILVO (B). This work was supported by the project “Formación de Talento Humano de Alto Nivel” (project number BPIN 2013000100103) approved by the “Fondo de Ciencia, Tecnología e Innovación”, from the “Sistema General de Regalías”; and “Gobernación del Tolima-Universidad del Tolima, Colombia” as the sole funding source of the first author Jose A. Fernandez-Gallego. Contribution of Jose L. Araus was supported in part by ICREA Academia, Generalitat de Catalunya, Spain.

## **References**

- Aasen, H., Honkavaara, E., Lucieer, A., Zarco-Tejada, P.J., 2018. Quantitative remote sensing at ultra-high resolution with UAV spectroscopy: A review of sensor technology, measurement procedures, and data correction workflows. *Remote Sens.* 10, 1–42. doi:10.3390/rs10071091
- Araus, J.L., Cairns, J.E., 2014. Field high-throughput phenotyping: the new crop breeding frontier. *Trends Plant Sci.* 19, 52–61. doi:10.1016/j.tplants.2013.09.008

- Araus, J.L., Kefauver, S.C., 2018. Breeding to adapt agriculture to climate change: affordable phenotyping solutions. *Curr. Opin. Plant Biol.*  
doi:10.1016/j.pbi.2018.05.003
- Araus, J.L., Kefauver, S.C., Zaman-Allah, M., Olsen, M.S., Cairns, J.E., 2018. Translating High-Throughput Phenotyping into Genetic Gain. *Trends Plant Sci.* doi:10.1016/j.tplants.2018.02.001
- Beale, M.H., Hagan, M.T., Demuth, H.B., 2015. *Neural Network Toolbox™ User's Guide*. The MathWorks, Inc.
- Belgiu, M., Drăgu, L., 2016. Random forest in remote sensing: A review of applications and future directions. *ISPRS J. Photogramm. Remote Sens.* 114, 24–31. doi:10.1016/j.isprsjprs.2016.01.011
- Berk, R.A., 2013. Random Forests, in: *Statistical Learning from a Regression Perspective*. Springer New York, New York, NY, pp. 1–63.  
doi:10.1007/978-0-387-77501-2\_5
- Box, G.E.P., 1949. A General Distribution Theory for a Class of Likelihood Criteria. *Biometrika* 36, 317. doi:10.2307/2332671
- Breiman, L., 2001. Random Forests, in: *Machine Learning*. pp. 5–32.  
doi:10.1023/A:1010933404324
- Cointault, F., Guerin, D., Guillemin, J., Chopinet, B., 2008. In-field *Triticum aestivum* ear counting using colour-texture image analysis. *New Zeal. J. Crop Hortic. Sci.* 36, 117–130. doi:10.1080/01140670809510227
- Cristianini, N., Scholkopf, B., 2002. Support Vector Machines and Kernel Methods: The New Generation of Learning Machines. *AI Mag.* 23, 31.
- Cristianini, N., Shawe-Taylor, J., 2000. *An Introduction to Support Vector Machines and Other Kernel-based Learning Methods*. Cambridge

- University Press, Cambridge. doi:10.1017/CBO9780511801389
- Deery, D., Jimenez-Berni, J., Jones, H., Sirault, X., Furbank, R., 2014. Proximal Remote Sensing Buggies and Potential Applications for Field-Based Phenotyping, *Agronomy*. doi:10.3390/agronomy4030349
- del Moral, L.F.G., Rharrabti, Y., Villegas, D., Royo, C., 2010. Evaluation of Grain Yield and Its Components in Durum Wheat under Mediterranean Conditions. *Agron. J.* 95, 266. doi:10.2134/agronj2003.0266
- Dobson, A.J., Barnett, A.G., 2008. *An Introduction to Generalized Linear Models*, Third Edition. Chapman and Hall/CRC, Boca Ratón, FL. doi:10.1201/9781584889519
- Fernandez-Gallego, Buchailot, M., Aparicio Gutiérrez, N., Nieto-Taladriz, M., Araus, J.L., Kefauver, S.C., 2019a. Automatic Wheat Ear Counting Using Thermal Imagery. *Remote Sens.* 11, 751. doi:10.3390/rs11070751
- Fernandez-Gallego, Kefauver, S.C., Aparicio Gutiérrez, N., Nieto-Taladriz, M.T., Araus, J.L., 2018a. Wheat ear counting in-field conditions: high throughput and low-cost approach using RGB images. *Plant Methods* 14, 22. doi:10.1186/s13007-018-0289-4
- Fernandez-Gallego, Kefauver, S.C., Gutiérrez, N.A., Nieto-Taladriz, M.T., Araus, J.L., 2018b. Automatic wheat ear counting in-field conditions: simulation and implication of lower resolution images, in: Neale, C.M., Maltese, A. (Eds.), *Proc. SPIE 10783, Remote Sensing for Agriculture, Ecosystems, and Hydrology XX*, 107830M. SPIE, p. 23. doi:10.1117/12.2500083
- Fernandez-Gallego, Kefauver, S.C., Vatter, T., Aparicio Gutiérrez, N., Nieto-Taladriz, M.T., Araus, J.L., 2019b. Low-cost assessment of grain yield in

- durum wheat using RGB images. *Eur. J. Agron.* 105, 146–156.  
doi:10.1016/j.eja.2019.02.007
- Ishag, H.M., Taha, M.B., 1974. Production and survival of tillers of wheat and their contribution to yield. *J. Agric. Sci.* 83, 117–124.  
doi:10.1017/S0021859600047079
- Jaud, M., Passot, S., Allemand, P., Le Dantec, N., Grandjean, P., Delacourt, C., 2018. Suggestions to Limit Geometric Distortions in the Reconstruction of Linear Coastal Landforms by SfM Photogrammetry with PhotoScan® and MicMac® for UAV Surveys with Restricted GCPs Pattern. *Drones* 3, 2.  
doi:10.3390/drones3010002
- Kefauver, S.C., Arous-Serret, I., Vergara-Díaz, O., Bort, J., El-haddad, G., Nieto-Taladriz, M.T., Aparicio, N., Arous, J.L., 2018. Challenges and Bottlenecks in UAV Phenotyping, in: *IGARSS 2018 - 2018 IEEE International Geoscience and Remote Sensing Symposium*. IEEE, pp. 8240–8243.
- Kelly, D., Vatsa, A., Mayham, W., Ngô, L., Thompson, A., Kazic, T., 2015. An opinion on imaging challenges in phenotyping field crops. *Mach. Vis. Appl.* 1–14. doi:10.1007/s00138-015-0728-4
- Khalid, S., Khalil, T., Nasreen, S., 2014. A survey of feature selection and feature extraction techniques in machine learning. *Proc. 2014 Sci. Inf. Conf. SAI 2014* 372–378. doi:10.1109/SAI.2014.6918213
- Kohavi, R., John, G.H., 1997. Wrappers for feature subset selection. *Artif. Intell.* 97, 273–324. doi:10.1016/S0004-3702(97)00043-X
- Kumar, G., Bhatia, P.K., 2014. A detailed review of feature extraction in image processing systems. *Int. Conf. Adv. Comput. Commun. Technol. ACCT* 5–

12. doi:10.1109/ACCT.2014.74
- Liu, K., Shi, W., Zhang, H., 2011. A fuzzy topology-based maximum likelihood classification. *ISPRS J. Photogramm. Remote Sens.* 66, 103–114.  
doi:10.1016/j.isprsjprs.2010.09.007
- Liu, Z., Zuo, M.J., Xu, H., 2012. Parameter selection for Gaussian radial basis function in support vector machine classification. *Proc. 2012 Int. Conf. Qual. Reliab. Risk, Maintenance, Saf. Eng. ICQR2MSE 2012* 576–581.  
doi:10.1109/ICQR2MSE.2012.6246300
- Madec, S., Jin, X., Lu, H., De Solan, B., Liu, S., Duyme, F., Heritier, E., Baret, F., 2019. Ear density estimation from high resolution RGB imagery using deep learning technique. *Agric. For. Meteorol.* 264, 225–234.  
doi:10.1016/j.agrformet.2018.10.013
- Marsum, M.A., Arsa, D.M.S., Hermawan, I., Jatmiko, W., Nurhadiyatna, A., 2018. Multicodebook Neural Network Using Intelligent K-Means Clustering Based on Histogram Information for Multimodal Data Classification. *2018 Int. Work. Big Data Inf. Secur. IWBIS 2018* 129–135.  
doi:10.1109/IWBIS.2018.8471699
- Maulik, U., Chakraborty, D., 2017. Remote Sensing Image Classification: A survey of support-vector-machine-based advanced techniques. *IEEE Geosci. Remote Sens. Mag.* 5, 33–52. doi:10.1109/MGRS.2016.2641240
- Minervini, M., Scharr, H., Tsafaris, S.A., 2015. Image Analysis: The New Bottleneck in Plant Phenotyping [Applications Corner]. *IEEE Signal Process. Mag.* 32, 126–131. doi:10.1109/MSP.2015.2405111
- Mitchell, T.M., 1997. *Thomas Mitchell-Machine learning*. McGraw-Hill, Inc., New York, NY, USA.

- Ortega-Terol, D., Hernandez-Lopez, D., Ballesteros, R., Gonzalez-Aguilera, D., 2017. Automatic hotspot and sun glint detection in UAV multispectral images. *Sensors (Switzerland)* 17, 1–16. doi:10.3390/s17102352
- Power, J.F., Alessi, J., 1978. Tiller development and yield of standard and semidwarf spring wheat varieties as affected by nitrogen fertilizer. *J. Agric. Sci.* 90, 97. doi:10.1017/S0021859600048632
- Qiu, R., Wei, S., Zhang, M., Li, H., Sun, H., Liu, G., Li, M., 2018. Sensors for measuring plant phenotyping: A review. *Int. J. Agric. Biol. Eng.* 11, 1–17. doi:10.25165/j.ijabe.20181102.2696
- Sadeghi-Tehran, P., Sabermanesh, K., Virlet, N., Hawkesford, M.J., 2017. Automated Method to Determine Two Critical Growth Stages of Wheat: Heading and Flowering. *Front. Plant Sci.* 8, 1–14. doi:10.3389/fpls.2017.00252
- Schneider, C.A., Rasband, W.S., Eliceiri, K.W., 2012. NIH Image to ImageJ: 25 years of image analysis. *Nat Meth* 9, 671–675.
- Sheppard, C., 2017. *Tree-based Machine Learning Algorithms: Decision Trees, Random Forests, and Boosting*. CreateSpace Independent Publishing Platform, Austin, Texas, USA.
- Simane, B., Struik, P.C., Nachit, M.M., Peacock, J.M., 1993. Ontogenetic analysis of yield components and yield stability of durum wheat in water-limited environments, *Euphytica*. doi:10.1007/BF00040410
- Singh, A., Ganapathysubramanian, B., Singh, A.K., Sarkar, S., 2016. Machine Learning for High-Throughput Stress Phenotyping in Plants. *Trends Plant Sci.* 21, 110–124. doi:10.1016/j.tplants.2015.10.015
- Slafer, G.A., Savin, R., Sadras, V.O., 2014. Coarse and fine regulation of wheat

- yield components in response to genotype and environment. *F. Crop. Res.* 157, 71–83. doi:10.1016/j.fcr.2013.12.004
- Stützel, H., Brüggemann, N., Inzé, D., 2016. The Future of Field Trials in Europe: Establishing a Network Beyond Boundaries. *Trends Plant Sci.* 21, 92–95. doi:10.1016/j.tplants.2015.12.003
- Syrris, V., Ferri, S., Ehrlich, D., Pesaresi, M., 2015. Image Enhancement and Feature Extraction Based on Low-Resolution Satellite Data. *IEEE J. Sel. Top. Appl. Earth Obs. Remote Sens.* 8, 1986–1995. doi:10.1109/JSTARS.2015.2417864
- Tripathy, S., Sahoo, P.L., 2015. A Survey of different methods of clustering for anomaly detection. *Int. J. Sci. Eng. Res.* 6, 351–357.
- Tso, B., Mather, P., 2009. *Classification Methods for Remotely Sensed Data, Second Edition.* CRC Press. doi:10.1201/9781420090741
- Velumani, K., Oude Elberink, S., Yang, M.Y., Baret, F., 2017. Wheat Ear Detection in Plots by Segmenting Mobile Laser Scanner Data, in: *ISPRS Annals of the Photogrammetry, Remote Sensing and Spatial Information Sciences.* pp. 149–156. doi:10.5194/isprs-annals-IV-2-W4-149-2017
- Zadoks, J., Chang, T., Konzak, C., 1974. A decimal growth code for the growth stages of cereals. *Weed Res.* 14, 415–421.
- Zhou, C., Liang, D., Yang, X., Xu, B., Yang, G., 2018a. Recognition of wheat spike from field based phenotype platform using multi-sensor fusion and improved maximum entropy segmentation algorithms. *Remote Sens.* 10. doi:10.3390/rs10020246
- Zhou, C., Liang, D., Yang, X., Yang, H., Yue, J., Yang, G., 2018b. Wheat Ears Counting in Field Conditions Based on Multi-Feature Optimization and



TWSVM. *Front. Plant Sci.* 9. doi:10.3389/fpls.2018.01024

Zhu, Y., Cao, Z., Lu, H., Li, Y., Xiao, Y., 2016. In-field automatic observation of wheat heading stage using computer vision. *Biosyst. Eng.* 143, 28–41.

doi:10.1016/j.biosystemseng.2015.12.015

Automatic wheat ear counting using machine learning based on RGB UAV  
imagery

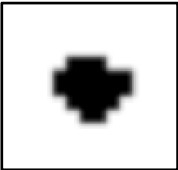
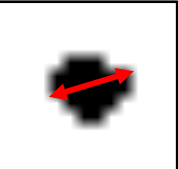
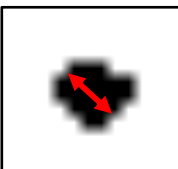
Jose A. Fernandez-Gallego<sup>1,2,3</sup>, Peter Lootens<sup>4</sup>, Irene Borra-Serrano<sup>4,5</sup>, Veerle  
Derycke<sup>6</sup>, Geert Haesaert<sup>6</sup>, Isabel Roldán-Ruiz<sup>4,7</sup>, Jose L. Araus<sup>1,2,\*</sup>, Shawn C.  
Kefauver<sup>1,2,\*</sup>

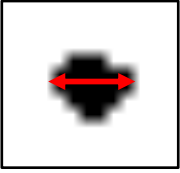
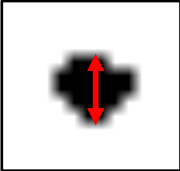
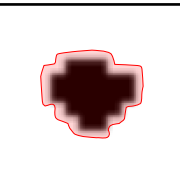
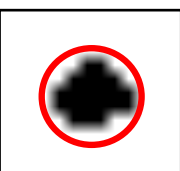
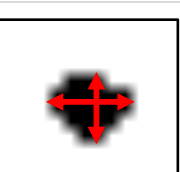

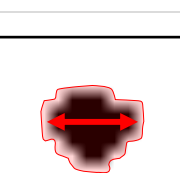
Supplemental file:

## Automatic wheat ear counting using machine learning based on RGB UAV imagery

Jose A. Fernandez-Gallego<sup>1,2,3</sup>, Peter Lootens<sup>4</sup>, Irene Borra-Serrano<sup>4,5</sup>, Veerle Derycke<sup>6</sup>, Geert Haesaert<sup>6</sup>, Isabel Roldán-Ruiz<sup>4,7</sup>, Jose L. Araus<sup>1,2,\*</sup>, Shawn C. Kefauver<sup>1,2,\*</sup>

**Supplementary Table 1.** Shape descriptors: In the feature extraction step, shape descriptors from the original Red/Green/Blue (RGB) image, such as area, Feret, width, height and circularity were extracted. The visual representation corresponds to one area segmented at the Find maxima step into the image processing system. The shape descriptors were calculated using the complete color image. In summary, 10 shape descriptors.

Feature	Visual representation	Description
<b>Area</b>		Area of selection in square pixels. This area is calibrated in meters units.
<b>Feret distance</b>		The longest distance between any two points along the selection boundary
<b>Min Feret distance</b>		The minimum caliper diameter

<b>Width</b>		The longest distance in the x-axis
<b>Height</b>		The longest distance in the y-axis
<b>Raw integrated density</b>		The sum of the values of the pixels in the image or selection
<b>Circularity</b>		$\text{Circularity} = \frac{4\pi \cdot \text{area}}{\text{perimeter}^2}$ Perfect circle → a value of 1.0 Elongated shape → a value close to 0.0
<b>Aspect ratio</b>		The minor x or y axis value measured
<b>Solidity</b>		Solidity = area / convex area
<b>Round</b>		$\text{Round} = \frac{4 \cdot \text{area}}{\pi \cdot \text{major axis}^2}$

**Supplementary Table 2.** Statistical descriptors: In the feature extraction step statistical information from the original Red/Green/Blue (RGB) image and its color channels, such as area, mean and standard deviation were extracted. These descriptors are measured using the value of the pixels of each area segmented at the Find maxima step into the image processing system. The statistical descriptors were calculated using the complete color image (5 descriptors); and in addition, the statistical descriptors were also calculated per each color channel (R, B and G color channel, 15 descriptors). In summary, 20 statistical descriptors were used.

<b>Feature</b>	<b>Description</b>
<b>Mean</b>	Arithmetic mean value
<b>Std</b>	Arithmetical standard deviation value
<b>Mode</b>	Value most frequently fund
<b>Max</b>	Maximum value
<b>Min</b>	Minimum value

**Supplementary Table 3.** Feature selection: The Sequential Feature Selection (SFS) was used to select the features. The complete shape descriptors and statistical descriptors (for the color image) were selected (15 descriptors). Moreover, the statistical descriptors Mean (in G color channel), Std (in R, G, B color channels), Max (in G color channel) were selected (5 descriptor) for each color channel, totaling 20 descriptors.

Feature	Selection			
	RGB	R	G	B
Area	✓	-	-	-
Feret distance	✓	-	-	-
Min Feret distance	✓	-	-	-
Width	✓	-	-	-
Height	✓	-	-	-
Raw integrated density	✓	-	-	-
Circularity	✓	-	-	-
Aspect radio	✓	-	-	-
Solidity	✓	-	-	-
Round	✓	-	-	-
Mean	✓	✗	✓	✗
Std	✓	✓	✓	✓
Mode	✓	✗	✗	✗
Max	✓	✗	✓	✗
Min	✓	✗	✗	✗

✓, selected; ✗ not selected; - not used





# Chapter 4

Automatic wheat ear counting using thermal imagery

Jose A. Fernandez-Gallego<sup>1,2,3</sup>, Ma. Luisa Buchailot<sup>1,2</sup>, Nieves Aparicio Gutiérrez<sup>4</sup>, María Teresa Nieto-Taladriz<sup>5</sup>, José Luis Araus<sup>1,2</sup> and Shawn C. Kefauver<sup>1,2</sup>

<sup>1</sup> Plant Physiology Section, Department of Evolutionary Biology, Ecology and Environmental Sciences, Faculty of Biology, University of Barcelona, Diagonal 643, 08028 Barcelona, Spain.

<sup>2</sup> AGROTECNIO (Center for Research in Agrotechnology), Av. Rovira Roure 191, 25198 Lleida, Spain.

<sup>3</sup> Programa de Ingeniería Electrónica, Facultad de Ingeniería, Universidad de Ibagué, Carrera 22 Calle 67, Ibagué 730001, Colombia.

<sup>4</sup> Instituto Tecnológico Agrario de Castilla y León (ITACyL), Ctra. Burgos Km. 119, 47071 Valladolid, Spain.

<sup>5</sup> Instituto Nacional de Investigación y Tecnología Agraria y Alimentaria (INIA), Ctra. de la Coruña Km. 7.5, 28040 Madrid, Spain.

Published in:

Remote Sensing (2019), Vol. 11(7), 751



## ABSTRACT

Ear density is one of the most important agronomical yield components in wheat. Ear counting is time-consuming and tedious as it is most often conducted manually in field conditions. Moreover, different sampling techniques are often used resulting in a lack of standard protocol, which may eventually affect inter-comparability of results. Thermal sensors capture crop canopy features with more contrast than RGB sensors for image segmentation and classification tasks. An automatic thermal ear counting system is proposed to count the number of ears using zenithal/nadir thermal images acquired from a moderately high resolution handheld thermal camera. Three experimental sites under different growing conditions in Spain were used on a set of 24 varieties of durum wheat for this study. The automatic pipeline system developed uses contrast enhancement and filter techniques to segment image regions detected as ears. The approach is based on the temperature differential between the ears and the rest of the canopy, given that ears usually have higher temperatures due to their lower transpiration rates. Thermal images were acquired, together with RGB images and in situ (i.e., directly in the plot) visual ear counting from the same plot segment for validation purposes. The relationship between the thermal counting values and the in situ visual counting was fairly weak ( $R^2 = 0.40$ ), which highlights the difficulties in estimating ear density from one single image-perspective. However, the results show that the automatic thermal ear counting system performed quite well in counting the ears that do appear in the thermal images, exhibiting high correlations with the manual image-based counts from both thermal and RGB images in the sub-plot validation ring ( $R^2 = 0.75\text{--}0.84$ ). Automatic ear counting

also exhibited high correlation with the manual counting from thermal images when considering the complete image ( $R^2 = 0.80$ ). The results also show a high correlation between the thermal and the RGB manual counting using the validation ring ( $R^2 = 0.83$ ). Methodological requirements and potential limitations of the technique are discussed



Article

# Automatic Wheat Ear Counting Using Thermal Imagery

Jose A. Fernandez-Gallego <sup>1,2,3</sup> , Ma. Luisa Buchailot <sup>1,2</sup>, Nieves Aparicio Gutiérrez <sup>4</sup> ,  
María Teresa Nieto-Taladriz <sup>5</sup>, José Luis Araus <sup>1,2,\*</sup>  and Shawn C. Kefauver <sup>1,2,\*</sup> 

<sup>1</sup> Plant Physiology Section, Department of Evolutionary Biology, Ecology and Environmental Sciences, Faculty of Biology, University of Barcelona, Diagonal 643, 08028 Barcelona, Spain; jfernaga46@alumnes.ub.edu (J.A.F.-G.); luisa.buchailot@gmail.com (M.L.B.)

<sup>2</sup> AGROTECNIO (Center for Research in Agrotechnology), Av. Rovira Roure 191, 25198 Lleida, Spain

<sup>3</sup> Programa de Ingeniería Electrónica, Facultad de Ingeniería, Universidad de Ibagué, Carrera 22 Calle 67, Ibagué 730001, Colombia

<sup>4</sup> Instituto Tecnológico Agrario de Castilla y León (ITACyL), Ctra. Burgos Km. 119, 47071 Valladolid, Spain; apagutni@itacyl.es

<sup>5</sup> Instituto Nacional de Investigación y Tecnología Agraria y Alimentaria (INIA), Ctra. de la Coruña Km. 7.5, 28040 Madrid, Spain; mt Nieto@inia.es

\* Correspondence: jaraus@ub.edu (J.L.A.); sckefauver@ub.edu (S.C.K.);  
Tel.: +34-934021469 (J.L.A.); +34-934021465 (S.C.K.)

Received: 18 January 2019; Accepted: 26 March 2019; Published: 28 March 2019



**Abstract:** Ear density is one of the most important agronomical yield components in wheat. Ear counting is time-consuming and tedious as it is most often conducted manually in field conditions. Moreover, different sampling techniques are often used resulting in a lack of standard protocol, which may eventually affect inter-comparability of results. Thermal sensors capture crop canopy features with more contrast than RGB sensors for image segmentation and classification tasks. An automatic thermal ear counting system is proposed to count the number of ears using zenithal/nadir thermal images acquired from a moderately high resolution handheld thermal camera. Three experimental sites under different growing conditions in Spain were used on a set of 24 varieties of durum wheat for this study. The automatic pipeline system developed uses contrast enhancement and filter techniques to segment image regions detected as ears. The approach is based on the temperature differential between the ears and the rest of the canopy, given that ears usually have higher temperatures due to their lower transpiration rates. Thermal images were acquired, together with RGB images and in situ (i.e., directly in the plot) visual ear counting from the same plot segment for validation purposes. The relationship between the thermal counting values and the in situ visual counting was fairly weak ( $R^2 = 0.40$ ), which highlights the difficulties in estimating ear density from one single image-perspective. However, the results show that the automatic thermal ear counting system performed quite well in counting the ears that do appear in the thermal images, exhibiting high correlations with the manual image-based counts from both thermal and RGB images in the sub-plot validation ring ( $R^2 = 0.75\text{--}0.84$ ). Automatic ear counting also exhibited high correlation with the manual counting from thermal images when considering the complete image ( $R^2 = 0.80$ ). The results also show a high correlation between the thermal and the RGB manual counting using the validation ring ( $R^2 = 0.83$ ). Methodological requirements and potential limitations of the technique are discussed.

**Keywords:** thermal images; ear counting; digital image processing; wheat

## 1. Introduction

High throughput plant phenotyping (HTPP) is a quantitative description of the functional and structural properties of the plant [1] for the purpose of crop breeding [2,3]. In the case of cereals,

e.g., wheat, besides grain yield, agronomical yield components are also assessed as part of plant phenotyping pipeline [4]. The accurate quantification of the number of ears per square meter, number of grains per ear and the thousand kernel weight, as the main yield components in wheat, are therefore essential in breeding programs [5]. In the case of ear counting, it is time-consuming and tedious as it is most often conducted manually in field conditions. Moreover, different subsampling techniques and derived protocols for calculation are often used resulting in a lack of standard protocol. As an alternative, several automatic ear counting techniques have been developed in the last years, mainly using as input high resolution RGB (Red/Green/Blue) images. Different image processing techniques have been used such as texture and hybrid color space [6,7], multi-features from color, grayscale and texture data [8]. Decorrelation stretch for color contrast enhancement and Support Vector Machine (SVM) as classification techniques [9,10] and convolutional neural network recognition have been also used [11]. Other approaches use frequency and spatial filter techniques as well as local peaks segmentation [12,13]. Even though the visual spectrum has been widely used for ear counting, there are general limitations to have into account in field conditions, such as solar light conditions (unwanted shadows and bright surfaces), wind conditions (blur ears), ears overlapping and size/shape variation (mostly depending of their more/less horizontal position) and spatial image resolution (camera/canopy distance and sensor size).

Recently, a fusion of multispectral and RGB images have been developed for ear counting estimation [14]. Though not yet applied to wheat ear counting, fruit defect detection using hyperspectral images, through image processing systems, has also been recently developed [15]. Therefore, although visual and multispectral information has been used for ear counting and hyperspectral for fruit defect detection, there is no information in the literature regarding thermal images for ear counting applications or segmentation on such a fine spatial scale, perhaps due to the comparatively low resolution and high cost of thermal cameras [2].

Thermal imagery is related with the transpirative status of the plant [16] that is separate from the visual characteristics that could result in the RGB imagery limitations. Thermal information has been used mainly for monitoring crop water status [17–22] and irrigation management [23,24]. However, previous studies have shown that, regardless of the water conditions during the growing season, there are often significant constitutive differences between leaf and ear temperature on sunny days [25], with ear temperature being higher than leaf temperature. This suggests that thermal imagery may provide a useful approach for ear counting [26]. Temperature distribution across a particular surface have been studied using image processing techniques; for instance, in segmentation applications using the thermal color map, thresholding and morphology operators in research related with orange, apple and almond tree orchards [27–29]. Other similar segmentation approaches have focused on the assessment of plant and leaf temperature separately in vegetables and soybean crops [30,31].

In this study, we propose an automatic wheat ear counting system using thermal images acquired holding the camera by hand above the canopy. We include data captured at three different experimental stations located in northern, central and southern Spain with different environmental conditions. An image processing system was developed to segment the wheat ears taking advantage of the thermal color map. A pipeline structure was designed to filter background and unwanted regions into the image using an adaptive contrast technique and morphological operators. Visual counting directly in the field (i.e., in situ) as well as ear counts derived from RGB images of the same plot segments were also added for the purposes of validating the thermal image and algorithm counting measurements.

## 2. Materials and Methods

### 2.1. Plant Material and Experimental Setup

Two sets of twenty-four post Green Revolution (i.e., semi-dwarf) durum wheat (*Triticum turgidum* L. subsp. *durum* (Desf) Husn.) cultivars (cvs Amilcar, Arcobaleno, Athoris, Avispa, Burgos, Claudio, Core, Don Norman, Don Ricardo, Dorondon, Euroduro, Gallareta, Iberus, Kiko Nick, Mexa, Olivadur,

Paramo, Pedroso, Regallo, Saragolla, Sculptur, Simeto, Solea and Vitron) were grown during two consecutive seasons. In the second year, the Haristide variety was planted instead of Paramo. Field trials were carried at the experimental stations of Colmenar de la Oreja (40°04' N, 3°31' W), near Aranjuez (Madrid province) and Coria del Rio (37°14' N, 6°03' W), near Sevilla during the 2016/2017 crop seasons and at Zamadueñas (41°42' N, 4°42' W), near Valladolid during the 2017/2018 crop season. The first two stations belong to the Instituto Nacional de Investigación y Tecnología Agraria y Alimentaria (INIA), while the third one belongs to the Instituto de Tecnología Agraria de Castilla y León (ITACyL) of Spain. The average annual precipitation and annual temperature is about 425 mm and 13.7 °C, 502 mm and 18.0 °C and 269 mm and 13.2 °C for Aranjuez, Sevilla and Valladolid, respectively. The meteorological data were obtained from the meteorological stations nearest to each experimental station using the SIAR (Sistema de Información Agroclimática para el Regadío) information system [32].

Aranjuez trials were fertilized before sowing with 450 kg ha<sup>-1</sup> of 8:15:15 (8% N, 15% P<sub>2</sub>O<sub>5</sub>, 15% K<sub>2</sub>O) fertilizer and in addition 185 kg ha<sup>-1</sup> of 46% urea was applied before stem elongation. Sevilla trials were fertilized before sowing with 500 kg ha<sup>-1</sup> of 15:15:15 (15% N, 15% P<sub>2</sub>O<sub>5</sub>, and 15% K<sub>2</sub>O) fertilizer and 100 kg ha<sup>-1</sup> of 46% urea was applied before stem elongation. Finally, Valladolid trials were fertilized before sowing with 300 kg ha<sup>-1</sup> of 8:15:15 (8% N, 15% P<sub>2</sub>O<sub>5</sub>, and 15% K<sub>2</sub>O) fertilizer; 150 kg ha<sup>-1</sup> of calcium ammonium nitrate (27% richness in nitrogen) was applied before tillering; and 150 kg ha<sup>-1</sup> of ammonium sulfate nitrate (26% richness in nitrogen) was applied before heading.

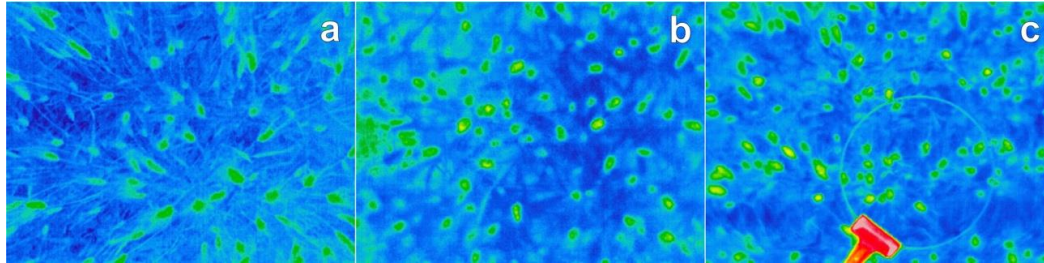
Two experimental conditions (rainfed and supplemental irrigation) were assayed at Aranjuez and Valladolid, while, in the case of Sevilla, only rainfed conditions were assayed. The genotypes were evaluated in 9 m<sup>2</sup> in size plots, 6 rows, 0.25 m apart and a planting density of 250 seeds per m<sup>2</sup>. Randomized blocks were used with three replicates and a total of 72 plots per trial (3 replicates × 24 genotypes). Supplemental irrigation and rainfed trials were planted on 22 December 2016 for Aranjuez and, in the case of Valladolid, supplemental irrigation and rainfed were planted on 13 November 2017 and 23 November 2017, respectively. The rainfed trial at Sevilla was planted on 15 December 2016. Accumulated rainfall and the average temperatures during the crop season for each experimental station were 134 mm and 14.4 °C; 261 mm and 15.7 °C; and 169 mm and 10.2 °C for Aranjuez (2016/2017), Sevilla (2016/2017) and Valladolid (2017/2018), respectively. For field trials under supplemental irrigation, eight irrigations were provided at Aranjuez, with a total of 420 mm of water, and eight irrigations were provided at Valladolid, with a total of 110 mm of water.

## 2.2. Thermal Images

Thermal images were acquired at Aranjuez, Sevilla and Valladolid using the MIDAS 320L infrared camera (DIAS infrared GmbH, Germany) with a -20 °C to 120 °C temperature range, 8–14 μm spectral range in one channel, 320 × 240 radiometric detector and 16-bit format using focal length in manual mode. All files were exported using the default settings for PYROSOFT Professional software (DIAS infrared GmbH, Germany) in BMP (bitmap file) format using 8 bits, and then images were converted to JPG format using 8 bits.

Thermal images from the complete trials (72 plots each) of Aranjuez (supplemental irrigation condition only) and Sevilla (rainfed), together with the first block (24 plots) from Valladolid (rainfed only), were captured for this study. For each plot, one thermal image was taken holding the camera by hand above the canopy and near the center of the plot. Images were acquired after midday in a zenithal/nadir plane at between 0.8 and 1 m distance at each particular growth stage (GS) using Zadoks growth stage [33] (Table 1). Spatial resolution was approximately 0.14 cm/pixel. Images were acquired on 5 May 2017 (10:00–11:00 UTC, GS = 61–65, anthesis), 25 April 2017 (10:00–11:00 UTC, GS = 69, grain filling) and 14 June 2018 (14:30–15:00 UTC, GS = 77, late grain filling) for Aranjuez, Sevilla and Valladolid, respectively. Figure 1 shows an example of thermal images acquired for each experimental station. The actual time of the data acquisition at each location was slightly different to allow for the

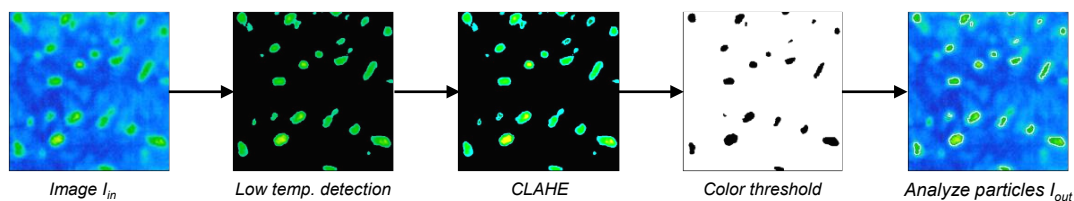
adequate contrast between the leaves and ears in the thermal images. Preliminary selection discarded images with acquisition or temperature problems such as blurred images or overcast conditions.



**Figure 1.** Images of plots acquired using the MIDAS 320L thermal camera: (a) Aranjuez (anthesis); (b) Sevilla (grain filling); and (c) Valladolid (late grain filling). The last image includes the ring used for validation purposes.

### 2.3. Automatic Thermal Ear Counting System

This work proposes an automatic image processing system based on the thermal color map using four steps: (1) *low temperature detection*; (2) *contrast limited adaptive histogram equalization (CLAHE)*; (3) *color threshold*; and (4) *analyze particles* command (Figure 2). The automatic system was developed in ImageJ open source software [34]. As a first step, *low temperature detection* uses the CIE  $L^*a^*b^*$  color space [35] to avoid the blue color values; the negative  $b^*$  values were filtered using the *color threshold* macro [34]. *CLAHE* method [36] was used to enhance the local contrast in small regions in the image. As a next step, *color threshold* macro was used to select the high temperature via the Hue/Saturation/Value (HSV) color space [37], represented in colors between red and green, which correspond to hue values from 2 to 120, and therefore closely related with the presence of ears. Finally, *analyze particles* function [34] was used to count and filter the regions detected as ears.



**Figure 2.** Automatic thermal ear counting system: (1) *low temperature detection*; (2) *contrast limited adaptive histogram equalization (CLAHE)*; (3) *color threshold*; and (4) *analyze particles* command, boundaries regions detected as an ear were underlined in white color.

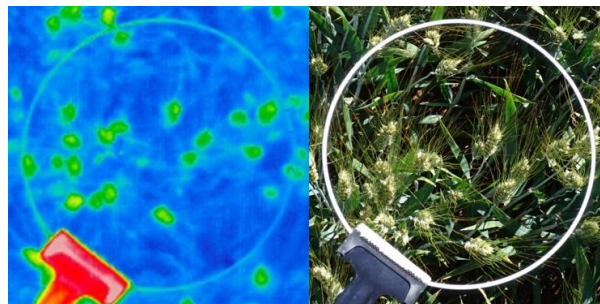
Color thermal maps were used for the ear detection system, and the CIE  $L^*a^*b^*$  color space was selected with the aim of detecting the lower temperatures in the image. This color space uses a Cartesian system of coordinates, where the positive  $b^*$  axis represents the amount of yellow and the negative  $b^*$  axis represents the amount of blue [35]; in that way, we filtered the negative  $b^*$  axis to avoid leaves, which are related with lower temperature. The  $a^*$  axis was not filtered for this step. The *CLAHE* algorithm was used to enhance the local contrast in edges and regions into the image and contribute to isolate overlapping or neighboring ears. The HSV color space uses the hue values from  $0^\circ$  to  $360^\circ$  to represent colors from red to magenta, while saturation and value (or brightness) have numbers from 0 to 100 [37]. This color space was used to segment high temperature represented in colors between green and red. Finally, *analyze particles* command was used to count and filter the regions detected as ears by the automatic algorithm.

## 2.4. Algorithm Validation

### Manual In Situ Counting and RGB Images

For validation purposes, a physical ring was placed on the top of the canopy for counting the number of ears in the exact ring area by visual inspection in the field. The ring has a radius of 0.1225 m. The ring was attached by an extension arm to the monopod used to acquire the RGB images. Thermal and RGB images were acquired at the same time as the visual (in situ) ear counting (inside the ring) was assessed in the first block (i.e., 24 plots) of the rainfed trial at Valladolid. Visual counting was always performed by the same person at the same position where the images were acquired. Approximately 15 s were spent for each counting using a clicker to keep track of the exact number and making sure to inspect the area inside the ring to accurately include all ears present by moving plants and changing perspective angles at each location. Additionally, RGB images from the same plot segments were acquired (at the same time than the thermal images) in a zenithal/nadir plane with a Sony QX1-ILCE camera (Sony Corporation, Japan), 20.1-megapixel resolution, with  $23.2 \times 15.4$  mm sensor size, using 16 mm focal lens and resolution of  $5456 \times 3632$  pixels. The images were taken using a monopod at 1 m above the canopy. The resulting RGB image spatial resolution was approximately 0.03 cm/pixel.

The presence of an ear inside the ring area assigned through the thermal images was checked by the RGB image (Figure 3) together with the in situ visual counting. In that way, it was assured that the temperature changes were due to the presence of an ear instead of soil, leaves or unwanted objects.



**Figure 3.** Thermal and RGB images were acquired for Valladolid at late grain filling. A ring was used as a reference area for validation purposes. The number of ears inside the ring area were counted using the thermal and the RGB images and, additionally, the number of ears was counted by visual inspection in the field. The black extension-arm that supported the ring showed higher temperature than ears and canopy (in red color), enabling it to be automatically extracted by morphology operators in the image processing system.

Two validation steps were developed using manual image-based counting. On the one hand, the ears inside the ring area (including the ring edge) in the thermal and RGB images were manually marked, and the visual ear counting data from the field and the algorithm results were also included. The results are referred to as *Ring-Manual-In-situ-Counting (Ring-MIC)*, *Ring-Manual-Thermal-Counting (Ring-MTC)*, *Ring-Manual-RGB-Counting (Ring-MRC)* and *Ring-Algorithm-Thermal-Counting (Ring-ATC)*. A set of 24 images and full counting datasets were used for each variable of the ring related measurements, thermal and RGB images. On the other hand, selected additional complete (full-sized) thermal images (without cropping to the size of the reference ring) were also manually marked (Figure 1). The result is referred to as the *Complete-Manual-Thermal-Counting (Complete-MTC)*. Finally, the number of ears automatically detected by the algorithm is referred to as the *Complete-Algorithm-Thermal-Counting (Complete-ATC)*. The ears manually marked in the images were counted using a simple algorithm developed for counting the number of colored marks present in the image. The markers were placed using the *Pencil tool* [34] with the same color value and circular



shape and size. In this way, the simple algorithm for the marker counting could be limited to search for precisely the same color and shape marks to then segment and count them.

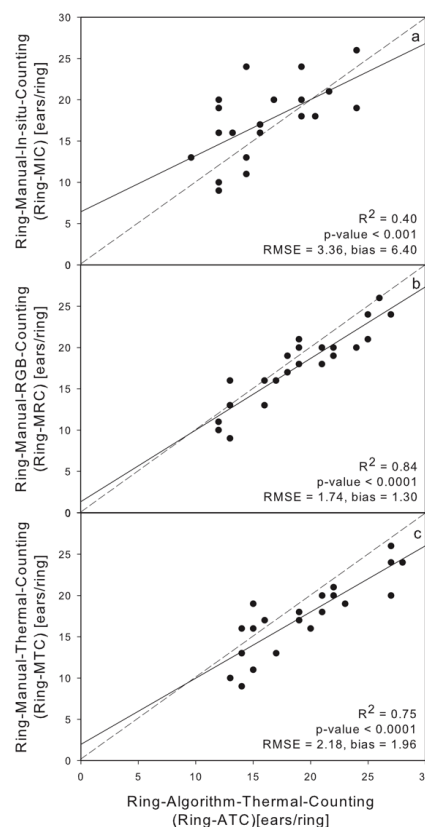
### 2.5. Statistical Analysis

Data analysis was performed using the open source software, RStudio 1.1.423 (R Foundation for Statistical Computing, Vienna, Austria). Linear regressions were used to analyze the relationship between manual image-base counting and automatic thermal ear counting. The data were plotted using SigmaPlot version 12 (Systat Software, Inc., San Jose, CA, USA).

## 3. Results

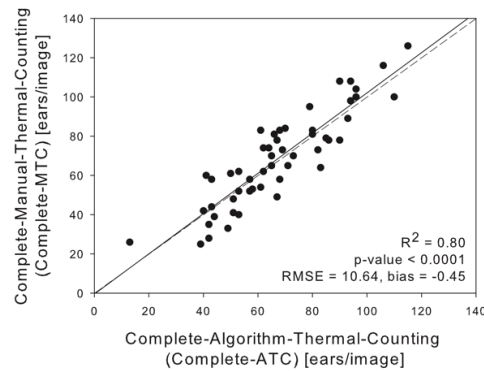
### 3.1. Linear Regression between Thermal, RGB, In Situ and Algorithm Counting

Linear regression of *Ring-MIC*, *Ring-MRC* and *Ring-MTC* against *Ring-ATC* was calculated for the 24 rainfed plots from Valladolid at late grain filling growth stage (Figure 4). The relationships between *Ring-ATC* against *Ring-MIC* ( $R^2 = 0.40$ ), *Ring-MRC* ( $R^2 = 0.84$ ) and *Ring-MTC* ( $R^2 = 0.75$ ) were positive and statistically significant ( $p$ -value < 0.001). Therefore, the weakest correlation was recorded against the visual counting in the field, which a priori represents the actual number of ears present. We also calculated the relationship between the thermal and the RGB manual counting using the ring, where a positive correlation with statistical significance was obtained ( $R^2 = 0.83$ ,  $p$ -value < 0.001). In addition, the relationship of *Ring-MRC* against *Ring-MIC* was positive and statistically significant ( $R^2 = 0.37$ ,  $p$ -value < 0.001), and similar in strength to the correlation between *Ring-ATC* and *Ring-MIC*.



**Figure 4.** Linear regression of the relationships using the ring area for: (a) *Ring-MIC* ( $R^2 = 0.40$ ); (b) *Ring-MRC* ( $R^2 = 0.84$ ); and (c) *Ring-MTC* ( $R^2 = 0.75$ ) vs. *Ring-ATC* using images from Valladolid rainfed trial at late grain filling. The dotted lines indicate the 1:1 slope.

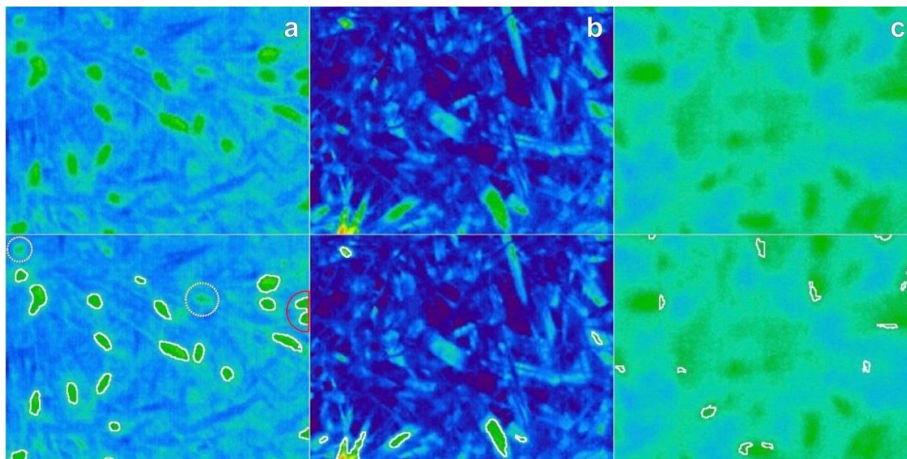
On the other hand, the relationship using the preselection of complete (full-sized) thermal images from Aranjuez, Sevilla and Valladolid against the algorithms counting (*Complete-ATC* vs. *Complete-MTC*) were also positive, statistically significant ( $R^2 = 0.80$ ,  $p$ -value  $< 0.001$ ) and close to 1:1 slope relationship (Figure 5).



**Figure 5.** Linear regression for *Complete-MTC* vs. *Complete-ATC* ( $R^2 = 0.80$ ) using the full-sized thermal images from Aranjuez, Sevilla and Valladolid at anthesis, grain filling and late grain filling, respectively. The dotted line indicates the 1:1 slope.

### 3.2. Understanding Acquisition and Algorithm Errors

Figure 6 shows three temperature image scenarios related with the acquisition protocol, wheat crop temperature and optimal algorithm considerations. The image in Figure 6a was acquired at around 10:30 UTC in Aranjuez (supplementary irrigation) when, at this time, the ears exhibited higher temperature than the canopy leaves due to direct sunlight conditions for several hours. In the case of low thermal image contrast (Figure 6b), there were no temperature differences observed between the ears and the rest of the canopy due image acquisition at 10:30 UTC in Sevilla, when overcast conditions inhibited any direct sunlight to increase ear temperatures. Thus, the ears could not be detected separately by the temperature sensor, resulting in some leaves being detected as an ear by the algorithm. On the other hand, Figure 6c shows an image acquired in Aranjuez at the same optimal daytime as Figure 6a, although the acquisitions distance used was less than 0.8 m by mistake, so that the ears visually appear blurred in the image; the algorithm could not isolate properly the ear regions. The images in Figure 6b,c may be considered as acquisition errors due to improper sky conditions and camera user error, respectively. Providing adequate sky conditions and correct camera settings, the algorithm errors related with ear identification are relatively minor (Figure 6a) and basically due to the inability of the algorithm to detect or separate very closely or overlapping ears in these circumstances (see red color semi-circle in Figure 6a; similarly, two ears were not identified, as shown by yellow circles in dots in Figure 6a) by the algorithm due to the lack of contrast.



**Figure 6.** Thermal images: (a) optimal temperature: higher ear temperature than canopy temperature; (b) low thermal image contrast: no temperature differences between canopy and ears; and (c) out-of-focus image: ears and canopy at high temperature, and the image was acquired at less than 0.8 m distance between the camera and the canopy. The boundary regions underlined in white color represent the ears automatically detected by the algorithm.

#### 4. Discussion

Ear density can be used as a target breeding trait in cereal phenotyping. To date, the few studies dealing with automatic ear counting in the field have mostly been performed using RGB images [6,8–13]. Besides the intrinsic low cost of this approach due to the easy operation and affordability of digital cameras, the high resolution of the natural color digital images is a major factor to consider as both a cost and a benefit. The use of RGB images may have limitations under certain field conditions, including the quality of the sky and light conditions, which can be overcome with sufficiently high spatial resolution, but which requires powerful computing capacities and makes its implementation more complex or less high throughput than expected. Other remote sensing approaches include the use of multispectral images [14], but the segmentation accuracy decreases as the canopy area observed within a single image increases, potentially due to the lower spatial resolution of these images and the reflectance angle dependence of multispectral data. Even LIDAR may be used [38] but its price and processing requirements may still be considered prohibitive and its size and weight makes it too cumbersome to be handheld or pole mounted for quick ground evaluation in field conditions. As an alternative, thermal images may be used. While thermal imagery may provide slightly lower spatial resolution compared to multispectral images, the possibilities for obtaining images with a much greater contrast between ears and leaves is much higher with thermal imaging. The increase in contrast provided by thermal imaging stems from large differences in ear and leaf transpiration rates, which directly affect cooling capacity and temperature. To ensure differences in temperature between the ears and the rest of the canopy, it is still recommended the images be acquired within a few hours of solar noon to reduce shadowing and sun angle effects. In fact, this recommendation may be extended for any passive remote sensing imaging technique.

Moreover, thermal cameras use radiation far from the visible and near infrared spectral regions and thus the factors that contribute to some of the limitations of RGB digital images such as brightness of other factors affecting light conditions [2,16,26] are removed. For that reason, thermal images have proven to be easier to process than RGB images, in part due to their lower resolution, without the lack of contrast and technical limitations of multisensory array multispectral imagers. In fact, the ears, and regardless of the water conditions, are usually several degrees warmer than the leaves [25], due to their constitutive lower stomatal conductance and thus transpiration rates compared with the leaves [39]. For this study, we measured the leaf and the ear temperature, with differences

within images ranging 1.9–5.0 °C, 2.1–3.4 °C and 2.0–5.0 °C for Aranjuez, Sevilla and Valladolid, respectively. The mean temperature differential between ears and leaves across all treatments needed for the algorithm to segment properly the ears was around 2.0 °C. Although, for this application, we used the thermal color map to focus on the contrast present due to relative temperature differences, it is also possible to work on the full radiometric kelvin information to get, for instance, the mean, range or specific ear(s) temperature from the thermal images using the same segmentation algorithm. It could represent additional useful information for phenotyping tasks as ear temperatures have been reported in some cases to be better correlated with grain yield than spectral vegetation indices and also provide comparable correlations as gene expression performance in predicting grain yield [25].

For additional thermal image algorithm validation purposes, visual in situ counting was developed using a ring to delimit a specific area over the crop while in the field and thus facilitate the manual counting. Although the ring has a small area, compared with the complete plot size, we obtained a relatively low  $R^2$  relationship against thermal image-based counting ( $R^2 = 0.40$ , Figure 4). This is most likely associated with the limited single image-perspective of the one zenithal/nadir thermal image or RGB image captured in the field. Some portion of the error could additionally be associated with human visual inspection errors in the field and potentially the subjectivity of the observer, as are often assumed to be major sources of error in manual ear counting in actual breeding programs; however, for this study, the researchers attempted to minimize the human error associated with the *Ring-MIC* ear counts to provide quality validation data. In the manual in situ counting in the field, it was necessary to both view the canopy from different angles as well as physically move plants to acquire accurate field validation data, representing a major difference between the in situ counting and the single image-perspective remote sensing approach of the automatic thermal image ear counting technique presented here. In previous studies on ear recognition, no information regarding the correlation between in situ visual ear counting and automatic ear counting was provided [6–14], but it is nonetheless an important point to consider as the entire image acquisition and processing pipeline represents a sum of errors. Of course, the approach for visual counting assayed was in fact much faster than the traditional ear counting procedures, which implies for example counting the total number of ears in one-meter linear row length. However, this approach is quite tedious (and of course takes much longer than the 15 s per plot as in our study). Nonetheless, we obtained good results using thermal imagery for ear counting with positive and strong relationships between the automatic thermal ear counting system and the manual image-based ear counting ( $R^2 = 0.84$  for *Ring-MRC*, Figure 4;  $R^2 = 0.75$  for *Ring-MTC*, Figure 4 and  $R^2 = 0.80$  for *Complete-MTC*, Figure 5). Furthermore, in all comparisons, the slope of the correlation was quite close to a 1:1 ratio, indicating very little bias toward over- or under-counting within the range of ear density in this study. Thus, the additional validation results provide support for the capacity of the automatic thermal image counting algorithm to count the ears that are present in the image with high precision and low bias. However, other potential sources of error in the thermal image counting pipeline should be considered in more detail.

Although we also detected limitations specific to the use of thermal imagery for ear counting, such as the observed crop temperature issues (Figure 6), there are also errors related to the general use of remote sensing imaging for ear counting, potentially applicable to any other single image or “snapshot” approaches regardless of the range of non-penetrating electromagnetic radiation employed. This is the case for instance of overlapping and hidden ears and might explain the rather low correlation between the *Ring-MRC* (single human eye perspective) and the *Ring-MIC* ( $R^2 = 0.37$ ). The use of additional oblique/off-nadir thermal imaging may provide improved canopy penetration, as for instance 3D surface models that suggest performance improvements when off-nadir images are incorporated [40,41], but may also come with other complications (consistency in oblique off-nadir angle, determination of optimal angle, and more complex 3D processing algorithms) or yet unknown errors.

**Table 1.** Comparative thermal and RGB data information in field conditions for ear counting applications.

	Thermal	RGB
Temperature of the Ears	Several degrees warmer than leaves [25].	Irrelevant.
Stage growth	From heading to near crop maturity [42].	From heading to near crop maturity [12].
Accuracy hour of the day and sky conditions	Clear sky conditions. After midday until 18:00, depending on plant water stress conditions.	Depends of the hour of the day, 8:00 to 18:30 [10], 8:00 to 17:00 [14], 9:00 to 16:00 [9], 12:00 to 16:00 and sky (preferably diffuse light) conditions [12].
Position of the camera	Zenithal/nadir.	Zenithal/nadir [6,10–13]; 45° above the horizontal [14].
Distance of the camera from crop	0.8–1 m.	0.85 m [6], 2.5 m [10], 2.9 m [11], 3.5 m [14], 0.8–1 m [12].
Spatial resolution from ground acquired images	Approximately 0.14 cm/pixel, depending on camera and distance from crop.	Ranging 0.01–0.25 cm/pixel [6,10–13]; depending on camera and distance from crop.
Possible algorithm errors	<ul style="list-style-type: none"> <li>-The algorithm presents errors when the air temperature is too low or high or the sky is too cloudy, or the conditions very windy, which may prevent differences between the canopy and the ear temperature appears.</li> <li>-The camera could be out-of-focus, potentially due to a very short image acquisition distance between the camera and the canopy.</li> <li>-In sparse canopies, soil temperature may affect the background.</li> <li>-Dry or senescent leaf canopy may affect the background.</li> </ul>	<ul style="list-style-type: none"> <li>-False positives where pixels are labeled as ears correspond to leaves and result in irregularities in the ear counting.</li> <li>-False negatives result in ears that are not detected by the algorithm because the contrast between the ear and soil is not great enough and the segmentation algorithm discarded that region.</li> <li>-The algorithm labeled the area as an ear, where the pixels are soil and noise being a result of background brightness caused by a foreign object [12].</li> </ul>

Thermal and RGB image data in field conditions are discussed throughout this work and each of the technology, acquisition and image processing steps show some limitations (summarized in Table 1). RGB sensors provide high frequency information (very high spatial resolution) that contributes to improvements in perceiving the existence of an ear separate from leaves, soil and other unwanted objects; even though similar texture characteristics can be found in the awns or in parts of the leaves for instance due to the high RGB resolution [12], these similarities between awns and ears actually increases the challenges for automatic RGB ear counting systems. On the other hand, thermal images filter high frequency details intrinsically due to the different technology that it uses to detect much longer wavelength radiation emissions and its low-resolution characteristics [16]; this helps in the automatic ear counting system implementation using thermal images. However, we could detect some similar RGB and thermal image errors, such as overlapping and non-identified ears, yet they may still provide some complimentary benefits together, such as more flexible image acquisition conditions or improved image feature extraction and opportunities for validation. Therefore, thermal and RGB fusion may in combination provide the best features of each technology in a way that could be acquired by new mobile phones that incorporate thermal sensors [2]. Even more advanced systems that include hyperspectral cameras [15] may also be considered in the future for ear counting purposes.

On the other hand, researcher visual interpretation of the RGB images was crucial in correctly locating the presence of ears in thermal images for the development of the thermal image ear counting algorithm. Thereby, the acquisition of thermal and RGB images at the same time may contribute further to the understanding and interpretation of the information in the thermal images, contributing to the development of a more robust algorithm for ear counting with thermal image color maps. In fact, the ears are usually several degrees warmer than leaves for only some parts of the day under the right conditions; thus, for ear counting purposes, it is necessary to select the optimal time of day for acquiring thermal images. The thermal images, when taken at the right moment, can provide, from an image processing system perspective, clearer information of the different components of the canopy;

however, in some cases, high temperature information could be associated with soil or unwanted objects that RGB images can help to avoid. Therefore, for future work, it may be the case that perhaps thermal and RGB fusion could be the next step for ear counting applications.

## 5. Conclusions

In our study, a thermal camera was used to develop an image processing system for automatic ear counting in field conditions. In favor of the thermal counting approach, ear density values estimated through thermal imaging can be processed much more rapidly as the size of the images is much smaller compared to high resolution RGB images used in other previous studies, while the increase in contrast allows for equally accurate assessments when the thermal images are captured under specific conditions. There should be a difference of at least 2 °C between the ear and leaf temperatures for this thermal ear counting algorithm to work. Although the correlation with manual in situ ear counts (*Ring-MIC*) was not very high, the algorithm did demonstrate high correlations with various manual image-based ear counts (*Ring-MRC*, *Ring-MTC*, *Complete-MTC*). In future applications, thermal imagery may be acquired from multiple perspectives (including off-nadir and oblique), or even thermal video data, for improved ear detection in comparison with in situ counts. However, further studies could use the same thermal image segmentation algorithm developed here for ear detection (Figure 2) to extract the temperature of ears and leaves separately for other phenotyping applications related to plant water stress effects or grain yield prediction. Thermal and RGB fusion, along with 3D imaging, could be the next steps for cereal ear counting in field conditions to take maximal advantage of the strengths of each imaging technology.

**Author Contributions:** Conceptualization, J.A.F.-G., M.L.B., J.L.A. and S.C.K.; methodology, J.A.F.-G., M.L.B., N.A.G., M.T.N.-T., J.L.A. and S.C.K.; software, J.A.F.-G.; validation, J.A.F.-G. and M.L.B.; formal analysis, J.A.F.-G., M.L.B., J.L.A. and S.C.K.; investigation, J.A.F.-G., M.L.B., N.A.G., M.T.N.-T., J.L.A. and S.C.K.; resources, N.A.G., M.T.N.-T., J.L.A. and S.C.K.; data curation, N.A.G. and M.T.N.-T.; writing—original draft preparation, J.A.F.-G., M.L.B., J.L.A. and S.C.K.; writing—review and editing, J.A.F.-G., J.L.A. and S.C.K.; visualization, J.A.F.-G. and M.L.B.; supervision, J.L.A. and S.C.K.; project administration, J.L.A.; funding acquisition, J.L.A.

**Funding:** This work was supported by MINECO, Spain (project number AGL2016-76527-R) as the primary funding support for the research project; the project “Formación de Talento Humano de Alto Nivel” (project number BPIN 2013000100103) approved by the “Fondo de Ciencia, Tecnología e Innovación”, from the “Sistema General de Regalías”; and “Gobernación del Tolima—Universidad del Tolima, Colombia” as the sole funding source of the first author J.A.F.-G. Contribution of J.L.A. was supported in part by ICREA Academia, Generalitat de Catalunya, Spain.

**Acknowledgments:** The authors of this research would like to thank the field management staff at the experimental stations of Colmenar de Oreja (Aranjuez) and Coria del Rio (Sevilla) of the Instituto Nacional de Investigación y Tecnología Agraria y Alimentaria (INIA) and Zamadueñas (Valladolid) of the Instituto de Tecnología Agraria de Castilla y León (ITACyL) for their continued support of our research.

**Conflicts of Interest:** The authors declare that they have no competing interests.

## References

1. Walter, A.; Liebisch, F.; Hund, A. Plant phenotyping: From bean weighing to image analysis. *Plant Methods* **2015**, *11*, 14. [[CrossRef](#)] [[PubMed](#)]
2. Araus, J.L.; Kefauver, S.C. Breeding to adapt agriculture to climate change: Affordable phenotyping solutions. *Curr. Opin. Plant Biol.* **2018**, *45 Pt B*, 237–247. [[CrossRef](#)]
3. Araus, J.L.; Cairns, J.E. Field high-throughput phenotyping: The new crop breeding frontier. *Trends Plant Sci.* **2014**, *19*, 52–61. [[CrossRef](#)] [[PubMed](#)]
4. Pask, A.; Pietragalla, J.; Mullan, D.; Reynolds, M. (Eds.) *Physiological Breeding II: A Field Guide to Wheat Phenotyping*; CIMMYT: Mexico D.F., Mexico, 2012; ISBN 9789706481825.
5. Slafer, G.A.; Calderini, D.F.; Miralles, D.J. Yield Components and Compensation in Wheat: Opportunities for Further Increasing Yield Potential. In *Increasing Yield Potential in Wheat: Breaking the Barriers*; CIMMYT International Symposium: Mexico D.F., Mexico, 1996; pp. 101–133.

6. Cointault, F.; Guerin, D.; Guillemin, J.; Chopinet, B. In-field *Triticum aestivum* ear counting using colour-texture image analysis. *N. Z. J. Crop Hortic. Sci.* **2008**, *36*, 117–130. [[CrossRef](#)]
7. Liu, T.; Sun, C.; Wang, L.; Zhong, X.; Zhu, X.; Guo, W. In-field wheatear counting based on image processing technology. *Nongye Jixie Xuebao/Trans. Chin. Soc. Agric. Mach.* **2014**, *45*, 282–290. [[CrossRef](#)]
8. Zhou, C.; Liang, D.; Yang, X.; Yang, H.; Yue, J.; Yang, G. Wheat Ears Counting in Field Conditions Based on Multi-Feature Optimization and TWSVM. *Front. Plant Sci.* **2018**, *9*, 1024. [[CrossRef](#)]
9. Zhu, Y.; Cao, Z.; Lu, H.; Li, Y.; Xiao, Y. In-field automatic observation of wheat heading stage using computer vision. *Biosyst. Eng.* **2016**, *143*, 28–41. [[CrossRef](#)]
10. Sadeghi-Tehran, P.; Sabermanesh, K.; Virlet, N.; Hawkesford, M.J. Automated Method to Determine Two Critical Growth Stages of Wheat: Heading and Flowering. *Front. Plant Sci.* **2017**, *8*, 252. [[CrossRef](#)]
11. Madec, S.; Jin, X.; Lu, H.; De Solan, B.; Liu, S.; Duyme, F.; Heritier, E.; Baret, F. Ear density estimation from high resolution RGB imagery using deep learning technique. *Agric. For. Meteorol.* **2019**, *264*, 225–234. [[CrossRef](#)]
12. Fernandez-Gallego, J.A.; Kefauver, S.C.; Aparicio Gutiérrez, N.; Nieto-Taladriz, M.T.; Araus, J.L. Wheat ear counting in-field conditions: High throughput and low-cost approach using RGB images. *Plant Methods* **2018**, *14*, 22. [[CrossRef](#)] [[PubMed](#)]
13. Fernandez-Gallego, J.A.; Kefauver, S.C.; Gutiérrez, N.A.; Nieto-Taladriz, M.T.; Araus, J.L. Automatic wheat ear counting in-field conditions: Simulation and implication of lower resolution images. In Proceedings of the Remote Sensing for Agriculture, Ecosystems, and Hydrology XX, Berlin, Germany, 10–13 September 2018; p. 23. [[CrossRef](#)]
14. Zhou, C.; Liang, D.; Yang, X.; Xu, B.; Yang, G. Recognition of wheat spike from field based phenotype platform using multi-sensor fusion and improved maximum entropy segmentation algorithms. *Remote Sens.* **2018**, *10*, 246. [[CrossRef](#)]
15. Jafri, M.Z.M.; Tan, S.C. Feature selection from hyperspectral imaging for guava fruit defects detection. In Proceedings of the SPIE Digital Optical Technologies, Munich, Germany, 25–29 June 2017.
16. Bhakta, I.; Phadikar, S.; Majumder, K. Importance of Thermal Features in the Evaluation of Bacterial Blight in Rice Plant. In *Annual Convention of the Computer Society of India*; Springer: Singapore, 2018; pp. 300–313. ISBN 9781489911827.
17. Bellvert, J.; Zarco-Tejada, P.J.; Girona, J.; Fereres, E. Mapping crop water stress index in a “Pinot-noir” vineyard: Comparing ground measurements with thermal remote sensing imagery from an unmanned aerial vehicle. *Precis. Agric.* **2014**, *15*, 361–376. [[CrossRef](#)]
18. Mangus, D.L.; Sharda, A.; Zhang, N. Development and evaluation of thermal infrared imaging system for high spatial and temporal resolution crop water stress monitoring of corn within a greenhouse. *Comput. Electron. Agric.* **2016**, *121*, 149–159. [[CrossRef](#)]
19. Buitrago, M.F.; Groen, T.A.; Hecker, C.A.; Skidmore, A.K. Changes in thermal infrared spectra of plants caused by temperature and water stress. *ISPRS J. Photogramm. Remote Sens.* **2016**, *111*, 22–31. [[CrossRef](#)]
20. Cohen, Y.; Alchanatis, V.; Sela, E.; Saranga, Y.; Cohen, S.; Meron, M.; Bosak, A.; Tsipris, J.; Ostrovsky, V.; Orolov, V.; et al. Crop water status estimation using thermography: Multi-year model development using ground-based thermal images. *Precis. Agric.* **2015**, *16*, 311–329. [[CrossRef](#)]
21. Grant, O.M.; Ochagavía, H.; Baluja, J.; Diago, M.P.; Tardáguila, J. Thermal imaging to detect spatial and temporal variation in the water status of grapevine (*Vitis vinifera* L.). *J. Hortic. Sci. Biotechnol.* **2016**, *91*, 44–55. [[CrossRef](#)]
22. Moran, M.S.; Clarke, T.R.; Inoue, Y.; Vidal, A. Estimating crop water deficit using the relation between surface-air temperature and spectral vegetation index. *Remote Sens. Environ.* **1994**, *49*, 246–263. [[CrossRef](#)]
23. Gonzalez-Dugo, V.; Zarco-Tejada, P.; Nicolás, E.; Nortes, P.A.; Alarcón, J.J.; Intrigliolo, D.S.; Fereres, E. Using high resolution UAV thermal imagery to assess the variability in the water status of five fruit tree species within a commercial orchard. *Precis. Agric.* **2013**, *14*, 660–678. [[CrossRef](#)]
24. Wang, Y.; Zhang, Y.; Zhang, R.; Li, J.; Zhang, M.; Zhou, S.; Wang, Z. Reduced irrigation increases the water use efficiency and productivity of winter wheat-summer maize rotation on the North China Plain. *Sci. Total Environ.* **2018**, *618*, 112–120. [[CrossRef](#)]
25. Vicente, R.; Vergara-Díaz, O.; Medina, S.; Chairi, F.; Kefauver, S.C.; Bort, J.; Serret, M.D.; Aparicio, N.; Araus, J.L. Durum wheat ears perform better than the flag leaves under water stress: Gene expression and physiological evidence. *Environ. Exp. Bot.* **2018**, *153*, 271–285. [[CrossRef](#)]

26. Araus, J.L.; Kefauver, S.C.; Zaman-Allah, M.; Olsen, M.S.; Cairns, J.E. Translating High-Throughput Phenotyping into Genetic Gain. *Trends Plant Sci.* **2018**, *23*, 451–566. [[CrossRef](#)] [[PubMed](#)]
27. Chandel, A.K.; Khot, L.R.; Osroosh, Y.; Peters, T.R. Thermal-RGB imager derived in-field apple surface temperature estimates for sunburn management. *Agric. For. Meteorol.* **2018**, *253–254*, 132–140. [[CrossRef](#)]
28. Gan, H.; Lee, W.S.; Alchanatis, V.; Ehsani, R.; Schueller, J.K. Immature green citrus fruit detection using color and thermal images. *Comput. Electron. Agric.* **2018**, *152*, 117–125. [[CrossRef](#)]
29. Camino, C.; Zarco-Tejada, P.J.; Gonzalez-Dugo, V. Effects of heterogeneity within tree crowns on airborne-quantified SIF and the CWSI as indicators of water stress in the context of precision agriculture. *Remote Sens.* **2018**, *10*, 4. [[CrossRef](#)]
30. Jiang, Y.; Shuang, L.; Li, C.; Paterson, A.H.; Robertson, J. Deep learning for thermal image segmentation to measure canopy temperature of Brassica oleracea in the field. In Proceedings of the 2018 ASABE Annual International Meeting, Detroit, MI, USA, 29 July–1 August 2018; American Society of Agricultural and Biological Engineers: St. Joseph, MI, USA, 2018; Volume 39, pp. 300–313.
31. Page, G.F.M.; Liénard, J.F.; Pruett, M.J.; Moffett, K.B. Spatiotemporal dynamics of leaf transpiration quantified with time-series thermal imaging. *Agric. For. Meteorol.* **2018**, *256–257*, 304–314. [[CrossRef](#)]
32. Agro-Climatic Information System for Irrigation (Sistema de Información Agroclimática para el Regadío, SIAR). Available online: <http://portal.mapama.gob.es/websiar/Inicio.aspx> (accessed on 20 February 2019).
33. Zadoks, J.; Chang, T.; Konzak, C. A decimal growth code for the growth stages of cereals. *Weed Res.* **1974**, *14*, 415–421. [[CrossRef](#)]
34. Schneider, C.A.; Rasband, W.S.; Eliceiri, K.W. NIH Image to ImageJ: 25 years of image analysis. *Nat. Methods* **2012**, *9*, 671–675. [[CrossRef](#)] [[PubMed](#)]
35. Malacara, D. Uniform Color Systems. In *Color Vision and Colorimetry: Theory and Applications*, 2nd ed.; SPIE: Bellingham, WA, USA, 2011; pp. 103–129.
36. Zuiderveld, K. Contrast Limited Adaptive Histogram Equalization. In *Graphics Gems*; Elsevier: Amsterdam, The Netherlands, 1994; pp. 474–485. ISBN 0-12-336155-9.
37. Su, C.H.; Chiu, H.S.; Hsieh, T.M. An efficient image retrieval based on HSV color space. In Proceedings of the 2011 International Conference on Electrical and Control Engineering, Yichang, China, 16–18 September 2011; pp. 5746–5749. [[CrossRef](#)]
38. Jimenez-Berni, J.A.; Deery, D.M.; Rozas-Larraondo, P.; Condon, A.; Tony, G.; Rebetzke, G.J.; James, R.A.; Bovill, W.D.; Furbank, R.T.; Sirault, X.R.R. High Throughput Determination of Plant Height, Ground Cover, and Above-Ground Biomass in Wheat with LiDAR. *Front. Plant Sci.* **2018**, *9*, 237. [[CrossRef](#)]
39. Tambussi, E.A.; Bort, J.; Guiamet, J.J.; Nogués, S.; Araus, J.L. The Photosynthetic Role of Ears in C3 Cereals: Metabolism, Water Use Efficiency and Contribution to Grain Yield. *CRC Crit. Rev. Plant Sci.* **2007**, *26*, 1–16. [[CrossRef](#)]
40. Singh, K.K.; Frazier, A.E. A meta-analysis and review of unmanned aircraft system (UAS) imagery for terrestrial applications. *Int. J. Remote Sens.* **2018**, *39*, 5078–5098. [[CrossRef](#)]
41. Smith, M.W.; Vericat, D. From experimental plots to experimental landscapes: Topography, erosion and deposition in sub-humid badlands from Structure-from-Motion photogrammetry. *Earth Surf. Process. Landf.* **2015**, *40*, 1656–1671. [[CrossRef](#)]
42. Berdugo, C.A.; Steiner, U.; Dehne, H.W.; Oerke, E.C. Effect of bixafen on senescence and yield formation of wheat. *Pestic. Biochem. Physiol.* **2012**, *104*, 171–177. [[CrossRef](#)]



© 2019 by the authors. Licensee MDPI, Basel, Switzerland. This article is an open access article distributed under the terms and conditions of the Creative Commons Attribution (CC BY) license (<http://creativecommons.org/licenses/by/4.0/>).







Low-cost assessment of grain yield in durum wheat using RGB images

Jose A. Fernandez-Gallego<sup>1,2,3</sup>, Shawn C. Kefauver<sup>1,2</sup>, Thomas Vattera<sup>3</sup>, Nieves Aparicio Gutiérrez<sup>4</sup>, María Teresa Nieto-Taladriz<sup>5</sup>, José Luis Araus<sup>1,2</sup>

<sup>1</sup> Plant Physiology Section, Department of Evolutionary Biology, Ecology and Environmental Sciences, Faculty of Biology, University of Barcelona, Diagonal 643, 08028, Barcelona, Spain

<sup>2</sup> AGROTECNIO (Center for Research in Agrotechnology), Av. Rovira Roure 191, 25198, Lleida, Spain

<sup>3</sup> Programa de Ingeniería Electrónica, Facultad de Ingeniería, Universidad de Ibagué, Carrera 22 Calle 67, 730001, Ibagué, Colombia

<sup>4</sup> Instituto Tecnológico Agrario de Castilla y León (ITACyL), Ctra. Burgos Km. 119, 47071, Valladolid, Spain

<sup>5</sup> Instituto Nacional de Investigación y Tecnología Agraria y Alimentaria (INIA), Ctra. de la Coruña Km. 7.5, 28040, Madrid, Spain

Published in:

European Journal of Agronomy (2019), Vol. 105

## ABSTRACT

The pattern of photosynthetic area of the canopy throughout the crop cycle is an important factor for determining grain yield in wheat. This work proposes the use of zenithal RGB images of the canopy taken in natural light conditions to derive vegetation indices as a low-cost approach to predict grain yield. A set of 23 varieties of durum wheat was monitored in three growing conditions (support irrigation, rainfed and late planting) and two sites (Aranjuez and Valladolid, Spain), totalling 6 field trials. For each plot, digital RGB images were taken periodically from seedling emergence to late grain filling. RGB-based Green Area (GA), Greener Area (GGA), Normalized Green Red Difference Index (NGRDI), Triangular Greenness Index (TGI) and a novel photosynthetic area index based on the CIE  $L^*u^*v^*$  colour space ( $u^*v^*A$ ) were compared to handheld spectroradiometer Normalised Difference Vegetation Index (NDVI) for reference. In the case of the irrigated and late planting trials the best phenotypic predictions of grain yield were achieved with the vegetation indices measured during the last part of the crop cycle (i.e. grain filling). For the rainfed trials the best phenotypic predictions were achieved with indices measured earlier (around heading). Among all the evaluated indices, the novel index performed the best. Considering the heritabilities of the evaluated RGB indices and their genetic correlations with grain yield, index-based predictions of grain yield were best in the early crop stages for both rainfed and irrigated conditions, while for late planting indices measured at different crop stages performed equally well.



## Low-cost assessment of grain yield in durum wheat using RGB images

Jose A. Fernandez-Gallego<sup>a,b,c</sup>, Shawn C. Kefauver<sup>a,b,\*</sup>, Thomas Vatter<sup>a,b</sup>,  
Nieves Aparicio Gutiérrez<sup>d</sup>, María Teresa Nieto-Taladriz<sup>e</sup>, José Luis Araus<sup>a,b,\*</sup>



<sup>a</sup> Plant Physiology Section, Department of Evolutionary Biology, Ecology and Environmental Sciences, Faculty of Biology, University of Barcelona, Diagonal 643, 08028, Barcelona, Spain

<sup>b</sup> AGROTECNIO (Center for Research in Agrotechnology), Av. Rovira Roure 191, 25198, Lleida, Spain

<sup>c</sup> Programa de Ingeniería Electrónica, Facultad de Ingeniería, Universidad de Ibagué, Carrera 22 Calle 67, 730001, Ibagué, Colombia

<sup>d</sup> Instituto Tecnológico Agrario de Castilla y León (ITACyL), Ctra. Burgos Km. 119, 47071, Valladolid, Spain

<sup>e</sup> Instituto Nacional de Investigación y Tecnología Agraria y Alimentaria (INIA), Ctra. de la Coruña Km. 7.5, 28040, Madrid, Spain

### ARTICLE INFO

#### Keywords:

Abiotic stresses  
Digital image processing  
Durum wheat  
Grain yield  
Heritability  
Low-cost phenotyping  
RGB indices  
NDVI

### ABSTRACT

The pattern of photosynthetic area of the canopy throughout the crop cycle is an important factor for determining grain yield in wheat. This work proposes the use of zenithal RGB images of the canopy taken in natural light conditions to derive vegetation indices as a low-cost approach to predict grain yield. A set of 23 varieties of durum wheat was monitored in three growing conditions (support irrigation, rainfed and late planting) and two sites (Aranjuez and Valladolid, Spain), totalling 6 field trials. For each plot, digital RGB images were taken periodically from seedling emergence to late grain filling. RGB-based Green Area (GA), Greener Area (GGA), Normalized Green Red Difference Index (NGRDI), Triangular Greenness Index (TGI) and a novel photosynthetic area index based on the CIE  $L^*u^*v^*$  colour space ( $u^*v^*A$ ) were compared to handheld spectroradiometer Normalised Difference Vegetation Index (NDVI) for reference. In the case of the irrigated and late planting trials the best phenotypic predictions of grain yield were achieved with the vegetation indices measured during the last part of the crop cycle (i.e. grain filling). For the rainfed trials the best phenotypic predictions were achieved with indices measured earlier (around heading). Among all the evaluated indices, the novel index performed the best. Considering the heritabilities of the evaluated RGB indices and their genetic correlations with grain yield, index-based predictions of grain yield were best in the early crop stages for both rainfed and irrigated conditions, while for late planting indices measured at different crop stages performed equally well.

### 1. Introduction

The photosynthetic area of the canopy is an important factor for determining grain yield. Rapid ground cover as well as stay green late in the crop cycle have potential grain yield benefits in Mediterranean environments where water is available early in the season but its availability declines around grain filling (Pask et al., 2012). Colour indices can discriminate plants from background using Red/Green/Blue (RGB) images. Studies have shown that RGB vegetation indices contribute to separate plants and soil in digital images (Woebbecke et al., 1993, 1995). Several studies have shown the applicability of RGB vegetation indices to obtain relevant information about crop status. For example, the Normalized Green-Red Difference Index (NGRDI) was used for aerial photography to estimate nutrient status and crop

biomass in trials such as alfalfa, corn soybean (Hunt et al., 2005), pea and oat (Hunt et al., 2014; Jannoura et al., 2015). The Triangular Greenness Index (TGI), which calculates the triangle area of the reflectance spectrum with vertices in red, green and blue wavelengths, allows estimation of chlorophyll concentration in leaves and the canopy (Hunt et al., 2014, 2013, 2011). Relative green area (GA) and relative greener green area (GGA) are two indices used to estimate the photosynthetic area of the canopy. They use the three-colour camera channels (Casadesús et al., 2007) and are based on the Intensity, Hue and Saturation (IHS) colour space (Judd and Wyszecki, 1967). Next to these established vegetation indices, our study proposes a new vegetation index, which uses the CIE  $L^*u^*v^*$  colour space (Robertson, 1977) in order to include the white reference for each image and force the *hue* and *chroma* values to be dependent on the luminance (*L*) (Malacara,

\* Corresponding authors at: Plant Physiology Section, Department of Evolutionary Biology, Ecology and Environmental Sciences, Faculty of Biology, University of Barcelona, Diagonal 643, 08028, Barcelona, Spain.

E-mail addresses: [jfernaga46@alumnes.ub.edu](mailto:jfernaga46@alumnes.ub.edu) (J.A. Fernandez-Gallego), [skefauver@ub.edu](mailto:skefauver@ub.edu) (S.C. Kefauver), [tvatter@ub.edu](mailto:tvatter@ub.edu) (T. Vatter), [apagutni@itacyl.es](mailto:apagutni@itacyl.es) (N. Aparicio Gutiérrez), [mtnieto@inia.es](mailto:mtnieto@inia.es) (M.T. Nieto-Taladriz), [jaraus@ub.edu](mailto:jaraus@ub.edu) (J.L. Araus).

<https://doi.org/10.1016/j.eja.2019.02.007>

Received 27 August 2018; Received in revised form 13 December 2018; Accepted 11 February 2019  
1161-0301/ © 2019 Elsevier B.V. All rights reserved.

2011).

Plant and background segmentation is complicated under field conditions by numerous factors including soil, shadows and unexpected miscellaneous objects such as rocks, weeds, and plant remains, or if the images are taken from the ground with a hand-held camera, factors such as the photographer's legs. Therefore the algorithms must be robust to accommodate these conditions (Bai et al., 2014, 2013; Guijarro et al., 2011; Wang et al., 2013). For this purpose CIE  $L^*u^*v^*$  is a colour space with better detection of colour in variable light conditions, overlapping leaves and shadows due to  $u^*v^*$ , being dependent proportionally on the Luminance ( $L^*$ ) according to the chromaticity diagram (Malacara, 2011).

Therefore, colour indices derived from RGB images may be used in crop management, and even as phenotypic tools for breeding that are aimed at increasing yield under different environmental conditions. For example, for crops such as wheat and maize, GA and GGA have shown similar or even better performance than a multispectral index like the Normalized Difference Vegetation Index (NDVI) in applications like predicting grain yield under different growing conditions including water status (Casadesús et al., 2007), availability of nitrogen (Kefauver et al., 2017; Vergara-díaz et al., 2016) and phosphorous (Gracia-Romero et al., 2017), or the presence of foliar diseases (Zhou et al., 2015). Therefore, estimating grain yield and other crop features using RGB vegetation indices such as the GA, GGA, NGRDI, TGI, and new colour space indices such as CIE  $L^*u^*v^*$  promises to contribute to an increased efficiency of crop management practices and phenotyping.

Durum wheat is by dedicated area the main herbaceous crop on the southern and eastern shores of the Mediterranean basin and among the most cultivated in Southern Europe (FAO et al., 2014). The climate change scenarios for the next decades predict higher temperatures and decreased precipitation, with subsequent increases in the frequency of drought and heat stresses in the Mediterranean Basin (Schlaepfer et al., 2017). As a consequence, adaptation measures for Mediterranean agriculture are needed, including an increased breeding effort or more efficient monitoring techniques for crop management. For example, precise high throughput field phenotyping (HTP) is perceived as one of the main bottlenecks hindering genetic advance in general (Araus et al., 2018), and the need to deploy affordable phenotyping techniques is perceived as a prerequisite for the national agricultural programs of developing countries and small seed companies (Araus and Kefauver, 2018). The objective of the current study was to evaluate different vegetation indices derived from RGB images, throughout the crop cycle, as a phenotypic trait to predict durum wheat yield under different water regime conditions. To achieve this objective, vegetation indices obtained by analysis of 4140 RGB images were correlated against grain yield and evaluated in terms of their ability to predict yield. Furthermore, genetic correlations of these indices against grain yield along

with the heritability of these indices were calculated. To further stress the low-cost nature of this approach, RGB images were acquired at ground level without the need of any platform, by using a hand-held camera. Besides the evaluation of the different RGB vegetation indices under different agronomical conditions, the objective of this study was to determine the best phenological stage of the crop to undertake measurements. In addition the NDVI was measured in half of the trials throughout the crop cycle and their correlations against grain yield compared with that of RGB indices.

## 2. Materials and methods

### 2.1. Plant material and growing conditions

A set of twenty-three post Green Revolution (i.e. semidwarf) durum wheat (*Triticum turgidum* L. subsp. *durum* [Desf] Husn.) cultivars (cvs Amilcar, Arcobaleno, Athoris, Avispa, Burgos, Claudio, Core, Don Norman, Don Ricardo, Dorondon, Euroduro, Gallareta, Iberus, Kiko Nick, Mexa, Olivador, Pedroso, Regallo, Saragolla, Sculptur, Simeto, Solea and Vitron) were grown, which have been widely cultivated in Spain during the past four decades. Field trials were carried out during the 2016/2017 crop season at the experimental stations of Colmenar de la Oreja (40° 04' N, 3° 31' W), near Aranjuez (Madrid Province), which belong to the Instituto Nacional de Investigación y Tecnología Agraria y Alimentaria (INIA) of Spain and at Zamadueñas (41° 42' N, 4° 42' W), near Valladolid, which belong to the Instituto de Tecnología Agraria de Castilla y León (ITACyL). The average annual precipitation of Aranjuez is about 425 mm and the average annual temperature is 13.7 °C, while at Valladolid the annual averages are 386 mm and 11.6 °C, respectively. In relation to the Aranjuez trials, the field was fertilized before sowing with 450 kg ha<sup>-1</sup> of 8:15:15 (8% N, 15% P<sub>2</sub>O<sub>5</sub>, 15% K<sub>2</sub>O) fertilizer. Further, 185 kg ha<sup>-1</sup> of 46% urea was applied before stem elongation. For the Valladolid trials, the field was fertilized before sowing with 300 kg ha<sup>-1</sup> of 8:15:15 fertilizer. A second application of fertilizer, consisting of 300 kg ha<sup>-1</sup> of calcium ammonium nitrate (27% richness in nitrogen), was applied before stem elongation. For the Valladolid trials, weed management was conducted using Amadeus Top 50gr/ha (50% p/p Tifensulfuron-metil, 25% p/p Tribenuron-metil) applied at the beginning of tillering, which corresponded to Zadoks scale around 20–23 (Zadoks et al., 1974). In the case of Aranjuez, weeds were removed manually throughout the crop season. For each site three growing conditions were assayed: supplemental irrigation (R+), rainfed (R-) and late planting (L). For each growing condition, genotypes were evaluated in plots of 6 × 1.5 m<sup>2</sup> in size, with a spacing distance of 0.2 m between rows and a planting density of 250 seeds per m<sup>2</sup>, using a randomized complete block design with three replicates, totalling 69 plots. Fig. 1 shows the field trials at Aranjuez experimental

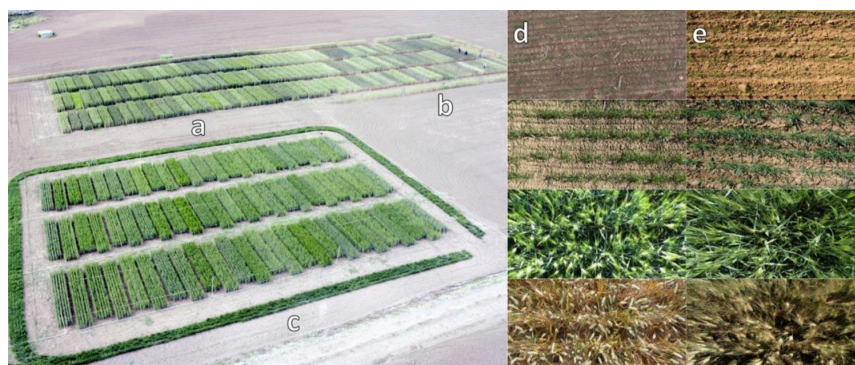


Fig. 1. Field trials of a) supplemental irrigation, b) rainfed and c) late planting at Aranjuez. Images of plots at different growth stages (from seedling growth to dough development) at d) Aranjuez and e) Valladolid experimental stations.

station for (a) supplemental irrigation, (b) rainfed and (c) late planting. The supplemental irrigation and rainfed trials were planted on December 22, 2016 and November 29, 2016, for Aranjuez and Valladolid, respectively; late planting was planted on March 1, 2017 and February 9, 2017, for Aranjuez and Valladolid, respectively and also subjected to supplemental irrigation. Accumulated rainfall during the 2016/2017 crop season for supplemental irrigation and rainfed trials was 134 mm and 124 mm and the average temperatures were 14.4 °C and 10.9 °C, for Aranjuez and Valladolid, respectively. Accumulated rainfall during the crop season for late planting was 98 mm and 71 mm and the average temperatures were 18.7 °C and 14.3 °C for Aranjuez and Valladolid, respectively. For trials under supplemental irrigation, eight irrigations were provided at Aranjuez, with a total of 420 mm of water, and nine irrigations at Valladolid, totalling 155 mm of water. Supplemental irrigation was provided from stem elongation to around two weeks after anthesis. In the case of late planting trials, nine irrigations were provided at Aranjuez and Valladolid, with a total of 540 mm and 155 mm of water, respectively, distributed all throughout the crop cycle. Emergency irrigation was provided to rainfed trials to ensure plant emergence; one irrigation at Aranjuez, with a total of 60 mm of water and three irrigations at Valladolid, with a total of 55 mm of water. Harvest was carried out in Aranjuez on July 19, 2017 for all three growing conditions, while for Valladolid, harvest was carried out on July 6, 2017 for supplemental irrigation and rainfed and on July 19, 2017 for late planting.

## 2.2. RGB images

RGB images at Aranjuez were acquired with a Canon IXUS 310 HS 12-megapixel resolution camera, with a 6.16 x 4.62 mm sensor size using 4 mm focal length lens and native resolution of 4000 × 3000 pixels. The images in Valladolid were acquired with a Nikon D70 6.1-megapixel resolution camera with a 23.7 x 15.6 mm sensor size using an 18 mm focal length lens and native resolution of 3008 × 2000 pixels. All images were taken using trigger speed and aperture programmed in automatic mode. Files were stored in JPG format using sRGB colour standard (Susstrunk et al., 1999). Images obtained at the Aranjuez field trials were resized to 4000 × 1500 pixels, as a way to discard background noise (e.g. pixels from the soil, adjacent plots or photographer's boots).

For each plot and day of measurement, one digital RGB image was taken under natural light conditions holding the camera by hand above the plant canopy, in a zenithal plane, at about one meter above the top of the canopy, near the centre of each plot. Measurements were acquired at least 3 times per month for each growing condition in 2017. In the case of Valladolid, imaging was performed between February 20 and June 5, February 9 and May 29, and April 6 and June 5 for supplementary irrigation, rainfed and late planting trials, respectively. In total 4140 images were obtained throughout the crop season. In addition, the ColorChecker Passport (colour chart, X-Rite, USA) was used for colour calibration purposes. One RGB image of the colour chart was taken in natural light conditions with each camera placed in a zenithal plane. For Aranjuez, imaging was performed between February 17 and June 1 for supplemental irrigation and rainfed trials, respectively; and between March 30 and June 1 for the late planting trial. Table 1 shows a summary of the database quantified by growth stage (GS), using the Zadoks growth scale (Zadoks et al., 1974) as well as the date of measurement in days after sowing and the calendar date. In addition, NDVI was determined for the three trials at Valladolid Experimental Station using a hand-held portable spectroradiometer (GreenSeeker, handheld crop sensor, Trimble, Sunnyvale, CA, USA) by passing the sensor over the middle of each plot at a constant height of 0.5 m above and perpendicular to the canopy. The measurements were performed periodically, between March 8 and June 5, March 8 and May 29, and April 4 and June 22 for supplemental irrigation, rainfed and late planting, respectively with a frequency similar to that for the RGB images

(Supplementary Table 1).

## 2.3. Image analysis

Vegetation indices were calculated from the RGB images using the open source BreedPix software to calculate the GA and GGA (Casadesús and Villegas, 2014), implemented along with the NGRDI and TGI as part of the open-source CerealScanner plugin (Kefauver et al., 2018; <https://integrativecropecophysiology.com/software-development/cerealscanner/>) developed for ImageJ software (Schneider et al., 2012). In addition, we tested a new algorithm formulated as the portion of green pixels within the range of 90° to 180° of the chromaticity diagram defined by the Cartesian  $u^*$  and  $v^*$  axes (here defined as  $u^*v^*$ A index). The  $u^*v^*$ A index was also included in the open-source CerealScanner plugin (Kefauver et al., 2018). Thus, the  $u^*v^*$ A index has been developed based in the 1976 CIE  $L^*u^*v^*$  colour space as a modification of the  $u^*v^*$  chromaticity diagram from the 1960 CIE Luv colour space:

$$u' = \frac{4X}{X + 15Y + 3Z} \quad (1)$$

$$v' = \frac{9Y}{X + 15Y + 3Z} \quad (2)$$

where  $u'$  and  $v'$  are defined as  $u' = u$  and  $v' = 1.5v$  and X, Y, Z are refined by the CIE XYZ colour space. In the same way, the CIE  $L^*u^*v^*$  colour space is defined by:

$$L^* = 116f\left(\frac{Y}{Y_n}\right) - 16 \quad (3)$$

$$u^* = 13L^*(u' - u_n) \quad (4)$$

$$v^* = 13L^*(v' - v_n) \quad (5)$$

where  $u_n$  and  $v_n$  are the coordinates for the nominal white colour and  $Y_n$  is part of the tristimulus values of the perfect diffusor (Malacara, 2011). Equations (4–5) show the dependence of the  $u^*v^*$  chromaticity diagram on the luminance ( $L^*$ ) and force the hue and chroma values to be dependent on the luminance ( $L^*$ ). To complement this, the differences ( $u' - u_n$ ) and ( $v' - v_n$ ) were used as a white reference for D65 daylight standard illumination (Burton and Moorhead, 1987). The equations (3–5) contribute towards reducing the colour perception problems caused by natural light changes, resulting in a conic shape luminance, with the vertex at the  $u^*v^*$  chromaticity origin, because when luminance decreases, colour differences are more difficult to perceive (Malacara, 2011). The hue angle using the  $u^*v^*$  chromaticity diagram is calculated using the formula:

$$h^* = \tan^{-1}\left[\frac{v^*}{u^*}\right] \quad (6)$$

where  $h^*$  is used to segment the green cover area of the image. Values from 90° to 180° are segmented as photosynthetic area of canopy, from blueish green to greenish yellow. The output of the  $u^*v^*$ A index is the percentage of the photosynthetic area estimated in the zenithal input image, ranging from 0 to 1. Fig. 1 (d) and (e) show a sample of the image database for the Aranjuez and Valladolid experimental stations. Fig. 2 shows a sample of the image database and indices at different growth stages. All indices have been calculated using ImageJ open source software (Schneider et al., 2012).

Previous to the present study we had tested the effect of calibrating the vegetation indices derived from the RGB images using the color chart. The results showed very high determination coefficients ( $R^2 \approx 0.98$ ) between the RGB indexes derived from the calibrated and uncalibrated images. This is why we did not consider the need to regularly (during the image acquisition) calibrate the images against the color chart in this study, since the absence of calibration may save time. Even so we tested the calibration using a single image of the color chart. To that end and for the two cameras used in this study we calibrated the

**Table 1**

Dataset summary for each experimental site the growing conditions and the measurement dates, expressed as calendar date (CD) and number of days after sowing (DAS), and corresponding growth stage (GS) expressed in the Zadoks growth scale. Within each trial category (rainfed, support irrigation or late planting) the GSs that are highlighted in green were tested for heritability and genetic correlation within a given growing conditions.

Support irrigation						Rainfed						Late planting					
Aranjuez			Valladolid			Aranjuez			Valladolid			Aranjuez			Valladolid		
CD	DAS	GS	GS	DAS	CD	CD	DAS	GS	GS	DAS	CD	CD	DAS	GS	GS	DAS	CD
17/02	57	15	15	83	20/02	17/02	57	15	15	72	09/02	30/03	30	15	15	55	06/04
01/03	69	16-19	16-19	100	09/03	01/03	69	16-19	16-19	101	10/03	12/04	43	20-22	20-22	60	11/04
14/03	82	20-27	23-27	114	23/03	14/03	82	23-27	23-27	120	29/03						
30/03	98	30-36	30-35	128	06/04	30/03	98	30-35	30-35	129	07/04	27/04	58	30-32	30-35	81	02/05
12/04	111	37-39	37-39	133	11/04				36-37	133	11/04						
			45-47	143	21/04	12/04	111	41-47	41-47	143	21/04	04/05	65	45-47	45-47	87	08/05
			52	148	26/04	27/04	126	55-57	55-57	148	26/04	12/05	73	55-57			
27/04	126	55-59	55-59	154	02/05	04/05	133	61-65	61-65	154	02/05	17/05	78	58-59	55-59	95	16/05
04/05	133	61	61	160	08/05				69	160	08/05	25/05	86	69	69	104	23/05
12/05	141	69	69	168	16/05	12/05	141	73	73	168	16/05						
17/05	146	75	75	177	23/05	17/05	146	77-79	77-79	181	29/06	01/06	93	75-79	75-79	115	05/06
25/05	154	81	81	188	05/06	25/05	154	87-89									
01/06	161	87				01/06	161	90-99									

complete set of plot images against the reference images of the colour chart acquired after completing the field evaluation. We used the color chart ColorChecker Passport (website: <https://www.xrite.com/categories/calibration-profiling/colorchecker-passport-photo>), payment and open source software: Lightroom CC (website: <https://lightroom.adobe.com>, using the free full-trial version) and open-source software ImageJ (website: <https://imagej.nih.gov/ij/>). With Lightroom we have used the standard color calibration for ColorChecker Passport and with ImageJ we have calibrated by

interpolation technique. In order to compare the results, we have calculated the regression coefficient between calibrated and uncalibrated the RGB indexes as well as their performance in predicting grain yield and their broad sense heritability.

2.4. Statistical analysis

Phenotypic data analysis was performed using the software package SAS 9.4 (SAS Institute Inc., Cary, NC, USA) and selecting *proc mixed* to

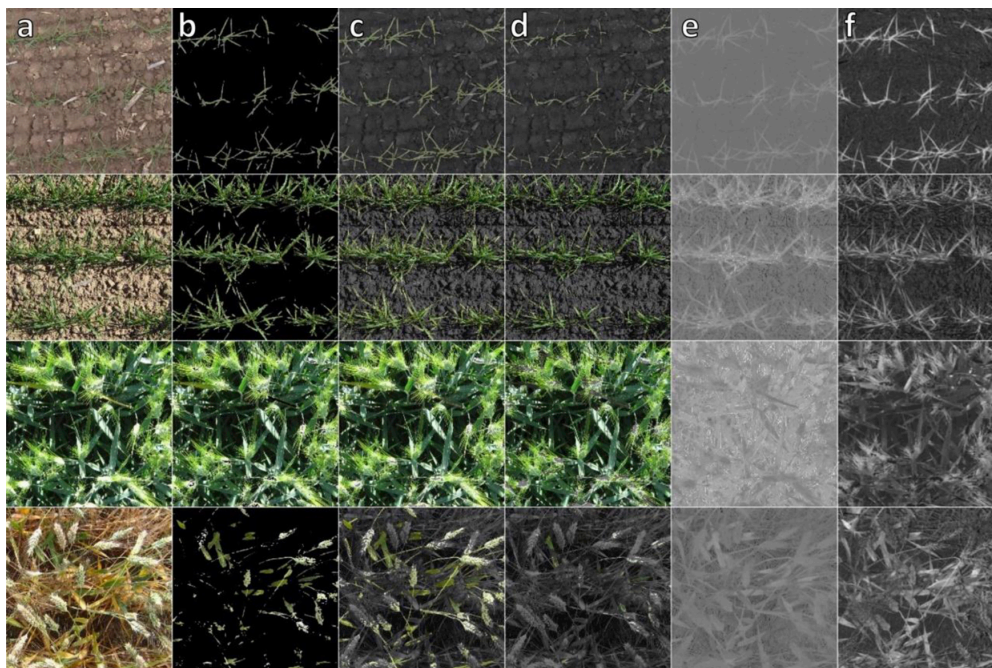


Fig. 2. Images of plots at different growth stages: a) the input image, and the tested indices b)  $u^* v^* A$ , c) GA, d) GGA e) NGRDI and f) TGI.

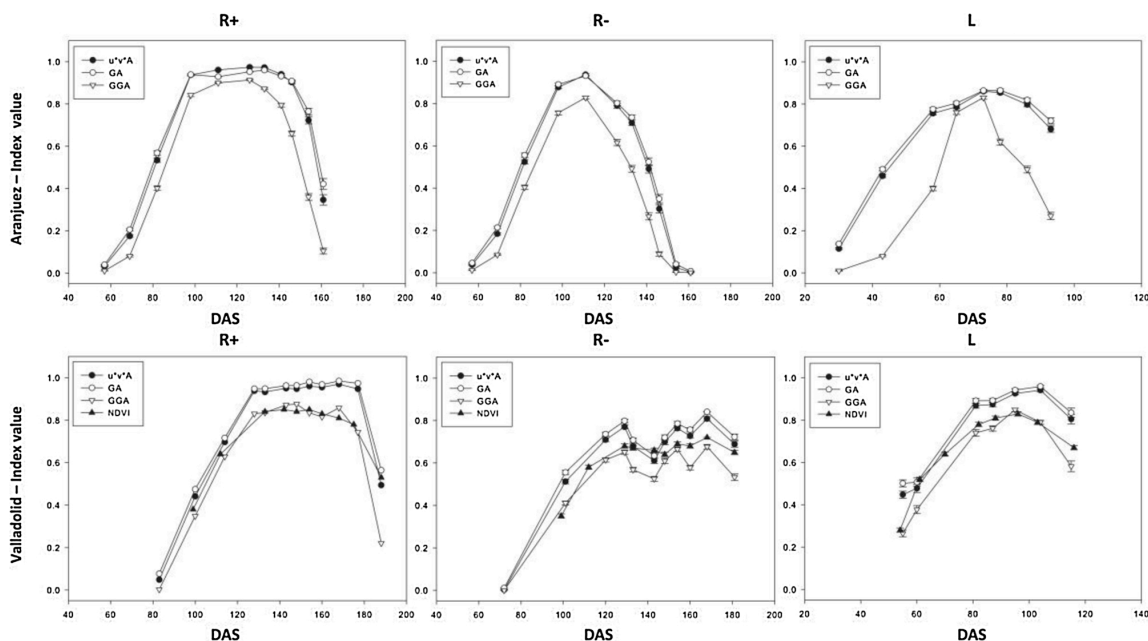


Fig. 3. Pattern of values of the three different RGB vegetation indices ( $u^*v^*A$ , GA, GGA) throughout the crop cycle measured in each of the six different trials of the study. In addition, the pattern for NDVI is shown for Valladolid. For each trial the values of all plots were used to calculate the standard error. Days after sowing (DAS) was used to normalize the crop duration.

estimate broad sense heritability and genetic correlation and *proc reg* for regression analysis.

To estimate the variance components for use in the calculation of broad sense heritability, all model parameters were set as random. Broad sense heritability across environments (Aranjuez and Valladolid; Equation 7) was calculated separately for the three growing conditions (support irrigation, rainfed and late planting) as:

$$h^2 = \frac{V_G}{V_G + \frac{V_{GE}}{e} + \frac{V_R}{r}} \tag{7}$$

Where genotypic variance is coded by ( $V_G$ ), genotype x environment variance is coded by ( $V_{GE}$ ), and residual variance is coded by ( $V_R$ ). The terms  $e$  and  $r$  indicate the number of environments and replicates, respectively.

Genetic correlation between RGB vegetation indices and yield was calculated separately for the three growing conditions. Environment x trait as well as environment x rep x trait interactions were set as fixed, with all remaining effects being set as random. Genetic correlation (Equation 8) was calculated as:

$$r_A = \frac{Cov_{XY}}{\sqrt{V_X + V_Y}} \tag{8}$$

where covariance between trait 1 and 2 (yield and the respective RGB vegetation index) is coded by ( $Cov_{XY}$ ), genotypic variance of trait 1 is coded by ( $V_X$ ), and genotypic variance of trait 2 is coded by ( $V_Y$ ). The standard error (Equation 9) of the genetic correlation was calculated using the delta method (Lynch and Walsh, 1998) as:

$$SE_{r_A} = \sqrt{r_A^2 \left[ \frac{var(V_X)}{4V_X^2} + \frac{var(V_Y)}{4V_Y^2} + \frac{var(Cov_{XY})}{Cov_{XY}^2} + \frac{2cov(V_X V_Y)}{4V_X V_Y} \right] - \frac{2cov(V_X Cov_{XY})}{2V_X Cov_{XY}} - \frac{2cov(V_Y Cov_{XY})}{2V_Y Cov_{XY}}} \tag{9}$$

where genotypic variance of trait 1 is coded by ( $V_X$ ), genotypic variance of trait 2 is coded by ( $V_Y$ ); variance of the variance of trait 1 and trait 2 is coded by ( $var(V_X)$ ) and ( $var(V_Y)$ ), respectively; covariance between

trait 1 and 2 is coded by ( $Cov_{XY}$ ); variance of the covariance between trait 1 and trait 2 is coded by ( $var(Cov_{XY})$ ); the covariance between the variances of trait 1 and trait 2 is coded by ( $var(V_X V_Y)$ ); covariance between the variance of trait 1 and the covariance is coded by ( $cov(V_X Cov_{XY})$ ); and the covariance between the variance of trait 2 and the covariance is coded by ( $cov(V_Y Cov_{XY})$ ).

To validate the robustness of the regression analysis, a five-fold cross-validation (CV) was performed. In total, 100 CV runs (20 times five-fold CV) were performed. For this, 100 subsets were extracted from the full genotype set. Subsets each included 80% of the data of the full genotype set, randomly selected. The subsets were taken as training sets for the calculation of regression estimates. The remaining 20% of the data was used as the validation set. To estimate the proportion of phenotypic variance explained by the model, the unbiased estimator  $R_{adj}^2$  (Draper and Smith, 1998) was calculated for each subset. As a measure of accuracy, the root mean square error (RMSE) was calculated. To determine the predictive ability  $R_{pred}^2$  of the model for yield, the regression estimates, estimated using the training sets, were used to predict the phenotypic value of the remaining 20% of the data forming the validation sets.  $R_{pred}^2$  was defined as the squared Pearson product-moment correlation between predicted and observed phenotypic values. Subsequently,  $R_{adj}^2$ ,  $R_{pred}^2$  and RMSE values were averaged over all 100 CV runs to obtain final estimates.

The capacity within each of the three growing environments (supplemental irrigation, rainfed and late planting) of a given vegetation index to serve as an indirect selection tool for assessing grain yield was evaluated as the comparison between the broad sense heritability ( $h^2$ ) of grain yield and the value of multiplying the  $h^2$  of a given vegetation index with the genetic correlation with grain yield to the power of two ( $r_A^2 \times h^2$ ), which was adapted from the equation of Falconer and Mackay (1996). Data was plotted using SigmaPlot version 12 (Systat Software, Inc., San Jose California USA).

### 3. Results

Average grain yield was 2735 and 2783 Kg ha<sup>-1</sup> under rainfed



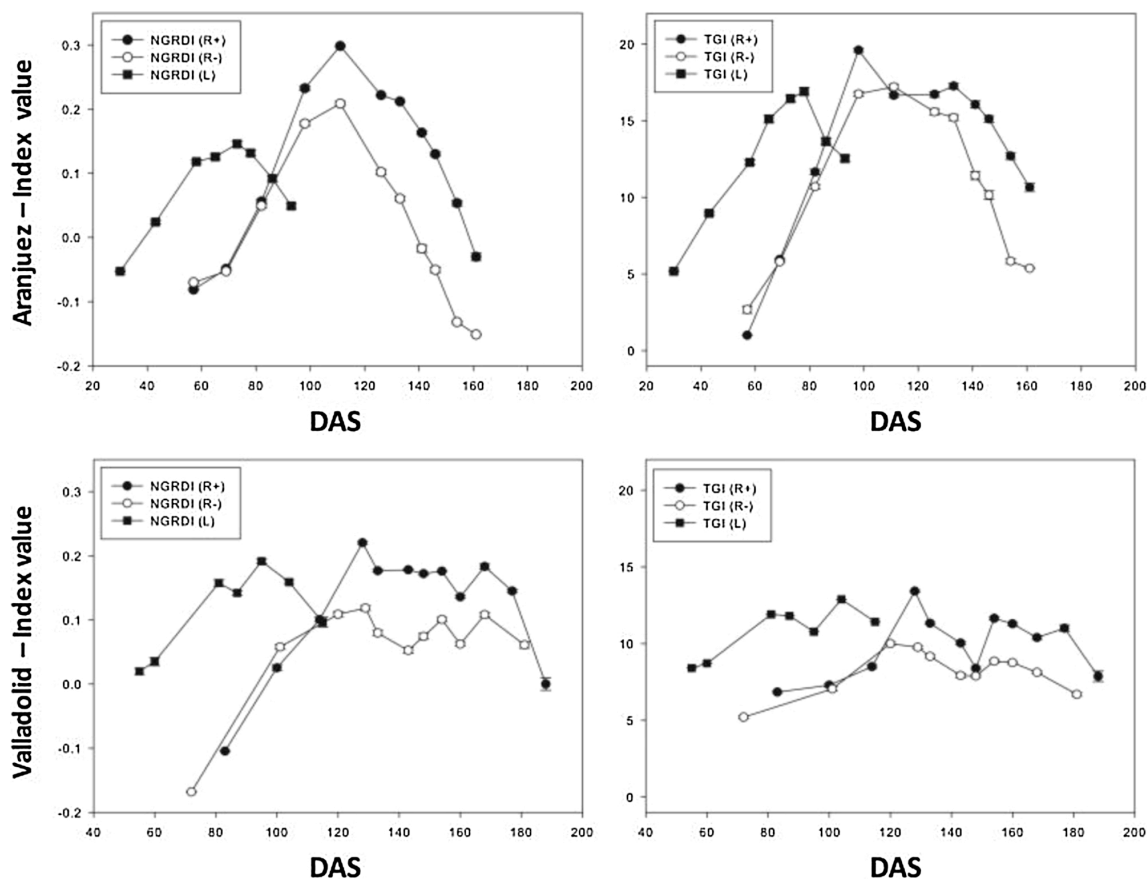


Fig. 4. Pattern of values of the NGRDI and TGI throughout the crop cycle measured in each of the six trials of the study. For each trial the values of all the plots were used to calculate the standard error. Days after sowing (DAS) was used to normalize the crop duration.

conditions in Aranjuez and Valladolid, respectively, while under support irrigation the yield increased to 4838 and 6937 Kg ha<sup>-1</sup>, respectively. In late planting the average values were 3779 and 5208 Kg ha<sup>-1</sup> (Supplementary Table 2).

### 3.1. RGB and NDVI vegetation indices

In general, the different RGB vegetation indices, particularly GA, and u<sup>\*</sup>v<sup>\*</sup>A, as well as the multispectral index NDVI followed a pattern similar to that of crop growth (Fig. 3). Values increased from the beginning, then reached a plateau from stem elongation to anthesis/early grain filling in the case of support irrigation and late planting trials or reached a maximum around anthesis in the rainfed trials, and then decreased. GGA showed similar patterns but with comparatively lower values. Values for these three indices ranged between 0 and 1. The NGRDI and TGI results as measured in support irrigation and rainfed trials also followed similar patterns of crop development, but only in the Aranjuez trials (Fig. 4). Values ranged from -0.2 to 0.3 and from 0 to 20 for the NGRDI and TGI, respectively.

### 3.2. Phenotypic correlation with grain yield within a trial

Predictions of grain yield based on the linear correlation between any of the vegetation indices and yield were evaluated for the 5 different RGB vegetation indices, measured during the crop growth, within each of the six different trials and additionally, NDVI was evaluated during the crop growth for Valladolid. Further, cross

validations were run. For supplemental irrigation and late planting, the most robust models between grain yield and the various vegetation indices were observed in the latest stages of the evaluation (around the second half of grain filling) with determination coefficient (R<sup>2</sup>) values around 0.6, while for rainfed trials the best performance was reached around heading, with R<sup>2</sup> values around 0.5 (Fig. 5; Supplementary File 1). Out of all the RGB indices, the GA, NGRDI and u<sup>\*</sup>v<sup>\*</sup>A reached the highest cross validation R<sup>2</sup> values across all growing conditions and experimental sites, while GGA and particularly the TGI showed lower R<sup>2</sup> (Fig. 5). Furthermore, we compared the performance of the indices formulated with uncalibrated images against that of calibrated images. In general, the determination coefficients between each calibrated and uncalibrated index were high (R<sup>2</sup> 0.91-0.99). The cross-validation results of RGB indexes calculated from calibrated images against grain yield, together with the broad sense heritability of the RGB indices formulated with calibrated images were lower than the case for the RGB indices derived from uncalibrated images (data not shown).

Concerning the NDVI measured in Valladolid station, under support irrigation, the NDVI achieved slightly higher cross validation R<sup>2</sup> values against grain yield than RGB indexes at around the second half of grain filling. In the case of rainfed, similar values were observed for NDVI and the RGB indexes. Finally, for late planting, the NDVI achieved a lower cross validation R<sup>2</sup> value than u<sup>\*</sup>v<sup>\*</sup>A, GA, NGRDI at around the second half of grain filling, whereas NDVI outperformed the RGB indices when measured around heading (Fig. 5).

R<sub>pred</sub><sup>2</sup> values obtained for the vegetation indices were comparable to the R<sup>2</sup> values obtained based on the training set (Fig. 5; Supplementary

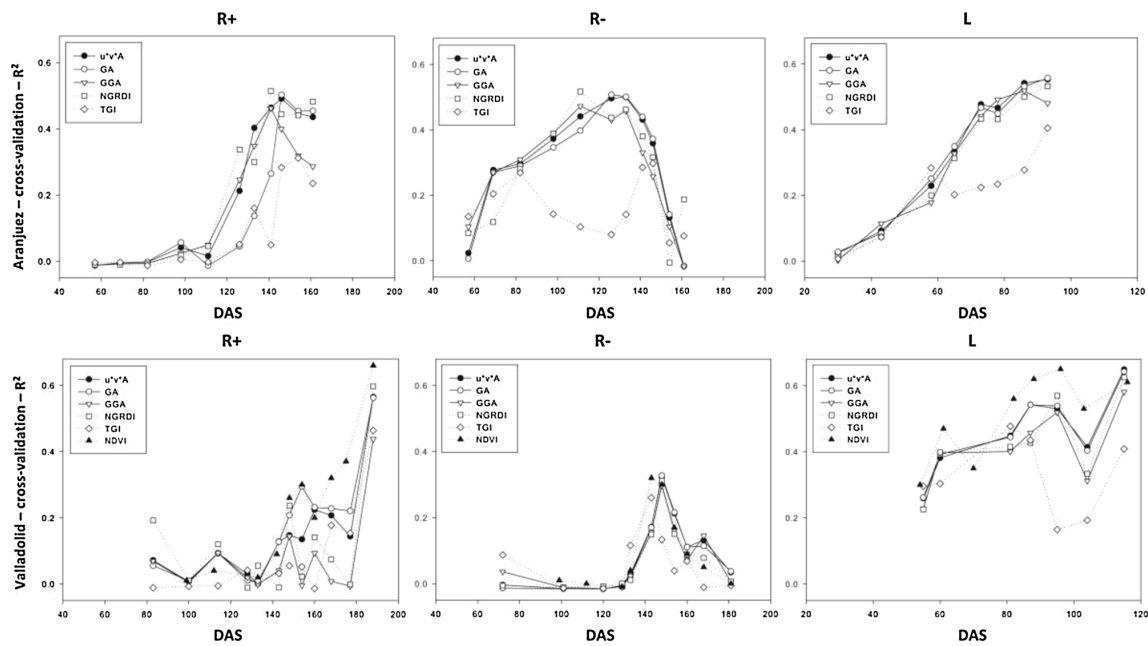


Fig. 5. Determination coefficient ( $R^2$ ) of the cross-validation results of the phenotypic correlations between a given vegetation index measured in a particular experimental site during the crop cycle against grain yield. Results are shown for the 6 trials included in the study. NDVI results are shown for Valladolid trials only. Days after sowing (DAS) was used to normalize the crop duration.

Fig. 1). The NGRDI achieved the highest cross validation  $R^2$  values a date of measurement before (during the crop cycle), compared with GA and  $u^*v^*A$  indices, particularly for Aranjuez in support irrigation and rainfed.

RMSE values were always higher in the Valladolid trials in the standard growing period but taking into consideration the larger range in yield in the genotypes at this location, the yield prediction was more precise than at Aranjuez (Supplementary File 1). In the late planting conditions, yield prediction based on the RMSE showed a slightly higher precision in the Aranjuez field trials (Supplementary File 1).

### 3.3. Heritability and genetic correlation

The strength of the genetic correlation of the vegetation indices with grain yield varied depending on the growing conditions and the vegetation index (Table 2). In terms of support irrigation, the highest determination coefficients were achieved at the early stages of crop growth (seedling emergence and tillering) and later during anthesis and grain filling, while for rainfed conditions the highest determination coefficients were reached at tillering and the beginning of stem elongation and further at heading and anthesis. In the case of late planting, the determination coefficients were in general higher than for the other two conditions and the highest values were achieved from tillering to heading. Except for a somewhat poorer performance from TGI, there was no clear trend in terms of the best performing vegetation index.

Broad sense heritability ( $h^2$ ) for yield and the different vegetation indices were calculated for each of the three different growing conditions (support irrigation, rainfed and late planting) including in each case the trials of the two sites. In the first two cases heritability for grain yield was moderate, while in late planting it increased markedly. In many cases vegetation indices achieved higher heritability estimates than yield for the three growing conditions. For both the support irrigation and the rainfed environments the highest heritabilities for vegetation indices were observed in the first part of the crop cycle, particularly during stem elongation and tillering; later heritabilities were also relatively high during grain filling (Table 2). For the late planting,

heritabilities of the vegetation indices increased progressively until heading and reached the maximum values during grain filling.

For each growing condition (rainfed, support irrigation and late planting) we compared the heritability of grain yield and the product between the heritability of a given vegetation index and the determination coefficient of the genetic correlation between this vegetation index and grain yield ( $r_A^2 \times h^2$ ). Regarding support irrigation,  $r_A^2 \times h^2$  for the  $u^*v^*A$  index measured at stem elongation had a higher value than the  $h^2$  of grain yield, while the values of NGRDI measured at milk stage were near to the  $h^2$  of grain yield (Fig. 6). For rainfed conditions, several indices exhibited a higher  $r_A^2 \times h^2$  product than the  $h^2$  of grain yield. This is the case for GGA measured at tillering, which exhibited the highest value, together with  $u^*v^*A$  measured at tillering and stem elongation, GA measured at tillering and stem elongation and TGI measured at stem elongation (Fig. 6). Regarding late planting, the  $u^*v^*A$  index reached its highest product value for  $r_A^2 \times h^2$ , followed by GA and GGA, but in all cases values were lower than the  $h^2$  of grain yield (Fig. 6).

### 4. Discussion

This study shows the use of RGB indices to assess grain yield is not just an affordable phenotyping approach by itself, but also allows other applications such as forecasting yield in advance. Predicting in advance the genotypic performance of grain yield also may have an economic impact in reducing the number of plots maintained to maturity and brought to grain harvest. Although we have calibrated the plot images using images of a colour chart acquired after taking the field measurements, it did not produce better cross-validation results, but rather the indices derived from corrected images tended to perform somewhat poorer. This may be due to the fact that under natural light conditions the RGB cameras have very few colour errors related with colour calibration (Penczek et al., 2014). Regarding the lower broad sense heritability of the indices derived from calibrated images, we consider this was because the result of using just one calibration image, rather than periodical calibration images intercalated during the plot image

**Table 2**  
Broad sense heritabilities ( $h^2$ ) of grain yield and the different vegetation indices evaluated within the three different growing conditions (support irrigation, rainfed and late planting) at two experimental stations (Aranjuez and Valladolid) during different crop stages (GS) following the Zadoks scale. In addition, the correlation coefficient  $\pm$  standard error ( $r_A \pm SE$ ) of the genetic correlations of the vegetation indices and grain yield are also included.

Irrigated	$h^2$ (grain yield)	Index	Seedling growth GS 15			Seedling growth GS 16-19			Tillering GS 20-27			Stem elongation GS 30-36			Stem elongation GS 37-39		
			$h^2$	$r_A \pm SE$	$h^2$	$r_A \pm SE$	$h^2$	$r_A \pm SE$	$h^2$	$r_A \pm SE$	$h^2$	$r_A \pm SE$	$h^2$	$r_A \pm SE$	$h^2$	$r_A \pm SE$	
Irrigated	0.45	$u^*v^*A$	0.80	0.19 $\pm$ 0.37	0.68	0.47 $\pm$ 0.39	0.82	0.55 $\pm$ 0.33	0.90	0.72 $\pm$ 0.28	0.30						
		GA	0.74	0.28 $\pm$ 0.38	0.69	0.47 $\pm$ 0.38	0.82	0.56 $\pm$ 0.33	0.90	0.72 $\pm$ 0.28	0.01						
		GGA	0.64	–	0.58	0.52 $\pm$ 0.43	0.83	0.51 $\pm$ 0.33	0.82	0.62 $\pm$ 0.34	0.52						
		NGRDI	0.60	0.60 $\pm$ 0.45	0.51	0.63 $\pm$ 0.46	0.82	0.61 $\pm$ 0.33	0.78	0.62 $\pm$ 0.34	0.73						
		TGI	0.55	0.59 $\pm$ 0.44	0.61	0.53 $\pm$ 0.42	0.35	0.24 $\pm$ 0.61	0.18	0.60 $\pm$ 1.03	0.54						
		Index															
Rainfed	$h^2$ (grain yield)	$u^*v^*A$	0.36	0.80 $\pm$ 0.61	0.64	0.47 $\pm$ 0.39	0.85	0.92 $\pm$ 0.40	0.77	0.72 $\pm$ 0.37	0.27						
		GA	0.66	0.71 $\pm$ 0.42	0.64	0.47 $\pm$ 0.38	0.83	0.91 $\pm$ 0.39	0.75	0.77 $\pm$ 0.39	0.13						
		GGA	0.00	–	0.58	0.52 $\pm$ 0.43	0.89	0.96 $\pm$ 0.40	0.79	0.64 $\pm$ 0.37	0.39						
		NGRDI	0.26	0.72 $\pm$ 0.84	0.40	0.63 $\pm$ 0.46	0.86	–	0.75	0.58 $\pm$ 0.39	0.17						
		TGI	0.54	0.53 $\pm$ 0.42	0.54	0.53 $\pm$ 0.42	0.39	0.24 $\pm$ 0.61	0.75	0.58 $\pm$ 0.39	0.08						
		Index															
Late planting	$h^2$ (grain yield)	$u^*v^*A$	0.32	0.66 $\pm$ 0.41	0.37	0.47 $\pm$ 0.39	0.37	0.57 $\pm$ 0.35	0.48	0.98 $\pm$ 0.19	0.58						
		GA	0.34	0.63 $\pm$ 0.39	0.36	0.47 $\pm$ 0.38	0.36	0.59 $\pm$ 0.35	0.46	0.98 $\pm$ 0.19	0.59						
		GGA	0.25	0.76 $\pm$ 0.55	0.31	0.52 $\pm$ 0.43	0.31	0.57 $\pm$ 0.38	0.45	0.95 $\pm$ 0.23	0.54						
		NGRDI	0.26	0.79 $\pm$ 0.53	0.29	0.64 $\pm$ 0.36	0.29	0.43 $\pm$ 0.44	0.36	0.93 $\pm$ 0.28	0.49						
		TGI	0.35	0.57 $\pm$ 0.38	0.34	0.64 $\pm$ 0.36	0.34	0.59 $\pm$ 0.37	0.41	0.85 $\pm$ 0.24	0.40						
		Index															
Irrigated	Stem elongation GS 37-39	$r_A \pm SE$	–	–	–	–	–	–	–	–	–	–	–	–	–		
		$h^2$	0.63 $\pm$ 0.36	0.42 $\pm$ 0.55	0.62	0.48 $\pm$ 0.39	0.75	0.24 $\pm$ 0.36	0.77	0.25 $\pm$ 0.36	0.84	0.42 $\pm$ 0.30	0.79	0.67 $\pm$ 0.27			
		Booting GS 41-47															
		$r_A \pm SE$	0.36 $\pm$ 0.70	0.65 $\pm$ 0.37	0.42	0.85 $\pm$ 0.45	0.24	0.29 $\pm$ 0.82	0.56	0.14 $\pm$ 0.53	0.36	1.05 $\pm$ 0.51	0.36	0.68 $\pm$ 0.37			
		$h^2$	0.39 $\pm$ 1.03	0.64 $\pm$ 0.37	0.45	0.84 $\pm$ 0.43	0.26	0.33 $\pm$ 0.77	0.56	0.17 $\pm$ 0.52	0.30	0.99 $\pm$ 0.45	0.30	0.69 $\pm$ 0.42			
		$r_A \pm SE$	0.32 $\pm$ 0.59	0.57 $\pm$ 0.45	0.31	0.72 $\pm$ 0.58	0.22	0.35 $\pm$ 0.84	0.56	0.45 $\pm$ 0.51	0.57	0.52 $\pm$ 0.47	0.57	0.31 $\pm$ 0.41			
	Rainfed	Booting GS 41-47	$r_A \pm SE$	–0.2 $\pm$ 1.46	0.25 $\pm$ 0.62	0.24	0.67 $\pm$ 0.71	0.07	0.49 $\pm$ 1.68	0.66	0.31 $\pm$ 0.45	0.46	0.89 $\pm$ 0.38	0.46	0.66 $\pm$ 0.31		
			$h^2$	0.42 $\pm$ 0.55	0.48 $\pm$ 0.39	0.75	0.24 $\pm$ 0.36	0.77	0.25 $\pm$ 0.36	0.84	0.42 $\pm$ 0.30	0.79	0.42 $\pm$ 0.30	0.79	0.67 $\pm$ 0.27		
			Booting GS 45-47														
			$r_A \pm SE$	0.76 $\pm$ 0.17	0.72 $\pm$ 0.16	0.67	0.73 $\pm$ 0.15	0.51	0.63 $\pm$ 0.26	0.67	0.72 $\pm$ 0.16	0.67	0.72 $\pm$ 0.16	0.67	0.72 $\pm$ 0.16		
			$h^2$	0.75 $\pm$ 0.19	0.73 $\pm$ 0.15	0.65	0.73 $\pm$ 0.15	0.43	0.63 $\pm$ 0.25	0.68	0.73 $\pm$ 0.15	0.68	0.73 $\pm$ 0.15	0.68	0.73 $\pm$ 0.15		
			$r_A \pm SE$	0.60 $\pm$ 0.26	0.73 $\pm$ 0.15	0.69	0.73 $\pm$ 0.15	0.56	0.56 $\pm$ 0.32	0.65	0.59 $\pm$ 0.21	0.65	0.59 $\pm$ 0.21	0.65	0.59 $\pm$ 0.21		
Late planting	Booting GS 45-47	$r_A \pm SE$	0.30 $\pm$ 0.42	0.65 $\pm$ 0.19	0.81	0.65 $\pm$ 0.19	0.56	0.37 $\pm$ 0.33	0.81	0.65 $\pm$ 0.19	0.81	0.65 $\pm$ 0.19	0.81	0.65 $\pm$ 0.19			
		$h^2$	0.60 $\pm$ 0.26	0.73 $\pm$ 0.15	0.62	0.73 $\pm$ 0.15	0.62	0.47 $\pm$ 0.28	0.69	0.73 $\pm$ 0.15	0.69	0.73 $\pm$ 0.15	0.69	0.73 $\pm$ 0.15			
		Booting GS 45-47															
		$r_A \pm SE$	0.76 $\pm$ 0.17	0.72 $\pm$ 0.16	0.67	0.73 $\pm$ 0.15	0.51	0.63 $\pm$ 0.26	0.67	0.72 $\pm$ 0.16	0.67	0.72 $\pm$ 0.16	0.67	0.72 $\pm$ 0.16			
		$h^2$	0.75 $\pm$ 0.19	0.73 $\pm$ 0.15	0.65	0.73 $\pm$ 0.15	0.43	0.63 $\pm$ 0.25	0.68	0.73 $\pm$ 0.15	0.68	0.73 $\pm$ 0.15	0.68	0.73 $\pm$ 0.15			
		$r_A \pm SE$	0.60 $\pm$ 0.26	0.73 $\pm$ 0.15	0.69	0.73 $\pm$ 0.15	0.56	0.56 $\pm$ 0.32	0.65	0.59 $\pm$ 0.21	0.65	0.59 $\pm$ 0.21	0.65	0.59 $\pm$ 0.21			

$G_{NEG}$ , negative genotypic variance value, missing values,  $0 > r_A > 1$ .

acquisition. The approach of using one calibration image doesn't take into account fast light changes in the field which actually might force the images to be wrongly calibrated from a single colour values. Therefore, we propose to use the automatic setting of the camera under natural light conditions.

The highest correlations of RGB indices with grain yield were observed when the canopy colour started to shift from green to yellow. In the rainfed trials this corresponded to post heading, when leaves below the penultimate leaf enter senescence, while in the less stressed conditions of supplemental irrigation the highest correlation indices occurred during grain filling. In the case of late planting under full irrigation, the behaviour was comparable to the normal planting under support irrigation. In fact, the different RGB vegetation indices share in common a capability to more or less distinguish the green colour from the other colours related to senescent leaves such as yellow, brown or grey, among others (Zaman-Allah et al., 2015). Interestingly, the differences in phenology across the set of durum wheat tested, in terms of date to heading, were minimal (Chairi et al., 2018). Therefore, genotypic differences in the pattern of changing canopy colour across the genotypes within each growing condition were not due to phenology but to the specific performance of the genotypes under each particular growing condition. At least for Aranjuez, the NGRDI achieved the highest cross validation  $R^2$  value a date of measurement before (during crop cycle) than GA and  $u^*v^*A$ , which may be due to the fact that the NGRDI is not prone to saturation (Elazab et al., 2016). Indeed, the GA and GGA indices have been reported as saturating earlier (Kefauver et al., 2015), which was observed in our study and was also the case with the  $u^*v^*A$  index. Therefore, compared to the response of the NGRDI, the saturating indices only capture genotypic differences in the greenest canopies when senescence is more advanced. In general, TGI was less correlated with grain yield than the other RGB indices, which may be due to TGI's lower sensitivity to green plant cover at the canopy scale in comparison to other RGB vegetation, even though it is more sensitive than other vegetation indices to chlorophyll content at leaf level (Hunt et al., 2014). The fact that the predicted  $R^2$  values were comparable to the cross validated  $R^2$  values obtained from the training set highlights the robustness of the identified correlations. For its part, in our study NDVI gave overall comparable results (or even slightly better), in terms of cross-validation  $R^2$  patterns, than the RGB indices. Even so there are still reasons for considering RGB images as a better alternative than the use of NDVI measured with affordable easy-to-handle spectroradiometer such is the case of the GreenSeeker. RGB cameras may be even cheaper than a low-cost spectroradiometer. Moreover RGB cameras are already incorporated in devices such as mobile phones, which makes the smartphone a very flexible alternative as a phenotyping platform as these images may be directly processed through mobile-installed apps (Araus and Kefauver, 2018). Moreover, the RGB images may provide additional information (besides the RGB indices) which is not captured by NDVI or other multispectral indices. For example from RGB images it is possible an automatic counting of seedling density (Liu et al., 2018) and ear density (Fernández-Gallego et al. 2018). Automatic determination of crop phenology stages such as dates of heading (Zhu et al., 2016) or even anthesis (Sadeghi-Tehran et al., 2017) is also possible from RGB images. Concerning the potential application of the cameras from smartphones our study tested two types of cameras: the first one is the Canon IXUS 310 HS camera (12-megapixel resolution and 6.16 x 4.62 mm sensor) and a very low price (less than 100 €). This camera has a 12-megapixel resolution and a small sensor size, which is comparable with those of mobile phone cameras. The second one, the Nikon D70 camera (6.1-megapixel resolution and 23.7 x 15.6 mm), has more professional sensor specifications and a medium price (around 300 €). We have obtained comparable results from both devices. That could contribute to move on into new applications using mobile phones to acquire and process information from the field using new technologies. Therefore, it is possible to use low-cost or small sensor sizes in the field with good accuracy for application

related with photosynthetic area assessment. We could conclude that devices with sensor size corresponding to mobile phone cameras or action cameras (GoPro) could be used for these applications. Thus, cameras devices, labor and computing steps could be developed in a low-cost way. Moreover, the images can be acquired by hand across the plots in a fraction of minute per plot.

Under normal planting conditions, and regardless of the water regime (rainfed or support irrigation), the strongest heritabilities ( $h^2$ ) and  $r_A^2 \times h^2$  values for the different vegetation indices were observed at early growth stages (Table 2; Fig. 6). In this case, the high  $r_A^2 \times h^2$

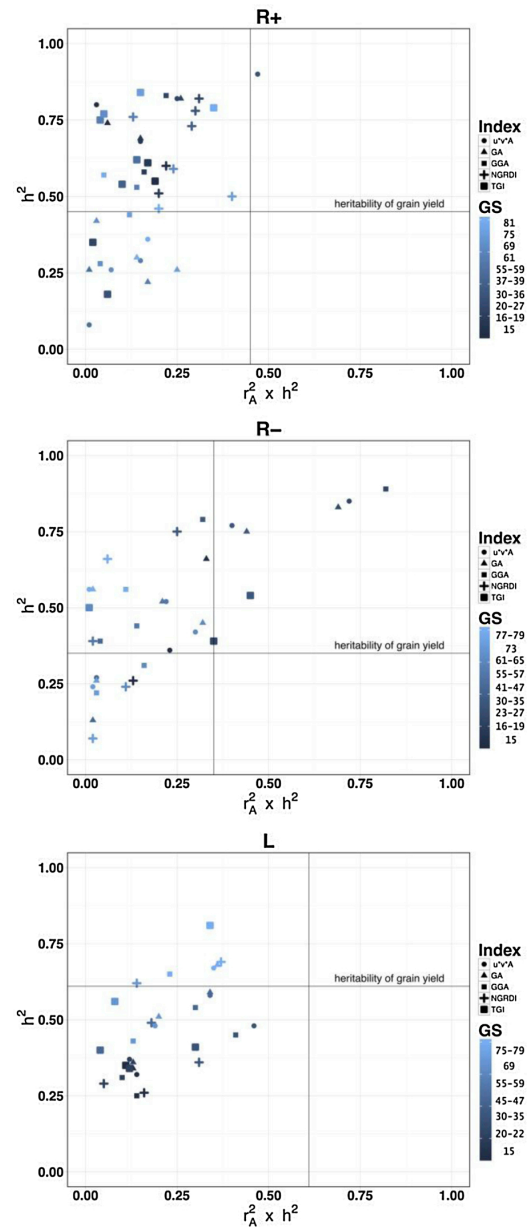


Fig. 6. Relationship between broad sense heritability ( $h^2$ ) for any of the vegetation indices and yield (vertical axis) and the product between the  $h^2$  of a given vegetation index and the determination coefficient of the genetic correlation ( $r_A^2$ ) between this vegetation index and grain yield ( $r_A^2 \times h^2$ ). Horizontal and vertical lines inside stand for the  $h^2$  of grain yield.

values are essentially due to the fact that the  $h^2$  values of the vegetation indices measured during early crop stages were much higher than the  $h^2$  for grain yield (Table 2). The high  $h^2$  values obtained for the indices during the early crop stages are in agreement with the fact that the pattern of crop establishment, particularly of soil covered by plants and tillering, is usually less dependent on environmental conditions than final grain yield (López-Castañeda et al., 1996; Rebetzke et al., 2004; Rebetzke and Richards, 1999). Therefore, the repeatability (which in fact is measured by  $h^2$ ) of early crop growth characteristics is higher than that of final grain yield. For several indices measured at the early stages of the crop cycle the value of the  $r_A^2 \times h^2$  product was higher than the  $h^2$  of grain yield (Fig. 6). This indicates that under normal planting conditions the indirect selection based on measuring a specific vegetation index at a given crop stage performs better than the direct selection based on the yield harvested (Richards et al., 2002).

In relation to the late planting trials grown under an intensive irrigation scheme, the  $h^2$  for grain yield was considerably higher than the  $h^2$  obtained for the normal planting date conditions grown under either rainfed or support irrigation (Table 2). However,  $h^2$  values for the different vegetation indices were lower, particularly in the early stages of the crop cycle (Table 2). This may be due to the fact that high temperature accelerates plant growth preventing the appearance of genotypic differences during crop establishment (Stone and Nicolas, 1995). Under that particular growing condition, the value of the  $r_A^2 \times h^2$  product was always lower than the  $h^2$  of the yield itself (Fig. 6). Despite this situation, indirect selection may still have provided the benefit of its lower cost and higher throughput via measurement of a specific RGB vegetation index at a certain moment during the crop cycle, rather than having to wait until maturity to harvest the crop. The cost per breeding plot of the whole harvesting process (until getting the yields) may go easily beyond € 15, plus the cost of maintaining the crop until maturity. By contrast the evaluation at ground level done by hand by walking through the plots takes a fraction of minute, which means that one worker provided with a camera may even record thousands of plots in a day. Further data processing via open source software only requires a few more minutes. The savings in cost and time will allow breeders to increase selection intensity, thus allowing greater genetic gains to be obtained (Araus et al., 2018; Araus and Kefauver, 2018).

## 5. Conclusions

Conventional cameras can be used to assess grain yield in durum wheat via RGB indices for yield prediction or screening purposes using a robust statistical approach. Changes in the colour of the canopy from green to yellow provide the best information on grain yield and early stages present better heritabilities ( $h^2$ ) and  $r_A^2 \times h^2$  values in normal planting conditions and, in the case of late planting, these values were better during the late stages.

Given that until now most HPT techniques are costly, and thus affordable by only a few research teams or breeding programs, the method tested in this study will serve as a cost efficient, easy-to-use alternative while maintaining high precision.

## Acknowledgments

The authors of this research would like to thank the field management staff at the experimental stations of Colmenar de Oreja (Aranjuez) of the Instituto Nacional de Investigación y Tecnología Agraria y Alimentaria (INIA) and Zamadueñas (Valladolid) of the Instituto de Tecnología Agraria de Castilla y León (ITACyL) for their continued support of our research. This work was supported by MINECO, Spain [project number AGL2016-76527-R] as the primary funding support for the research project; and the project “Formación de Talento Humano de Alto Nivel” [project number BPIN 2013000100103] approved by the “Fondo de Ciencia, Tecnología e Innovación”, from the “Sistema General de Regalías”, “Gobernación del Tolima - Universidad del

Tolima, Colombia” as the sole funding source of the first author JAF. JLA acknowledges the support from ICREA Academia, Generalitat de Catalunya, Spain.

## Appendix A. Supplementary data

Supplementary material related to this article can be found, in the online version, at doi:<https://doi.org/10.1016/j.eja.2019.02.007>.

## References

- Araus, J.L., Kefauver, S.C., 2018. Breeding to adapt agriculture to climate change: affordable phenotyping solutions. *Curr. Opin. Plant Biol.* <https://doi.org/10.1016/j.pbi.2018.05.003>.
- Araus, J.L., Kefauver, S.C., Zaman-Allah, M., Olsen, M.S., Cairns, J.E., 2018. Translating high-throughput phenotyping into genetic gain. *Trends Plant Sci.* <https://doi.org/10.1016/j.tplants.2018.02.001>.
- Bai, X.D., Cao, Z.G., Wang, Y., Yu, Z.H., Zhang, X.F., Li, C.N., 2013. Crop segmentation from images by morphology modeling in the CIE L\*a\*b\* color space. *Comput. Electron. Agric.* 99, 21–34. <https://doi.org/10.1016/j.compag.2013.08.022>.
- Bai, X., Cao, Z., Wang, Y., Yu, Z., Hu, Z., Zhang, X., Li, C., 2014. Vegetation segmentation robust to illumination variations based on clustering and morphology modelling. *Biosyst. Eng.* 125, 80–97. <https://doi.org/10.1016/j.biosystemseng.2014.06.015>.
- Burton, G.J., Moorhead, I.R., 1987. Color and spatial structure in natural scenes. *Appl. Opt.* 26, 157. <https://doi.org/10.1364/AO.26.000157>.
- Casadesús, J., Villegas, D., 2014. Conventional digital cameras as a tool for assessing leaf area index and biomass for cereal breeding. *J. Integr. Plant Biol.* 56, 7–14. <https://doi.org/10.1111/jipb.12117>.
- Casadesús, J., Kaya, Y., Bort, J., Nachit, M.M., Araus, J.L., Amor, S., Ferrazzano, G., Maalouf, F., Maccaferri, M., Martos, V., Ouabou, H., Villegas, D., 2007. Using vegetation indices derived from conventional digital cameras as selection criteria for wheat breeding in water-limited environments. *Ann. Appl. Biol.* 150, 227–236. <https://doi.org/10.1111/j.1744-7348.2007.00116.x>.
- Chairi, F., Vergara-Díaz, O., Vatter, T., Aparicio, N., Nieto-Taladriz, M.T., Kefauver, S.C., Bort, J., Serret, M.D., Araus, J.L., 2018. Post-green revolution genetic advance in durum wheat: the case of Spain. *F. Crop. Res.* 228, 158–169. <https://doi.org/10.1016/j.fcr.2018.09.003>.
- Draper, N.R., Smith, H., 1998. *Applied Regression Analysis*. John Wiley & Sons, Inc, Hoboken, NJ, USA. <https://doi.org/10.1002/9781118625590>.
- Elazab, A., Ordóñez, R.A., Savin, R., Slafer, G.A., Araus, J.L., 2016. Detecting interactive effects of N fertilization and heat stress on maize productivity by remote sensing techniques. *Eur. J. Agron.* 73, 11–24. <https://doi.org/10.1016/j.eja.2015.11.010>.
- Falconer, D.S., Mackay, F.C., 1996. *Introduction to Quantitative Genetics*, 4th ed. Pearson, Essex, England.
- FAO, IFAD, WFP, 2014. *The State of Food Insecurity in the World*. Food and Agriculture Organization of the United Nations, Rome.
- Gracia-Romero, A., Kefauver, S.C., Vergara-Díaz, O., Zaman-Allah, M.A., Prasanna, B.M., Cairns, J.E., Araus, J.L., 2017. Comparative performance of ground vs. aerially assessed RGB and multispectral indices for early-growth evaluation of maize performance under phosphorus fertilization. *Front. Plant Sci.* 8, 1–13. <https://doi.org/10.3389/fpls.2017.02004>.
- Gujjarro, M., Pajares, G., Riomoros, I., Herrera, P.J., Burgos-Artizzu, X.P., Ribeiro, A., 2011. Automatic segmentation of relevant textures in agricultural images. *Comput. Electron. Agric.* 75, 75–83. <https://doi.org/10.1016/j.compag.2010.09.013>.
- Hunt, E.R., Cavigelli, M., Daughtry, C.S.T., McMurtrey, J.E., Walthall, C.L., 2005. Evaluation of digital photography from model aircraft for remote sensing of crop biomass and nitrogen status. *Precis. Agric.* 6, 359–378. <https://doi.org/10.1007/s11119-005-2324-5>.
- Hunt, E.R., Daughtry, C.S.T., Eitel, J.U.H., Long, D.S., 2011. Remote sensing leaf chlorophyll content using a visible band index. *Agron. J.* 103, 1090–1099. <https://doi.org/10.2134/agronj2010.0395>.
- Hunt, E.R., Doraiswamy, P.C., McMurtrey, J.E., Daughtry, C.S.T., Perry, E.M., Akhmedov, B., 2013. A visible band index for remote sensing leaf chlorophyll content at the canopy scale. *Int. J. Appl. Earth Obs. Geoinf.* 21, 103–112. <https://doi.org/10.1016/j.jag.2012.07.020>.
- Hunt, E.R., Daughtry, C.S.T., Mirsky, S.B., Hively, W.D., 2014. Remote sensing with simulated unmanned aircraft imagery for precision agriculture applications. *IEEE J. Sel. Top. Appl. Earth Obs. Remote Sens.* 7, 4566–4571. <https://doi.org/10.1109/JSTARS.2014.2317876>.
- Jannoura, R., Brinkmann, K., Uteau, D., Bruns, C., Joergensen, R.G., 2015. Monitoring of crop biomass using true colour aerial photographs taken from a remote controlled hexacopter. *Biosyst. Eng.* 129, 341–351. <https://doi.org/10.1016/j.biosystemseng.2014.11.007>.
- Judd, D.B., Wyszecki, G., 1967. *Color in Business, Science, and Industry*, 2nd ed. John Wiley & Sons. John Wiley & Sons.
- Kefauver, S.C., El-Haddad, G., Vergara-Díaz, O., Araus, J.L., 2015. RGB picture vegetation indexes for high-throughput phenotyping platforms (HTPPs). In: Neale, C.M.U., Maltese, A. (Eds.), *Remote Sensing for Agriculture, Ecosystems, and Hydrology XVII*. SPIE, pp. 9. <https://doi.org/10.1117/12.2195235>. Proceedings.
- Kefauver, S.C., Vicente, R., Vergara-Díaz, O., Fernandez-Gallego, J.A., Kerfal, S., Lopez, A., Melichar, J.P.E., Serret Molins, M.D., Araus, J.L., 2017. Comparative UAV and field phenotyping to assess yield and nitrogen use efficiency in hybrid and

- conventional barley. *Front. Plant Sci.* 8, 1–15. <https://doi.org/10.3389/fpls.2017.01733>.
- Kefauver, S.C., Kerfal, S., Fernandez-Gallego, J.A., El-Haddad, G., Araus, J.L., 2018. CerealScanner. [WWW Document]. URL. <https://integrativecropphysiology.com/software-development/cerealscanner/>.
- Liu, T., Yang, T., Li, C., Li, R., Wu, W., Zhong, X., Sun, C., Guo, W., 2018. A method to calculate the number of wheat seedlings in the 1st to the 3rd leaf growth stages. *Plant Methods* 14, 1–14. <https://doi.org/10.1186/s13007-018-0369-5>.
- López-Castañeda, C., Richards, R.A., Farquhar, G.D., Williamson, R.E., 1996. Seed and seedling characteristics contributing to variation in early vigor among temperate cereals. *Crop Sci.* 36, 1257. <https://doi.org/10.2135/cropsci1996.0011183X003600050031x>.
- Lynch, M., Walsh, B., 1998. *Genetics and Analysis of Quantitative Traits*, 1998. Sinauer Associates, Sunderland, MA.
- Malacara, D., 2011. Uniform color systems. *Color Vision and Colorimetry: Theory and Applications*, second edition. SPIE, 1000 20th Street, Bellingham, WA 98227-0010 USA, pp. 103–129. <https://doi.org/10.1117/3.881172.ch6>.
- Pask, A., Pietragalla, J., Mullan, D., Reynolds, M. (Eds.), 2012. *Physiological Breeding II: A Field Guide to Wheat Phenotyping*. CIMMYT, Mexico D.F.
- Penczek, J., Boynton, P.A., Splett, J.D., 2014. Color error in the digital camera image capture process. *J. Digit. Imaging* 27, 182–191. <https://doi.org/10.1007/s10278-013-9644-1>.
- Rebetzke, G.J., Richards, R.A., 1999. Genetic improvement of early vigour in wheat. *Aust. J. Agric. Res.* 50, 291. <https://doi.org/10.1071/A98125>.
- Rebetzke, G., Botwright, T., Moore, C., Richards, R., Condon, A., 2004. Genotypic variation in specific leaf area for genetic improvement of early vigour in wheat. *Food Crop. Res.* 88, 179–189. <https://doi.org/10.1016/j.fcr.2004.01.007>.
- Richards, R.A., Rebetzke, G.J., Condon, A.G., van Herwaarden, A.F., 2002. Breeding opportunities for increasing the efficiency of water use and crop yield in temperate cereals. *Crop Sci.* 42, 111. <https://doi.org/10.2135/cropsci2002.0111>.
- Robertson, A.R., 1977. The CIE 1976 color-difference formulae. *Color Res. Appl.* 2, 7–11. <https://doi.org/10.1002/j.1520-6378.1977.tb00104.x>.
- Sadeghi-Tehran, P., Sabermanesh, K., Virlet, N., Hawkesford, M.J., 2017. Automated method to determine two critical growth stages of wheat: heading and flowering. *Front. Plant Sci.* 8, 1–14. <https://doi.org/10.3389/fpls.2017.00252>.
- Schlaepfer, D.R., Bradford, J.B., Lauenroth, W.K., Munson, S.M., Tietjen, B., Hall, S.A., Wilson, S.D., Duniway, M.C., Jia, G., Pyke, D.A., Lkhagva, A., Jamiyansharav, K., 2017. Climate change reduces extent of temperate drylands and intensifies drought in deep soils. *Nat. Commun.* 8, 14196. <https://doi.org/10.1038/ncomms14196>.
- Schneider, C.A., Rasband, W.S., Eliceiri, K.W., 2012. NIH Image to ImageJ: 25 years of image analysis. *Nat. Method* 9, 671–675.
- Stone, P., Nicolas, M., 1995. A survey of the effects of high temperature during grain filling on yield and quality of 75 wheat cultivars. *Aust. J. Agric. Res.* 46, 475. <https://doi.org/10.1071/AR9950475>.
- Susstrunk, S., Buckley, R., Swen, S., 1999. Standard RGB color spaces. *7th Color and Imaging Conference Final Program and Proceedings* 127–134.
- Vergara-díaz, O., Zaman-Allah, M.A., Masuka, B., Hornero, A., Zarco-Tejada, P., Prasanna, B.M., Cairns, J.E., Araus, J.L., 2016. A novel remote sensing approach for prediction of maize yield under different conditions of nitrogen fertilization. *Front. Plant Sci.* 7, 1–13. <https://doi.org/10.3389/fpls.2016.00666>.
- Wang, Y., Wang, D., Zhang, G., Wang, J., 2013. Estimating nitrogen status of rice using the image segmentation of G-R thresholding method. *Field Crops Res.* 149, 33–39.
- Woebecke, D.M., Meyer, G.E., Von Bargen, K., Mortensen, D.A., 1993. Plant species identification, size, and enumeration using machine vision techniques on near-binary images. DeShazer, J.A., Meyer, G.E. (Eds.), *Proc. SPIE 1836, Optics in Agriculture and Forestry*. International Society for Optics and Photonics 208–219. <https://doi.org/10.1117/12.144030>.
- Zadoks, J., Chang, T., Konzak, C., 1974. A decimal growth code for the growth stages of cereals. *Weed Res.* 14, 415–421.
- Zaman-Allah, M., Vergara, O., Araus, J.L., Tareknege, A., Magorokosho, C., Zarco-Tejada, P.J., Hornero, A., Albà, A.H., Das, B., Craufurd, P., Olsen, M., Prasanna, B.M., Cairns, J., 2015. Unmanned aerial platform-based multi-spectral imaging for field phenotyping of maize. *Plant Methods* 11, 35. <https://doi.org/10.1186/s13007-015-0078-2>.
- Zhou, B., Elazab, A., Bort, J., Vergara, O., Serret, M.D., Araus, J.L., 2015. Low-cost assessment of wheat resistance to yellow rust through conventional RGB images. *Comput. Electron. Agric.* 116, 20–29. <https://doi.org/10.1016/j.compag.2015.05.017>.
- Zhu, Y., Cao, Z., Lu, H., Li, Y., Xiao, Y., 2016. In-field automatic observation of wheat heading stage using computer vision. *Biosyst. Eng.* 143, 28–41. <https://doi.org/10.1016/j.biosystemseng.2015.12.015>.

## Low-cost assessment of grain yield in durum wheat using RGB images

Jose A. Fernandez-Gallego<sup>1,2,3</sup>, Shawn C. Kefauver<sup>1,2</sup>, Thomas Vattera<sup>3</sup>, Nieves Aparicio Gutiérrez<sup>4</sup>, María Teresa Nieto-Taladriz<sup>5</sup>, José Luis Araus<sup>1,2</sup>

Supplemental material:

## Low-cost assessment of grain yield in durum wheat using RGB images

Jose A. Fernandez-Gallego, Shawn C. Kefauver, Thomas Vatter, Nieves Aparicio

Gutiérrez, María Teresa Nieto-Taladriz, José Luis Araus

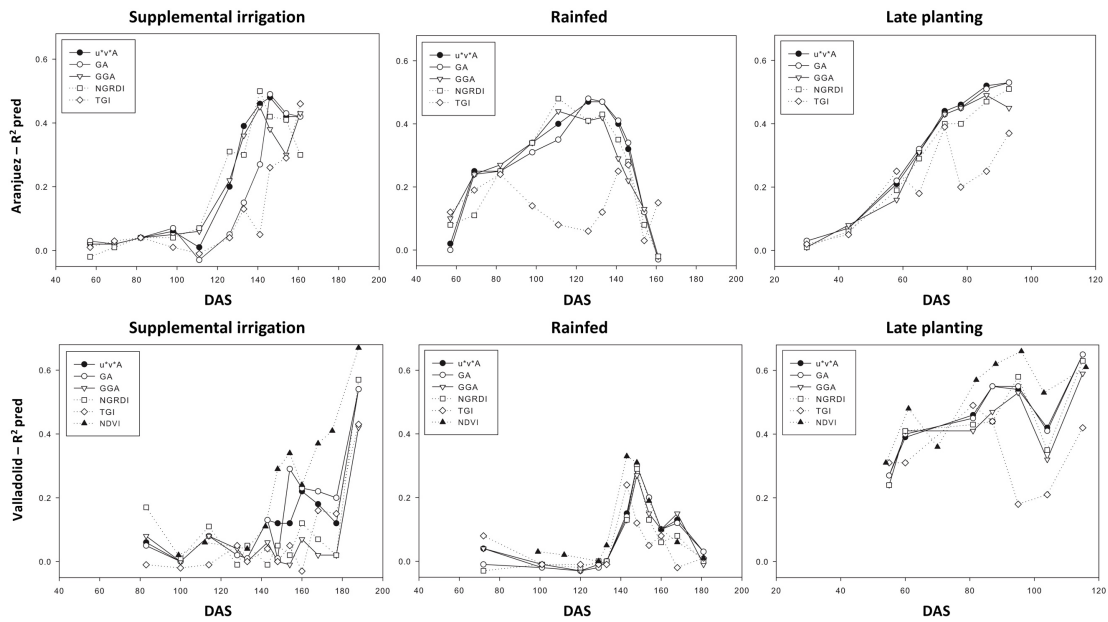


Fig. S1. Predictive ability  $R^2_{pred}$  of the model for yield for each vegetation index, based on the regression estimates, estimated using the training set.



## Low-cost assessment of grain yield in durum wheat using RGB images

Jose A. Fernandez-Gallego, Shawn C. Kefauver, Thomas Vatter, Nieves Aparicio

Gutiérrez, María Teresa Nieto-Taladriz, José Luis Araus

Support irrigation Valladolid			Rainfed Valladolid			Late planting Valladolid		
GS	DAS	CD	GS	DAS	CD	GS	DAS	CD
16-19	99	08/03	16-19	99	8/03	15	53	04/04
23-27	112	21/03	23-27	112	21/03	20-22	60	11/04
37-39	133	11/04	30-35	129	07/04	23-27	69	20/04
45-47	142	20/04	36-37	133	11/04	30-35	81	02/05
52	148	26/04	41-47	143	21/04	45-47	87	08/05
55-59	154	02/05	55-57	148	26/04	55-59	95	16/05
61	160	08/05	61-65	154	02/05	69	104	23/05
69	168	16/05	69	160	08/05	75-79	117	05/06
75	177	23/05	73	168	16/05			
81	188	05/06	77-79	181	29/06			

**Supplementary Table 1.** NDVI measurement summary for Valladolid experimental site the growing conditions and the measurement dates, expressed as calendar date (CD) and number of days after sowing (DAS), and corresponding growth stage (GS) expressed in the Zadoks growth scale.

## Low-cost assessment of grain yield in durum wheat using RGB images

Jose A. Fernandez-Gallego, Shawn C. Kefauver, Thomas Vatter, Nieves Aparicio

Gutiérrez, María Teresa Nieto-Taladriz, José Luis Araus

Experimental station	Trial	Mean	Min.	Max.
Aranjuez	Support irrigation	4838	3463	6030
	Rainfed	2735	1607	3583
	Late sowing	3779	2947	5057
Valladolid	Support irrigation	6937	5919	7811
	Rainfed	2783	1713	3787
	Late sowing	5208	4085	7133

**Supplementary Table 2.** Grain yield for each of the three trials of Aranjuez and Valladolid stations. Mean values for the entire trial and minimum and maximum values of single plots ( $\text{kg ha}^{-1}$ )







## GENERAL DISCUSSION

Image processing techniques for plant phenotyping have been used from acquisition to classifications tasks; under field conditions, it was mainly studied for difficult changing sunlight and shadow conditions, and isolation of plants and organs within the image (Kelly et al., 2015; L. Li et al., 2014). These techniques can be used for plant phenotyping through different types of platforms equipped with visual, multispectral and hyperspectral cameras (Fahlgren et al., 2015). Moreover, different types of machine learning techniques can be developed for segmentation and discriminations tasks instead of human eye inspection (Gori, 2018). Depending on the phenological stage and the sensor technology (or the human eye inspection), many phenotypic traits can be assessed such as plant density, ear density, ear temperature, cover fraction, peduncle length, awn length, plant height, leaf size, leaf rolling, weed inspection, lodging, weed infestation, chlorophyll content, and many others (Araus et al., 2018; Pask et al., 2012). Image processing systems must adapt to the field conditions to contribute to the extraction of comparable traits from crops in order to move toward the high throughput plant phenotyping (HTPP) improvement. The correct balance in acquisition technology, data processing strategy and phenological stage selection would seem to be the best way forward. The optimal daytime and light conditions must be taken into account for each sensor technology and application. We have used the Zadoks scale to recognize the phenological stage by growth stage (GS) codes from GS 00 to GS 99; which corresponded to germination/dry seed (GS 00) and ripening/secondary dormancy lost (GS 99) (Zadoks et al., 1974).

This work has mainly considered the assessment of two traits (i) ear density and (ii) photosynthetic area of the canopy. Even though the image processing systems were tested principally for wheat, many of the techniques can be used for other crops, and have been particularly extended and tested for barley.

## **1. Ear counting using image processing systems**

For ear density, we have developed ear counting systems for ground and aerial platforms using RGB and thermal imagery under low- and high-resolution imaging conditions. These systems were designed for field data acquisition experiences and specific image characteristics. The validation was performed primarily using image-based data.

### **Ear counting using RGB imagery**

We proposed the use RGB images acquired using a simple method holding the camera by hand at around 1 m (ground platform, in Chapter 1 and Chapter 2), and also using a more complex method mounting the camera on a drone at around 25 m a.g.l. (aerial platform, in Chapter 3). In both cases, we could observe similar limitations and requirements due to the visual wavelength characteristics such as shadows and bright surfaces and overlapping ears. Sunlight reflections on leaves could be one of the most important limitation for the automatic ear counting systems proposed. On the one hand, with the ground platform the sunlight reflections are similar to ears into the image, and additionally, the image processing system used local peaks (based mainly on the bright color information) as the principal characteristic to isolate ears from leaves and unwanted objects. For those reasons, ears and sunlight reflections may be

confused with each other. On the other hand, from the aerial platform the sunlight reflects off of bending leaves under direct sunlight conditions, and also the low spatial resolution did not allow for correct visual differentiation between ears and leaves using orthomosaic images. Despite these limitations, both the automatic ear counting systems have achieved high accuracy (e.g.  $R^2 = 0.75$  and  $R^2 = 0.89$ ; using ground and aerial platforms, best results respectively). In both platforms we further improved the system; in the first one, we added the training and classifying step (Chapter 3) in order to increase the robustness of the image processing system; and in the second one, we employed a higher resolution RGB camera (and lower flight altitude) in order to increase the number of matching features found from the Structure from Motion (SfM) process used to build the orthomosaic with higher spatial resolution (Aasen et al., 2018).

### **Ear counting using thermal imagery**

We purposed the use of thermal images acquired holding the thermal camera by hand at approximately 1 m (ground platform, in Chapter 4) above the canopy surface. We also observed some limitations using this data such as low spatial resolution, no temperature differences between canopy and ears (depending on the acquisition time) and overlapping ears. Low spatial resolution was identified the most important limitation for the proposed automatic ear counting system. Thermal imagery can avoid shadows and bright surfaces (the main RGB limitation); and moreover, thermal images filter high frequency details intrinsically due to the manner in which this technology detects much longer wavelength radiation emissions. In that way, these images are less sensitive to overlapping and provide enhanced information towards differentiating ears from



leaves which in turn contributes to simplify the image processing tasks. However, its low spatial resolution is still a major issue and this technology sensor cannot yet be used from an aerial platform for this reason. On the other hand; for the development of the thermal ear counting algorithm, visual interpretation of RGB images (RGB images acquired at the same time as the thermal images) was crucial in correctly locating the presence of ears in thermal images. Despite these limitations, the thermal image based automatic ear counting systems have achieved high accuracy ( $R^2 = 0.80$ ) (Fernandez-Gallego et al., 2019a). This system may furthermore be improved using a thermal and RGB fusion sensor to be able to increase the spatial resolution in order to cover more footprint area at higher distances.

### **1.1. Phenological stage and data acquisition time for ear density**

The ear density trait can be estimated from anthesis to late grain filling using RGB and thermal imagery (Chapter 1, Chapter 2, Chapter 3 and Chapter 4). At late grain filling in the rainfed trial (near to maturity), the ground level algorithm did not perform as well in ear identification ( $R^2 = 0.17$ , GS 91) when automatic and manual image-based counting were compared. The late growth stage did not permit consistent ear identification due to the lack of contrast between the leaves and ears. However, from anthesis (support irrigation and rainfed) to late grain filling (support irrigation) the approach had good accuracy. Even under low resolution scenarios the determination coefficient was higher at late grain filling under support irrigation ( $R^2 = 0.75$ , GS 81) than anthesis under support irrigation and rainfed ( $R^2 = 0.62$ , GS 61-65,  $R^2 = 0.51$ , GS 61-65), respectively, when automatic and manual image-based counting were compared. This comparison

at late grain filling using the aerial level algorithm could not be done, this was mainly due to sunlight/sunlint and resolution issues (Ortega-Terol et al., 2017). However, the determination coefficient was also higher at a later stage in the aerial data in the same way as the ground data - the correlation at grain filling ( $R^2 = 0.89$ , GS 75) was higher than at the anthesis ( $R^2 = 0.83$ , GS 61) growth stage. Using thermal imagery, the determination coefficients performed almost the same, although we compared growth stages between experimental stations instead of use the same site. The determination coefficient was higher at grain filling in Seville ( $R^2 = 0.76$ , GS 69; *unpublished results*) than anthesis in Aranjuez ( $R^2 = 0.65$ , GS 61-65; *unpublished results*); but the correlation decreased at late grain filling in Valladolid ( $R^2 = 0.70$ , GS 77; *unpublished results*) compared with grain filling in Seville (shown above) when automatic and manual image-based counting were compared.

## **1.2. Ear density trait and grain yield**

The ear counting systems in field conditions (including also manual in-situ counting) has shown low correlation with GY when all data plots were used in cross-validated linear regression (LR) models. Using ground scale images (Chapter 1 and Chapter 2), the automatic ear counting system achieved relatively low correlation with GY ( $R^2 = 0.30$ ), yet it was higher than the manual in-situ counting ( $R^2 = 0.24$ ) when compared to GY. In the same way when using aerial images (Chapter 3), the automatic ear counting system also achieved low correlation ( $R^2 = 0.28$ ) with grain yield, and also for this platform, it was higher than the manual in-situ counting ( $R^2 = 0.02$ ) when compared with GY. Two main explanations have been presented, (a) dynamic compensation mechanisms

between the ear density and number of kernels per ear (Slafer et al., 2014; Slafer and Savin, 2007); and (b) hidden ears, due to zenithal images only consider the upper ears which frequently correspond to the main and primary tillers (Ishag and Taha, 1974). On the other hand, when genotyping (G), nitrogen (N) fertilization, and G + N effects were included in cross-validated multiple linear regression (MLR) models; the relationship between ear counting (automatic and manual counting) and GY increased. Best predictions ( $R^2 = 0.41-0.46$ ) were achieved when G + N effects were included, followed by N ( $R^2 = 0.34-0.36$ ) and G ( $R^2 = 0.06-0.20$ ) effects; which suggest that the relationship between ear density and GY is more supported by the N treatment factors than genotypic differences. Additionally, grouping by N treatment and using a LR model, the best relationship ( $R^2 = 0.46$ ) was achieved for the lower N treatment, it may observations that, at lower N levels, the contribution of secondary and tertiary tillers to GY is usually minor if not negative. In summary, the automatic ear density can explain around 30% (under different nitrogen treatment) (Fernandez-Gallego et al., 2019b, 2018a) and around 50% (under low N conditions) of the variability in yield (Fernandez-Gallego et al., paper under review). This system could be improved using 3-dimensional data to assess the ear size/volume.

## **2. Photosynthetic area of the canopy using image processing systems**

Regarding RGB indexes, we have proposed the novel vegetation index  $u^*v^*A$  to estimate the green canopy area associated with the photosynthetic area of the canopy (Chapter 5). This index has shown good performance even though a conventional camera with very low resolution and very small size sensor was used. The Canon IXUS 310 HS camera (12-megapixel resolution, 6.16 x 4.62mm

sensor size and price less than 100 €) achieved comparable results to those obtained with the Nikon D70 camera (6.1-megapixel resolution, 23.7 x 15.6 mm sensor size and price around 300 €) and a hand-held portable spectroradiometer (GreenSeeker, price around 500 €). This contributes to the move towards the use of low-cost and small sized sensors such as action cameras (GoPro) or mobile phone cameras. On the other hand, the approach of using the color calibration experiment with a color chart (the ColorChecker Passport, in Chapter 5) did not improve the results. At the beginning of the experiment, we assumed that this step would improve the information provided by the RGB sensor and therefore we would have better data; nevertheless, the color information did not change, we had very high determination coefficient ( $R^2 \approx 0.98$ ) between the RGB indexes derived from the calibrated and un-calibrated images, at least for the acquired database of 4,140 images taken at ground level. Moreover, this calibrated images (when the RGB indexes were used for GY prediction) tended to perform somewhat poorer; this is maybe because we have only used one calibration image (taken at the beginning of each block), and single image doesn't take into account fast light changes in the field which actually might force the images to be wrongly calibrated from a single color values. Besides the fact that under natural light conditions the RGB cameras have very few color errors related with color calibration (Penczek et al., 2014). Furthermore, the  $u^*v^*A$  index force the hue and chroma values to be dependent to the luminance ( $L^*$ ) and contribute to the reduction of the color perception problems caused by natural light changes; in that way, green pixels from the canopy can be better interpreted due to color differences are more difficult to perceive when luminance decreases (Malacara, 2011), mainly in cases such as variable light conditions, overlapping ears and

shadows. Therefore, we proposed to take more periodical calibration images intercalated during the plot image acquisition or; in a simpler way, to use the automatic setting of the camera under natural light conditions.

## **2.1. Phenological stage and data acquisition time for photosynthetic area of the canopy**

The photosynthetic area trait can be estimated from seedling growth (GS 10) to late grain filling (GS 99). Although in general, the area indexes ( $u \cdot v \cdot A$ , GA, GGA) and Normalized Difference Vegetation Index (NDVI) followed a pattern similar to that of crop growth in both experimental stations; the NGRDI, TGI indexes only followed this pattern in one of them (Chapter 5). This may be due to NGRDI and TGI are more related with the nutrient status and crop biomass; and chlorophyll concentration, respectively; than photosynthetic area estimation (Hunt et al., 2014, 2013, 2011, 2005; Jannoura et al., 2015). However, the NGRDI index achieved the highest determination coefficient value (at least for Aranjuez) when it was correlated with grain yield. In addition, it was achieved a date of measurement before  $u \cdot v \cdot A$  and GA, which may be due to the fact that this type of index can saturate (Kefauver et al., 2015), but NGRDI is not as prone to saturation (Elazab et al., 2016). This could be an important factor to take into account to improve the performance RGB indexes. Furthermore, the best performance of the RGB indexes (best correlation with grain yield) were observed when the canopy color started to shift from green to yellow, which correspond to the second half of grain filling (GS 75-79) under support irrigation and late planting conditions and heading (GS 55-57) under rainfed conditions. Although we observed similar performance using a multispectral index (GreenSeeker)

compared to RGB indexes, the use of modified color-infrared (CIR) cameras could be useful. A conventional RGB camera can be used to build a CIR camera removing the internal “hot mirror filter” to enable recoding the near infrared (NIR) information (Lehmann et al., 2017). This modification allows to acquired infrared data with much higher resolution per measurement than the individual points acquired by GreenSeeker device. Besides that, the two-dimensional information would still be available for image processing tasks avoiding parallax issues of multispectral (multi-lens) cameras (Jhan et al., 2017).

## **2.2. Photosynthetic area of the canopy trait and grain yield**

The photosynthetic area of the canopy in field conditions, assessed by RGB-derived indices, has shown to be highly correlated with GY regardless the growing conditions (Chapter 5). We have compared Green Area (GA), Greener Area (GGA), Normalized Green Red Difference Index (NGRDI) and Triangular Greenness Index (TGI) (Casadesús et al., 2007; Hunt et al., 2014, 2013, 2011, 2005) with a novel photosynthetic area index ( $u^*v^*A$ ) (Fernandez-Gallego et al., 2019c) based on the CIE  $L^*u^*v^*$  color space (Robertson, 1977). Even though, using previous RGB indexes of the literature (GA, GGA, NGRDI, TGI) and the novel vegetation index ( $u^*v^*A$ ) we have achieved almost the same or better relationship with GY; the best performance of the RGB indexes were achieved at the second half of grain filling (GS 75-79,  $R^2 \approx 0.6$ ) under support irrigation and late planting conditions, and heading (GS 55-57,  $R^2 \approx 0.5$ ) under rainfed conditions. Further analysis such as broad sense heritability ( $h^2$ ) and genetic correlation ( $r_A$ ) showed better results from the  $u^*v^*A$  index than the GA, GGA, NGRDI and TGI indexes. Regarding heritability of RGB index and heritability of

grain yield, under normal planting conditions (support irrigation and rainfed); for several indexes measured at early stages, the value of the  $h^2 \times r_A^2$  product (Falconer and Mackay, 1996) was higher than the  $h^2$  of the grain yield. This shows that under normal planting conditions the indirect selection based on RGB indexes performs better than the direct selection based on the yield harvested (Richards et al., 2002). In the case of late planting condition, in several indexes and particularly at early stages, the value of the  $h^2 \times r_A^2$  product was lower than the  $h^2$  of the grain yield. This may be due to the fact that high temperature accelerates the plant growth thus preventing the appearance of genotypic differences (Stone and Nicolas, 1995). Thus, under normal planting conditions at early stages, indirect selection may still have provided a higher throughput via measurement of a specific RGB vegetation index and the benefit of its lower cost, rather than having to wait until maturity to harvest the crop. The early stages seem to be the best phenological stages for saving in cost and time and increase the selection intensity. The cost per breeding plot of the whole harvesting process (until getting the yields) may go easily beyond € 15, plus the cost of maintaining the crop until maturity. By contrast the evaluation at ground level done by hand by walking through the plots takes a fraction of minute, which means that one worker provided with a camera may even record thousands of plots in a day (Fernandez-Gallego et al., 2019c).

### **3. Equipment considerations and future works**

#### **3.1. Equipment considerations**

The software could be a restriction for HTPP, several types of open source and payment software, sensors and platforms are being used for plant

phenotyping tasks in the different research centers and experimental station around the world. In our case, the CerealScanner software (Chapter 2), developed for ear counting estimation and the  $u^*v^*A$  index calculation, operate within the open source software ImageJ (Schneider et al., 2012). More information is available and software contacts can be found at the URL: <https://integrativecropecophysiology.com/softwaredevelopment/cerealscanner/>. The thermal ear counting system was also developed within ImageJ. Although we have programmed mainly using open source software in this work, for the ear counting system using an aerial platform we have combined open source software ImageJ (version 2.0.0-rc-69, NIH, Bethesda, MD, USA) for processing and feature extraction; and commercial software such as Agisoft Photoscan (version 1.2.3, Agisoft LLC, St. Peterburg, Russia) for build the geo-referenced ortophotos, Halcon (version 11, MVTec Software GmbH, Munich, Germany) for orthomosaic preprocessing and MATLAB (version R2014b, MathWorks, Inc., MA, USA) for training and classifying. The use of commercial software, costly sensors and remote sensing approaches cannot be considered as a negative characteristic; however, the experiment repeatability in developing countries or small companies could be a limitation (Araus et al., 2015) to take into account.

### **3.2. Future works**

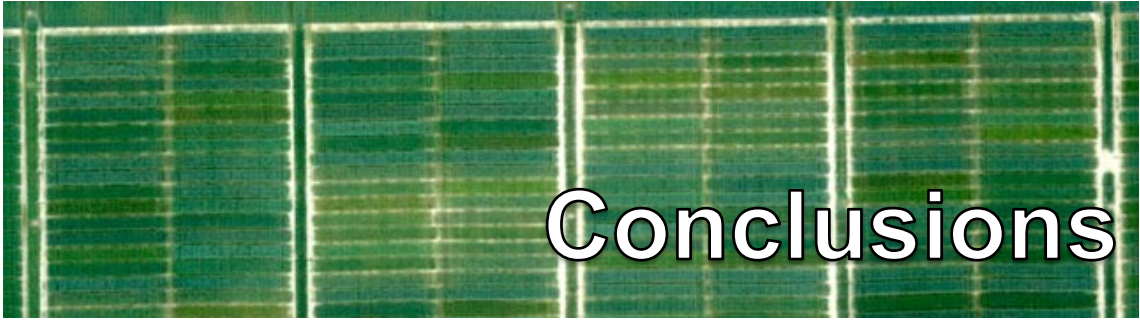
Many different algorithm adaptations can be designed from the new sensors and new platform technology. Future works concerns higher sensor resolution, multi-sensor and multi-data integration. Regarding ear counting, we have developed an accurate image processing system; however future work and



improvements may include, (i) at ground level, we would like to include a machine learning stage in order to improve the ear detection, especially for protocol acquisition errors such as images with oblique angles, changing sunlight conditions and sub-optimal distances between the camera and the canopy; (ii) at aerial level, we would like to use a higher resolution camera such as the Phase One iXU-100 with 100-mega-pixel resolution and 53.4 x 40.0 mm sensor size or a UAV such as the DJI Mavic 2 Pro equipped with 20-mega-pixel resolution and 35.0 x 28.0 mm at a lower distance from the canopy in order to acquire more canopy details that could help to increase the ear detection accuracy and the orthomosaic reconstruction; (iii) using thermal imagery, we would like to use a thermal/RGB fusion camera or a higher thermal resolution camera or such as the FLIR T1020 in order to have more spatial resolution at highest distances, this could contribute to differentiates better the surfaces into the image at similar ear temperatures using morphological operates; (iv) 3-dimensional imagery, we would like to estimating the ear size/volume, along our research we have confirmed the dynamic compensation mechanisms among agronomical yield components, perhaps using 3-dimentional information to estimate the ear size/volume could be useful for grain yield prediction. Regarding photosynthetic area estimation we have obtained almost the same or better results compared with other RGB and NDVI indexes; however, we would like to use a CIR camera to study the canopy reflectance including the NIR information that provide less sunlight and shadows issues than an RGB camera and more spatial resolution than a NDVI hand-held device. Moreover, the CIR imagery could the used to calculate multispectral indexes or design a new one using image processing techniques.

Finally, the new UAV platforms and its integrated sensors could be a key factor; for instance, the new DJI Mavic 2 Enterprise Dual equipped with an RGB and thermal camera, Global Positions System (GPS) and Global Navigation Satellite System (GLONAS). This visual and thermal and position data integration could be useful to the robust interpretation of the crop for plant phenotyping purposes. Even though, the thermal sensor has relatively low resolution for ear counting or ear temperature estimation, this platform allows low flight altitude that increases image spatial resolution without wind turbulence affecting the crop canopy. Moreover, future technology improvements of this type of platform and sensors are expected. In that way, future sceneries with higher resolution sensors and data integration could be projected for plant phenotyping tasks.





# Conclusions



## CONCLUSIONS

1. Frequency domain filters were essential in the RGB pre-processing steps to avoid a wide frequency range information from awns, leaves and unwanted objects into the image when employed for ear counting. Although high frequency information contributes to discrimination tasks, redundancy information reduces accuracy and complicates image processing algorithms. Frequency domain filters maintain the essential information, connect the pixels regions of each object; and therefore, simplify following algorithms in the image processing pipeline.
2. However, the RGB color space is the standard provided by the camera sensor technology. The interpretation of the ambient light conditions during image capture and its proper image representation for each phenotyping trait in other color spaces should be considered, such as HSI, CIE L\*a\*b or CIE L\*u\*v or others, especially for automatic imaging systems under field conditions.
3. Ear counting systems have demonstrated high accuracy under field conditions in low- and high- resolution scenarios to estimate the number of visible ears within an image. The best relationships of ear density with GY were achieved in trials under low nitrogen conditions; this could indicate more applicability to real growing conditions in production fields.
4. Random forest (RF) has achieved the best performance in training and classifying tasks using multi-dimensional data. The bootstrapping

aggregation and the many learners used provide robustness against outliers and noise and less sensitivity when applied to remote sensing data.

5. The performance of the RGB and thermal ear counting system were comparable; however, from the implementation and computation requirements point of view, thermal data is considerably simpler than RGB data. For mobile applications, thermal imagery processing could be easily handled for the mobile device's own processing power. On the other hand, optimal thermal image data capture is more sensitive to environmental conditions.
6. The best correlation between GY and RGB indexes were achieved when the canopy color started to shift from green to yellow, which corresponds to the second half of grain filling under support irrigation and late planting conditions and heading under rainfed conditions. Perhaps, the use of those more yellow color characteristics instead of focus on the green color characteristics could be an opportunity to improve the performance of RGB indexes.
7. Although the correlation between different RGB indexes and GY were quite similar across the experimental sites and measurements dates, combining all data to calculate  $h^2$  and  $r_A$  for each index, the results were considerably better for the newly developed  $u^*v^*A$  than the other RGB indexes. The white reference and luminance characteristics of the CIE  $L^*u^*v^*$  color space improved the data for  $h^2$  and  $r_A$  analysis.

8. The color calibration did not improve the information provided by the RGB sensor under natural light conditions. Conversely, the indexes from calibrated images tended to perform somewhat poorer than indexes from un-calibrated images taken using the automatic settings of the cameras used in this research.
  
9. The use of low-cost devices and a hand-help acquisition platform, such as conventional cameras with small sensor size or to hold the camera by hand, were not a limitation to achieve comparable or better results than state-of-the-art complex platforms or higher resolution sensors used in similar experiments.









## **TÉCNICAS DE PROCESAMIENTO DE IMÁGENES RGB Y TÉRMICAS COMO HERRAMIENTA PARA FENOTIPADO DE CULTIVOS**

### **Introducción:**

Las existencias mundiales de cereales deben aumentar para satisfacer la creciente demanda. Actualmente, el maíz, el arroz y el trigo son los principales cultivos a nivel mundial, otros cereales como la cebada, el sorgo y la avena están también bien ubicados en la lista. En 2019, la FAO pronostica un aumento en la producción de cereales del 1,2% desde 2018, que corresponde a 2.685 millones de toneladas. Europa contribuye con alrededor del 20% de la producción mundial de cereales, principalmente en cultivos de trigo y cebada que cubren más del 70% de la superficie cultivada. La productividad de los cultivos se ve afectada directamente por factores del cambio climático como el calor, la sequía, las inundaciones o las tormentas. De hecho, en países que experimentan una alta exposición y riesgo relacionado con la variabilidad climática y climas extremos, al menos el 80% de la variabilidad de producción interanual puede explicarse por factores relacionados con el clima. Los investigadores coinciden en que el cambio climático global está teniendo un gran impacto en la productividad de los cultivos. Además, se prevé que las temperaturas aumentarán al menos 0.2 °C por década durante los próximos 30 años; adicionalmente, para fines de este siglo, la temperatura aumentará hasta 4.5 °C. El calentamiento global aumentará

las tasas de respiración de la planta, al mismo tiempo que acortará la duración del cultivo y, por lo tanto, reducirá la productividad y el rendimiento.

Es por esto que muchos estudios se han centrado en escenarios de cambio climático y más específicamente en estrés abiótico en cereales. Por ejemplo, en el caso de estrés por calor, las altas temperaturas entre antesis y llenado de grano pueden disminuir el rendimiento del grano, probablemente debido al reducido tiempo que tiene el cultivo para capturar recursos. El estrés hídrico asociado con una disminución en la precipitación, debido a un aumento en la demanda transpirativa impulsada por el calor (o ambos juntos) pueden dar como resultado el cierre de estomas como un medio para reducir la pérdida de agua, lo que posteriormente aumenta la temperatura de las hojas. El estrés por salinidad, a menudo debido al aumento del nivel del mar, también puede afectar el crecimiento de los cereales y el rendimiento de los granos.

Para hacer frente al cambio climático y escenarios ambientales futuros, el mejoramiento de plantas es una de las principales alternativas; incluso se considera que las técnicas de mejoramiento contribuyen en mayor medida al aumento del rendimiento que el manejo del cultivo. Los programas de mejora se centran en identificar genotipos con altos rendimientos y calidad para actuar como progenitores y promover los mejores individuos para desarrollar nuevas variedades de plantas. Los mejoradores utilizan los datos fenotípicos, el desempeño de las plantas y los cultivos, y la información genética para mejorar el rendimiento mediante la selección (GxE, donde G y E indican factores genéticos y ambientales). Se deben tener en cuenta más factores para aumentar el rendimiento, como por ejemplo, la educación de los agricultores, los incentivos

económicos y el uso de nuevas tecnologías (GxExM, donde M indica manejo del cultivo).

Los agricultores han llevado a cabo el fenotipado de plantas durante mucho tiempo, ya que año tras año, siguieron la tendencia natural de seleccionar la mejor semilla de las variedades de mayor rendimiento para la replantación. El fenotipado plantas está relacionado con las características observables (o medibles) de la planta mientras crece el cultivo, así como con la asociación entre el fondo genético de la planta y su respuesta al medio ambiente (GxE). En el fenotipado tradicional, las mediciones se clasifican manualmente, lo cual es tedioso, consume mucho tiempo y es propenso a errores subjetivos. Sin embargo, hoy en día la tecnología está involucrada en muchas aplicaciones. Desde el punto de vista del fenotipado de plantas, la tecnología se ha incorporado como una herramienta. El uso de técnicas de procesamiento de imágenes que integran sensores y algoritmos son por lo tanto una alternativa para evaluar automáticamente (o semiautomáticamente) estas características.

### **Objetivos:**

El objetivo principal de esta tesis es desarrollar técnicas de procesamiento de imágenes para el fenotipado de plantas usando imágenes RGB y térmicas.

Objetivos específicos:

- Desarrollar algoritmos para la detección y el conteo de espigas de trigo utilizando imágenes cenitales RGB y térmicas sobre el cultivo y realizar la validación utilizando conteo manual en las imágenes. En el caso de las imágenes RGB, el objetivo adicional es desarrollar las configuraciones

específicas para plataformas terrestres y aéreas. Usar esta variable como componente agronómica para estudiar su relación con el rendimiento del cultivo.

- Desarrollar un protocolo utilizando índices de vegetación RGB para fenotipado y predicción del rendimiento del cultivo de trigo en diferentes condiciones de crecimiento.

### **Resumen por capítulo:**

#### **Capítulo 1**

El número de espigas por unidad de superficie (densidad de espigas) es uno de los principales componentes del rendimiento agronómico para determinar el rendimiento en trigo. Una evaluación rápida de este atributo puede contribuir a monitorear la eficiencia de las prácticas de manejo de cultivos, predicción temprana del rendimiento o ser utilizada como una característica fenotípica en los programas de mejoramiento. Actualmente, el número de espigas se cuenta manualmente, lo que lleva mucho tiempo. Además, no existe un protocolo estandarizado para contar espigas. Se propone un algoritmo automático de conteo de espigas para estimar la densidad de espigas en condiciones de campo utilizando imágenes digitales en color tomadas desde arriba del cultivo en condiciones de luz natural. Los ensayos de campo se llevaron a cabo en dos lugares de España durante la temporada de cultivos 2014/2015 en un conjunto de 24 variedades de trigo duro con dos condiciones de crecimiento por lugar. El algoritmo para contar utiliza tres pasos: (i) filtro Laplaciano en frecuencia elegido

para eliminar los elementos de baja y alta frecuencia que aparecen en una imagen, (ii) filtro Mediana para reducir el ruido aún presente alrededor de las espigas y (iii) segmentación de los picos locales dentro de la imagen. Los resultados demuestran una alta tasa de acierto (superior al 90%) entre el conteo por algoritmo y manual de espigas con baja desviación estándar (alrededor del 5%). La correlación entre el conteo por algoritmo y rendimiento fueron significativas y mayores que la correlación del conteo manual realizado en campo. Los resultados demuestran que el conteo automático de espigas realizados con las imágenes adquiridas alrededor de la antesis se correlacionó mejor con el rendimiento que con las imágenes adquiridas en etapas posteriores. El bajo rendimiento del conteo de espigas en las etapas tardías de llenado de granos se asoció con la pérdida de contraste en la imagen. El desarrollo de métodos robustos, de bajo costo y eficientes para evaluar la densidad espigas de trigo, como un componente agronómico importante del rendimiento, es muy relevante para los esfuerzos de fenotipado dirigidos al aumento del rendimiento. Aunque la etapa fenológica de las mediciones es importante, el sistema de procesamiento presentado parece ser adecuado para plataformas aéreas u otras plataformas automatizadas.

## **Capítulo 2**

La densidad de espigas, o el número de espigas por metro cuadrado (espigas/m<sup>2</sup>), es central en muchos programas de mejoramiento de cultivos de cereales, como en trigo y cebada, debido a que es un componente importante para estimar rendimiento. Por esto, una técnica rápida, eficiente y estandarizada para evaluar la densidad de espigas ayudaría a mejorar el manejo agrícola,



proporcionando mejoras en las predicciones de rendimiento previo a la cosecha, o incluso podría usarse como una herramienta para el mejoramiento de cultivos. Las técnicas actuales para estimar la densidad de espigas no solo son laboriosas y requieren mucho tiempo, sino que además no tienen un protocolo estandarizado, ya sea por metro lineal, área cuadrada, o una extrapolación basada en la densidad de espigas y número plantas después de la cosecha. Se presenta un algoritmo automático de conteo de espigas para estimar la densidad de espigas utilizando imágenes cenitales del cultivo bajo condiciones de luz solar natural. Se utilizaron diferentes ensayos de campo de trigo duro y cebada distribuidos geográficamente en España durante las temporadas de cultivo 2014/2015 y 2015/2016 en ensayos de riego y seco. El protocolo de tres fases incluye la etapa de crecimiento del cultivo y la planificación de las condiciones del campo, pautas para la adquisición de las imágenes y un algoritmo de tres pasos: (i) filtro Laplaciano en frecuencia para eliminar información de baja y alta frecuencia no deseados, (ii) filtro Mediana para reducir el ruido de alta frecuencia y (iii) segmentación y conteo utilizando los picos máximos locales. Se realizaron ajustes al algoritmo correspondientes a la resolución de la cámara, distancia focal y distancia entre la cámara y el dosel del cultivo. Los resultados demuestran una alta tasa de acierto (superior al 90%) y valores de  $R^2$  (de 0.62-0.75) entre el conteo con algoritmos y conteo manual en imágenes de trigo duro y cebada.

### **Capítulo 3**

En el trigo y otros cereales, el número de espigas por unidad de área es uno de los principales componentes determinantes del rendimiento. Una evaluación automática de este parámetro puede contribuir al avance del fenotipado y

monitoreo de trigo. No existe un protocolo estándar para el recuento de espigas en el campo, y además requiere mucho tiempo. Se propone un sistema automático de conteo de espigas utilizando técnicas de aprendizaje de maquina basadas en imágenes RGB adquiridas de una plataforma aérea. La evaluación se realizó en un conjunto de 12 variedades de trigo de invierno con 3 tratamientos de nitrógeno durante la temporada 2017-2018. El sistema automático desarrollado utiliza técnicas de filtrado de frecuencia, segmentación, extracción de características y clasificación para discriminar las espigas en la imagen. La relación entre el conteo manual basado en imágenes y el conteo por algoritmo para entrenamiento, clasificación y validación exhibió alta precisión y eficiencia. Además, un conteo manual de espigas en campo fue realizado. Se compararon las correlaciones entre el conteo automático y conteo manual de espigas en campo contra el rendimiento. Las correlaciones fueron más fuertes con el sistema de conteo automático de espigas, particularmente considerando el tratamiento con N más bajo. Se discuten los requisitos metodológicos y las limitaciones.

#### **Capítulo 4**

La densidad de espigas es uno de los componentes agronómicos de rendimiento más importantes en trigo. El conteo de espigas lleva mucho tiempo y es tedioso, ya que se realiza con mayor frecuencia de forma manual en condiciones de campo. Además, a menudo se utilizan diferentes técnicas de muestreo, lo que resulta en una falta de protocolo estandarizado, que eventualmente puede afectar la comparabilidad de los resultados. Los sensores térmicos capturan las características del dosel de cultivo con más contraste que los sensores RGB para

tareas de segmentación y clasificación de imágenes. Se propone un sistema de conteo automático de espigas utilizando imágenes térmicas cenitales adquiridas de una cámara térmica portátil de resolución moderadamente alta. En este estudio, se utilizaron tres sitios experimentales en diferentes condiciones de crecimiento en España en un conjunto de 24 variedades de trigo duro. El sistema automático desarrollado utiliza técnicas para mejorar el contraste y técnicas de filtrado para segmentar las regiones detectadas como espiga. Este enfoque se basa en las diferencias de temperatura entre las espigas y el resto del dosel, dado que las espigas generalmente tienen temperaturas más altas por sus más bajas tasas de transpiración. Se realizó la adquisición de imágenes térmicas, junto con imágenes RGB y el conteo visual de espigas en campo en el mismo segmento del cultivo para fines de validación. La relación entre el conteo usando imágenes termales y el conteo visual en campo fue bastante débil ( $R^2 = 0.40$ ), lo que resalta las dificultades para estimar la densidad de espigas desde una sola perspectiva de la imagen. Sin embargo, los resultados muestran que el sistema de conteo automático de espigas utilizando imágenes térmicas funciona bastante bien en el conteo de las espigas que aparecen en la imagen, exhibiendo altas correlaciones con los conteos manuales basados en imágenes térmicas y RGB al usar un aro físico de validación ( $R^2 = 0.75\text{--}0.84$ ). El conteo automático de espigas también exhibió una alta correlación con el conteo manual de las imágenes térmicas cuando se considera la imagen completa ( $R^2 = 0.80$ ). Los resultados también muestran alta correlación entre el conteo manual al utilizar imágenes térmicas y RGB con un aro físico de validación ( $R^2 = 0.83$ ). Se discuten los requisitos metodológicos y las posibles limitaciones de la técnica.

## Capítulo 5

El área fotosintética del dosel a lo largo del ciclo de cultivo es un factor importante para determinar el rendimiento en trigo. Este trabajo propone el uso de imágenes cenitales RGB del dosel tomadas en condiciones de luz natural para evaluar índices de vegetación para predecir el rendimiento como un enfoque de bajo costo. Se monitoreó un conjunto de 23 variedades de trigo duro en tres condiciones de cultivo (riego, seco y siembra tardía) en dos lugares (Aranjuez y Valladolid, España), con un total de 6 ensayos de campo. Para cada parcela, se tomaron periódicamente imágenes digitales RGB desde la emergencia de las plántulas hasta el llenado tardío del grano. El área verde (GA y GGA), índice normalizado de la diferencia entre rojo y verde (NGRDI), índice triangular de verdor (TGI) y un nuevo índice  $u^*v^*A$ , para calcular el área fotosintética basado en el espacio de color CIE  $L^*u^*v^*$ , fueron comparados como referencia con el índice de vegetación de diferencia normalizada (NDVI) usando un espectroradiómetro de mano. En el caso de los ensayos de riego y siembra tardía, las mejores predicciones fenotípicas con rendimiento se lograron con los índices de vegetación medidos durante la última parte del ciclo del cultivo (es decir, llenado de grano). Para los ensayos de seco, las mejores predicciones fenotípicas se lograron con índices medidos anteriormente (alrededor de espigado). Entre todos los índices evaluados, el nuevo índice tuvo el mejor desempeño. Considerando las heredabilidades y correlaciones genéticas de los índices RGB evaluados con rendimiento, las predicciones de rendimiento basadas en índices fueron mejores en las primeras etapas de cultivo en condiciones de riego y de seco, mientras que en condiciones de siembra tardía los índices medidos tuvieron buen desempeño en diferentes etapas del cultivo.

## Conclusiones:

1. Los filtros en el dominio de la frecuencia fueron esenciales para el preprocesamiento de imágenes RGB para evitar un amplio rango de frecuencias en aristas, hojas y objetos no deseados en la imagen para el conteo de espigas. Aunque la información de alta frecuencia contribuye a tareas de discriminación, la información redundante reduce la precisión y complica los algoritmos de procesamiento de imágenes. Los filtros de dominio de frecuencia mantienen la información esencial, conectan los píxeles las regiones de cada objeto; y por lo tanto, simplifican los algoritmos posteriores en el sistema de procesamiento de imágenes.
2. Aunque, el espacio de color RGB es el estándar proporcionado por la tecnología del sensor de la cámara. La interpretación de las condiciones de luz ambiental durante la captura de las imágenes y su adecuada representación en la imagen para cada característica para fenotipado debe ser considerada en otros espacios de color, como HSI, CIE L\*a\*b, CIE L\*u\*v u otros, especialmente para sistemas de imágenes automáticas bajo condiciones de campo.
3. Los sistemas de conteo de espigas han demostrado una alta precisión en condiciones de campo en escenarios de baja y alta resolución para estimar el número de espigas visibles dentro de una imagen. Las mejores relaciones de densidad de espigas con rendimiento se lograron en ensayos en condiciones de bajo contenido de nitrógeno; esto podría indicar una

mayor aplicabilidad en condiciones reales de crecimiento en campos de producción.

4. Random forest (RF) ha logrado el mejor rendimiento en tareas de entrenamiento y clasificación utilizando datos multidimensionales. Bootstrapping aggregation y la gran cantidad de learners utilizados proporcionan robustez frente a valores atípicos, ruido y menor sensibilidad cuando es aplicado en datos obtenidos por teledetección.
5. El rendimiento de los sistemas de conteo de espigas RGB y térmico fue comparable; sin embargo, desde el punto de vista de los requisitos de implementación y cálculo, los datos térmicos son considerablemente más simples que los datos RGB. Para aplicaciones móviles, las imágenes térmicas podrían ser más fácilmente procesadas. Por otro parte, la captura óptima de datos, utilizando imágenes térmicas, es más sensible a las condiciones ambientales.
6. La mejor correlación entre rendimiento y los índices RGB se logró cuando el color del dosel comenzó a cambiar de verde a amarillo, lo que corresponde a la segunda mitad de llenado de grano en condiciones de riego y siembra tardía, y a espigado en condiciones de secano. Quizás, el uso de más de estas características de color amarillo en lugar de centrarse en las características de color verde podría ser una oportunidad para mejorar el rendimiento de los índices RGB.

7. Aunque la correlación entre los diferentes índices RGB y rendimiento fueron bastante similares en las estaciones experimentales y fechas de adquisición, combinando todos los datos para calcular  $h^2$  y  $r_A$  para cada índice, los resultados fueron considerablemente mejores para el nuevo índice  $u^*v^*A$  en comparación con los otros índices RGB. La referencia de blancos y las características de luminancia del espacio de color CIE  $L^*u^*v^*$  mejoraron los datos para el análisis de  $h^2$  y  $r_A$ .
8. La calibración de color no mejoró la información proporcionada por el sensor RGB en condiciones de luz natural. Por el contrario, los índices de las imágenes calibradas tendieron a tener un desempeño algo peor que los índices de las imágenes no calibradas tomadas en configuración automática con las cámaras utilizadas en esta investigación.
9. El uso de dispositivos de bajo costo y una plataforma de adquisición manual, como cámaras convencionales con un tamaño de sensor pequeño o sosteniendo la cámara con la mano, no fueron una limitación para lograr resultados comparables o mejores que complejas plataformas del estado del arte o sensores con más alta resolución usados en experimentos similares.



# References





## REFERENCES

- Aasen, H., Honkavaara, E., Lucieer, A., Zarco-Tejada, P.J., 2018. Quantitative remote sensing at ultra-high resolution with UAV spectroscopy: A review of sensor technology, measurement procedures, and data correction workflows. *Remote Sens.* 10, 1–42. doi:10.3390/rs10071091
- Aber, J.S., Marzoff, I., Ries, J.B., 2010. Basic Principles of Small-Format Aerial Photography. *Small-Format Aer. Photogr.* 15–22. doi:10.1016/b978-0-444-53260-2.10002-x
- Abhinandan, K., Skori, L., Stanic, M., Hickerson, N.M.N., Jamshed, M., Samuel, M.A., 2018. Abiotic Stress Signaling in Wheat – An Inclusive Overview of Hormonal Interactions During Abiotic Stress Responses in Wheat. *Front. Plant Sci.* 9, 1–25. doi:10.3389/fpls.2018.00734
- Andrade-Sanchez, P., Gore, M.A., Heun, J.T., Thorp, K.R., Carmo-Silva, A.E., French, A.N., Salvucci, M.E., White, J.W., 2014. Development and evaluation of a field-based high-throughput phenotyping platform. *Funct. Plant Biol.* 41, 68–79. doi:10.1071/FP13126
- Araus, J.L., Cairns, J.E., 2014. Field high-throughput phenotyping: the new crop breeding frontier. *Trends Plant Sci.* 19, 52–61. doi:10.1016/j.tplants.2013.09.008
- Araus, J.L., Elazab, A., Vergara, O., Cabrera-Bosquet, L., Serret, M.D., Zaman-Allah, M., Cairns, J.E., 2015. New Technologies for Phenotyping, in: *Phenomics*. Springer International Publishing, Cham, pp. 1–14. doi:10.1007/978-3-319-13677-6\_1
- Araus, J.L., Kefauver, S.C., 2018. Breeding to adapt agriculture to climate

- change: affordable phenotyping solutions. *Curr. Opin. Plant Biol.*  
doi:10.1016/j.pbi.2018.05.003
- Araus, J.L., Kefauver, S.C., Zaman-Allah, M., Olsen, M.S., Cairns, J.E., 2018. Translating High-Throughput Phenotyping into Genetic Gain. *Trends Plant Sci.* doi:10.1016/j.tplants.2018.02.001
- Arroyo, J., Guijarro, M., Pajares, G., 2016. An instance-based learning approach for thresholding in crop images under different outdoor conditions. *Comput. Electron. Agric.* 127, 669–679.  
doi:10.1016/j.compag.2016.07.018
- Asseng, S., Foster, I., Turner, N.C., 2011. The impact of temperature variability on wheat yields. *Glob. Chang. Biol.* 17, 997–1012. doi:10.1111/j.1365-2486.2010.02262.x
- Bawden, O., Kulk, J., Russell, R., McCool, C., English, A., Dayoub, F., Lehnert, C., Perez, T., 2017. Robot for weed species plant-specific management. *J. F. Robot.* 34, 1179–1199. doi:10.1002/rob.21727
- Bernstein, L., Bosch, P., Canziani, O., Chen, Z., Christ, R., 2008. IPCC, 2007: Climate Change 2007: Synthesis Report, Contribution of Working Groups I, II and III to the Fourth Assessment Report of the Intergovernmental Panel on Climate Change [Core Writing Team, Pachauri, R.K and Reisinger, A. (eds.)]. IPCC: Geneva, Switzerland.
- Bonadies, S., Lefcourt, A., Gadsden, S.A., 2016. A survey of unmanned ground vehicles with applications to agricultural and environmental sensing, in: Valasek, J., Thomasson, J.A. (Eds.), *Autonomous Air and Ground Sensing Systems for Agricultural Optimization and Phenotyping*. p. 98660Q.  
doi:10.1117/12.2224248

- Bos, I., Caligari, P., 1995. Selection Methods in Plant Breeding, 10.1007/97. ed. Springer Netherlands, Dordrecht. doi:10.1007/978-94-015-8432-6
- Brugger, A., Behmann, J., Paulus, S., Luigs, H.-G., Kuska, M.T., Schramowski, P., Kersting, K., Steiner, U., Mahlein, A.-K., 2019. Extending Hyperspectral Imaging for Plant Phenotyping to the UV-Range. *Remote Sens.* 11, 1401. doi:10.3390/rs11121401
- Busemeyer, L., Mentrup, D., Möller, K., Wunder, E., Alheit, K., Hahn, V., Maurer, H.P., Reif, J.C., Würschum, T., Müller, J., Rahe, F., Ruckelshausen, A., 2013. Breedvision - A multi-sensor platform for non-destructive field-based phenotyping in plant breeding. *Sensors (Switzerland)* 13, 2830–2847. doi:10.3390/s130302830
- Casadesús, J., Kaya, Y., Bort, J., Nachit, M.M., Araus, J.L., Amor, S., Ferrazzano, G., Maalouf, F., Maccaferri, M., Martos, V., Ouabbou, H., Villegas, D., 2007. Using vegetation indices derived from conventional digital cameras as selection criteria for wheat breeding in water-limited environments. *Ann. Appl. Biol.* 150, 227–236. doi:10.1111/j.1744-7348.2007.00116.x
- Chemura, A., Mutanga, O., Dube, T., 2017. Separability of coffee leaf rust infection levels with machine learning methods at Sentinel-2 MSI spectral resolutions. *Precis. Agric.* 18, 859–881. doi:10.1007/s11119-016-9495-0
- Cocozza, C., Pulvento, C., Lavini, A., Riccardi, M., d'Andria, R., Tognetti, R., 2013. Effects of increasing salinity stress and decreasing water availability on ecophysiological traits of quinoa (*Chenopodium quinoa* Willd.) grown in a mediterranean-type agroecosystem. *J. Agron. Crop Sci.* 199, 229–240. doi:10.1111/jac.12012

- Cointault, F., Guerin, D., Guillemin, J., Chopinet, B., 2008. In-field *Triticum aestivum* ear counting using colour-texture image analysis. *New Zeal. J. Crop Hortic. Sci.* 36, 117–130. doi:10.1080/01140670809510227
- Cozzolino, D., 2017. The role of near-infrared sensors to measure water relationships in crops and plants. *Appl. Spectrosc. Rev.* 52, 837–849. doi:10.1080/05704928.2017.1331446
- Deery, D.M., Rebetzke, G.J., Jimenez-Berni, J.A., James, R.A., Condon, A.G., Bovill, W.D., Hutchinson, P., Scarrow, J., Davy, R., Furbank, R.T., 2016. Methodology for High-Throughput Field Phenotyping of Canopy Temperature Using Airborne Thermography. *Front. Plant Sci.* 7, 1–13. doi:10.3389/fpls.2016.01808
- Drusch, M., Del Bello, U., Carlier, S., Colin, O., Fernandez, V., Gascon, F., Hoersch, B., Isola, C., Laberinti, P., Martimort, P., Meygret, A., Spoto, F., Sy, O., Marchese, F., Bargellini, P., 2012. Sentinel-2: ESA's Optical High-Resolution Mission for GMES Operational Services. *Remote Sens. Environ.* 120, 25–36. doi:10.1016/j.rse.2011.11.026
- Du, M., Noguchi, N., 2017. Monitoring of wheat growth status and mapping of wheat yield's within-field spatial variations using color images acquired from UAV-camera System. *Remote Sens.* 9. doi:10.3390/rs9030289
- Elazab, A., Ordóñez, R.A., Savin, R., Slafer, G.A., Araus, J.L., 2016. Detecting interactive effects of N fertilization and heat stress on maize productivity by remote sensing techniques. *Eur. J. Agron.* 73, 11–24. doi:10.1016/j.eja.2015.11.010
- Fahlgren, N., Gehan, M.A., Baxter, I., 2015. Lights, camera, action: High-throughput plant phenotyping is ready for a close-up. *Curr. Opin. Plant Biol.*

24, 93–99. doi:10.1016/j.pbi.2015.02.006

Falconer, D.S., Mackay, F.C., 1996. Introduction to Quantitative Genetics, 4th ed. Pearson, Essex, England.

FAO, 2019. FAO Cereal Supply and Demand Brief [WWW Document]. URL <http://www.fao.org/worldfoodsituation/csdb/en/> (accessed 6.20.19).

FAO, IFAD, UNICEF, WFP, WHO, 2018. The State of Food Security and Nutrition in the World 2018. Building climate resilience for food security and nutrition, Building climate resilience for food security and nutrition. doi:10.1093/cjres/rst006

Farooq, M., Bramley, H., Palta, J.A., Siddique, K.H.M., 2011. Heat stress in wheat during reproductive and grain-filling phases. *CRC. Crit. Rev. Plant Sci.* 30, 491–507. doi:10.1080/07352689.2011.615687

Fernandez-Gallego, Buchailot, M., Aparicio Gutiérrez, N., Nieto-Taladriz, M., Araus, J.L., Kefauver, S.C., 2019a. Automatic Wheat Ear Counting Using Thermal Imagery. *Remote Sens.* 11, 751. doi:10.3390/rs11070751

Fernandez-Gallego, Buchailot, M.L., Gracia-Romero, A., Vatter, T., Diaz, O. V., Aparicio Gutiérrez, N., Nieto-Taladriz, M.T., Kerfal, S., Serret, M.D., Araus, J.L., Kefauver, S.C., 2019b. Cereal Crop Ear Counting in Field Conditions Using Zenithal RGB Images. *J. Vis. Exp.* e58695, 10. doi:10.3791/58695

Fernandez-Gallego, Kefauver, S.C., Aparicio Gutiérrez, N., Nieto-Taladriz, M.T., Araus, J.L., 2018a. Wheat ear counting in-field conditions: high throughput and low-cost approach using RGB images. *Plant Methods* 14, 22. doi:10.1186/s13007-018-0289-4

Fernandez-Gallego, Kefauver, S.C., Gutiérrez, N.A., Nieto-Taladriz, M.T., Araus, J.L., 2018b. Automatic wheat ear counting in-field conditions:

simulation and implication of lower resolution images, in: Neale, C.M., Maltese, A. (Eds.), Proc. SPIE 10783, Remote Sensing for Agriculture, Ecosystems, and Hydrology XX, 107830M. SPIE, p. 23.

doi:10.1117/12.2500083

Fernandez-Gallego, Kefauver, S.C., Vatter, T., Aparicio Gutiérrez, N., Nieto-Taladriz, M.T., Araus, J.L., 2019c. Low-cost assessment of grain yield in durum wheat using RGB images. *Eur. J. Agron.* 105, 146–156.

doi:10.1016/j.eja.2019.02.007

Fischer, R.A. (Tony), Edmeades, G.O., 2010. Breeding and Cereal Yield Progress. *Crop Sci.* 50, S-85. doi:10.2135/cropsci2009.10.0564

Font, D., Pallejà, T., Tresanchez, M., Teixidó, M., Martínez, D., Moreno, J., Palacín, J., 2014. Counting red grapes in vineyards by detecting specular spherical reflection peaks in RGB images obtained at night with artificial illumination. *Comput. Electron. Agric.* 108, 105–111.

doi:10.1016/j.compag.2014.07.006

FSIN, 2017. Global Report on Food Crises 2017. World Food Program. 145.

Gonzalez-de-Soto, M., Emmi, L., Perez-Ruiz, M., Aguera, J., Gonzalez-de-Santos, P., 2016. Autonomous systems for precise spraying – Evaluation of a robotised patch sprayer. *Biosyst. Eng.* 146, 165–182.

doi:10.1016/j.biosystemseng.2015.12.018

Gori, M., 2018. Machine Learning: A constraint-based approach. Morgan Kaufmann.

Gracia-Romero, A., Kefauver, S.C., Vergara-Díaz, O., Zaman-Allah, M.A., Prasanna, B.M., Cairns, J.E., Araus, J.L., 2017. Comparative Performance of Ground vs. Aerially Assessed RGB and Multispectral Indices for Early-

- Growth Evaluation of Maize Performance under Phosphorus Fertilization. *Front. Plant Sci.* 8, 1–13. doi:10.3389/fpls.2017.02004
- Guo, W., Rage, U.K., Ninomiya, S., 2013. Illumination invariant segmentation of vegetation for time series wheat images based on decision tree model. *Comput. Electron. Agric.* 96, 58–66. doi:10.1016/j.compag.2013.04.010
- Guo, W., Zheng, B., Duan, T., Fukatsu, T., Chapman, S., Ninomiya, S., 2017. EasyPCC: Benchmark Datasets and Tools for High-Throughput Measurement of the Plant Canopy Coverage Ratio under Field Conditions. *Sensors* 17, 798. doi:10.3390/s17040798
- Hou, M., Tian, F., Zhang, T., Huang, M., 2019. Evaluation of canopy temperature depression, transpiration, and canopy greenness in relation to yield of soybean at reproductive stage based on remote sensing imagery. *Agric. Water Manag.* 222, 182–192. doi:10.1016/j.agwat.2019.06.005
- Hunt, E.R., Cavigelli, M., Daughtry, C.S.T., McMurtrey, J.E., Walthall, C.L., 2005. Evaluation of Digital Photography from Model Aircraft for Remote Sensing of Crop Biomass and Nitrogen Status. *Precis. Agric.* 6, 359–378. doi:10.1007/s11119-005-2324-5
- Hunt, E.R., Daughtry, C.S.T., Eitel, J.U.H., Long, D.S., 2011. Remote sensing leaf chlorophyll content using a visible band index. *Agron. J.* 103, 1090–1099. doi:10.2134/agronj2010.0395
- Hunt, E.R., Daughtry, C.S.T., Mirsky, S.B., Hively, W.D., 2014. Remote sensing with simulated unmanned aircraft imagery for precision agriculture applications. *IEEE J. Sel. Top. Appl. Earth Obs. Remote Sens.* 7, 4566–4571. doi:10.1109/JSTARS.2014.2317876
- Hunt, E.R., Doraiswamy, P.C., McMurtrey, J.E., Daughtry, C.S.T., Perry, E.M.,



- Akhmedov, B., 2013. A visible band index for remote sensing leaf chlorophyll content at the canopy scale. *Int. J. Appl. Earth Obs. Geoinf.* 21, 103–112. doi:10.1016/j.jag.2012.07.020
- Ishag, H.M., Taha, M.B., 1974. Production and survival of tillers of wheat and their contribution to yield. *J. Agric. Sci.* 83, 117–124. doi:10.1017/S0021859600047079
- Jähne, B., 2005. *Digital Image Processing*. Springer-Verlag, Berlin/Heidelberg. doi:10.1007/3-540-27563-0
- Jannoura, R., Brinkmann, K., Uteau, D., Bruns, C., Joergensen, R.G., 2015. Monitoring of crop biomass using true colour aerial photographs taken from a remote controlled hexacopter. *Biosyst. Eng.* 129, 341–351. doi:10.1016/j.biosystemseng.2014.11.007
- Jensen, J.R., 2007. *Remote sensing of the environment : an earth resource perspective*. Pearson Education Limited.
- Jeppesen, J.H., Jacobsen, R.H., Jørgensen, R.N., Halberg, A., Toftegaard, T.S., 2017. Identification of High-Variation Fields based on Open Satellite Imagery. *Adv. Anim. Biosci.* 8, 388–393. doi:10.1017/s2040470017000693
- Jhan, J.P., Rau, J.Y., Haala, N., Cramer, M., 2017. Investigation of parallax issues for multi-lens multispectral camera band co-registration. *Int. Arch. Photogramm. Remote Sens. Spat. Inf. Sci. - ISPRS Arch.* 42, 157–163. doi:10.5194/isprs-archives-XLII-2-W6-157-2017
- Jimenez-Berni, J.A., Deery, D.M., Rozas-Larraondo, P., Condon, A. (Tony) G., Rebetzke, G.J., James, R.A., Bovill, W.D., Furbank, R.T., Sirault, X.R.R., 2018. High Throughput Determination of Plant Height, Ground Cover, and Above-Ground Biomass in Wheat with LiDAR. *Front. Plant Sci.* 9, 1–18.

doi:10.3389/fpls.2018.00237

Jin, X., Liu, S., Baret, F., Hemerlé, M., Comar, A., 2017. Estimates of plant density of wheat crops at emergence from very low altitude UAV imagery.

Remote Sens. Environ. 198, 105–114. doi:10.1016/j.rse.2017.06.007

Kefauver, S.C., El-Haddad, G., Vergara-Diaz, O., Araus, J.L., 2015. RGB picture vegetation indexes for High-Throughput Phenotyping Platforms (HTPPs), in: Neale, C.M.U., Maltese, A. (Eds.), Remote Sensing for Agriculture, Ecosystems, and Hydrology XVII. SPIE Proceedings, p. 9.

doi:10.1117/12.2195235

Kefauver, S.C., Vergara-Diaz, O., El-Haddad, G., Das, G., Suresh, L.M., Cairns, J., Araus, J.L., 2016. Semi-automatic digital image impact assessments of Maize Lethal Necrosis (MLN) at the leaf, whole plant and plot levels, in: AGU Fall Meeting Abstracts.

Kefauver, S.C., Vicente, R., Vergara-Díaz, O., Fernandez-Gallego, J.A., Kerfal, S., Lopez, A., Melichar, J.P.E., Serret Molins, M.D., Araus, J.L., 2017.

Comparative UAV and Field Phenotyping to Assess Yield and Nitrogen Use Efficiency in Hybrid and Conventional Barley. Front. Plant Sci. 8, 1–15.

doi:10.3389/fpls.2017.01733

Kelly, D., Vatsa, A., Mayham, W., Ngô, L., Thompson, A., Kazic, T., 2015. An opinion on imaging challenges in phenotyping field crops. Mach. Vis. Appl.

1–14. doi:10.1007/s00138-015-0728-4

Kirchgessner, N., Liebisch, F., Yu, K., Pfeifer, J., Friedli, M., Hund, A., Walter, A., 2017. The ETH field phenotyping platform FIP: a cable-suspended

multi-sensor system. Funct. Plant Biol. 44, 154. doi:10.1071/FP16165

Lehmann, J.R.K., Prinz, T., Ziller, S.R., Thiele, J., Heringer, G., Meira-Neto,

- J.A.A., Buttschardt, T.K., 2017. Open-Source Processing and Analysis of Aerial Imagery Acquired with a Low-Cost Unmanned Aerial System to Support Invasive Plant Management. *Front. Environ. Sci.* 5, 1–16.  
doi:10.3389/fenvs.2017.00044
- Leinonen, I., Jones, H.G., 2004. Combining thermal and visible imagery for estimating canopy temperature and identifying plant stress. *J. Exp. Bot.* 55, 1423–1431. doi:10.1093/jxb/erh146
- Li, H., Lee, W.S., Wang, K., 2014. Identifying blueberry fruit of different growth stages using natural outdoor color images. *Comput. Electron. Agric.* 106, 91–101. doi:10.1016/j.compag.2014.05.015
- Li, L., Zhang, Q., Huang, D., 2014. A review of imaging techniques for plant phenotyping. *Sensors (Switzerland)* 14, 20078–20111.  
doi:10.3390/s141120078
- Liu, S., Baret, F., Abichou, M., Boudon, F., Thomas, S., Zhao, K., Fournier, C., Andrieu, B., Irfan, K., Hemmerlé, M., Solan, B. de, 2017. Estimating wheat green area index from ground-based LiDAR measurement using a 3D canopy structure model. *Agric. For. Meteorol.* 247, 12–20.  
doi:10.1016/j.agrformet.2017.07.007
- Lleó, L., Barreiro, P., Ruiz-Altisent, M., Herrero, A., 2009. Multispectral images of peach related to firmness and maturity at harvest. *J. Food Eng.* 93, 229–235. doi:10.1016/j.jfoodeng.2009.01.028
- Madec, S., Jin, X., Lu, H., De Solan, B., Liu, S., Duyme, F., Heritier, E., Baret, F., 2019. Ear density estimation from high resolution RGB imagery using deep learning technique. *Agric. For. Meteorol.* 264, 225–234.  
doi:10.1016/j.agrformet.2018.10.013

- Malacara, D., 2011. Uniform Color Systems, in: Color Vision and Colorimetry: Theory and Applications, Second Edition. SPIE, 1000 20th Street, Bellingham, WA 98227-0010 USA, pp. 103–129. doi:10.1117/3.881172.ch6
- Manley, M., du Toit, G., Geladi, P., 2011. Tracking diffusion of conditioning water in single wheat kernels of different hardnesses by near infrared hyperspectral imaging. *Anal. Chim. Acta* 686, 64–75. doi:10.1016/j.aca.2010.11.042
- Martin-Guay, M.O., Paquette, A., Dupras, J., Rivest, D., 2018. The new Green Revolution: Sustainable intensification of agriculture by intercropping. *Sci. Total Environ.* 615, 767–772. doi:10.1016/j.scitotenv.2017.10.024
- Meyer, G.E., Neto, J.C., 2008. Verification of color vegetation indices for automated crop imaging applications. *Comput. Electron. Agric.* 63, 282–293. doi:10.1016/j.compag.2008.03.009
- Navulur, K., 2006. *Multispectral Image Analysis Using the Object-Oriented Paradigm*. CRC Press. doi:10.1201/9781420043075
- Ortega-Terol, D., Hernandez-Lopez, D., Ballesteros, R., Gonzalez-Aguilera, D., 2017. Automatic hotspot and sun glint detection in UAV multispectral images. *Sensors (Switzerland)* 17, 1–16. doi:10.3390/s17102352
- Pask, A., Pietragalla, J., Mullan, D., Reynolds, M. (Eds. ., 2012. *Physiological Breeding II: A Field Guide to Wheat Phenotyping*. CIMMYT, Mexico D.F.
- Payne, A.B., Walsh, K.B., Subedi, P.P., Jarvis, D., 2013. Estimation of mango crop yield using image analysis - Segmentation method. *Comput. Electron. Agric.* 91, 57–64. doi:10.1016/j.compag.2012.11.009
- Penczek, J., Boynton, P.A., Splett, J.D., 2014. Color Error in the Digital Camera Image Capture Process. *J. Digit. Imaging* 27, 182–191.

doi:10.1007/s10278-013-9644-1

Peres, M., 2017. *Laboratory Imaging & Photography*. Routledge, New York, NY.

Perez-Sanz, F., Navarro, P.J., Egea-Cortines, M., 2017. Plant phenomics: An overview of image acquisition technologies and image data analysis algorithms. *Gigascience* 6, 1–18. doi:10.1093/gigascience/gix092

Pitas, I., 2000. *Digital Image Processing Algorithms and Applications*. John Wiley & Sons, Inc., New York, NY.

Pound, M.P., French, A.P., 2014. An introduction to images and image analysis, in: Gupta, S.D., Ibaraki, Y. (Eds.), *Plant Image Analysis: Fundamentals and Applications*. CRC Press, p. 24. doi:10.1201/b17441

Power, J.F., Alessi, J., 1978. Tiller development and yield of standard and semidwarf spring wheat varieties as affected by nitrogen fertilizer. *J. Agric. Sci.* 90, 97–108. doi:10.1017/S0021859600048632

Prieto-Blanco, X., Montero-Orille, C., Couce, B., de la Fuente, R., 2008. Optical Configurations for Imaging Spectrometers, in: Graña, M., Duro, R.J. (Eds.), *Studies in Computational Intelligence, Studies in Computational Intelligence*. Springer Berlin Heidelberg, Berlin, Heidelberg, pp. 1–25. doi:10.1007/978-3-540-79353-3\_1

Rasmussen, J., Ntakos, G., Nielsen, J., Svensgaard, J., Poulsen, R.N., Christensen, S., 2016. Are vegetation indices derived from consumer-grade cameras mounted on UAVs sufficiently reliable for assessing experimental plots? *Eur. J. Agron.* 74, 75–92. doi:10.1016/j.eja.2015.11.026

Richards, R.A., Rebetzke, G.J., Condon, A.G., van Herwaarden, A.F., 2002. Breeding Opportunities for Increasing the Efficiency of Water Use and Crop Yield in Temperate Cereals. *Crop Sci.* 42, 111.

doi:10.2135/cropsci2002.0111

Robertson, A.R., 1977. The CIE 1976 Color-Difference Formulae. *Color Res.*

*Appl.* 2, 7–11. doi:10.1002/j.1520-6378.1977.tb00104.x

Sankaran, S., Khot, L.R., Espinoza, C.Z., Jarolmasjed, S., Sathuvalli, V.R., Vandemark, G.J., Miklas, P.N., Carter, A.H., Pumphrey, M.O., Knowles, R.R.N., Pavek, M.J., 2015. Low-altitude, high-resolution aerial imaging systems for row and field crop phenotyping: A review. *Eur. J. Agron.* 70, 112–123. doi:10.1016/j.eja.2015.07.004

Schils, R., Olesen, J.E., Kersebaum, K.C., Rijk, B., Oberforster, M., Kalyada, V., Khitrykau, M., Gobin, A., Kirchev, H., Manolova, V., Manolov, I., Trnka, M., Hlavinka, P., Paluoso, T., Peltonen-Sainio, P., Jauhiainen, L., Lorgeou, J., Marrou, H., Danalatos, N., Archontoulis, S., Fodor, N., Spink, J., Roggero, P.P., Bassu, S., Pulina, A., Seehusen, T., Uhlen, A.K., Żyłowska, K., Nieróbca, A., Kozyra, J., Silva, J.V., Maçãs, B.M., Coutinho, J., Ion, V., Takáč, J., Mínguez, M.I., Eckersten, H., Levy, L., Herrera, J.M., Hiltbrunner, J., Kryvobok, O., Kryvoshein, O., Sylvester-Bradley, R., Kindred, D., Topp, C.F.E., Boogaard, H., de Groot, H., Lesschen, J.P., van Bussel, L., Wolf, J., Zijlstra, M., van Loon, M.P., van Ittersum, M.K., 2018. Cereal yield gaps across Europe. *Eur. J. Agron.* 101, 109–120. doi:10.1016/j.eja.2018.09.003

Schneider, C.A., Rasband, W.S., Eliceiri, K.W., 2012. NIH Image to ImageJ: 25 years of image analysis. *Nat Meth* 9, 671–675.

Sellar, G.R., Boreman, G.D., 2005. Classification of imaging spectrometers for remote sensing applications. *Opt. Eng.* 44, 013602. doi:10.1117/1.1813441

Sharma, J.R., 2006. *Statistical and Biometrical Techniques in Plant Breeding*. New Age International (P) Ltd., Publishers, New Delhi, India.

- Slafer, G.A., Savin, R., 2007. Physiology of Crop Yield, in: Encyclopedia of Plant and Crop Science. Taylor & Francis, New York, pp. 1–4.  
doi:10.1081/E-EPCS-120029758
- Slafer, G.A., Savin, R., Sadras, V.O., 2014. Coarse and fine regulation of wheat yield components in response to genotype and environment. *F. Crop. Res.* 157, 71–83. doi:10.1016/j.fcr.2013.12.004
- Sonka, M., Hlavac, V., Boyle, R., 1993. Image pre-processing, in: Image Processing, Analysis and Machine Vision. Springer US, Boston, MA, pp. 56–111. doi:10.1007/978-1-4899-3216-7\_4
- Stajanko, D., Lakota, M., Hočevár, M., 2004. Estimation of number and diameter of apple fruits in an orchard during the growing season by thermal imaging. *Comput. Electron. Agric.* 42, 31–42. doi:10.1016/S0168-1699(03)00086-3
- Stone, P., Nicolas, M., 1995. A survey of the effects of high temperature during grain filling on yield and quality of 75 wheat cultivars. *Aust. J. Agric. Res.* 46, 475. doi:10.1071/AR9950475
- Sugiura, R., Fukagawa, T., Noguchi, N., 2003. Field Information System Using an Agricultural 1073–1078.
- Tattaris, M., Reynolds, M.P., Chapman, S.C., 2016. A Direct Comparison of Remote Sensing Approaches for High-Throughput Phenotyping in Plant Breeding. *Front. Plant Sci.* 7, 1–9. doi:10.3389/fpls.2016.01131
- Thapa, S., Jessup, K.E., Pradhan, G.P., Rudd, J.C., Liu, S., Mahan, J.R., Devkota, R.N., Baker, J.A., Xue, Q., 2018. Canopy temperature depression at grain filling correlates to winter wheat yield in the U.S. Southern High Plains. *F. Crop. Res.* 217, 11–19. doi:10.1016/j.fcr.2017.12.005
- Tyagi, V., 2018. Understanding Digital Image Processing, Deep Learning for

- Image Processing Applications. CRC Press. doi:10.1201/9781315123905
- Vasuki, A., Govindaraju, S., 2017. Deep Neural Networks for Image Classification, in: Hemanth, D.J., Estrela, V.V. (Eds.), Deep Learning for Image Processing Applications. IOS Press, pp. 27–49.
- Vergara-Diaz, O., Kefauver, S.C., Elazab, A., Nieto-Taladriz, M.T., Araus, J.L., 2015. Grain yield losses in yellow-rusted durum wheat estimated using digital and conventional parameters under field conditions. *Crop J.* 3, 200–210. doi:10.1016/j.cj.2015.03.003
- Vicente, R., Vergara-Díaz, O., Medina, S., Chairi, F., Kefauver, S.C., Bort, J., Serret, M.D., Aparicio, N., Araus, J.L., 2018. Durum wheat ears perform better than the flag leaves under water stress: Gene expression and physiological evidence. *Environ. Exp. Bot.* 153, 271–285. doi:10.1016/j.envexpbot.2018.06.004
- Virlet, N., Sabermanesh, K., Sadeghi-Tehran, P., Hawkesford, M.J., 2017. Field Scanalyzer: An automated robotic field phenotyping platform for detailed crop monitoring. *Funct. Plant Biol.* 44, 143–153. doi:10.1071/FP16163
- Wang, J., Vanga, S., Saxena, R., Orsat, V., Raghavan, V., 2018. Effect of Climate Change on the Yield of Cereal Crops: A Review. *Climate* 6, 41. doi:10.3390/cli6020041
- Wang, Y., Wang, D., Zhang, G., Wang, J., 2013. Estimating nitrogen status of rice using the image segmentation of G-R thresholding method. *F. Crop. Res.* 149, 33–39. doi:10.1016/j.fcr.2013.04.007
- Woebbecke, D.M., Meyer, G.E., Bargaen, K. Von, Mortensen, D.A., 1995. Shape Features for Identifying Young Weeds Using Image Analysis. *Trans. ASAE* 38, 271–281. doi:10.13031/2013.27839



- Yang, G., Liu, J., Zhao, C., Li, Zhenhong, Huang, Y., Yu, H., Xu, B., Yang, X., Zhu, D., Zhang, X., Zhang, R., Feng, H., Zhao, X., Li, Zhenhai, Li, H., Yang, H., 2017. Unmanned Aerial Vehicle Remote Sensing for Field-Based Crop Phenotyping: Current Status and Perspectives. *Front. Plant Sci.* 8. doi:10.3389/fpls.2017.01111
- Yol, E., Toker, C., Uzun, B., 2015. Traits for Phenotyping, in: Kumar, J., Pratap, A., Kumar, S. (Eds.), *Phenomics in Crop Plants: Trends, Options and Limitations*. Springer India, New Delhi, pp. 11–26. doi:10.1007/978-81-322-2226-2\_2
- Yu, K., Kirchgessner, N., Grieder, C., Walter, A., Hund, A., 2017. An image analysis pipeline for automated classification of imaging light conditions and for quantification of wheat canopy cover time series in field phenotyping. *Plant Methods* 13, 15. doi:10.1186/s13007-017-0168-4
- Zadoks, J., Chang, T., Konzak, C., 1974. A decimal growth code for the growth stages of cereals. *Weed Res.* 14, 415–421.
- Zheng, Q., Huang, W., Cui, X., Shi, Y., Liu, L., 2018. New spectral index for detecting wheat yellow rust using sentinel-2 multispectral imagery. *Sensors (Switzerland)* 18, 1–19. doi:10.3390/s18030868
- Zhou, C., Liang, D., Yang, X., Xu, B., Yang, G., 2018a. Recognition of wheat spike from field based phenotype platform using multi-sensor fusion and improved maximum entropy segmentation algorithms. *Remote Sens.* 10. doi:10.3390/rs10020246
- Zhou, C., Liang, D., Yang, X., Yang, H., Yue, J., Yang, G., 2018b. Wheat Ears Counting in Field Conditions Based on Multi-Feature Optimization and TWSVM. *Front. Plant Sci.* 9. doi:10.3389/fpls.2018.01024

Zhu, Y., Cao, Z., Lu, H., Li, Y., Xiao, Y., 2016. In-field automatic observation of wheat heading stage using computer vision. *Biosyst. Eng.* 143, 28–41.

doi:10.1016/j.biosystemseng.2015.12.015





